UNIVERSITY OF SOUTHAMPTON

FACULTY OF ENGINEERING, SCIENCE AND MATHEMATICS

School of Chemistry

Characterisation of PtMo and PtW electrocatalysts for fuel cells using *in-situ* XAS and INS techniques

by

Colin Ross King

Thesis for the degree of Doctor of Philosophy

January 2007

UNIVERSITY OF SOUTHAMPTON

ABSTRACT

FACULTY OF ENGINEERING, SCIENCE AND MATHEMATICS

School of Chemistry

Doctor of Philosophy

CHARACTERISATION OF PtMo AND PtW ELECTROCATAYSTS FOR FUEL CELLS USING *IN-SITU* XAS AND INS TECHNIQUES

By Colin Ross King

The continuing development of catalysts for hydrogen oxidation in Polymer Electrolyte Membrane Fuel Cells (PEMFCs) requires a greater understanding of the catalyst structure and how this relates to the performance, as well as knowledge of the mechanism taking place.

The electrocatalytic activity of a series of carbon supported PtMo and PtW anode catalysts towards the electro-oxidation of CO and oxidation of methanol was studied. An *in situ* X-ray Absorption Spectroscopy (XAS) mini cell was used in order to obtain data using fluorescence detection. It was found that catalysts prepared by the co-deposited method were the most well-mixed, although not at all alloyed, with the samples consisting of Pt-rich cores with oxides of the secondary metal being prominent at the surface. Operating conditions were seen to be significant, with the co-deposited PtMo samples capable of being oxidised with potential in both half cell and mini cell conditions. A PtMo catalyst with a 2: 1 ratio had the highest activity for hydrogen oxidation when operating with reformate fuel streams. Preparation of a surface modified PtMo/C catalyst was achieved using an organometallic precursor and found to offer good control of the deposition of the Mo.

Inelastic Neutron Scattering (INS) studies were carried out on Pt and PtMo-based electrocatalysts to investigate the interactions of the H_2 molecule with hydrogen and carbon monoxide modified surfaces. For the Pt/C catalyst it was found that the hydrogen atoms are located predominantly in hollow (three-fold) sites on Pt(111), with some contribution from hydrogen on multi-fold adsorption sites on a Pt(110) plane. Dihydrogen molecules were seen to interact strongly with the H/Pt surface for the Pt and PtMo based catalysts, while only a weak interaction was observed with the carbon monoxide-modified surface.

Table of Contents

ACKNOWLEDGMENTS

Firstly, I would like to thank my supervisor, Dr. Andrea Russell, for all of her support and encouragement over the last four years, and particularly for those Thanksgiving dinners. I would also like to thank all those at Johnson Matthey who have helped me during my PhD: Dave Thompsett, Sarah Ball, Brian Theobald and Martin Hogarth. For their help at Daresbury, I would like to thank Bob Bilsborrow and Chris Corrigan. Thanks also to Dr "Timmy" Ramirez-Cuesta and Dr Philip Mitchell for all of their help and support with the INS experiments and theory.

Thanks must also go to the many members of the Russell group, both past and present. Firstly, to Abbe for welcoming me into the group and showing that you don't have to be slightly crazy to work here, but it helps; and Richard for proving that it's possible to go swimming in the Daresbury canal and live to speak of it. The long service award of friendship must go to Helen, for putting up with me for the whole of my 8 years and Southampton, and still speaking to me at the end of it. Thanks also to Peter, fellow "dream team" member (and co-creator of Thunderball), for keeping me sane during the long night shifts at Daresbury by consistently thrashing me at Pool and Darts for three years straight; to Dave for introducing me to the dance I like to call "the funky grasshopper"; Kate, whose constant wedding talk has probably put me off for life, Suzanne for keeping me healthy (!), and to Fabrice for being the only person I know for whom one drink really is too much. I would also like to thank Chris, Sohrab and Gurgit for helping me to settle in when I first started, and also to Piotr, Gael, Praba and Dai. Thanks to you all for being such great friend over the years and making this such a fun place to work.

Finally, thanks to my family, who have been supportive throughout my whole university career, but will be equally pleased to know that I'm finally going to stop being a student and go out into that "real world" you keep telling me so much about.

Chapter One: Introduction

This chapter will briefly cover the development of fuel cell technology and introduce the theory behind their operation, as well as going into some detail on the current work involved in the area of catalyst development. More specific literature reviews closely related to the work undertaken for this project can be found at the start of the subsequent relevant chapters.

1 General introduction

1.1 The energy crisis

Global energy consumption is an ever-increasing phenomenon; one which cannot be allowed to continue unabated in its current form. For more than a hundred years, these growing demands for power have been met predominantly via the combustion of fossil fuels such as coal, petroleum and natural gas. At the start of the twentieth century when electricity was still in its infancy, and cars were merely a burgeoning technology, these fuels were seen as cheap and plentiful. Throughout the latter half of the last century, a gradual shift in perception has occurred that can be traced to two significant realisations. The first was that the advent and increased usage of new technologies meant that demands for power had increased more than anyone could have previously thought possible. Clearly there is only a finite stock of fossil fuel supplies and that once they begin to run low, the price will only increase. The second more pressing matter is the growing awareness of the detrimental effects that are being wreaked upon the environment. It is now known that the release of vast quantities of carbon dioxide gas into the atmosphere is playing a significant role in the process of global warming. This is compounded by the release of NO_x and SO_x compounds along with various forms of particulate matter that are harmful both to the environment and to the health and well-being of humans, plants and animals. Various governments around the world are now actively seeking to reduce their output of these pollutants. One notable example is that of California. Known to have the worst air pollution of any state in America through a combination of excessive car usage, coupled with the hot weather

and mountainous topography; recent legislation has been introduced with the aim of reducing the amount of harmful emissions. Part of this legislation stipulates that, by 2010, 10% of vehicles sold or rented in the state should be a Zero Emission Vehicle (ZEV) [1]. One proposed solution to this problem is the use of fuel cell powered vehicles.

1.2 The history of the fuel cell

The principle of the fuel cell was originally reported by Christian Friedrich Schoenbein in 1838. A system of hydrogen and oxygen filled in tubes was set up, which were immersed in dilute sulphuric acid and contained within them a platinum foil each. He observed that after disconnection from a current /voltage source, a potential was still observed between the platinum foils. In 1839, Sir William Grove reported a similar result [2]. Grove continued his experiments with the aim of showing that this process (a reversal of the electrolysis of water) could be used, in principle, to produce electricity. Three years later, he demonstrated the first lab-scale fuel cell, consisting of four glass cells filled with dilute sulphuric acid, which were coupled in series, and utilising thin platinum electrodes.

Fuel cell research continued over the course of the next hundred years, although without any real impetus for bringing working technology to the market. Fossil fuels were cheap and abundant, while the adverse environmental effects associated with their use were not yet fully appreciated. The next major innovation occurred during the 1930s when Francis Bacon began researching his own fuel cell system. In 1938, Bacon was able to demonstrate a working high pressure reversible cell [3]. The electrodes were made from nickel gauze and were activated by alternately oxidizing and reducing in air and hydrogen, respectively. A tube of asbestos soaked with 27 % potassium hydroxide solution served as a separator. Bacon continued his work over the course of the next twenty years, attempting to overcome technical challenges such as corrosion, and was finally able to demonstrate an operational fuel cell stack in 1959. At the same time, Pratt and Whitney sought to license the system and were soon able to adapt the technology to power the Apollo spacecraft. This Alkaline Fuel Cell (AFC) seemed a prudent choice at the time given that it would not only produce electricity, but provide

heating and generate water; the latter also being used to cool the shuttle compartments. Ultimately, the cost of such devices was considerable due to the large amount of precious metal catalyst required. This meant that the expansion of fuel cells from this niche market into the mainstream required developing new ways of lowering the overall cost. In addition, the AFC was found to be sensitive to the presence of carbon dioxide, as it would react with the alkaline electrolyte to produce carbonates. This required the fuel source to be pure hydrogen, whilst any carbon dioxide had to be removed from the air supply containing the oxygen.

Fuel cell research over the last fifty years has seen the development of several different kinds of fuel cell; operating at both low and high temperatures. Some of these will be discussed in more depth in section 2. Recent research has concentrated on improving the component materials, as well as lowering the amount of platinum used in the preparation of the electrodes, as this represents a significant cost factor. Considerable strides have been made in this area with the platinum loading of electrodes decreasing from about 4 mg cm^{-2} used in in the proton exchange membrane fuel cells (PEMFC) for the Gemini space flights, to about 0.4 mg cm^{-2} or less at present [4].

1.3 Applications

Continuing advances being made in fuel cell technology have led to increased interest in developing different systems for the automotive industry as well as for both stationary and portable power applications.

The introduction of the California environmental legislation has furthered the cause of using fuel cells as a power source for cars and buses. The PEMFC is currently the most promising choice for several reasons. These include low operating temperatures allowing rapid start-up, a solid polymer electrolyte that won't leak out of the cell and the highest efficiencies and power densities out of all the current fuel cell types. The first fuel cell car, developed by DaimlerChrysler and affiliates, was demonstrated in 1994.

2 Fuel Cell Principles

2.1 Fuel cell overview

Fuel cells, like batteries, are used to convert chemical energy into electrical energy without a combustion process. The fuel cell is not a closed system; it requires a continuous supply of fuel (commonly hydrogen or methanol) from an external source. In a PEMFC, for example, hydrogen is oxidized at the anode, yielding protons and electrons. The protons migrate through an ion-conducting electrolyte membrane to the cathode. This membrane is non-conducting for electrons, thereby forcing them to pass through an external load-carrying circuit. At the cathode, oxygen is reduced; combining with the protons and electrons to yield water. This process is shown schematically in figure 1:

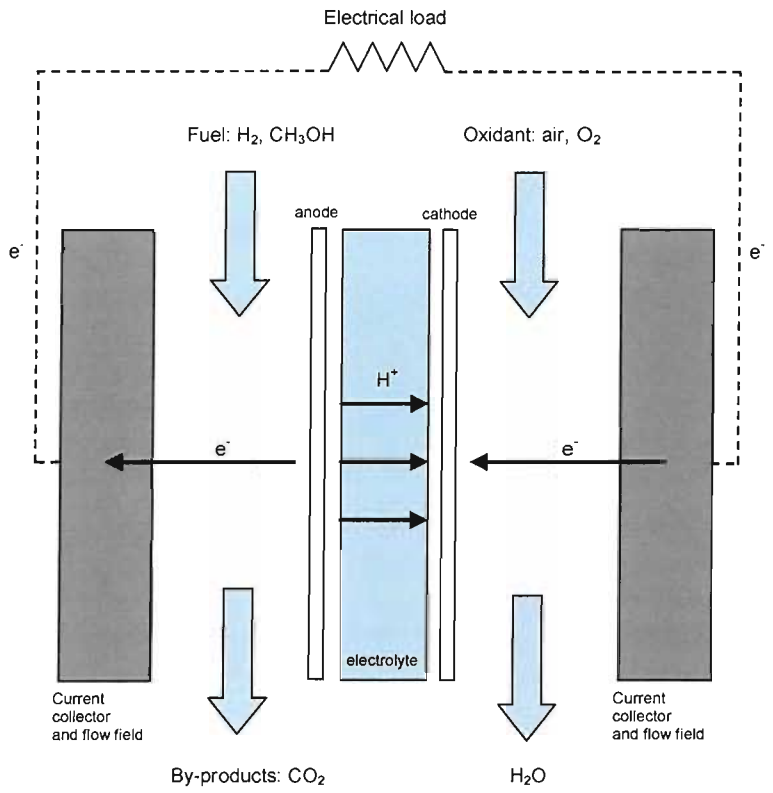

Figure 1 Schematic of a PEM fuel cell

The reaction at the anode is:

$$H_2 \longrightarrow 2H^+ + 2e^- \qquad E^0 = 0.0 \text{ V vs. RHE} \qquad \textbf{Eq. 1}$$

The reaction at the cathode is:

$$O_2 + 4H^+ + 4e^- \longrightarrow 2H_2O \qquad E^0 = 1.23 \text{ V vs. RHE} \qquad \textbf{Eq. 2}$$

The overall reaction can therefore be written as:

$$2H_2 + O_2 \longrightarrow 2H_2O \qquad E^0 = 1.23 \text{ V vs. RHE} \qquad \textbf{Eq. 3}$$

The maximum electrical energy obtainable and efficiencies of the system can be obtained using the basic thermodynamic equations for a reversible electrochemical transformation. The available electrical energy that can be obtained is related to the Gibbs free energy, as seen in equation 4:

$$\Delta G = -nFE \qquad \textbf{Eq. 4}$$

where ΔG is the Gibbs free energy (kJ mol^{-1}), n is the number of electrons transferred per mole of reactants, F is the Faraday constant (96485 C mol^{-1}), and E is the cell voltage for the specific chemical reaction [5].

The thermodynamic efficiency of the energy conversion requires consideration of the reaction enthalpy and entropy. These functions are related to the Gibbs free energy as seen in the Gibbs-Helmholtz relationship (see equation 5):

$$\Delta G = \Delta H - T\Delta S \qquad \textbf{Eq. 5}$$

The thermodynamic or ideal efficiency of energy conversion, ξ_{th}, is related to the reaction enthalpy by the following equation:

$$\xi_{th} = \frac{\Delta G}{\Delta H} = 1 - \frac{T\Delta S}{\Delta H} \qquad \textbf{Eq. 6}$$

If the thermal cell voltage is defined as $E_H^o = -\Delta H / nF$, then the thermodynamic efficiency can be expressed as:

$$\xi_{th} = \frac{E^o}{E_H^o} \qquad \textbf{Eq. 7}$$

For example, for the fuel cell reaction shown in equation 3, for standard conditions, E^o = 1.23 V and E_H^o = 1.48 V, giving ξ_{th} = 0.83 [6].

2.2 Types of fuel cell

There are several different types of fuel cell system. These vary in types of fuel required, the electrolyte that is used and the temperature at which they can operate effectively. This means that each system is better suited for a specific application. The fuel cells are defined by the type of electrolyte that they utilise.

2.2.1 Alkaline Fuel Cells (AFC)

The AFC was the first fuel cell system to be developed. During the 1960s, AFCs were used to generate electricity on board the Apollo and Gemini space missions, as described previously in section 1.2. It is a simple system operating with an aqueous KOH electrolyte, and requiring pure H_2 as a fuel. It operates at temperatures of around 70 °C, classifying this as a low-temperature fuel cell system. Hydroxyl ions diffuse continuously from the cathode to the anode. Once there, they react with hydrogen producing electrons and water. The water travels from the anode to the cathode where it reacts with oxygen and the incoming electrons to regenerate hydroxyl ions. The oxygen reduction kinetics are considerably faster in an alkaline electrolyte than in acidic media, making the AFC a relatively efficient system [7]. The major disadvantage, however, is the sensitivity of the electrolyte to the presence of CO_2. Hydroxyl ions react with CO_2 to form carbonates, which are not very soluble in strong

alkaline environments. Solid carbonate crystals can then block the electrolyte pathways [8]. AFCs must, therefore, operate with pure reactant gases, H_2 and O_2, which increases their difficulty and cost of operation. This makes these types of system suitable for niche markets like the space program and defense applications, although greatly limits their usefulness in mass market commercial applications.

2.2.2 Phosphoric Acid Fuel Cells (PAFC)

The PAFC was first tested in the 1970s and has been extensively studied. This system was developed as part of a drive to develop a fuel cell with a much higher CO_2 tolerance compared with the AFC, enabling the use of air as a supply of oxidant gas, and reformate as the supply of hydrogen. While phosphoric acid is only partially dissociated at room temperature, leading to very low conductivity; at temperatures above 150 °C, the conductivity is greatly increased. The PAFC is classified as a low-temperature fuel cell, although operating at close to 200 °C requires a longer warm-up time. This, coupled with the use of a highly corrosive electrolyte, requires a complex system design making these cells large, heavy and expensive. Despite this, these cells have become commercially available, mostly as large stationary power units, and increasingly for smaller local combined heat and power (CHP) systems for buildings such as hospitals.

2.2.3 Molten Carbonate Fuel Cells (MCFC)

The MCFC is a high-temperature fuel cell; commonly operated at temperatures of 650 to 700 °C. The electrolyte is a mixture of Li_2CO_3 and K_2CO_3, stabilised in a $LiAlO_2$ matrix. At high temperatures, the salts become molten and conductive to carbonate ions. At the anode, these ions combine with hydrogen to produce carbon dioxide, water and electrons. The CO_2 evolved at the anode is transferred to the cathode where it reacts with oxygen and electrons to form more carbonate ions. Oxygen reduction kinetics are greatly accelerated compared with a PAFC because of the higher temperatures involved, allowing the use of cheaper catalysts with lower noble metal loadings. The MCFC can operate with a variety of fuels; the high operating temperature negates the need for a separate fuel processor as the cell itself can act as an

internal reformer, directly converting hydrocarbons and petroleum-based fuels into hydrogen. The high operating temperature also makes these cells more tolerant to the presence of CO, which can poison the catalyst when adsorbed on the surface. Increased complexity of cell design due to the use of a molten electrolyte at high temperature again dictates a significant start-up time as well as being large in size. They are slow to respond to changes in electricity demand and, as such, are best suited to large stationary power applications.

2.2.4 Solid Oxide Fuel Cells (SOFC)

The second high-temperature system is the SOFC. These cells operate at even greater temperatures than the MCFC; typically 700 – 1000 °C. At these temperatures, oxygen reduction kinetic limitations become negligible. These cells utilise a solid ceramic electrolyte that shows very high conductivity to oxide ions, especially above 900 °C. The use of a solid electrolyte removes any problems of electrolyte leakage. The electrolyte is typically ZrO_2 stabilised with Y_2O_3. At the cathode, oxygen ions are produced which migrate to the anode where they combine with hydrogen. The main disadvantage with this type of system is finding suitable construction materials. The high temperatures can cause shortened operating lifetimes as thermal expansion effects and material instabilities become significant. Despite this, research is still on-going with the hope of eventually utilizing this technology in commercial applications; predominantly stationary power generation.

The other fuel cell system to be discussed is the Proton Exchange Membrane Fuel Cell (PEMFC). This will be discussed more fully in the next section.

3 Proton Exchange Membrane Fuel Cell (PEMFC)

3.1 Applications of a PEMFC

The PEMFC operates in a similar way to the SOFC in that it utilises a solid electrolyte. This takes the form of a proton-conducting solid polymer membrane. The most commonly employed membrane, Nafion®, only works below 150 °C as water losses above this temperature drastically reduce conduction. This system is therefore classified as a low temperature fuel cell. These cells were originally developed for use in the Gemini spacecraft, although the instability of the polystyrene sulphonate polymer used at the time led to NASA replacing this cell with the AFC for its later Apollo missions (as described in section 1.2). Improvements in the types of membrane used have led to the PEMFC rapidly becoming the desired system for automotive applications due to their small size and high performance. Ballard and Daimler-Chrysler have already demonstrated a series of NECARs that run on PEMFC technology and many European cities now have fuel cells buses in operation that store hydrogen in on-board compressed gas cylinders [9].

3.2 PEMFC structure

The core of the PEM fuel cell consists of a membrane electrode assembly (MEA), which is placed between two flow-field plates. These plates act as current collectors and the flow fields allow even distribution of fuel and oxygen to the electrodes. The MEA is made up of an anode and cathode, each coated on one side with a thin catalyst layer, and separated by the proton-conducting solid polymer electrolyte membrane. In order to provide sufficient voltage for the desired applications, these unit cells can be connected in series to form a fuel cell stack. Figure 2 shows an expanded diagram of a PEMFC stack and unit cell.

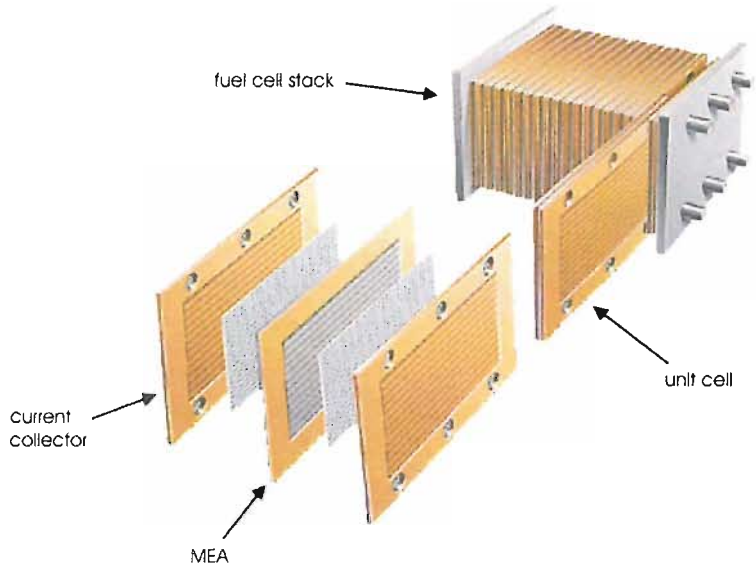

Figure 2 **Expanded view showing the structure of a fuel cell stack and unit cell for a PEMFC [10]**

3.3 Fuels for use with PEMFCs

3.3.1 Hydrogen

As described in section 2.1, a PEMFC requires a hydrogen fuel source. The hydrogen is electrochemically oxidized at the anode; being converted in the process into protons and electrons. The protons migrate through the membrane, while the electrons travel around an external circuit. The use of pure hydrogen as a fuel presents a problem with regard to its storage because it exists as a gas at standard temperature and pressure. Hydrogen is commonly stored in compressed gas cylinders. While this is a reasonable solution for fuel storage on buses, etc. the size and mass prove to be much more restrictive when dealing with smaller vehicles such as cars. A second alternative is to store hydrogen as a liquid by cryogenic means. In theory, the same amount of fuel can now be stored in a smaller volume. However, the fuel tanks must be extremely well-insulated; not to mention the significantly larger amount of energy required producing liquid hydrogen compared with storing it as a compressed gas. A third solution is the storing of hydrogen as metal hydrides. This is obviously a safer and more space-saving method of hydrogen storage, although at present the H-densities are not sufficient enough to compete with compressed gas storage [11]. Possible alternatives currently under investigation include graphite nanostructures, which can store hydrogen in

gaseous form within their crystal structure [12], and the use of zeolites. The latter can store hydrogen by using elevated temperatures and pressures to force hydrogen gas into the molecular sieves [7]. The hydrogen is then trapped by cooling the matrix and can be released when required by heating. So far, potassium zeolites have been found to store more hydrogen than rubidium– and sodium zeolites [13].

3.3.2 Reformate

One solution to getting around the problems with storing and supplying pure hydrogen to a PEMFC is to use reformate. Basically, this allows the use of liquid hydrocarbon fuels that can be stored with greater ease. The fuel cell is now fitted with a fuel reformer, which will convert the liquid fuel into hydrogen ready for use at the anode. The fuel, or reformate, supplied by the reformer is predominantly hydrogen, however significant quantities of various by-products such as CO_2 and CO constitute part of the fuel stream. This can be explained by studying the methods by which methanol can be converted into hydrogen.

One method is partial oxidation, as seen in equation 8:

$$CH_3OH + \tfrac{1}{2}O_2 \longrightarrow CO_2 + 2H_2 \qquad \textbf{Eq. 8}$$

This is an exothermic reaction involving partial burning of the fuel in oxygen, yielding carbon dioxide and hydrogen.

The other method is steam reforming, as seen in equation 9 for methanol:

$$CH_3OH + H_2O \longrightarrow CO_2 + 3H_2 \qquad \textbf{Eq. 9}$$

This is the overall equation for the process that begins with methanol vapour being passed over a catalyst, splitting it into CO and hydrogen. Water vapour then oxidises the CO, yielding CO_2 and some additional hydrogen. This process yields three molar equivalents of hydrogen per mole of methanol compared with two when using partial

oxidation. Unfortunately, steam reforming is an endothermic reaction requiring an input of energy.

The major drawback with using reformate results from the reverse water gas shift reaction converting some of the carbon dioxide and hydrogen into carbon monoxide and water (the back reaction seen in equation 10):

$$CO + H_2O \leftrightarrow CO_2 + H_2 \qquad \textbf{Eq. 10}$$

Even the small amount of CO present in a typical reformate fuel stream (0.5 to 2 %) will drastically lower the performance of a PEMFC. CO acts as a poisoning species by strongly binding to Pt catalytic sites, effectively blocking them from use by the hydrogen molecules. The amount of CO can be greatly lowered by the use of a water gas shift reactor to convert CO back into CO_2 and more hydrogen. This involves heating above 200 °C and passing the gas over CuO/ZnO catalysts. Selective catalytic oxidiation methods can also be used to lower the CO concentration further. Unfortunately, the use of a reformer with a fuel cell increases the cost and complexity of the overall system; a problem only exasperated by the need for additional shift and selective oxidation reactors.

3.3.3 Methanol

The most desirable fuel cell system is one which can be supplied with a liquid fuel, such as methanol, and be able to convert this fuel into useful power at the anode directly. The Direct Methanol Fuel Cell (DMFC) is currently the most promising system of this type. The technology is essentially the same as a PEMFC, however the catalyst is used to oxidize methanol directly, rather than requiring the fuel to first be converted into hydrogen. This negates the need for a reformer, reducing the cost, size and complexity of the overall system. The use of a liquid fuel, as seen with the reformer system, allows much greater ease when it comes to storage and transport compared with hydrogen gas. A further advantage of the DMFC with regard to the hydrogen and reformate PEMFCs, is that it no longer requires complicated

humidification and heat management hardware modules, as this is now provided by the dilute methanol-water mixture circulating around the system [14].

The reactions at the anode and cathode can be seen in equations 11 and 12 respectively:

$$CH_3OH + H_2O \longrightarrow CO_2 + 6H^+ + 6e^- \qquad E^0 = 0.046 \text{ V vs. RHE} \qquad \textbf{Eq. 11}$$

$$3/2O_2 + 6H^+ \longrightarrow 3H_2O \qquad E^0 = 1.23 \text{ V vs. RHE} \qquad \textbf{Eq. 12}$$

The overall reaction is therefore:

$$CH_3OH + H_2O + 3/2O_2 \longrightarrow CO_2 + 3H_2O \qquad E^0 = 1.18 \text{ V vs. RHE} \qquad \textbf{Eq. 13}$$

The ideal efficiency, ξ_{th}, for this process is 0.97 [6]. Despite this, the power density that can be achieved by the DMFC is currently significantly lower when compared to a PEMFC operating with hydrogen. There are a number of potential problems with DMFCs that lead to performance losses. As in the PEMFC, the kinetics of oxygen reduction at the cathode are low (see section 3.7, this chapter). Further kinetic losses occur at the anode due to poor electrochemical activity. This is the result of the oxidation of methanol on platinum being a less facile process than the corresponding catalytic oxidation of hydrogen. The mechanism for methanol electrooxidation is believed to occur via several steps. The methanol is first adsorbed onto the catalyst surface, followed by the sequential stripping of protons and electrons, as seen in equations 14-18. The adsorption of methanol requires several neighbouring catalyst sites to be available, i.e. free from hydrogen. This occurs near 0.2 V vs. RHE on polycrystalline Pt.

$$Pt + CH_3OH \longrightarrow Pt - (CH_3OH)_{ads} \qquad \textbf{Eq. 14}$$

$$Pt - (CH_3OH)_{ads} \longrightarrow Pt - (CH_2OH)_{ads} + H^+ + e^- \qquad \textbf{Eq. 15}$$

$$Pt - (CH_3O)_{ads} \longrightarrow Pt - (CHOH)_{ads} + H^+ + e^- \quad \textbf{Eq. 16}$$

$$Pt - (CH_2O)_{ads} \longrightarrow Pt - (COH)_{ads} + H^+ + e^- \quad \textbf{Eq. 17}$$

$$Pt - (CHO)_{ads} \longrightarrow Pt - (CO)_{ads} + H^+ + e^- \quad \textbf{Eq. 18}$$

This process leads to the formation of carbon-containing intermediates, such as linearly bonded $-CO_{ads}$ and COH_{ads}, which have been detected spectroscopically [15,16]. The adsorbed CO will effectively poison the surface until oxygen species from the electrosorption and dissociation of water on neighbouring sites are provided to oxidize the CO to form CO_2. However, there is only a strong interaction between water and the catalyst surface at potentials above 0.4 – 0.45 V vs. RHE [17].

$$Pt + H_2O \longrightarrow Pt - OH_{ads} + H^+ + e^- \quad \textbf{Eq. 19}$$

The CO is then oxidized as seen in equation 20 [18]:

$$Pt - OH_{ads} + Pt - (CO)_{ads} \longrightarrow CO_2 + H^+ + e^- \quad \textbf{Eq. 20}$$

In order to counter these kinetic losses at the electrodes, unsupported catalysts are often used, typically with Pt loadings of 5 – 10 mg cm^{-2}. This is too high for mass-market commercial applications, so current research involves the development of more efficient catalysts that can match the PEMFC for performance and Pt loading.

A further problem with the DMFC is that of methanol crossover. The perflurosulfonic acid membranes that are currently in use are permeable to methanol; with the unfortunate effect that methanol can cross from the anode to the cathode via diffusion and electro-osmotic drag. This can result in electrochemical processes competing with the oxygen reduction reaction, creating a mixed potential effect that will lower the cathode efficiency. In addition, the methanol/water solution can effectively flood the cathode preventing effective diffusion of the air/oxygen gas stream to the electrode, resulting in mass transport losses. Increasing the membrane thickness can greatly

reduce the amount of methanol crossover, although this will inevitably increase the cell resistance requiring a trade-off between the two factors.

3.4 The membrane

PEMFCs utilise a solid polymer electrolyte (SPE) membrane that is proton-conducting and is sandwiched between the anode and cathode. The most important membrane of this type is the polymeric perfluorinated membrane known as Nafion®. Manufactured for over 35 years by DuPont, this membrane was the first commercial membrane; being used by the United States in their space and military enterprises. Nafion® has a polytetrafluoroethylene (PTFE)-based hydrophobic backbone with sulphonated hydrophilic sidechains, as seen in figure 3:

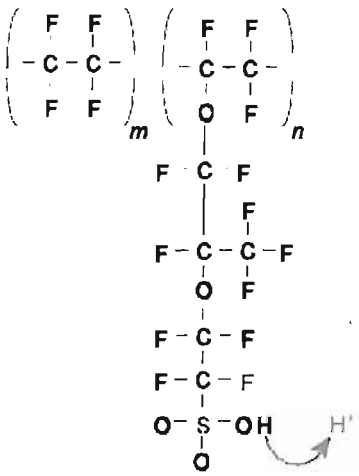

Figure 3 **Chemical structure of Nafion® where the ration *n* to *m* (i.e. active sites to inactive chain monomers) determines the acidity of the electrolyte.**

Perfluorinated membranes were able to overcome the degradation issues present with the polystyrene-divinylbenzene sulfonic acid membranes utilised in the Gemini Space Program, by virtue of the strength of the C-F bond over that of the C-H bond [19]. Charge transport occurs via proton transfer from one sulfonic acid group to the next, with the membrane itself being strongly hydrated in order to aid conduction. The high electronegativity of the fluorine atom, bonded to the same carbon as the SO_3H group leads to superacid properties, resulting in a two-fold increase in proton conductivity

with respect to the earlier polystyrene sulfonic acids [4]. In addition, Nafion is chemically inert in both reducing and oxidising environments [7].

Nafion membranes can be produced with a range of thicknesses. Initially, these were extrusion-cast films with thicknesses of 5 and 7 mm [20]. More recently, membranes with thicknesses of between 25 to 250 μm are being produced with the aim of reducing iR losses within the fuel cell. A number of groups have investigated the effects of using a range of different membrane thicknesses [21-23]. Predominantly, it was found that thinner membranes afforded better performance at high current densities; the greatest performance when operating at high temperatures (up to 80 °C). In addition, thinner membranes provide better water management characteristics with decreased flooding of the cathode. There is a limiting effect to how thin the membranes can be taken, however, as the crossover of reactant gases from one electrode to the other increases with thinner membranes.

Currently, efforts are taking place to improve the PEMFC membranes by decreasing their susceptibility to crossover effects when their thickness is reduced (a very significant problem with direct methanol fuel cells), and to increase their water-retaining abilities, as they have been found to dry out at higher operating temperatures, drastically reducing their conduction properties. Higher operating temperatures are desired because of the increased CO tolerance it provides. Research in these areas has led to the development of "hybrid" membranes whereby hydrophilic metal oxide particles, such as SiO_2 and TiO_2, are incorporated into the membrane [24,25].

3.5 Gas Diffusion Electrode

Platinum catalysts are the standard choice for use in PEM fuel cells due to the activity of Pt for both hydrogen oxidation at the anode and oxygen reduction at the cathode. The high cost of this metal prohibits the use of pure Pt catalysts so, instead, high surface area Pt nanoparticles supported on carbon (commonly XC72R) are utilised. Typical loadings vary between 10 and 60 wt. % Pt, with metal particle sizes of between 2 and 6 nm. These particle sizes give rise to high dispersions of Pt on the surface (typically 50 %), ensuring a large number of active sites available for catalysis. The

carbon support must also have high electrical conductivity, give good reactant access to the electrocatalysts, have good water handling capabilities, and, as with the Pt itself, be resistant to corrosion within the acidic operating environments [26].

To prepare the electrode, the catalyst is first mixed with an ionomeric binder (typically Nafion) to form an ink. This binder will ensure good contact between the catalyst and the solid polymer membrane it will be pressed against in the MEA. The ink is then applied to a gas diffusion layer, carbon paper for example; usually via screen printing, painting or manual spreading techniques. The arrangement of the electrode in this way maximises the three-phase boundary between the supply of gas, the catalyst particle and the ionic conductor.

A cross-section through a typical gas diffusion electrode can be seen in figure 4.

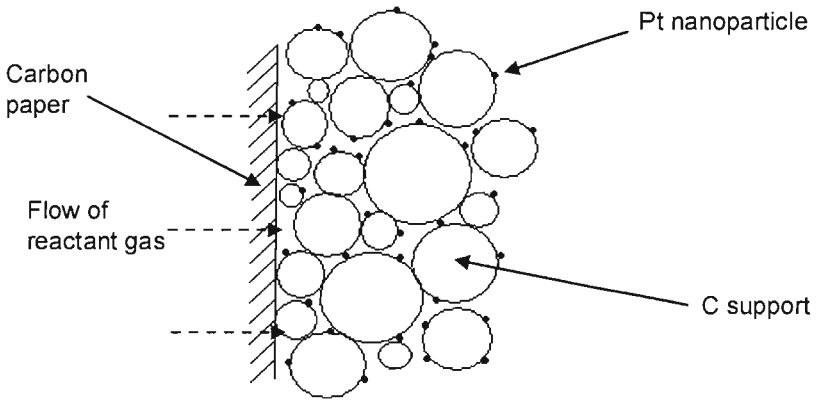

Figure 4 **Cross-section through a typical gas diffusion electrode**

3.6 Anode catalysts

The oxidation of hydrogen is an extremely facile process on platinum catalysts. However, the presence of even ppm amounts of CO can rapidly poison the platinum surface (section 3.3.2). CO is present as a by-product in reformate fuel streams and formed as an intermediate in methanol oxidation. In order to reduce the levels of CO, additional components to the fuel cell are required, such as shift reactors and catalytic preferential oxidation reactors. A second option is the development of catalysts that are more tolerant to the presence of CO. These catalysts tend to be carbon-supported Pt nanoparticles as before, modified by the addition of one or more secondary metals.

A large number of metals have been investigated including Ru, Mo, W, Co, Sn and Cr. The most well-known catalyst of this type is the PtRu alloy. MEAs containing this catalyst at the anode have been shown to have significantly higher current densities at all potentials than an MEA based on pure Pt when operating with reformate fuel streams containing ppm levels of CO [27], due to the lower overpotential for CO oxidation on PtRu mixtures [28].

The mechanism proposed for this enhancement is the bifunctional process first postulated by Watanabe *et al* [29] and involves water activation by Ru, leading to OH species:

$$Ru + H_2O \longrightarrow Ru - OH + H^+ + e^- \qquad \textbf{Eq. 21}$$

These OH species are then involved in the promotion of CO to CO_2 on neighbouring Pt sites.

$$Pt - CO + Ru - OH \longrightarrow CO_2 + H^+ + e^- + Pt + Ru \qquad \textbf{Eq. 22}$$

These alloy catalysts are also thought to operate via an intrinsic mechanism, whereby the addition of a secondary metal alters the chemisorption properties of the catalyst so that the CO coverage is lowered with respect to H_2 oxidation sites as a result of a weakening of the Pt-CO bond [30,31].

3.7 Cathode catalysts

Pt-based catalysts are also used for the oxygen reduction reaction (ORR) at the cathode of PEM fuel cells. The oxygen reduction reaction (ORR) in acid electrolytes can occur by a number of pathways. One of these is the direct four-electron pathway (equation 23):

$$O_2 + 4H^+ + 4e^- \longrightarrow 2H_2O \qquad E^0 = 1.23V \text{ vs RHE} \qquad \textbf{Eq. 23}$$

Alternatively, it can proceed by an indirect process beginning with a two-electron reduction reaction (equation 24), giving rise to the formation of hydrogen peroxide

$$O_2 + 2H^+ + 2e^- \longrightarrow H_2O_2 \qquad E^0 = 0.68V \text{ vs RHE} \qquad \textbf{Eq. 24}$$

This is followed by either a series two-electron reduction

$$H_2O_2 + 2H^+ + 2e^- \longrightarrow 2H_2O \qquad E^0 = 1.77V \text{ vs RHE} \qquad \textbf{Eq. 25}$$

or a chemical decomposition process:

$$2H_2O_2 \rightarrow 2H_2O + O_2 \qquad \textbf{Eq. 26}$$

The direct four-electron pathway is preferred in order to obtain maximum efficiency and avoids corrosion by peroxide species.

Unlike the hydrogen oxidation reaction at the anode, the kinetics for the ORR reaction are particularly slow, resulting in high overpotential losses at the cathode. This is the major limiting factor with current PEMFC technology. Current research aims to develop Pt-based cathode catalysts that are more active for the ORR than Pt alone, while aiming to ensure that it takes place via the direct four-electron pathway. As with the anode catalysts, the approach used is to alloy the platinum with a secondary metal. Work in the 1980s centred on Pt-based alloys for oxygen reduction in PAFCs, with many of the alloys tested showing higher kinetic performance than pure Pt analogues. A PtCr alloy was found to be the most stable catalytic system. This work carried over into PEMFCs, with Johnson Matthey testing a number of different systems such as PtFe, PtMn, PtNi, PtCr, PtZr and PtTi alloys. Leaching of the secondary metal proved to be a problem for the PtFe, PtMn and PtNi alloys [26], while the others showed no such leaching and demonstrated improved performance relative to platinum.

4 Project Aims and Objectives

The brief review of fuel cell technology presented in this chapter has described a number of problems currently facing the development of PEMFCs for future commercial use. The work presented in this thesis will concentrate on anode catalysts for hydrogen oxidation that show increased CO tolerance compared to pure Pt. A range of techniques will be used in order to test catalyst performances and elucidate the catalyst structure, as well as attempt to study the surface interactions that form part of the mechanism for hydrogen oxidation and how this is affected by the presence of CO.

PtMo and PtW catalysts have been found to show improved performance over pure Pt catalysts in terms of CO tolerance. The catalyst performances have been assessed using electrochemical techniques such as cyclic voltammetry and polarisation measurements carried out under liquid and solid polymer electrolyte environments. X-ray Absorption Spectroscopy (XAS) techniques have been used to study the structure of fuel cell catalysts. XAS provides information on the local coordination of the element under study, including type of neighbours, their number and distance relative to the absorbing atom. The nature of the XAS technique allows data to be collected *in situ*, whereby the environment of the catalyst samples can approximate those found in working fuel cells. Information obtained on catalyst performance in terms of the mechanism for CO electro-oxidation will be correlated with the structural information obtained from XAS techniques. Carbon-supported PtMo and PtW catalysts are characterised in chapters three and four respectively.

Inelastic Neutron Scattering (INS) allows the interactions of hydrogen with a catalyst surface to be probed; information not readily available by other spectroscopic techniques due to the low mass of the hydrogen atom. This is possible due to the high scattering cross section of hydrogen, which is greater than for any other element. *Ex situ* measurements have been made for Pt/C and PtMo/C, and a Mo modified Pt/C catalyst when dosed with dihydrogen, followed by poisoning the surface with CO, in an attempt to study the locations and strengths of interaction between hydrogen and the catalytic surface. These results are presented in chapter five.

5 References

1. Lloyd, A. C. *Journal of Power Sources* **2000**, *86*, 57.
2. Grove, W. R. *Philosophical Magazine* **1839**, *14*, 127.
3. Sandstede, G.; Cairns, E. J.; Bagotsky, V. S.; Wiesener, K. Chapter 12: History of low temperature fuel cells. In *Handbook of Fuel Cells - Volume 1: Fundamentals and Survey of Systems*; John Wiley and Sons, 2003.
4. Costamagna, P.; Srinivasan, S. *Journal of Power Sources* **2001**, *102*, 242.
5. Winter, M.; Brodd, R. J. *Chemical Reviews* **2004**, *104*, 4245.
6. Vielstich, W. Chapter 4: Ideal and effective efficiencies of cell reactions and comparison to carnot cycles. In *Handbook of Fuel Cells - Volume 1: Fundamentals, Technology and Applications*; John Wiley &Sons Ltd., 2003.
7. Carrette, L.; Friedrich, K. A.; Stimming, U. *Chemphyschem* **2000**, *1*, 162.
8. Cifrain, M.; Kordesch, K. Chapter 14: Hydrogen/oxygen (Air) fuel cells with alkaline electrolyte. In *Handbook of Fuel Cells - Volume 1: Fundamentals, Technology and Applications*; John Wiley & Sons, Ltd., 2003.
9. http://www.ballard.com.
10. http://www.xcellsis.com.
11. Sandrock, G. Chapter 8: Hydride storage. In *Handbook of Fuel Cells - Volume 3: Fuel Cell Technology and Applications Part 1*; John Wiley & Sons Ltd., 2003.
12. Liu, C.; Fan, Y. Y.; Liu, M.; Cong, H. T.; Cheng, H. M.; Dresselhaus, M. S. *Science* **1999**, *286*, 1127.
13. Weitkamp, J. Zeolites as Media for Hydrogen Storage. In *http://www.uni-stuttgart.de/sfb270/B7_E.htm*, 2000.
14. Hogarth, M. P.; Ralph, T. R. *Platinum metals Rev.* **2003**, *46*, 146.
15. Christensen, P. A.; Hamnett, A.; Munk, J.; Troughton, G. L. *Journal of Electroanalytical Chemistry* **1994**, *370*, 251.
16. Iwasita, T.; Nart, F. C. *Journal of Electroanalytical Chemistry* **1991**, *317*, 291.
17. Iwasita, T. *Electrochimica Acta* **2002**, *47*, 3663.
18. Hamnett, A. Chapter 18: Direct Methanol Fuel Cells (DMFC). In *Handbook of Fuel Cells - Volume 1: Fundamentals, Technology and Applications*; John Wiley &Sons Ltd., 2003.

19. Perry, M. L.; Fuller, T. F. *Journal of the Electrochemical Society* **2002**, *149*, S59.
20. Banerjee, S.; Curtin, D. E. *Journal of Fluorine Chemistry* **2004**, *125*, 1211.
21. Srinivasan, S.; Ticianelli, E. A.; Derouin, C. R.; Redondo, A. *Journal of Power Sources* **1988**, *22*, 359.
22. Tsampas, M. N.; Pikos, A.; Brosda, S.; Katsaounis, A.; Vayenas, C. G. *Electrochimica Acta* **2006**, *51*, 2743.
23. Freire, T. J. P.; Gonzalez, E. R. *Journal of Electroanalytical Chemistry* **2001**, *503*, 57.
24. Alberti, G.; Casciola, M. *Solid State Ionics* **2001**, *145*, 3.
25. Baradie, B.; Dodelet, J. P.; Guay, D. *Journal of Electroanalytical Chemistry* **2000**, *489*, 101.
26. Ralph, T. R.; Hogarth, M. P. *Platinum metals Rev.* **2002**, *46*, 3.
27. Ralph, T. R.; Hogarth, M. P. *Platinum metals Rev.* **2002**, *46*, 117.
28. Gasteiger, H. A.; Markovic, N. M.; Ross, P. N. *Journal of Physical Chemistry* **1995**, *99*, 8290.
29. Watanabe, M.; Motoo, S. *Journal of Electroanalytical Chemistry* **1975**, *60*, 275.
30. Hoogers, G.; Thompsett, D. *Cattech* **2000**, *3*, 106.
31. Igarashi, H.; Fujino, T.; Zhu, Y. M.; Uchida, H.; Watanabe, M. *Physical Chemistry Chemical Physics* **2001**, *3*, 306.

Chapter Two: Experimental Methods – Theory and Practice

This chapter will describe the experimental methods used, from the theoretical background to the practical methods employed. This will cover catalyst preparation and electrode fabrication, electrochemical techniques, X-Ray Absorption Spectroscopy and Inelastic Neutron Scattering.

1 Catalyst Preparation

This project has involved the testing of a variety of novel Pt-based electrocatalysts with the aim of finding improved catalysts for hydrogen and methanol oxidation at the anode in Proton Exchange Membrane fuel cells and Direct Methanol fuel cells. These catalysts were manufactured and provided by Johnson Matthey. However, Controlled Surface Modification techniques were used in the preparation of Pt/C catalysts with Mo deposited on the surface as part of this project.

1.1 Reagents and Materials

The known reagents and materials used in the manufacture of the catalysts and electrodes as well as their electrochemical testing can be found in Table 1:

Table 1 Materials and Reagents listed with supplier

Reagent / material	Supplier
Nafion® solution (5 wt. %) in alcohol	Aldrich
Nafion® solution (12.5 wt. %) aqueous	Johnson Matthey
Concentrated Sulphuric Acid (98 %)	Aldrich
Vulcan XC-72R carbon black	Cabot Corporation
Carbon paper TGPH-090	E-TEK, Inc.
Platinum supported on carbon	Johnson Matthey
Palladium supported on carbon	E-TEK, Inc.
Platinum-Molybdenum supported on carbon	Johnson Matthey
Platinum-Tungsten supported on carbon	Johnson Matthey
Platinum-Ruthenium supported on carbon	Johnson Matthey
CSR Molybdenum modified Platinum on carbon (when not prepared 'in-house')	Open University
Flemion® SH30 membrane	Asahi Glass, Co.
Molybdenyl acetoacetonate	Alfa Aesar
Toluene	Fisher Scientific
Hydrogen gas	BOC Gases
Carbon Monoxide gas	BOC Gases
5 % Hydrogen in nitrogen gas mixture	BOC Gases
Reformate	BOC Gases
Nitrogen gas	BOC Gases
Helium gas	BOC Gases

The water used in the fabrication of electrodes and in electrochemical tests was ion exchange treated using a Barnstead Nanopure system giving water with a measured resistivity of 18 MΩ cm.

1.2 Catalyst preparation

The catalysts used in this thesis were prepared by either Johnson Matthey using proprietary methods [1], or by Controlled Surface Modification techniques undertaken by both the Open University or 'in-house' as part of the work undertaken for this project.

1.2.1 Preparation of catalysts by Johnson Matthey

The catalysts supplied by Johnson Matthey are supported on carbon black (commonly XC72R). These supports are chosen because of their large mesoporous area (>75 m^2g^{-1}) and graphitic character giving good electronic conductivity [2]. Using unsupported Pt would be prohibitively expensive so the catalysts are carbon-supported using a high dispersion of Pt to obtain the desired active area. The electrocatalyst layers on the electrode need to be fairly thin (typically between 5 and 20 μm) to increase the rate of proton migration and reactant gas permeability, in turn minimizing the cell potential losses. Platinum loadings are therefore relatively high so as to keep the layer thickness down. Loadings of 10 – 40 wt. % Pt or above are typical, although the greater the chosen wt. %, the larger the typical Pt particle size. Essentially this can reduce the available metal area, so a method of producing the catalysts that provides a good dispersion of Pt is needed. To achieve this, Johnson Matthey use a preparation method whereby the Pt group metals are precipitated using chemical reduction and an aqueous slurry of carbon black support [1,3]. This has allowed particle sizes of less than 4 nm even when using a 40 wt. % loading. For the bimetallic catalysts (PtMo, PtW, etc.), both metals ideally should be in contact with each other. However, the catalyst should retain a high level of dispersion. In the case of PtMo, this is achieved by co-deposition of the platinum and a hydrous molybdenum oxide/hydroxide precipitate onto the carbon support followed by thermal reduction at elevated temperatures under inert gas flow [2]. Commonly, this would be 650 °C, 900 °C or 1000 °C under nitrogen, or occasionally 1000 °C under argon. These various heat treatments are used, not only to reduce the sample, but to try to control the level of alloying in the sample. The PtW samples were prepared by depositing tungsten onto a pre-formed Pt/carbon catalyst. These were then

annealed to 800 °C in a H_2/N_2 atmosphere before switching to argon and annealing completed at 1000 °C.

1.2.2 Preparation of CSR Molybdenum Modified Platinum

Controlled Surface Reaction (CSR) techniques were devised as a way of selectively depositing a second metal on the surface of Pt/C nanoparticles so as to control the relative location of the two metals. This is achieved via a selective surface reaction between an organometallic compound of the second metal (M_2-R), and the reduced surface of the first (M_1-H). $PtMoO_x/C$ catalysts have previously been prepared by Crabb *et al* [4] using tetraallyldimolybdenum as the organometallic precursor. The preparation and characterisation of this precursor has been reported by Cotton *et al* [5]. This compound is highly sensitive to air and moisture, necessitating the use of a glove box and an argon atmosphere in the preparation of the catalyst. The modification of the Pt/C surface involved the reduction under hydrogen of approximately 1 g of a 19.5 wt. % Pt/C sample at 473 K for 3 h. After purging in nitrogen, a solution of tetraallyldimolybdenum in ether was added to the reaction vessel and reacted under hydrogen for 12 h at room temperature, before being reduced at 373 K for 8 h, then at 473 K for 3 h. The catalyst was then washed with cold distilled water. The reaction was believed to proceed by the formation of an organometallic fragment of the molybdenum precursor on the platinum surface followed by the thermal decomposition of the resulting intermediate in a hydrogen atmosphere (as shown in equation 1):

$$PtH/C + Mo_2A_4 \rightarrow PtMo/C + 4C_3H_8 \qquad \textbf{Eq. 1}$$

where A = allyl group. The reaction progress was monitored by gas chromatography of the exhaust gas, which detected the presence of propane.

The second method described here was used to produce a 2:1 surface ratio PtMo catalyst by a Controlled Surface Reaction and was undertaken using a molybdenyl acetoacetonate organometallic precursor. This was chosen because this compound was not air sensitive so was easier to handle. In addition, the PtMo catalysts prepared using the former CSR method were found to have a much lower yield of Mo on the surface than expected. A suitable amount of 20 % Pt/C was weighed out (approximately 3 g)

and added to a round bottomed flask. Nitrogen was flowed over the sample at room temperature for 30 min. The sample was then heated at 200 °C under hydrogen for 4 h to reduce the sample. After cooling back to room temperature, the gas flow was switched back to nitrogen. The required amount of organometallic precursor required for a ½ monolayer was calculated using the following formula:

$$\text{Precursor} = \frac{\text{Pt fraction} * \text{Mass Pt/C} * \text{Dispersion} * \text{Monolayer} * \text{RMM precursor}}{\text{RAM of Pt}} \quad \textbf{Eq. 2}$$

In this instance, the Pt fraction (of a 20% Pt/C sample) was 0.2, the mass of Pt/C was 3 g, the dispersion was known to be 0.48 (i.e. almost half of all the Pt atoms are on the surface of the nanoparticle), the desired monolayer coverage is 0.5, the RMM of the precursor is 326.16 g mol^{-1} and the RAM of Pt is 195.08 g mol^{-1}.

A measured quantity of molybdenyl acetylacetonate (0.2350 g) was added to 100 mL toluene and sonicated in an ultra-sonic bath for 1 h, resulting in a yellow solution with a small amount remaining as a suspension. This was then transferred to a dropper attached to the reaction vessel (see figure 1):

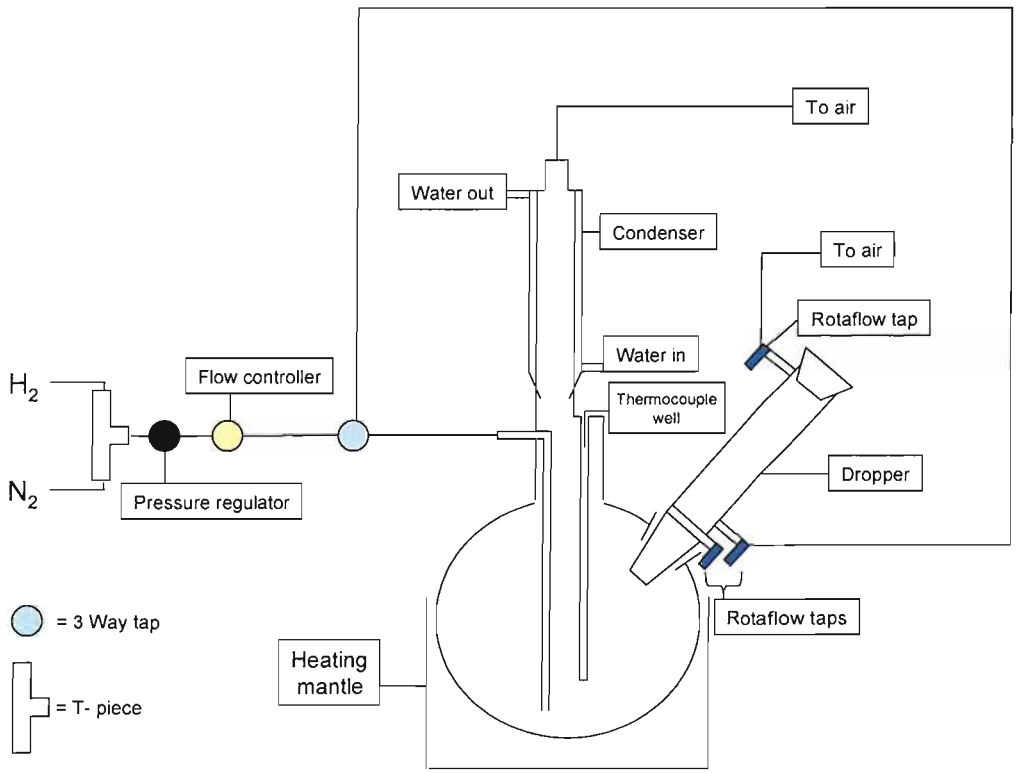

Figure 1 **Diagram of the reaction vessel set-up for the CSR catalyst preparation**

Nitrogen was purged through the toluene/precursor suspension for 20 min and then the solution added to the round-bottomed flask containing the pre-reduced Pt/C catalyst, whilst stirring under nitrogen. A colour change of yellow to brown/red was observed. The mixture was left purging with nitrogen overnight. Hydrogen was then flowed through the mixture at 80 °C for 8 h, with stirring. After cooling to room temperature, the mixture was purged with nitrogen for 20 min and then exposed to air. The solid catalyst sample was collected by filtration. The sample was heat treated to 200 °C under hydrogen for 3 h. A control experiment was performed using only the carbon support, where it was found that no reaction with the organometallic precursor took place, indicating that the Mo will only be deposited on Pt nanoparticles. It was assumed that by using a known quantity of Mo precursor as calculated in equation 2, a ½ monolayer of Mo would be deposited, all in contact with Pt sites and not forming any Mo multilayers.

For the purposes of testing a CSR molybdenum modified platinum sample using Inelastic Neutron Scattering, the reaction was scaled up in order to produce enough sample to obtain sufficient signal. Essentially the same procedure was followed; however larger quantities and reaction vessels were required. Purging times were doubled in order to adjust for the larger reaction vessel volume. 20 g of a 40 % Pt/C catalyst was taken and placed in a modified 1000 ml round bottomed flask and reduced under hydrogen. A measured quantity of molybdenyl acetylacetonate (1.728 g) was added to 500 mL toluene, and transferred into the round bottomed flask for the reaction to proceed as before. The time taken for the reaction to go to completion increased to 20 h.

1.3 Electrode Preparation

This section describes the preparation methods of the three main types of electrode used in this project. These include those used for electrochemical half cell measurements as well as those used for X-ray Absorption Spectroscopy (XAS) studies in both a half cell and a single cell (see section 3.2).

1.3.1 Preparation of button electrodes by paste spreading

Gas diffusion button electrodes for the purposes of catalyst testing using cyclic voltammetry were prepared using both a paste spreading and painting method. In both cases, the desired Pt loading is usually between 0.5 and 1 mg cm^{-2}. This section describes the paste spreading method, which can also be used to achieve metal loadings up to 5 mg cm^{-2} if necessary. A known quantity of catalyst that would give the required loading for the area to be prepared was weighed out and formed into an ink by the addition of 1 ml of distilled water and 15 % Nafion® in aqueous alcohol; the quantity of which was chosen to give a 85: 15 total catalyst to Nafion® solids mass ratio in the dried ink. The ink was mixed in an ultrasonic bath and allowed to slowly dry until it formed a thick paste, which was then spread evenly onto a 3 x 3 cm square area of pre-weighed carbon paper (TGPH-090) using a spatula and a metal template. This method involves the deposition of a relatively thick layer all at once. Once the catalyst layer has been spread onto the carbon paper, it is then placed between two pieces of greaseproof paper and pressed between metal plates. The pressure was held between 1.8 and 3 bar while increasing the temperature to 100 °C, then holding at 10 bar for 3 min. This process helps to spread the catalyst out more evenly and improves the binding of the electrode components as the ionomer flows at such temperatures. Circular electrodes of area 1.32 cm^2 were punched out and boiled in distilled water until they sunk when fully hydrated.

Larger electrodes of 2.54 cm^2 were required for use in the *in-situ* XAS half cell with accompanying higher loadings of 3 – 5 mg Pt cm^{-2}; used in order to obtain a suitable edge jump in the region of 0.3 - 1 (see section 3.1).

1.3.2 Preparation of button electrodes by painting method

The painting method was used for both the smaller half cell electrodes with lower metal loadings and also for making MEAs (see section 1.3.3, this chapter). The catalyst inks were prepared by taking a known amount of catalyst and adding 15 % Nafion® in aqueous alcohol such that the catalyst to Nafion® solids ratio was 70: 30 as required. Distilled water was added to make sure the ink was fluid enough to be painted. A Fisher Scientific Power Gen 125 homogeniser was then used to mix the ink. A circle of

carbon paper measuring 5.31 cm^2 was cut out and wetted with IPA before painting to help produce a smooth and even catalyst layer. The catalyst layer was painted on to the carbon paper using a small, fine paintbrush. After each layer was added, the electrode was heated on a hot plate at 120 °C for 10 – 20 s until the ink was dry. The carbon paper was then weighed each time. The desired weight for the correct loading was calculated using equation 3:

$$\text{Pt loading} = \frac{\text{ink weight/ g} \times \text{\% catalyst in dried layer} \times \text{\% Pt in catalyst}}{\text{electrodearea/ cm}^2} \qquad \textbf{Eq. 3}$$

Once the desired loading was achieved, the electrode was hot pressed as before, and button electrodes of 1.32 cm^2 were punched out as needed. Painting is used for achieving lower loadings; commonly 0.1 – 1 mg Pt cm^{-2}. By painting the ink while it is still fairly liquid, one layer at a time, a smoother and more even catalyst coating is produced. This method also makes it easier to obtain a desired loading.

1.3.3 MEA preparation

MEAs for XAS experiments were prepared by painting inks onto carbon paper circles (TGPH-090, 11 % PTFE) with an area of 12.57 cm^2. All catalysts under investigation for this project were for potential use as anode catalysts in working fuel cells. The inks were prepared using 45 wt. % Nafion® with respect to the total catalyst used. This was achieved by adding 2.0 g of 10 % Nafion® solution in water to 0.25 g of catalyst. The inks were then well-mixed using a Silverson (laboratory stirrer) for 5 min. Each carbon paper circle was first wetted using 10 % IPA solution in water, and the catalyst layers painted on using a fine paintbrush. After each coat, the electrode was placed on a hot plate for a few seconds at 120 °C to dry before weighing. The weights were used to calculate the loading based on equation 3. The catalyst coatings had to remain quite thin, while keeping the loadings as high as reasonably practical to obtain reasonable XAS data. Keeping the layer thin reduces the resistance effects and maximises the amount of Pt in contact with the fuel and electrolyte. Thicker layers also have a tendency to crack. To this end, Pt loadings of 1 mg cm^{-2} were used, although the loadings of the secondary metal would be inherently smaller. For the cathodes, inks were prepared of Pd / C; either a 33 wt. % Nafion® to total catalyst (20 wt. % Pd /

Shawinigan), or 45 wt. % Nafion® to total catalyst (10 wt. % Pd / Shawinigan). Pd was used because it is a good catalyst for dissociative adsorption of hydrogen in the same way as Pt. The presence of a H_2/H^+ redox couple makes this a suitable choice for a reference hydrogen electrode. Pd is not used as a cathode catalyst in real fuel cell systems because it is a much poorer oxygen reduction catalyst than Pt. The EXAFS information is required for the anode side only meaning that the cathode must not contain the same element of interest, or any element that has a similar absorption edge. The loadings used for the cathodes were 0.3 mg Pd cm^{-2}.

To produce an MEA, a 7 x 7 cm^2 square of Flemion® SH30 membrane was sandwiched between overlaying anode and cathode catalyst electrodes with the catalyst layers against the membrane. Flemion® membrane is similar to Nafion®, however it possesses a carboxylate functionality as opposed to a sulphonate functionality, and is believed to stay hydrated better than Nafion®). The MEA was then placed between PTFE and paper sheets and hot pressed at 150 °C, 230 psi for 2 min (see figure 2).

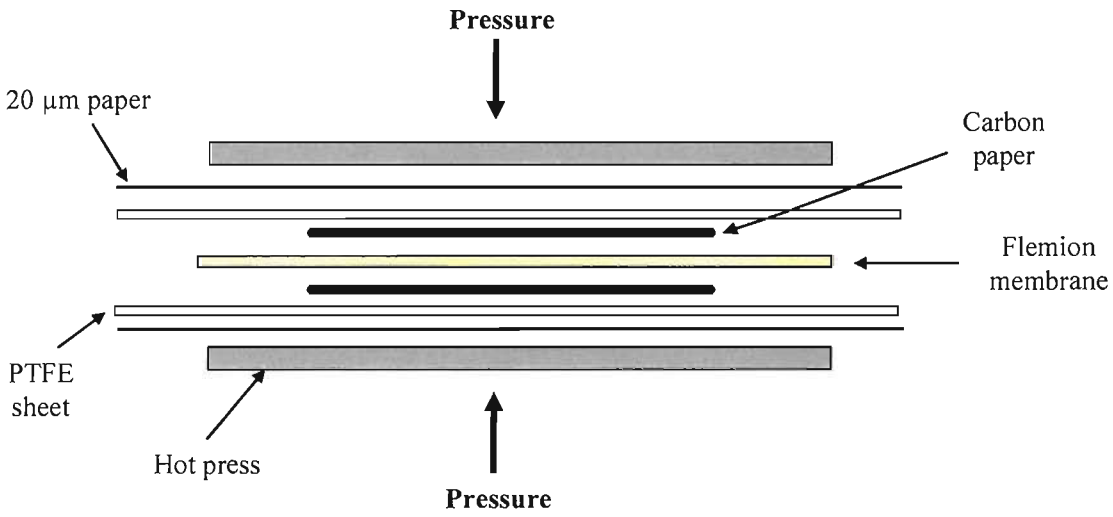

Figure 2 **Arrangement used for hot pressing MEAs showing positioning of PTFE sheet and 20μm paper used to ensure even compression**

MEAs were also prepared for the purposes of collecting electrochemical performance data in an *in situ* single cell. While the same basic procedure was employed, the ratio of catalyst to Nafion® solids was adjusted to 70: 30 and the anodes were prepared by painting on inks to give loadings of 0.22 mg Pt cm^{-2}. The cathodes consisted of carbon paper with a screen printed catalyst layer of 60 wt. % Pt/Shawinigan with a loading of 0.38 mg Pt cm^{-2}. Electrodes were punched out with an area of 3.14 cm^2.

2 Electrochemical Methods

Instrumental electrochemistry is an important technique used in the characterisation of the physical and electrical properties of the catalysts. Half-cell techniques involving cyclic voltammetry are used to calculate catalytic surface areas and probe adsorption processes. Catalyst performance can also be studied with polarisation curves whereby a potential is applied to an electrode and the stationary current response is measured after each potential step. These measurements are obtained in both half- and single-cell arrangements.

2.1 Linear Sweep and Cyclic Voltammetry

These two techniques involve the linear ramping of an applied potential with time. The simplest of these is Linear Sweep Voltammetry (LSV) where the electrode potential is swept from one potential to another in one direction (positive or negative) at a known sweep rate, *v*. The current response is then measured as a function of potential. The form that the current response takes will be representative of the specific charge transfer processes taking place on the surface of the working electrode.

Cyclic Voltammetry (CV) is the extension of Linear Sweep Voltammetry, whereby the potential is swept between two limits at a known sweep rate as before; with the scan direction reversing upon reaching the second potential limit and returning to the original potential. If so desired, this process can be continued many times. Cyclic voltammetry has been used in this project for determining the oxidation potential for carbon monoxide and using the corresponding stripping peak for calculating catalytic surface areas, as described below in section 2.2.5.

2.2 Apparatus and experimental procedure

This section describes the apparatus and experimental set-up for the collection of data using cyclic voltammetry. All of the electrodes used in the course of this work contain platinum, thus the method and interpretation involved will be illustrated by reference to a CV of a Pt disc electrode in acid.

2.2.1 Electrochemical cell

A three-electrode cell (see fig 3) was used with the Pt-based catalyst prepared as a button electrode (see section 1.3, this chapter) as the working electrode, platinum gauze as the counter electrode and a mercury mercurous sulphate (MMS) reference electrode.

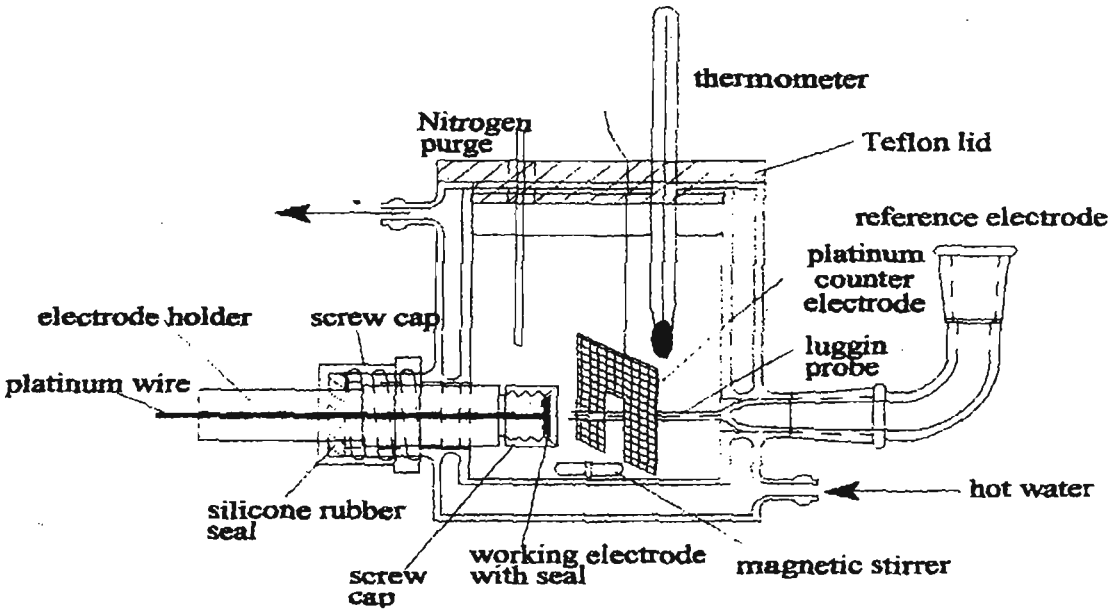

Figure 3 **Diagram of the three-electrode cell used for half cell testing of fuel cell electrodes [6]**

The electrode of interest was held in place by a screw-on flange so that it was positioned in contact with the Pt wire that was connected as the working electrode. The electrodes were connected to an Electrochemie Autolab PGSTAT30, which is a computer controlled combined potentiostat and waveform generator that controls the system. A three electrode system is required because, although only two electrodes are needed for a complete electrical circuit, measurement of any electrochemical processes becomes complicated as soon as any significant current is passed, such as potential drop across the cell due to the solution resistance and polarisation of the opposing electrode. The applied potential of the working electrode is therefore held relative to a stable reference electrode in order to be more accurately controlled, while the potentiostat controls the electronics to ensure that current passes from the working electrode to the counter electrode only. In the half-cell set-up, the reference electrode is used with a luggin capillary, which allows the potential between reference and working electrodes

to be measured over a very small distance (ideally a few mm), minimizing the effects of solution resistance (iR drop) [7].

The half cell reaction for the MMS reference electrode is:

$$Hg_2SO_4 + 2e^- \rightarrow 2Hg + SO_4^{2-} \qquad E^0 = 0.654 \text{ V vs. RHE} \qquad \textbf{Eq. 4}$$

All measured potentials are relative to this electrode and have been converted to potentials vs. RHE (reversible hydrogen electrode). The value for the reference potential can actually vary from electrode to electrode (anywhere from -0.6 to-0.7 V, resulting from temperature effects, absorption of organics, salt precipitation and small changes in sulphate concentration occurring over long periods due to migration across the salt bridge) so the reference electrodes must first be calibrated in order to provide accurate results. This is done before each experiment by placing the reference electrode in a beaker of 1M sulphuric acid, along with a Pt gauze electrode over which hydrogen gas is flowing, and measuring the potential between the two.

2.2.2 Practical procedure

The cell was set up as shown in figure 3. The electrolyte used was normally 2.5 M $H_2SO_{4\,(aq)}$, which was purged with nitrogen for twenty minutes before any experiments to displace dissolved oxygen. A stirrer bar was used to keep the solution well-mixed during purging, but was turned off when measurements were being taken. The experiment was then run with nitrogen gas flowing at low pressure over the surface of the electrolyte. The electrode was cycled between 0.0 and 1.0 V vs. RHE at 10 mV s^{-1} until a stable CV was reached, i.e. when no change was observed between two successive scans. This would yield a CV similar to that seen in figure 4.

In order to obtain information concerning the oxidation potential of carbon monoxide and the catalytic surface area, a CV was needed of a CO poisoned catalyst surface. This required a pre-treatment program to be set up. The electrode was held at 0.05 V vs. RHE for 60 min. For the first 30 min, CO was bubbled through the solution with stirring, followed by purging with nitrogen for the last 30 min to remove any dissolved CO from solution. This method should ensure that a full monolayer of CO would be

adsorbed onto the catalyst surface while ensuring that once it has been oxidized, no CO will be readsorbed back onto the surface on the following reverse scan. As before, the stirrer was turned off and nitrogen blown gently over the surface of the electrolyte, while a scan was recorded from 0.0 to 1.0 V vs. RHE.

2.2.3 Platinum disc cyclic voltammogram

Figure 4 shows a typical platinum CV obtained using a platinum disc electrode. This is a solid metal disc that is first polished manually using an aqueous slurry of alumina powder (1.0 μm, 0.3 μm and 0.05 μm particle sizes used successively) on a velvet pad in order to renew the surface and remove any adsorbed species. The features present can be split into three main regions. Below is a description of the processes that are taking place in each region.

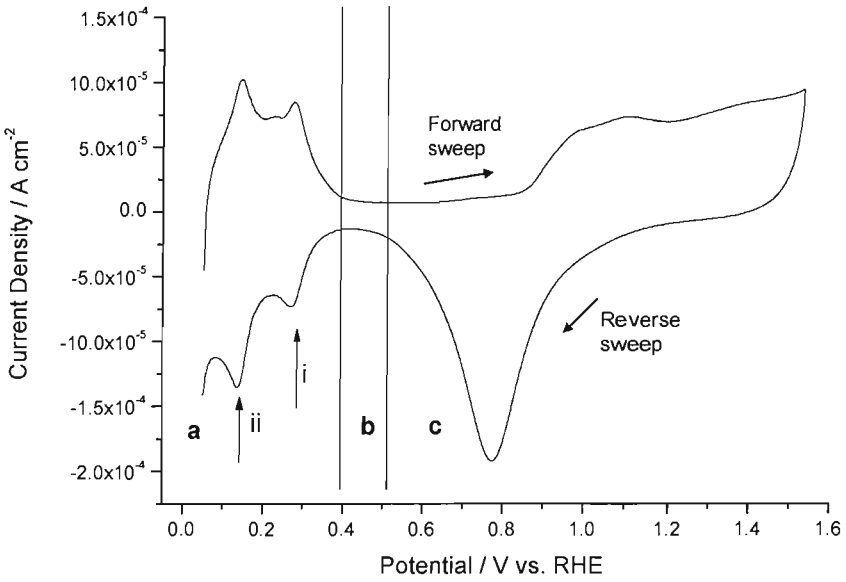

Figure 4 **CV of a 70 mm Pt disc electrode in 1 M H_2SO_4 at 100 mV s^{-1}; CV started at 0.05 V with an upper potential limit of 1.55 V vs RHE**

Region **a** is the **hydrogen region.** The peaks present correspond to adsorption (reverse scan) and desorption (forward scan) of hydrogen on the surface of the platinum. There are two distinct peaks, **i** and **ii**, which correspond to strongly and weakly adsorbed hydrogen respectively; i.e. peak **i** on the forward scan requires a more positive potential to oxidize the hydrogen from the surface. The increase in the current at ~ 0 V vs RHE

on the reverse scan indicates the evolution of molecular hydrogen, $H_{2(g)}$. The area underneath the hydrogen (H) adsorption or desorption peaks yields the charge involved in reduction or oxidation of a single monolayer of hydrogen. This area can be used to calculate the surface area of the platinum electrode. In practice however, only the adsorption peaks should be used for this type of calculation. This is because the area under the desorption peaks may include contribution from any H_2 trapped in the system after H_2 evolution, which is then reoxidized during the following forward scan. Equation 5 shows the adsorption process for hydrogen on platinum.

$$Pt + H^+ + e^- \rightarrow Pt\text{-}H_{ads} \qquad \textbf{Eq. 5}$$

Region **b** is the **double layer region.** This part of the CV shows the current flowing as a result of charging of the double layer by the ions in the electrolyte migrating to the electrode surface; no Faradaic processes are taking place. The charging current is proportional to the scan rate, ν, thus, if the scan rate is increased, the charging current also increases. This is observed as an increase in the separation of the forward and reverse sweeps as indicated by the arrows in region **b** of the diagram. To minimize this effect, slower scan rates are utilized; commonly 10 mV s^{-1} for this work.

Region **c** is the **oxide region.** This region begins between 0.8 and 0.9 V vs RHE when OH species from the water adsorb onto the platinum surface:

$$Pt + H_2O \rightarrow Pt - OH_{ads} + H^+ + e^- \qquad \textbf{Eq. 6}$$

Once a layer has formed, place exchange occurs, whereby oxygen moves into the bulk of the metal:

$$Pt\text{-}OH_{ads} \rightarrow PtO + H^+ + e^- \qquad \textbf{Eq. 7}$$

Further layers will then build up on the surface, which is why the current does not return to zero.

Upon reversing the sweep direction, the oxide stripping peak is found at 0.78 V vs. RHE. The position of the peak and the area underneath can vary depending on the

upper potential limit corresponding to the extent/depth of oxide formation. The stripping peak shifts to a slightly more negative potential for thicker oxide layers, as a greater driving force or a longer period of time is required to reduce a thicker oxide layer. The area under the oxide stripping peak can not be used for surface area measurement of Pt because the oxide forms a multilayer structure; not a monolayer.

2.2.4 Cyclic voltammogram of platinum poisoned by carbon monoxide

The effect of poisoning the catalyst surface with carbon monoxide can be seen in figure 5.

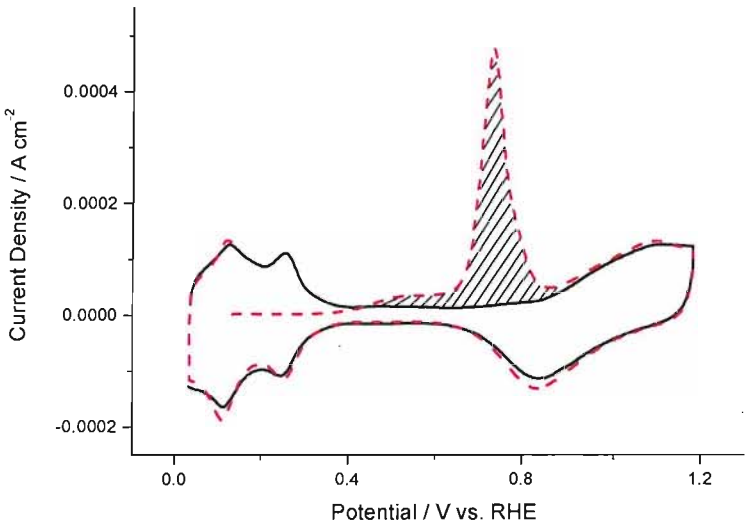

Figure 5 **CV of a platinum disc electrode in 1 M H_2SO_4 after a 30 min CO purge followed by a 30 min N_2 purge at 0.05 V vs RHE, scan rate = 10 mV s^{-1} Dotted (red) line: first scan; solid line: second scan. CV started at 0.125 V and cycled between 0.03 V and 1.20 V vs RHE**

On the first scan there are no longer any hydrogen desorption peaks on the forward scan. This region has been suppressed due to the presence of a complete (or almost complete) monolayer of carbon monoxide present on the surface, which has blocked all the available Pt sites preventing adsorption of hydrogen. The point at 0.43 V where the dotted line crosses the solid line is known as the onset potential, and is taken to be the point at which oxidation of CO_{ads} to CO_2 begins (see equation 8):

$$Pt - CO + H_2O \rightarrow Pt + CO_2 + 2H^+ + 2e^- \qquad E^0 = -0.10 \text{ V vs. RHE} \qquad \textbf{Eq. 8}$$

The peak maximum for this process is at 0.73 V vs. RHE. This is 0.83 V more positive than the standard reversible potential for this process. CO binds very strongly to Pt sites and a large overpotential is required due to the slow kinetics of CO oxidation. The peak position is used as a measure of the CO tolerance of a particular catalyst; higher tolerance being indicated by a shift to more negative potentials. On the reverse scan the surface is now free of CO allowing hydrogen to be adsorbed on the surface again. The second cycle of the CV has reverted back to that seen before any CO purging took place as evidenced by the return of the hydrogen desorption peaks on the forward scan.

2.2.5 Calculating catalytic surface area using the CO stripping peak

The carbon monoxide stripping peak can be used to calculate the platinum surface area. The area under the peak (denoted by shading) is equal to the charge. The charge passed should be double that obtained when measuring the hydrogen adsorption peaks because the oxidation of CO is a two-electron process. The CO oxidation peak is used because the catalysts investigated for this project often have redox peaks present in the cyclic voltammograms that overlap with the hydrogen adsorption peaks. The charge passed under the CO stripping peak is divided by the area of the electrode to give the charge passed per cm^2. The observed charge for a monolayer of linearly bonded CO on a planar electrode is 420 $\mu C\ cm^{-2}$ [8]. The surface area of Pt that is electrochemically active is calculated as seen in equation 9:

$$Pt_{area} = \frac{\text{Measured CO Charge } /\mu C}{420\ \mu C\ cm^{-2}\ Pt} \qquad \textbf{Eq. 9}$$

This value is then divided by the Pt loading in order to give the value for the active area of Pt per gram of Pt in the catalyst, which is known as the mass normalised area (Pt_{area_m}), as shown in equation 10:

$$Pt_{area_m}\left(m^2 Pt\ g^{-1} Pt\right) = \frac{Pt_{area} / cm^2 Pt}{\text{Pt loading}\left(mgPtcm^{-2}\right) \times \text{electrode area}\left(cm^2\right) * 10} \qquad \textbf{Eq. 10}$$

The mass normalised Pt area provides a useful measure of the active area of the catalyst electrode for comparison with other catalysts.

2.3 Polarisation

Polarisation refers to the difference between the thermodynamic cell voltage and the measured cell voltage. Steady state polarisation experiments have been undertaken as way of comparing the performance of different catalysts and identifying where inefficiencies arise. These experiments are carried out potentiostatically whereby a potential is applied to the electrode and the current response is measured once a steady state condition has been reached. Figure 6 shows a typical polarisation curve of cell voltage versus current for fuel cells:

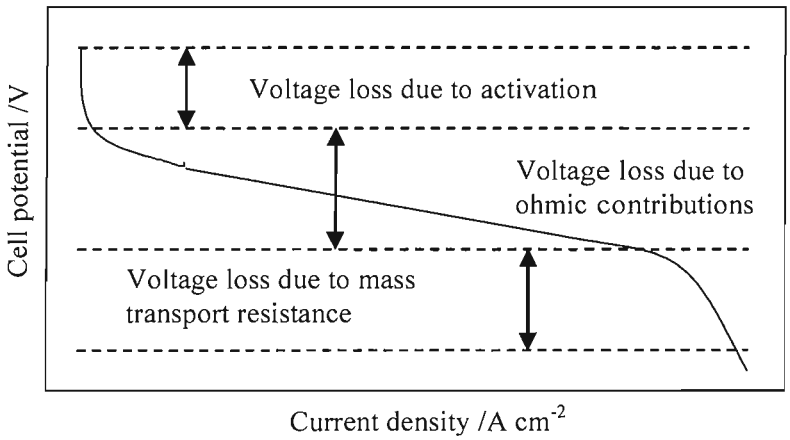

Figure 6 Polarisation curve identifying the different inefficiencies of a fuel cell

The uppermost horizontal dotted line in figure 8 represents the thermodynamic cell potential (which for a PEM fuel cell should equal 1.23 V) and corresponds to maximum efficiency. However, in practice, efficiencies arise that lead to deviations of the electrode potential from its thermodynamic value. These are (i) cell potential losses at the anode and cathode due to the activation overpotential at each, (ii) a linear drop in cell potential mainly resulting from the ohmic losses in electrolyte between the electrodes and (iii) mass transport losses, which eventually cause the cell potential to drop to zero at high current density. These three factors all contribute to the overpotential, η, of the electrode, which quantifies the deviation of the cell potential (E), from the equilibrium potential (E_0) as follows:

$$\eta = E - E_0 \qquad \textbf{Eq. 11}$$

The activation overpotential is associated with poor electrode kinetics at voltages close to the rest voltage. The rate of reaction at the electrode surface can be increased by using electrocatalysts with low activation resistance and increasing the active surface area. Whilst the activation overpotential arises due to voltage losses at both electrodes, the largest contribution by far comes from the cathode as a result of the sluggish O_2 reduction kinetics. Gasteiger *et al* have reported a cathode overpotential loss of 400 mV at 1.5 A cm^{-2} [9].

The ohmic losses are caused by the resistance of the electrolyte to the flow of ions and the resistance of the electrodes and current collectors to the flow of electrons. These can be accounted for using a current interrupt method and will be discussed in more detail in section 2.3.1.

The potential drop at high current densities results from depletion of reactants at the electrode surface due to mass transport being too slow to keep up with the reaction rate. This is particularly problematic with gas-feed electrodes; and is especially noticeable with the oxygen reduction reaction at the cathode, where the presence of water being formed creates an additional barrier to the transport of oxygen to the electrode.

Additional information can be obtained from the polarisation curves by using Tafel analysis. This involves plotting the data as ln(i) against E (or the overpotential, η) as seen in figure 7. The point of intersection of the extrapolated Tafel lines is used to determine i_o, the standard exchange current. This is a quantity related to the rate of the electrode reactions; small values of i_o indicate an irreversible process where a high overpotential is required to induce current flow, while high values of i_o indicate a reversible process where little or no overpotential is required to drive the reaction. The value of α, the transfer coefficient, can be derived from the gradient of the Tafel lines. The value of α provides an insight into how the transition state is influenced by the potential.

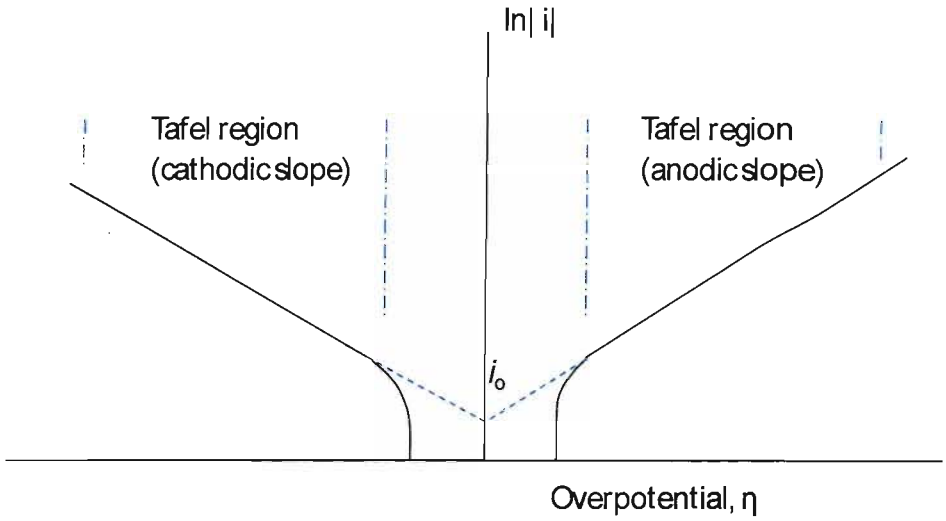

Figure 7 Example diagram of Tafel analysis

By plotting electrochemical data in this way, it also provides a quick visual guide when attempting to compare the performance of a series of catalysts; the higher performing catalysts producing larger current densities at a given potential within the linear region.

2.3.1 Methanol oxidation

Half cell polarisation measurements were carried out to investigate the performance of anode catalysts on methanol oxidation. A three-electrode cell was used as described in section 2.2. After determining the metal area using CO stripping in 1 M H_2SO_4, the electrode was transferred to a cell with 2 M methanol in 1 M $H_2SO_{4(aq)}$. To avoid methanol evaporation, the electrolyte was not purged with nitrogen. The electrode was conditioned by cycling between 0.05 and 0.8 V vs. RHE with a scan rate of 10 mV s^{-1}. The electrode was then polarised using the same potential range and a step potential of 0.05 V. The current was recorded after a stabilisation time of 30 seconds. The temperature was controlled by connecting the cell to a water bath which pumped water through the outer jacket of the cell allowing the procedure to be carried out at 30 °C and 80 °C. Current interrupt measurements were taken at 0.65, 0.7 and 0.75 V vs. RHE to correct the data for cell resistance.

Current interrupt measurements were carried out in order to account for the ohmic losses. These were performed using the Autolab potentiostat. The technique involves

switching off the current and measuring the potential-time curve. As soon as the current is switched off, the potential difference across the ohmic resistance is zero and the charged double layer is discharged. The curve corresponding to the discharge can be extrapolated to the start, t = 0, which allows determination of the iR drop. The current is measured just before the cell is switched off allowing the uncompensated resistance to be calculated.

2.3.2 Single cell polarisation measurements

MEAs were prepared for electrochemical performance testing as described in section 1.3.3. The MEAs were assembled within a single- or mini-cell, which is described in greater detail in sections 3.2.7 – 3.2.8 of this chapter. The cell was formed of two graphite plate current collectors held in place on either side by two Perspex end plates. The MEA is placed between the graphite plates during assembly and compressed to 70 % thickness by tightening the bolts used to hold the plates together and measuring the distance between the plates until the desired compression is achieved. The graphite plates fulfil a number of purposes; acting as current collectors, as well as containing the access channels for fuel and oxidant to the anode and cathode respectively. The circular gas flow fields of the graphite plates have an area of 3.14 cm^2; this being the same as the electrode areas of the MEA.

A water bath is used to operate the cell at 80 °C, by pumping water through a channel within the cell. Fuel and oxidant gases are humidified before reaching the catalyst layers in order to prevent the solid electrolyte membrane from drying out. Gas flow rates of 60 and 40 ml min^{-1} were used for the cathode and anode respectively, and the cell pressure regulators adjusted to keep both sides of the mini cell pressurised to 14 pounds per square inch gauge (psig). The system was first flushed with nitrogen gas. Setting the cathode as the working electrode, and the anode as the counter/reference electrode, the anode gas was switched to hydrogen, with nitrogen as the cathode gas. Once a stable open circuit potential had been reached, the cell was polarised to 0.5 V vs. RHE and the current measured. This current quantifies the hydrogen crossover from the anode to the cathode, and was usually found to be below 20 mA.

CO stripping measurements were collected at the cathode using cyclic voltammetry. The potential was held at 0.125 V vs. RHE with CO flowed over the cathode for two

mins, followed by 43 mins with the cathode gas switched back to nitrogen. CVs were then measured by cycling from a lower limit of 0.075 V to an upper limit of 1.0 V vs. RHE, with a scan rate of 10 mV s^{-1}. Successive scans were recorded until no CO was present.

Steady state polarisation measurements were recorded when operating the cell under fuel cell conditions. Oxygen gas was flowed to the cathode, while polarisation curves were measured with hydrogen to the anode. Ten fast polarisation curves were recorded first in order to condition the cell. The potential was first held at 0.65 V vs. RHE for 3 min before measuring between 0.95 and 0.65 V vs. RHE, using a step potential of 0.05 V and a maximum time interval of 5 s. Two normal polarisation curves were then recorded in the same manner, with the maximum time interval increased to 60 s. Current interrupt measurements were taken at 0.05 V intervals from 0.9 to 0.6 V vs. RHE and back again, to correct the data for cell resistance. Further polarisation curves were then obtained in the same way with the anode gas switched first to 100 ppm CO in H_2; followed by 1 % CO in H_2.

CO stripping measurements were then collected at the anode using cyclic voltammetry, after switching the connections so that the anode was now the working electrode. With the cathode gas now switched to hydrogen, CO stripping CVs were obtained for the anode using the same procedure described above for the cathode.

3 X-Ray Absorption Spectroscopy (XAS)

XAS techniques allow determination of local structure within samples and so are not limited to materials possessing long range order, unlike XRD. Two sequential processes form the basis of X-ray absorption, which lead to the XAS spectra being composed of two parts: the X-ray Absorption Near Edge Structure (XANES) region and the Extended X-ray Absorption Fine Structure (EXAFS) region. These techniques are able to provide structural information on the supported metal particles of fuel cell electrocatalysts. This includes bond distances, coordination numbers and identification of nearest neighbour atoms. One of the main benefits of XAS techniques is that data

can be obtained from samples *in-situ*; i.e. properties of the catalysts can be measured when under potential control in an electrochemical cell in real fuel cell operating conditions.

3.1 Theoretical aspects of XAS

3.1.1 General Principles

The passing of X-rays through a material gives rise to a corresponding loss of intensity as X-ray photons are absorbed by the material. The loss of intensity is proportional to both the initial intensity, (I_0), and the path length through the sample, (x). The parameter used to describe this absorption through a given medium is the absorption coefficient, (μ), which is a function of the photon energy (E) and is found in equation 12, which is used to quantify the loss in intensity:

$$dI = -\mu I\, dx \qquad \textbf{Eq. 12}$$

Integration over the path length gives rise to the Beer-Lambert equation (equation 13).

$$I = I_o e^{-\mu(E)x} \qquad \textbf{Eq. 13}$$

As the energy of the X-ray photons is increased, a critical point is reached where a large absorption jump occurs. This corresponds to excitation of a core electron into either an empty valence state or into the continuum (the photoelectric effect), (see figure 8).

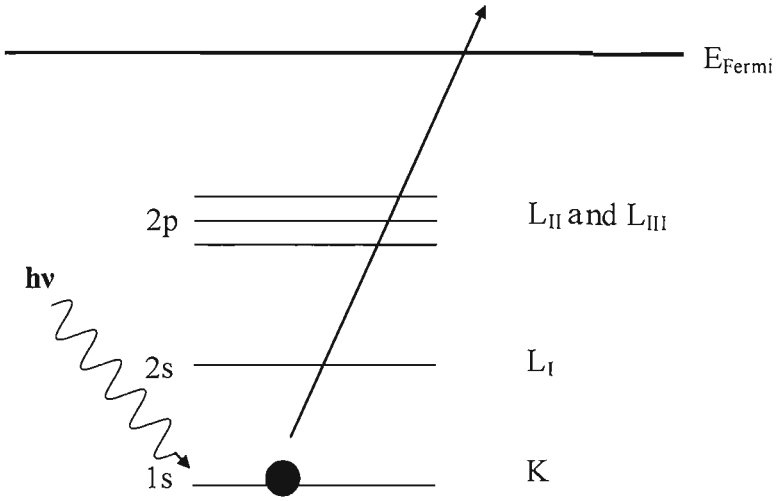

Figure 8 **Diagram of the photoelectric effect showing an incident X-ray (hυ) causing excitation of a core electron into the continuum. K, L_I, L_{II} and L_{III} are labels used to denote the orbital from which the electron is ejected.**

This electron is ejected with kinetic energy E_k (see Eq. 14):

$$E_k = h\nu - E_{binding} \qquad \textbf{Eq. 14}$$

The core electron is ejected from different levels depending upon the energy of the X-rays. K, L and M-edges are labelled according to the principle quantum number of the orbital from which the core electron was ejected. For example, K, L_I, L_{II}, L_{III} correspond to the excitation of an electron from the $1s(^2S_{1/2})$, $2s(^2S_{1/2})$, $2p(^2P_{1/2})$, $2p(^2P_{3/2})$ orbitals respectively. The terms symbols in brackets convey information on the electronic configuration where the letter S or P indicates the total orbital angular momentum number, L, (S when L = 0; P when L = 1), the left superscript gives the multiplicity of the term (the value of 2S + 1, where S is the total spin angular momentum quantum number), and the right subscript is the value of the total angular momentum quantum number, J.

The absorbance is calculated as shown in equation 15:

$$\mu x = \ln\left(\frac{I_{incident}}{I_{transmitted}}\right) \qquad \textbf{Eq. 15}$$

The intensity of the absorption edge is determined by the X-ray linear absorption coefficient, (μ). This is proportional to the probability of absorption of a photon according to Fermi's Golden Rule (equation 16):

$$\mu(E) = \frac{8\pi e^2 \omega^3 n}{hc^3} \cdot \left|\langle \psi_f \left| \hat{e} \cdot r \right| \psi_i \rangle\right|^2 \cdot \delta(E_f - E_i - h\nu) \qquad \textbf{Eq. 16}$$

This is a function of the initial state $|\psi_i\rangle$ and final state $|\psi_f\rangle$ wavefunctions where $\hat{e}$ represents the electric field polarisation vector of the photon and r the coordinate vector of the photon [10]. E_i and E_f refer to the energies of the initial and final eigenstates respectively [11], while the delta function describes the conservation of energy.

The ejected photoelectron can be viewed as a spherical wave with wave vector, k. This is represented by equation 17, where m_e is the mass of the electron, h is Plank's constant and E_0, the zero point of energy in k-space, is taken to be the inflection point of the absorption edge and is determined by taking the derivative of the edge region and measuring the peak maximum.

$$k = \sqrt{\left(\frac{8\pi^2 m_e}{h^2}\right)(h\nu - E_0)} \qquad \textbf{Eq. 17}$$

For energies at or just above the absorption edge, the photoelectrons have low kinetic energy. These electrons interact with valence electrons and give rise to the XANES part of the spectrum. After approximately 50 eV beyond the edge, the photoelectrons have higher kinetic energy, allowing them to be ejected into the continuum where they are then backscattered by neighbouring atoms. The outgoing and backscattered waves will then interact either constructively or destructively (see figure 9) giving rise to the oscillations seen in the EXAFS region of the XAS spectrum as seen in figure 10.

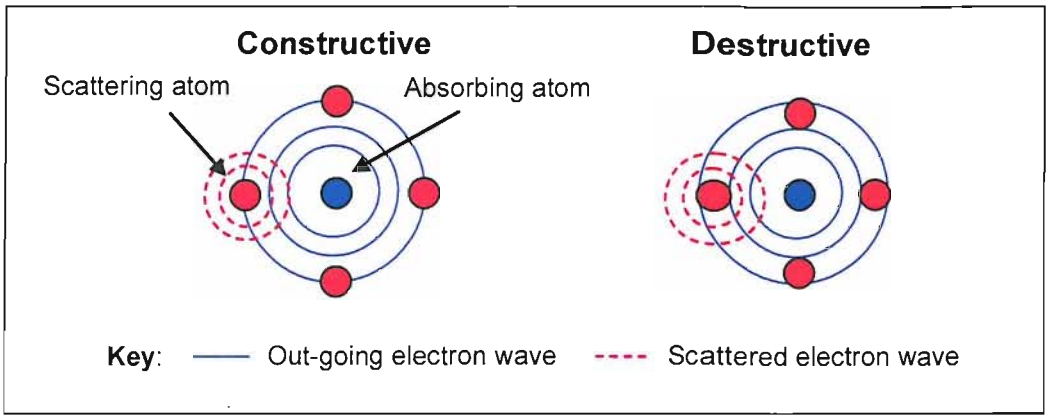

Figure 9 **Schematic of the interference patterns in the final state wave-functions (The rings represent the maxima of the forward scattered and back scattered waves)**

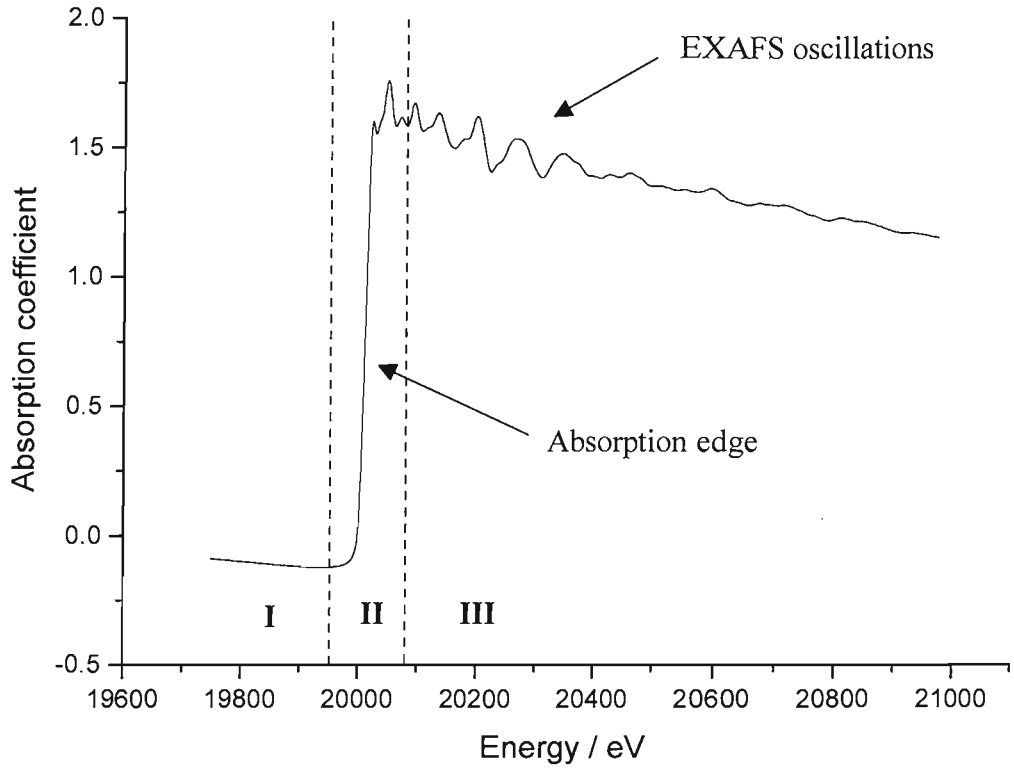

Figure 10 **XAS spectrum of a Mo foil at the Mo K-edge showing: I – pre-edge region, II – edge and XANES region, III – EXAFS region**

The interference is evident in the final state wavefunction, ψ_f, which can be represented as in equation 18:

$$\psi_f = \psi_{outgoing} + \psi_{backscattered} \qquad \textbf{Eq. 18}$$

It is the interference between the outgoing and backscattered wavefunctions which affects the absorption coefficient. Above the edge this is defined as follows:

$$\mu_{tot} = \mu_0 \cdot (1 + \chi) \qquad \textbf{Eq. 19}$$

where μ_0 is the background absorption of a free atom with no scattering from neighbours, while the EXAFS oscillations are given by χ and are defined as the normalized oscillatory part of μ. The EXAFS can be extracted from the data as a function of the wavevector, k, in the following equation:

$$\chi(k) = \frac{\mu_{tot}(k) - \mu_0(k)}{\mu_0(k)} \qquad \textbf{Eq. 20}$$

The XAS spectrum shown in figure 10 can be explained in terms of the different phenomena that occur in three regions as a function of the energy of the incident photons.

Region I is the pre-edge region where the X-ray energy is not yet sufficient to excite a core electron of the element of interest. Region II contains the absorption edge corresponding to the large jump in absorption when a core electron is excited into a higher valence level or the continuum. This region contains the XANES part of the XAS spectra.

The XANES region is generally described as being from the edge position (E_0) to 50 eV above the edge, and provides information on local symmetry and electronic structure. The edge position provides information on the oxidation state of the absorber. Features in this region arise from electronic transitions from the core energy level to empty or half-filled orbitals (e.g. $s \rightarrow p$, or $p \rightarrow d$). One of the features that is often visible in the XANES region is a large peak in the absorption coefficient called the "white line"; so-called because it showed up as a prominent white line when first detected on

photographic film. This feature generally arises due to a high density of final states and is influenced by the corresponding symmetries of these states [12]. However, there are many other factors that can affect the details in the XANES region; some of which are still poorly understood. These include transition probabilities, resonance, and many body effects such as multiple scattering. These phenomena combine to make analysis of the XANES region more complicated than the accompanying EXAFS data. One technique that can be used is white line analysis, which allows fractional d-electron occupancies to be calculated for the element of interest in the samples being investigated, e.g. Pt in catalyst samples [13].

Region III is the EXAFS region, beginning at around 50 eV beyond the absorption edge at which point the ejected photoelectrons have high kinetic energy and the ejected electron can be thought of as a nearly free electron wavefunction. This region continues for several hundred eV with backscattering of this wave giving rise to interference effects which provide the fine structure seen in the EXAFS oscillations. The backscattering effect is greatest with the neighbours nearest to the emitting atoms, and single scattering dominates.

3.1.2 Modern development of EXAFS theory and analysis

The EXAFS phenomenon was first reported as a technique in the 1920s by Friche *et al* [14], although it was over forty years before sources that were bright enough and tunable became available and a viable method of extracting useful information from the raw data was developed. The first advancement began with Sayers *et al* in 1971 [15] who suggested that structural information of solids could be obtained from the EXAFS region. This is achieved by first isolating the oscillatory part of the absorption coefficient (the χ or chi- function) and plotting this against the wavevector, k. They then applied Fourier analysis to convert the experimental data into a radial structure function with features corresponding to the coordination structure of neighbouring atoms, as well as deriving a mathematical expression to describe the EXAFS oscillations. This work was expanded upon by Lee *et al* in 1975 [16], eventually leading to the development of the plane wave scattering theory. Their treatments of the EXAFS made use of several approximations in order to simplify the modelling and

calculations. By treating the neighbouring atoms as point scatterers and assuming that the scattering atom – neighbouring atom bond distance is much larger than the atomic radii, the spherical wave can be thought of in terms of a plane wave, which greatly simplifies the mathematics while giving good correlation between experiment and theory. This theory does break down below k ~ 3 $Å^{-1}$ requiring the development and use of more complicated simulations, such as curved or spherical wave theory. The other most important approximation used is that single scattering dominates. This means that the outgoing photoelectron wave is only back scattered once before returning to the central absorbing atom. In many cases however, the effect of multiple scattering is not negligible and the paper by Lee *et* al detailed ways of calculating this effect [16], with further work contributed by Zabinsky *et al* [17]. A pictorial representation of a single scattering path and two possible multiple scattering pathways are shown in figure 11:

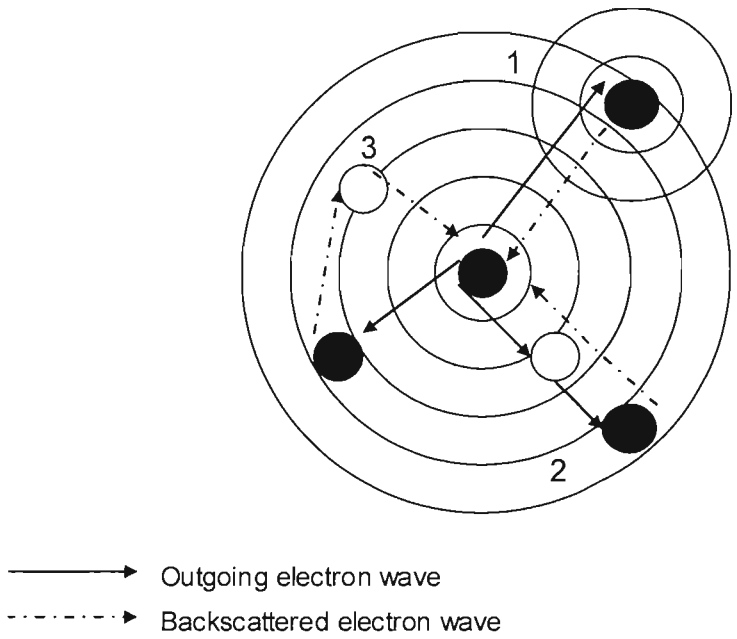

Figure 11 1) single scattering path; 2) and 3) multiple scattering paths

The calculations developed in the 1970's form the basis of modern EXAFS analysis. The EXAFS function, $\chi(k)$, is a summation of the sine waves produced from the outgoing photoelectron wavefunction, together with the backscattered wavefunction from each co-ordination shell, j.

$$\chi(k) = \sum_{j=1}^{shells} A_j(k) \sin \delta_j(k) \qquad \textbf{Eq. 21}$$

The formula contains an amplitude term, A_j, which is expressed below in Eq. 22:

$$A_j(k) = \frac{N_j}{kR_j^2} S_0^2 F_j(k) e^{-2k^2\sigma_j^2} e^{\frac{-2R_j}{\lambda(k)}} \qquad \textbf{Eq. 22}$$

where N_j is the number of atoms of type j at distance R_j from the absorber atom.
S_0 is the amplitude reduction factor used to account for energy loss arising from multi-electron effects and central atom 'shake-up and shake-off' due to relaxation processes after photo-ionisation. This scaling factor varies between elements, although usually has a value between 0.7 and 0.8.
F_j is the backscattering amplitude from the jth atom (element specific) and can be extracted from reference compounds or calculated theoretically [18].

$e^{-2k^2\sigma_j^2}$ is the Debye Waller term. This is used to account for the smearing out of the EXFAS data due to disorder in the system. This is partly caused by thermal effects, which cause the atoms to vibrate around their equilibrium positions, as well as structural disorder (whereby all the neighbouring atoms in a specific shell will not be at exactly the same distance from the central atom). σ_j^2 is the relative mean squared disorder along the distance between the absorbing atom and neighbouring atom, j.

$e^{\frac{-2R_j}{\lambda(k)}}$ is a damping factor accounting for the decay of the wave due to the finite lifetime of the excited state; the size of the effect depending on the ratio of the distance travelled to the electron mean free path, λ. This is responsible for the relatively short photoelectron range (few tens of Å) in a material analysed by EXAFS.

The second part of the EXAFS expression (equation 21) is a sine function that determines the frequency of the oscillations as determined by interatomic distances and energy.

$$\sin \delta(k) = \sin\left(2kR_j + \varphi_j(k)\right) \qquad \textbf{Eq. 23}$$

The sine function consists of the interatomic distance R_j between the absorber atom and the backscattering atom as well as a phase factor $\varphi_j(k)$, which can be expressed as follows:

$$\varphi_j(k) = 2\varphi_{absorber}(k) + \varphi_{backscatterer}(k) \qquad \textbf{Eq. 24}$$

The contribution from the absorber to the overall phase factor is double that from the backscattering atoms because the photoelectron sees the potential created by this atom twice.

The phase shift accounts for the small difference between the measured and geometric interatomic distances and is typically a few tenths of an Å. The value of the phase shift must be obtained from reference compounds or calculated theoretically.

The EXAFS equation can, therefore, be used to calculate the distance to the neighbouring atom (R_j), the co-ordination number (N_j) and the Debye Waller factor as long as the scattering properties of the neighbouring atom ($F_j(k)$ and $\delta_j(k)$) and the mean free path, $\lambda(k)$ are known, and the amplitude reduction factor, S_0, has been calculated.

3.1.3 Data analysis

The extraction of the EXAFS data and corresponding fitting to obtain structural information were accomplished using the Daresbury suite of software: EXCALIB, EXBROOK and EXCURV98. All these programs are available on the XRSSERV1 computer at the Daresbury facility. The basic procedure is outlined below.

The raw data is read into the ECALIB program, which allows a number of scans of the same experiment to be added together, improving the signal to noise ratio. In fluorescence mode scans from faulty detectors can be removed. This program also converts the energy scale from millidegrees (corresponding to the monochromator position) into electron volts.

The EXBROOK program is used to extract the EXAFS data from the spectrum. The first step in this process is pre-edge subtraction to remove the background and identification of the edge position, E_0. The edge position is obtained from the peak position of the maximum in the first derivative of the spectrum (see figure 13), as long as there are no sharp features in the pre-edge region, which may give rise to more than one maximum. In this instance, the 2nd peak maximum is taken as the edge position.

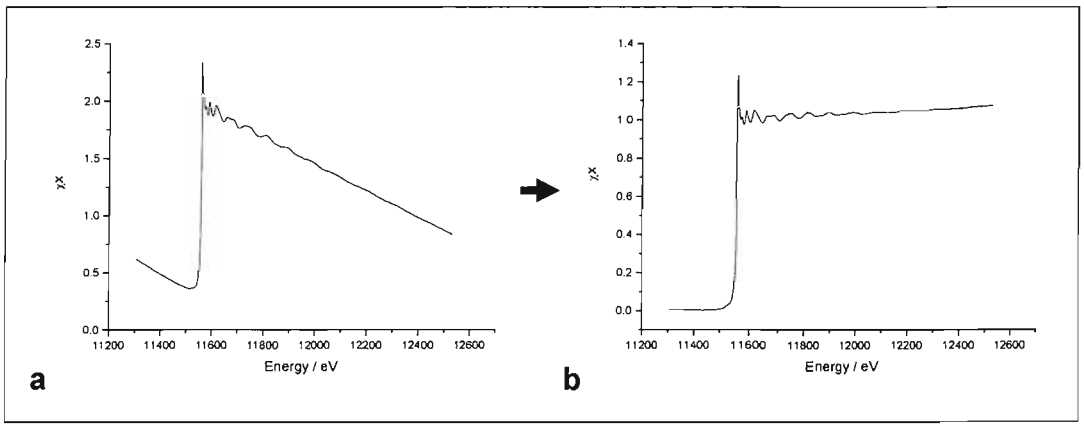

Figure 12 Pre-edge background subtraction and normalisation

A background subtraction is performed involving the fitting of a quadratic function to the pre-edge, which is then subtracted from the whole spectrum, (see figure 12). This removes the near-linear variation in the absorbance with energy caused by the other atoms in the sample. The energy range is then rescaled accordingly to $(E_{hv} - E_0)$, with E_{hv} representing the photon energy, so that the inflection point lies at 0 eV, where $E_{hv} = E_0$.

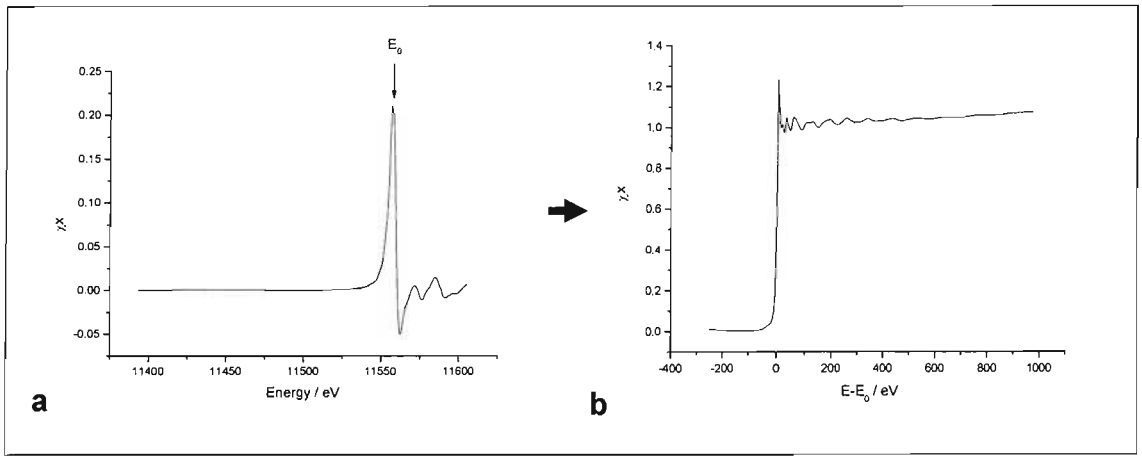

Figure 13 Edge position identification

The data is then normalised giving an edge jump of one, placing the measured spectrum on a per absorber atom basis, thereby taking into account the concentration of the sample.

The last part of the EXBROOK program involves the post-edge background subtraction and extraction of the chi data (the EXAFS oscillations beginning at approximately 50 eV beyond the edge). The post-edge background contains variations in μ past the absorption edge, corresponding to the absorption of the free atom. This is removed using a cubic spline smoothing algorithm. To ensure that no information is lost, the spline must not follow the EXAFS oscillations, but ideally pass through the centre of the oscillations, following the background trend. A smoothing factor, *SM* (equation 25 [19]), is entered to adjust the spline function of the background, *BCK*, while the weight factor, *WE,* can be used to enhance the high *k* part of the spectrum. The aim is to not remove any probable EXAFS oscillations along with the background, but to eliminate low-frequency oscillations that will distort low r (Å) information in the Fourier Transform. Adjustments are made to the smoothing factor and the effects are monitored by observation of the $\chi(k)$, derivative of $\chi(k)$, and FT plots. The aim is to obtain chi data where the amplitude is evenly distributed above and below the axis (figure 14) and where the first peak of the Fourier Transform, usually found between 1.8 and 3 Å, is maximised whilst minimising contributions below 1 Å, which are believed to not contain any real information.

$$\sum_{i=1}^{NPTS} \frac{(\mu_i - BCK_i)^2}{e^{-WEk_i^2}} \leq SM \qquad \textbf{Eq. 25}$$

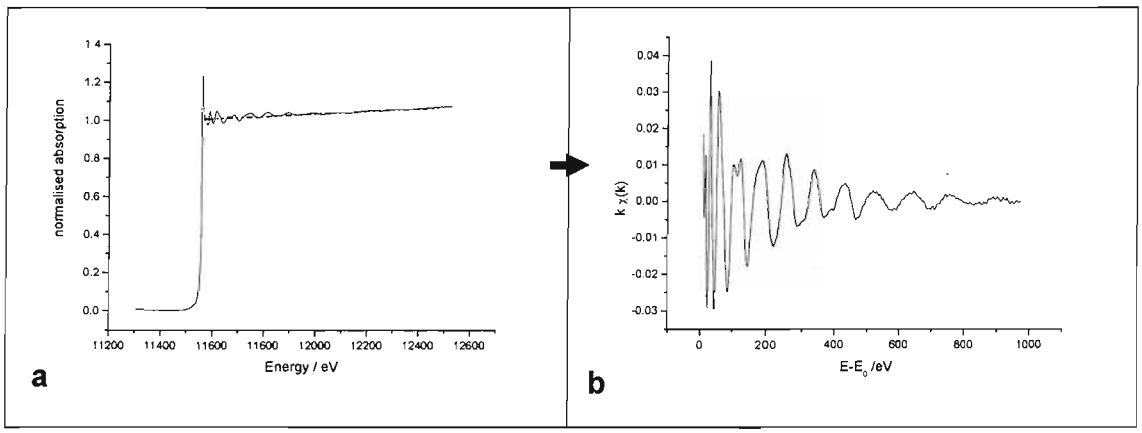

Figure 14 **a) Selection of cubic spline for post-edge background removal b) chi data**

The chi data from EXBROOK can then be read into the EXCURV98 [20] program, which was used to fit the data. The energy range is converted from eV into *k*-space ($Å^{-1}$), which evens out the amplitude across the width of the spectrum. This conversion proceeds as seen in equation 26:

$$k = \left(\frac{2m_e}{\hbar} (E_{hv} - E_0) \right)^{1/2} \qquad \textbf{Eq. 26}$$

The data in EXCURV98 is displayed as both chi data and as the corresponding Fourier Transform (see figure 15).

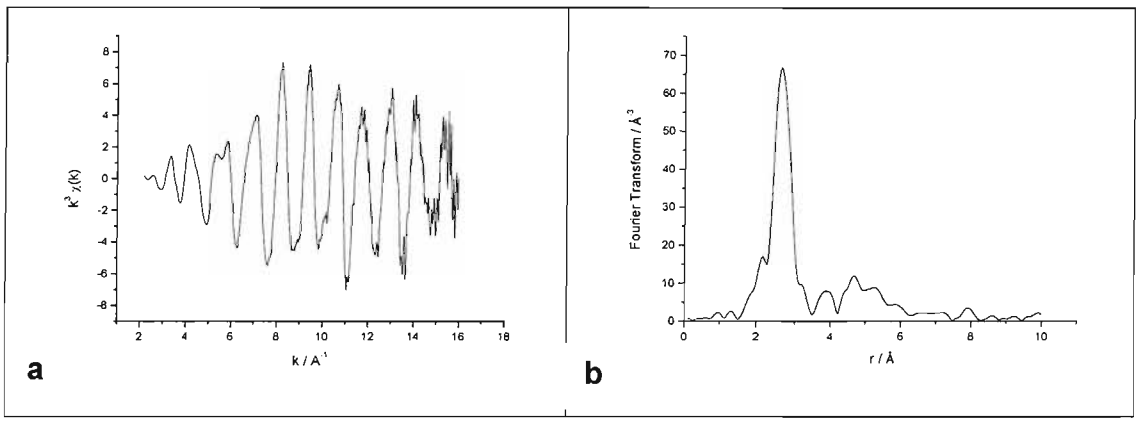

Figure 15 **a) chi data as a function of *k*-space b) corresponding Fourier transform**

The EXCURV98 program is able to produce a theoretical EXAFS spectrum using rapid curved wave theory [21] and Rehr Albers multiple scattering theory [11,22,23] by inputting likely values for the unknown variables [co-ordination number (N), neighbouring atom distance (r) and Debye Waller factor ($2\sigma^2$)] for proposed neighbours. These values are then refined iteratively along with the shift in the Fermi energy (E_F) to yield a closer fit between the experimental and the theoretical data. This is achieved using a least-squares minimization of the fit index. The goodness of fit is represented by the R_{EXAFS} value and is calculated as seen in equation 27:

$$R_{EXAFS} = \sum_i^N \frac{1}{\sigma_i} \left(\left| \chi_i^{\exp}(k) - \chi_i^{fit}(k) \right| \right) \times 100\% \qquad \textbf{Eq. 27}$$

where N is the number of data points, σ_i the standard deviation for each data point, i, and $\chi_i^{exp}(k)$ and $\chi_i^{th}(k)$ the experimental and theoretical EXAFS, respectively. An R_{EXAFS} value of 20 – 30 % normally indicates a good fit. Errors in the parameters are estimated from standard deviations. The number of statistically justified free parameters, n, that may be fitted should also be taken into account when fitting the data. This is estimated using the Nyqvist theorem (equation 28):

$$n = \frac{2\Delta k \Delta r}{\pi} + 1 \qquad \textbf{Eq. 28}$$

where Δk and Δr are the ranges in k- and r-space over which there is useful data.

The data in EXCURV98 is shown in the form of a chi plot and the corresponding Fourier Transform plot with experimental and theoretical data overlaid in each. The radial distribution function (real part of the Fourier Transform) is a useful guide when fitting, because the peak positions give the coordination shell radii, while peak heights correspond to coordination numbers, and peak widths give an idea of disorder.

The amplitude of the EXAFS oscillations decreases with k so it is often advantageous to multiply the EXAFS function by k^i, where i = 1, 2, or 3. The data can be weighted to shift the emphasis of the EXAFS data to low k-space where influence from low Z neighbours (e.g. oxygen) dominates (k^1-weighting); or to high k-space where influence from high Z neighbours (e.g. metal neighbours) dominates (k^3-weighting). k^2-weighted data is often used as a compromise, when it is desirable to look at data with contributions from both high and low Z neighbours.

3.2 Experimental aspects of XAS

3.2.1 The synchrotron source

EXAFS measurements are made at the Synchrotron Radiation Source (SRS) at the Daresbury Laboratory, Warrington, U.K. Synchrotron radiation provides an intense and

highly polarized source of X-rays that is continuous and tunable. The basic lay-out of the SRS can be found in figure 16:

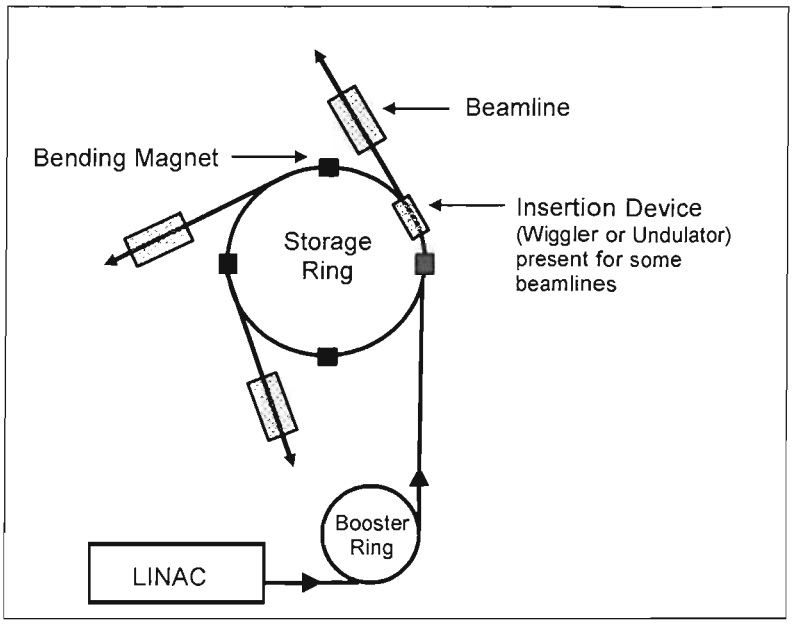

Figure 16 Schematic of the Synchrotron Radiation Source (SRS) [24] (Not to scale)

To produce Synchrotron radiation, electrons are first emitted from a heated filament and accelerated under high vacuum in a Linear Accelerator (LINAC). The acceleration is provided by a klystron, which generates high-frequency microwaves that interact with the electrons, propelling them to greater velocities. When the electron energy reaches 12 MeV, pulses of the electron beam are injected into a booster ring. The electrons are now arranged in a series of bunches, equidistant apart, travelling in synchronous orbit and are accelerated further by 500 MHz radiation, reaching an electron energy of 600 MeV. At this point the electron beam is injected into the main storage ring. The electron beam is subjected to further microwave radio-frequency fields from klystron cavities and accelerated to an energy of 2 GeV; at which point their velocity is close to the speed of light. Dipole bending magnets are used for steering the electron beam around the curve of the storage ring. Every time the beam changes direction, a loss of energy occurs. This loss is in the form of electromagnetic radiation, emerging tangentially from the storage ring into onto a beamline. The energy loss due to the emission of synchrotron radiation is replaced by RF power; however, significant losses in beam intensity still occur due to collisions between electrons and gas molecules. This

requires a fresh beam to be injected at regular intervals, usually once or twice every twenty four hours at the SRS.

Insertion devices, such as wigglers and undulators, are also often found as part of a synchrotron. These are included in the straight section of the storage ring and are comprised of a periodic dipole magnetic structure. When the electron beam enters such a device, it is forced to oscillate in the horizontal plane, in phase with the magnetic periodicity. The beam is forced to follow a trajectory of increased curvature causing radiation of amplified intensity to be emitted, essentially shifting the spectrum to higher energies. The nature of the electron motion depends on the magnetic field strength and the wavelength corresponding to the alternating periodicity of the device. If an undulator is used, the resulting electron motion is generally considered to be linear; the resulting radiation obtained being most often used for soft X-ray experiments. If a wiggler is used, the effect is to cause the electron motion to become highly non-linear leading to radiation of harmonics. This leads to even higher energy radiation that is more useful for hard X-ray experiments.

Synchrotron radiation is typically of the order of 10^6 times more intense than conventional X-ray machines. This makes EXAFS a particularly effective technique for the study of fuel cell catalysts where the element under study is often present in very low concentrations (e.g. Pt loadings of 0.3 mg cm^{-2} are frequently utilized), and the thickness of the catalyst layer is restricted to ensure full participation of the catalyst particles in the electrochemical reactions.

3.2.2 Beamline station 16.5

The SRS at Daresbury Laboratory has over 30 beamlines operating at a range of different energies, allowing the study of many diverse systems. The EXAFS work in this project was undertaken on station 16.5; a station specifically designed for X-ray absorption spectroscopy of dilute samples. This station operates at an energy range of 7 keV to 40 keV with a multipole wiggler source enhancing the flux and brightness of the light. Vertical collimation is provided by a 1.2 m uncoated plane mirror. This is followed by a water-cooled Si (220) double crystal monochromator, where the second crystal is dynamically bent to provide horizontal focus. The monochromator is used to

select a well-defined photon energy from the source. This is accomplished using reflections from the crystal planes as a function of the incident angle θ_i according to the Bragg relation:

$$n\lambda = 2d\sin(\theta_i) \qquad \textbf{Eq. 29}$$

Where λ is the wavelength of light, d is the spacing of the atoms in the crystal and θ_i is the angle of incidence. The second crystal is positioned at the same angle as the first crystal to correct for the angular deflection. The light reaching the second crystal is not perfectly monochromatic due to the presence of higher harmonics; that is, multiples of the original energy reflected by the first crystal. These can be removed by "detuning" of the second crystal, i.e. adjusting the position of the second crystal with respect to the first, because the higher harmonics have a smaller acceptance angle than the fundamental. This means that while the acceptance angle for the fundamental has a large overlap there is little overlap for the higher harmonics resulting in small reflectivity of the monochromator [25]. Typically, a harmonic rejection of 50 % was used for the Pt and W L_{III} and L_{II} edges, while 70 % was used for higher energy edges such as the Mo K.

The station is equipped with an Ortec 30-element solid state detector, which is used for fluorescence measurements.

3.2.3 Transmission mode

There are two main modes for the collection of XAS data: transmission and fluorescence. In a transmission experiment, the intensity of the X-ray photons is measured before and after the beam comes into contact with the sample under investigation in order to calculate the absorption due to the sample. A basic set-up for this type of experiment is shown below in figure 17:

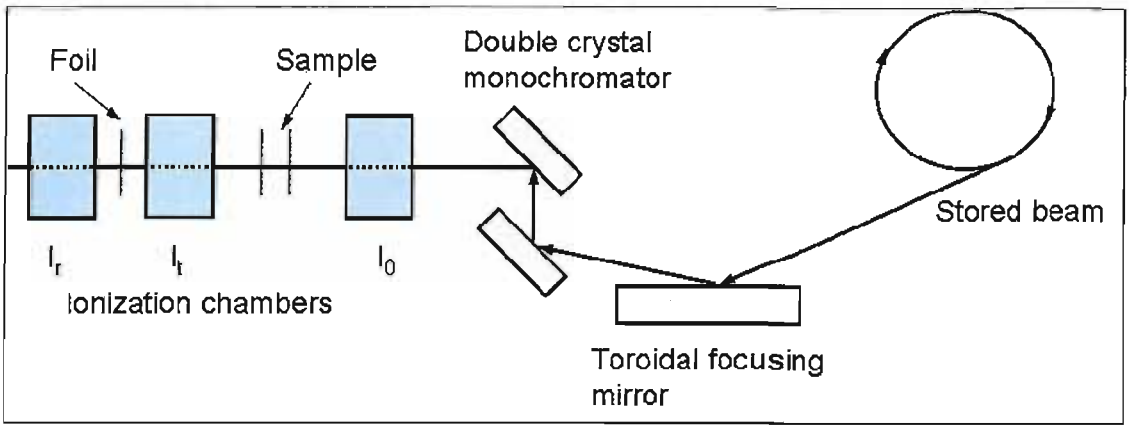

Figure 17 Schematic of the transmission experimental setup

The variation in absorption by the sample with increasing photon energy is monitored using ion chambers positioned before and after the sample. The first ion chamber measures the incoming intensity, I_0, while the second measures the transmitted intensity, I_t, after the beam has passed through the sample. The absorption of X-rays by the sample is given by $\ln (I_0 / I_t)$. Each ion chamber is filled with an inert gas mixture that is calibrated to absorb 20 % (in the case of I_0) and 80 % (in the case of I_t) of the incident flux. The ion chambers contain two metal plates, with a constant potential applied between them, so that ions are attracted to the negative side and the electrons to the positive. The size of the resultant current that flows is therefore directly related to the number of photons entering the chamber.

A third ion chamber can also be used, I_r. This is a reference chamber and is filled with the same gas mixture as I_t. A metal foil of the element being studied is placed between I_t and I_r, allowing the energy to be calibrated each time. This is important for XANES studies where an exact edge position is required because the energy readings without this calibration can sometimes drift slightly with time.

Transmission mode is used when there is a high concentration of the element under study in the sample. If the sample is too dilute, then the absorption will be correspondingly weak, leading to poor quality EXAFS data. The sample must not also be so thick that all of the X-rays are absorbed and nothing gets through. In addition, the concentration of any other elements present must not be so high as to absorb all the X-rays. All of these factors must be considered when preparing a sample for study. An

ideal absorption edge, μx, is generally considered to be between 0.3 and 1.0. The mass of sample required to give this absorption edge can be calculated as follows:

$$mass = \frac{(\mu x)(area)}{(\mu / \rho)} \qquad \textbf{Eq. 30}$$

where (μ / ρ) is the mass absorption coefficient of the element of interest, with ρ being the density.

Mass absorption coefficients for all elements have been published by McMaster *et al* [26]. It should be noted that this mass is of the element in question only, requiring the fraction of this element in the total sample to be calculated. The absorption for all other elements in the sample must be deduced using their mass absorption coefficients leading to a total absorption for the whole sample. The value of this must be kept below 2.5 to prevent self-absorption effects that can lead to errors in coordination numbers. Polyethylene and boron nitride are common compounds used when forming sample pellets for EXAFS studies due to their low mass absorption values.

Care must be taken in the manufacture of sample pellets (see section 3.2.5) for transmission studies so that there are no pin holes (or larger holes) through which incident X-rays can pass through unaffected. In addition, the sample must be completely homogenous; being well-mixed with any polyethylene or boron nitride used as diluent. The pellet is usually compressed to hold its' shape in the pellet holder and ensure even sample thickness.

3.2.4 Fluorescence mode

Fluorescence experiments are undertaken when the sample is very dilute leading to an indiscernible difference between the absorption before and after the edge. In such instances, detection of fluorescence photons is used to obtain the XAS spectra. When a core electron is emitted at the absorption edge, a core hole remains that is instantaneously filled by an outer shell electron. This relaxation process gives rise to an emission of fluorescence radiation that is dependent on the difference in energy between

the outer and inner energy levels and is thus characteristic of the absorbing element. For small values of the absorption coefficient, μ, of the species, the X-ray fluorescence is proportional to μ. The fluorescence EXAFS signal consists of only a small fraction of the total absorption and is proportional to the incident intensity as follows:

$$\mu(E) = \frac{I_{fluorescence}}{I_o} \qquad \textbf{Eq. 31}$$

I_0 is taken from the first ionization chamber, (see figure 18).

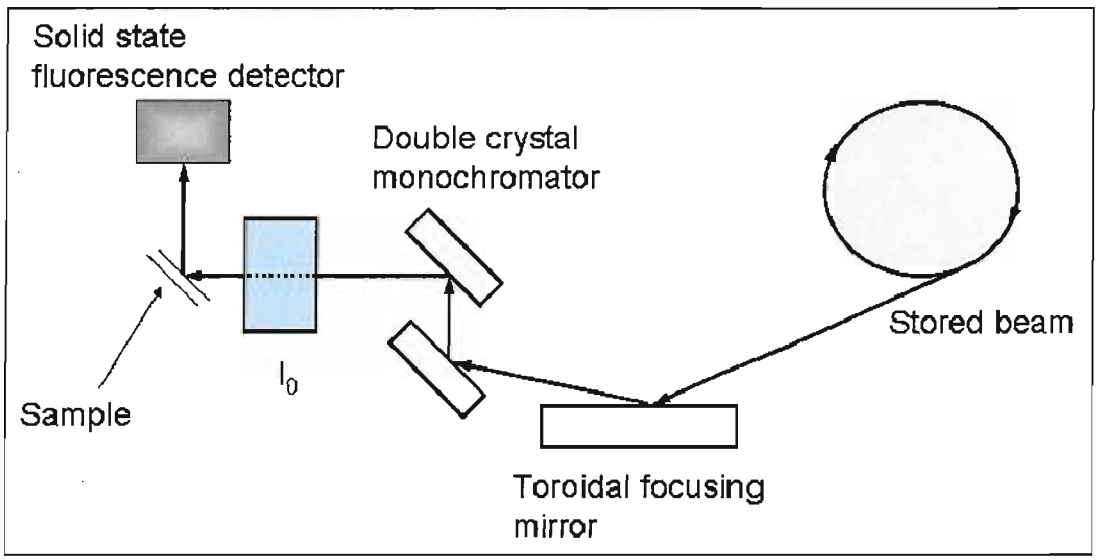

Figure 18 Schematic of the experimental setup for fluorescence mode

In the fluorescence mode, the signal is absent before the edge and present after the edge giving a greater contrast for more dilute samples. The sample is positioned at an angle of 45° to the incident beam, with the solid state fluorescence detector positioned orthogonal as seen in figure 18. This is done so as to maximize the solid angle seen by the detector and helps to reduce the amount of scatter, which is the main source of noise with this technique.

3.2.5 Catalyst sample pellets

The catalyst samples can be analysed in a number of ways. Electrodes for half cell and mini cell studies can be prepared as described in section 1.3. The simplest option for gaining basic structural information on a catalyst is to take the powder sample and make

it into a pellet that can be analysed in air, or under a specific gas, e.g. hydrogen, carbon monoxide etc., using a specially designed gas treatment cell (although this was not required for this project and will not be described further here).

The pellets were prepared by measuring out the desired quantities of catalyst sample and boron nitride with the values obtained from equation 30 and then grinding them together with a pestle and mortar. A die press was then used to form the pellet. The pellet holder is made of stainless steel with a pellet size of 0.72 cm^2 and can be clamped either face-on to the incoming beam for transmission experiments or at 45° for fluorescence experiments.

3.2.6 Electrochemical half cell measurements

XAS studies of fuel cell catalysts have shown significant differences when being run in an as-prepared state compared with under potential control in an electrochemical cell [27]. It is therefore vital to study the catalyst structure in conditions approaching those found in real, operating fuel cells. The first step towards this goal is to measure XAS spectra of catalyst electrodes in an electrochemical half cell. Catalyst samples were prepared as electrodes for study in the half cell as described in section 1.3.1. The cell itself was based on a transmission electrochemical design by Herron *et al* [28] and reported by Maniguet *et al* [29]. The cell used was a version of this cell that had been modified to use for fluorescence EXAFS studies.

The cell is formed of two circular acrylic plates. One of these has a circular Kapton window and gold wire contact, upon which the carbon paper backed working electrode is placed. Kapton is a polyimide polymer which is acid resistant and transparent to X-rays, making it ideal for the electrochemical cell. The second plate has four ports connected to the central reservoir; the inlet and outlet for pumping acid into the cell, connection for the MMS reference electrode, as well as a Pt gauze counter electrode that is positioned inside the reservoir. The two plates are screwed together with the aid of two acrylic supports, which also help with positioning the cell in front of the X-ray beam. Unlike the transmission cell reported by Maniguet *et al* [29], only one Kapton window is present because the cell is used in fluorescence and positioned at 45° to the incoming beam, meaning that there is no requirement for an exit window. The ports are

all positioned on the non-window side so as not to obstruct the path of the beam and/or the fluorescence photons and to allow positioning of the cell closer to the fluorescence detectors.

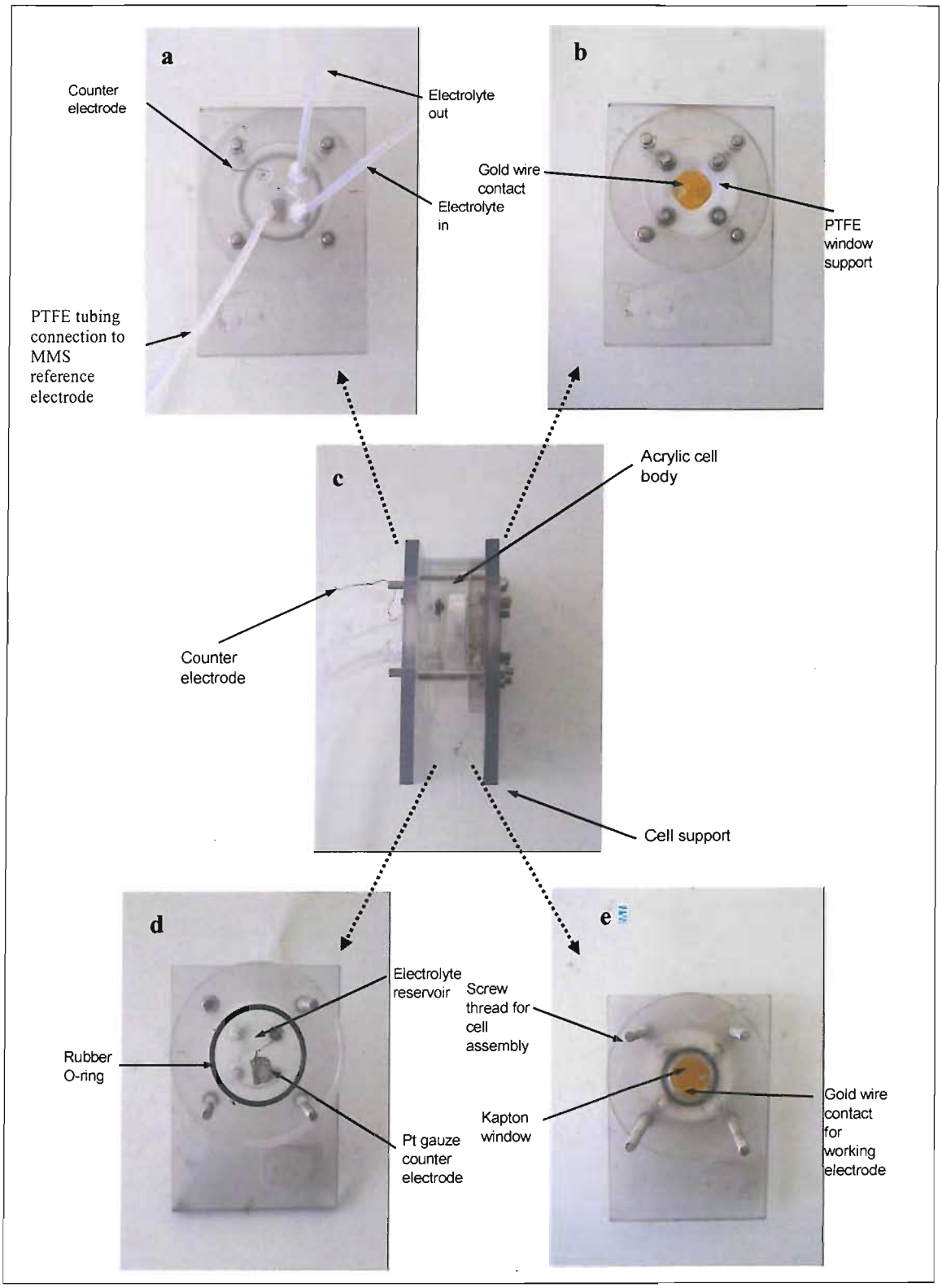

Figure 19 **Annotated pictures of the fluorescence electrochemical XAS half cell a) back exterior, b) front exterior, c) side-on view, d) back interior and e) front interior**

The electrolyte used is 1 M $H_2SO_{4\,(aq)}$, which is pumped into the cell using a peristaltic pump. The electrolyte fills up the central reservoir so that all electrodes are completely in contact with electrolyte at all times. Any air bubbles that arise, often as a result of changes in applied potential, are removed using the pump. If left unchecked, bubbles in the path of the beam can create noise in the XAS spectra due to random density fluctuations, and may also block contact to the reference electrode.

An Electrochemie Autolab PGSTAT30, computer controlled combined potentiostat and waveform generator, was connected to the three-electrode system and used to control the applied potential.

3.2.7 Electrochemical mini cell measurements

The next step in the move towards realistic sample environments was the development of a single cell design that allowed XAS measurements to be made under conditions more closely approximating those found in a real fuel cell. The use of a single cell removes the need for a liquid electrolyte by the use of a solid polymer electrolyte membrane between the anode and the cathode to form an MEA. The first single cells for XAS use were reported by Viswanathan *et al* [30] and by Roth *et al* [31], both of which were designed to operate in the transmission mode. The single cell by Viswanathan was a modification based upon the half cell design by Herron *et al* [28], with graphite plates that had been milled down to a thickness of 4mm behind the flow fields in order to reduce the impedance of the X-rays. The anode catalyst under study was carbon supported Pt-Ru, while a Pd/C cathode was used so as to avoid averaging the XAS signal from both sides. Roth used a commercially available fuel cell adapted for XAS in a similar fashion. For the purposes of obtaining information only on the Pt-Ru/C anode catalyst, a small area of Pt/C catalyst was removed from the adjoining cathode in line with the X-ray beam. However, this is likely to affect the current distribution in the corresponding region on the anode catalyst, reducing the usefulness of the data obtained [18].

Unlike electrodes in half cells, catalyst utilisation is an important factor to consider when dealing with single cell measurements. In a half cell, the electrodes exist in a flooded environment where the entire catalyst is likely to be in contact with electrolyte.

This is in contrast to single cells, in which the only parts of the catalyst being utilized are those that are present at the three-phase boundary in contact with both the carbon support for electronic conductivity and with the membrane for proton conductivity. XAS is an averaging technique, i.e. the spectra reflect the average coordination environment on a per atom basis, making it crucial to maximise the catalyst utilisation. For the data to be useful, it must representative of all the catalyst in the same electrochemical or chemical state and not distorted by the presence of unutilised catalyst. The catalyst layer must also be sufficiently porous to allow the reactant gases to reach the catalyst particles and for any products to leave.

The best way to maximise catalyst utilisation is by employing thin films. This results in the unfortunate side effect of lowering the total XAS signal due to the reduced metal content. In reality, a trade-off is normally required; by having the metal loading as low as possible, while still keeping it high enough to make data collection a viable process. Viswanathan *et al* used a 1:1 Pt-Ru / XC72-R (30 wt. % metals) catalyst with an electrode metal loading of 0.6 mg cm^{-2} (corresponding to a Pt loading of 0.4 mg cm^{-2} and a Ru loading of 0.2 mg cm^{-2}). This low loading in transmission mode considerably reduces the signal: noise ratio, making EXAFS analysis more difficult. As a result, only the XANES region was reported. Roth *et al* used a higher metal loading of 1.2 mg cm^{-2} and EXAFS data at the Pt L_3 edge recorded. However, optimal data quality in transmission mode is achieved with a change in absorption at the edge of at least 0.3, requiring 1.7 mg Pt cm^{-2} and 4.4 mg Ru cm^{-2} at the Pt L_{III} and Ru K edges respectively. [26] Catalyst utilisation becomes a problem with the layer thicknesses required for these desired loadings so the layers were kept thin for the project reported in this thesis. Typically, Pt loadings of between 0.8 and 1.0 mg cm^{-2} were used with corresponding loadings of the secondary element (normally Mo) between 0.2 and 0.5 mg cm^{-2} depending on the ratio of the two metals. This necessitated the use of an XAS cell that could be operated in fluorescence mode. Recently such a cell has been designed and tested by Wiltshire *et al* [32] in a collaborative effort between the University of Southampton and Johnson Matthey.

3.2.8 Cell design and set-up

A schematic of the basic cell design can be seen in figure 20:

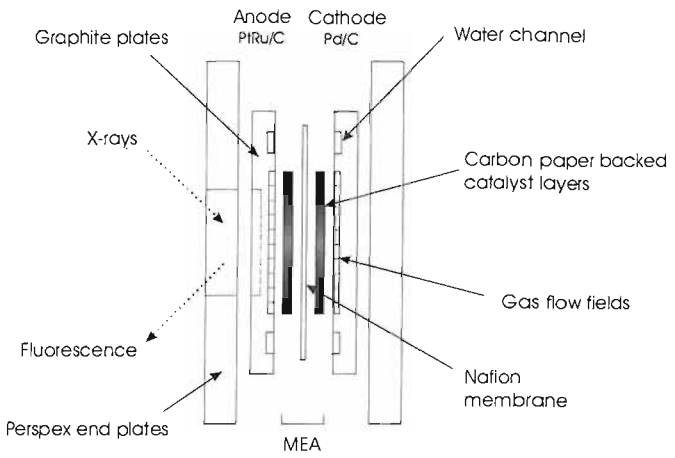

Figure 20 Schematic cross-section of the XAS fluorescence min cell

The cell as shown here was formed of two graphite plate current collectors held in place on either side by two Perspex end plates. Six threaded screws with two alignment pins were used to assemble the cell together, ensuring correct alignment of the plates. The MEA (as described in section 1.3.2) is placed between the graphite plates during assembly.

The graphite plates fulfil a number of purposes; acting as current collectors, as well as containing the access channels for fuel and oxidant to the anode and cathode respectively, as seen in figure 21.

The plates were made from Le Carbone graphite grade RF. This afforded them with good electronic conductivity while being corrosion resistant and soft enough so that the gas flow fields and water channels can be easily machined. In addition, this material has a low density of 1.77 g cm^{-3}, which minimises the absorption of the X-rays by the graphite. It does, however, lack mechanical strength, affecting the minimum plate thickness that can be achieved, resulting in a trade-off between strength and degree of X-ray absorption [33]. The plate against which the electrode of interest will be placed was milled down to a thickness of 1.5 mm in a 60 x 16 mm window, as seen in figure 21 (a), in order to minimise X-ray absorption.

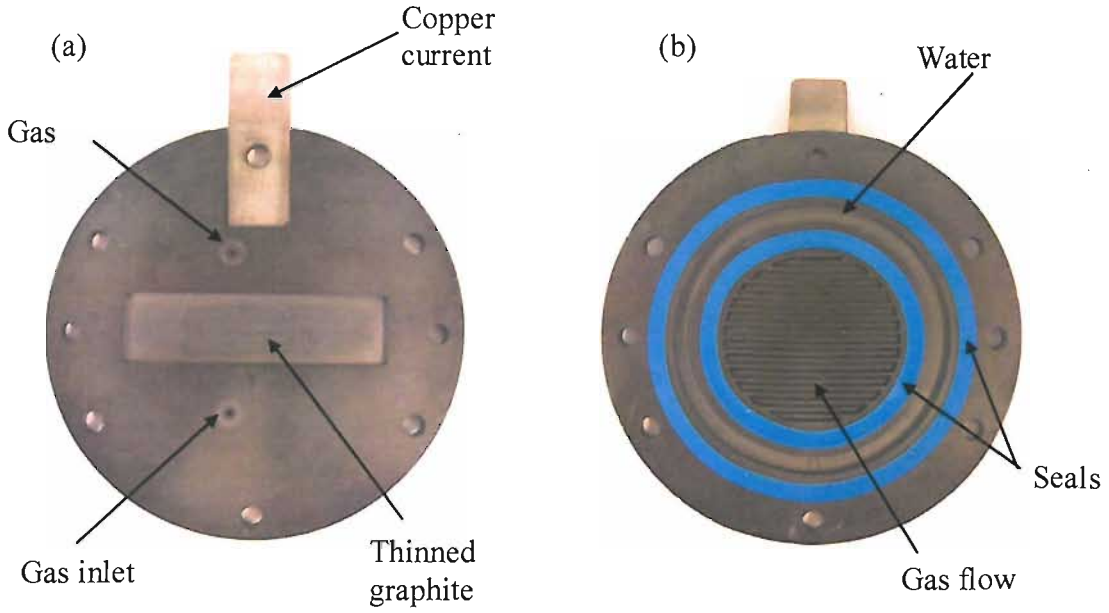

Figure 21 **a) Graphite plate showing thinned region and b) interior of graphite plate showing gas flow field and water channel**

A copper current collector sits at the top of each plate. It was found that there was a significant potential drop between the copper current collectors and the graphite plate [34] when using these in a two-electrode set-up so a four-electrode set-up was devised. A hole was drilled into each graphite plate near the current collectors into which a gold pin was set. The potential is then applied across the two pins, while the current is measured at the copper current collectors. The circular gas flow fields are the same diameter as the electrodes on the MEA. The flow fields utilise a serpentine design to transport gases to the gas diffusion carbon backing layer of each electrode; the inlet and outlet at the bottom and top of the flow field respectively. A water channel around the outside of the flow field is used to continually hydrate the MEA membrane when the cell is in operation. For this purpose, the membrane layer of an MEA extends out beyond the limit of the electrode to a distance such that the outside edge of the membrane lies past the set of inner seals, within the water channel region; although not extending as far as the outer seals. Each graphite plate houses its own inner and outer silicone rubber seal. Once the cell is assembled and heated, the seals expand slightly to form a water and gas tight seal.

When assembling the cell, the seals and flow field plates were cleaned using cotton buds and isopropyl alcohol (IPA). The thickness of the MEA to be used was measured

before placing it in the cell. Depending on the carbon paper used, the thickness was usually between 0.6 and 0.7 mm. The mini cell was set up by first positioning the MEA so that the anode side is against the windowed graphite plate and the electrode lies exactly within the gas flow field. The opposing plate is positioned on the other side and the two clamped together with the aid of the two end plates. The six threaded screws are tightened so that the distance between the graphite plates is 0.4 mm. The MEAs are therefore compressed to 70 % of their original value, ensuring good electrical contact with the graphite plates.

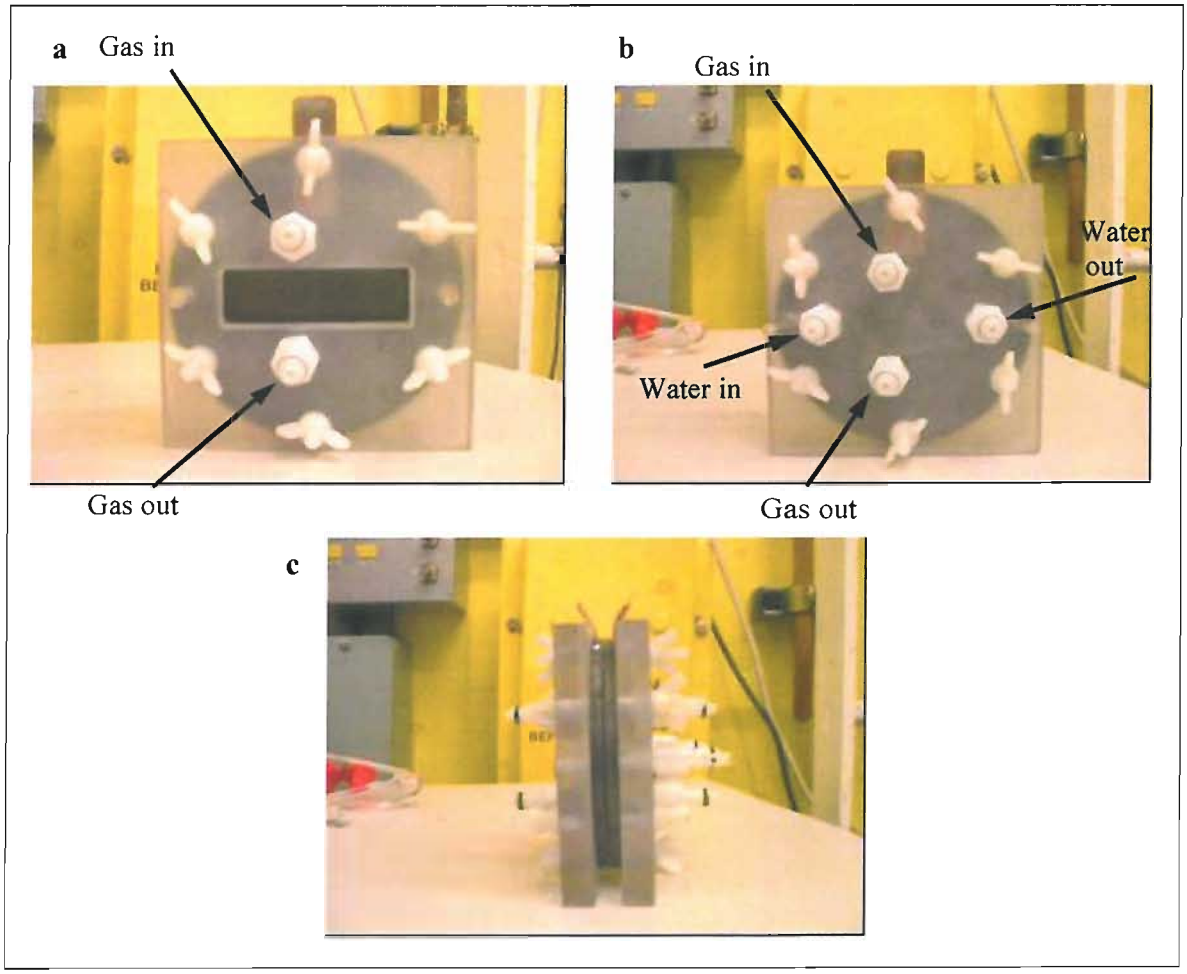

Figure 22 Assembled mini cell a) front view, b) back view and c) side-on view [34]

The MEA was conditioned by pumping a 40 % aqueous methanol solution through the anode and cathode flow fields using a peristaltic pump for 20 minutes. After this time, the flow fields were flushed through with purified water for a further 20 mins. This process boosts the water retaining properties of the membrane. During the experiment,

purified water was continuously pumped around the water channel in order to keep the membrane hydrated.

In developing the mini cell, it was found that cell performance and reproducibility suffered as a result of the membrane drying out leading to increased cell resistance [34,35]. This indicated that, even with formation of water at the cathode, the use of a water channel, and conditioning of the MEA with methanol, the membrane remained dehydrated. This effect was likely exasperated by the use of dry gases, which carry moisture out of the cell. A humidification system was developed by Wiltshire in collaboration with Johnson Matthey [34]. The system was designed to be internal so that the cell and humidification would be self-contained and minimise space. The humidifiers themselves (see figure 23) use Membrane Substrate Assemblies (MSAs). These are similar to MEAs, consisting of a Nafion® membrane with carbon paper on either side. The carbon paper is not hot pressed to the membrane in this instance.

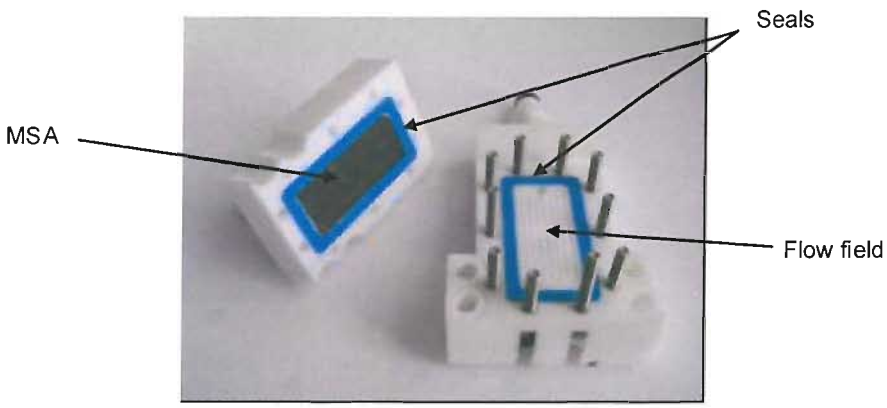

Figure 23 **Interior view of a humidifier showing the positions of the MSA and flow field [34]**

Purified water is first heated to 80 °C in a water bath before being passed through a flow field over one side of the membrane. The reactant or oxidant gas is then flowed over the other side of the membrane where it picks up moisture carrying it directly into the MEA in the cell. Both anode and cathode require their own separate humidification system. These were designed so that, on the anode side especially, the humidifier could be attached to the cell without blocking the graphite window and adsorbing a large amount of the X-rays. The humidifiers were therefore designed to be attached above the level of the graphite window as shown below in figure 24:

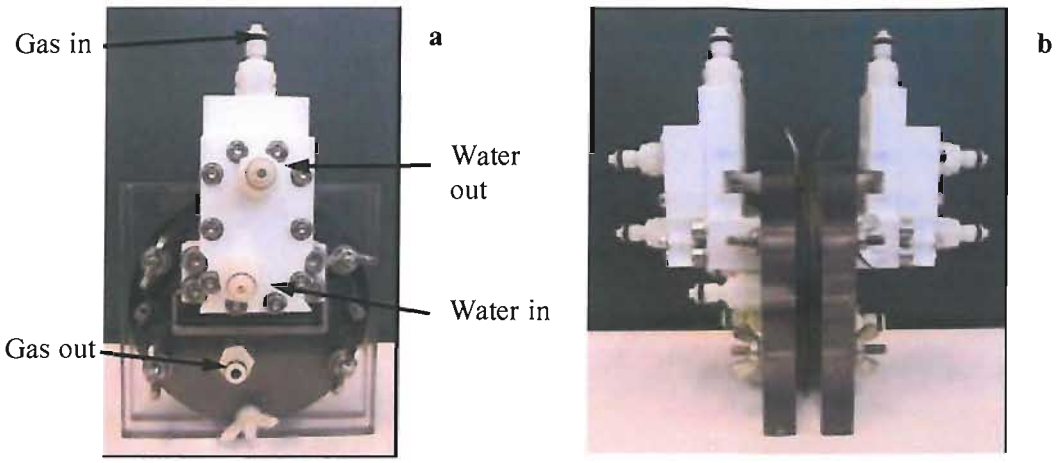

Figure 24 **Annotated pictures showing the assembled XAS mini cell incorporating the internal humidification systems a) front (anode) view and b) side view [31,34]**

Electrochemical measurements were again obtained using an Electrochemie Autolab PGSTAT30, combined potentiostat and waveform generator, in conjunction with an Electrochemie Autolab BSTR10A current booster. This allowed currents up to 10 A to be reached without overloading the potentiostat. The anode operated as the working electrode in these experiments. The cathode took on a dual role of both counter electrode and reference electrode. This is achieved by passing hydrogen over the Pd or Pt electrode; bringing the potential close to 0 V vs RHE as a result of the H_2/H^+ redox couple.

Data collection was obtained in the same way as for the fluorescence half cell. The mini cell was placed in the path of the X-ray beam at an angle of 45° and fluorescence detectors at 90° used to monitor the resulting emission. Figure 25 shows a picture giving an overview of the experimental setup on a beamline at the Daresbury laboratory. The mini-cell was situated between two ionisation chambers, I_o and I_t. The second ionisation chamber was not used as the XAS spectra were collected in the fluorescence mode. The gases were ported in from cylinders located outside of the hutch. The outlet gases were bubbled through water so that the flow rate could be monitored. An extraction system was used to remove waste gases from the hutch. The water bath was positioned as close as possible to the mini-cell to reduce heat loss. The mini-cell temperature was monitored using a thermocouple.

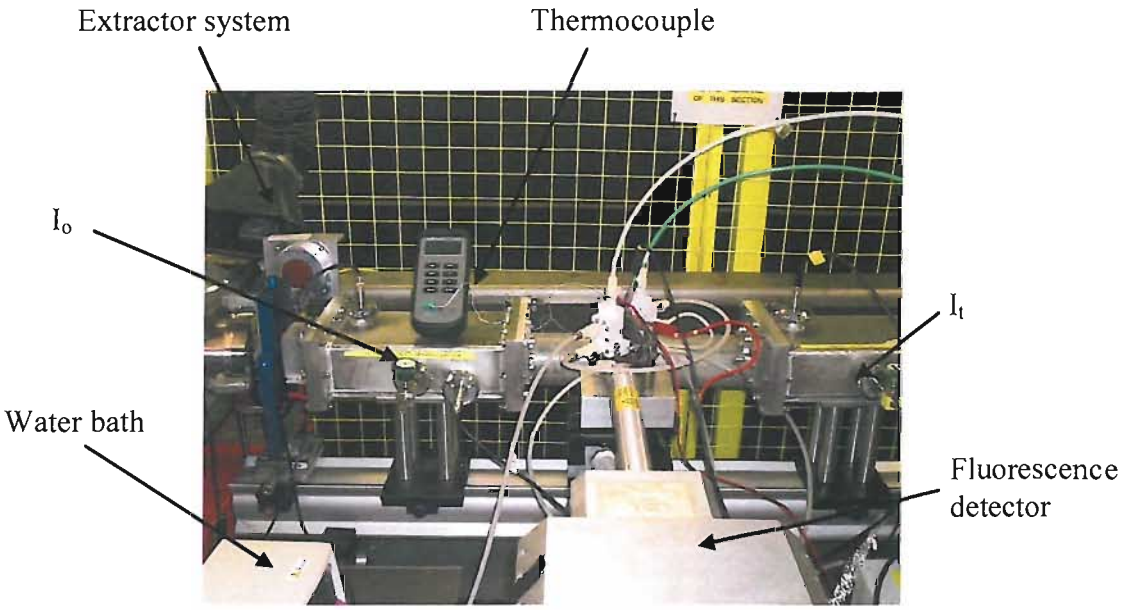

Figure 25 **Picture of the experimental setup used on a beam station at the Daresbury laboratory**

4 Inelastic Neutron Scattering

Inelastic Neutron Scattering (INS) is a useful tool for studying the structure and dynamics of condensed matter. Like XAS, the INS technique can be used in circumstances where X-ray diffraction cannot, i.e. with materials that do not display long range order. Unlike X-ray techniques, INS is most useful in the study of hydrogen-containing materials due to the high scattering cross-section of hydrogen. This section will describe the theory behind INS, as well as the experimental procedures involved in obtaining INS spectra and how the data is analysed with the aid of quantum mechanical modelling techniques.

4.1 Introduction to Neutron Scattering

The discovery of neutrons came in 1932 when Chadwick bombarded beryllium with α-particles and observed the emission of neutral particles with a mass close to that of a proton [36]. These particles were named neutrons and were found to possess zero charge and a magnetic moment (spin ½). Like X-rays, neutrons can be used to study the microscopic structure of materials, although they interact with matter in different ways. In X-ray diffraction experiments, X-rays (photons) are scattered by the electron clouds surrounding the atoms. The degree of X-ray scatter is directly proportional to the number of electrons that an element has, making it a poor technique for the study of lighter atoms such as hydrogen and oxygen. In contrast, neutrons are scattered by the atomic nuclei. Thus, neutron scattering yields information on the actual positions of the atoms rather than the electrons. In addition, because neutrons are neutral particles, they are not scattered by charge repulsion effects but rather via nuclear forces. The density of solid matter is not an issue with neutron scattering due to the short range nature of these forces (of the order of a few fermis; 10^{-15} m). This gives very low beam attenuation in comparison with other techniques, such as X-ray diffraction, which usually require thin samples. Generally, neutrons can pass easily through metal containers, such as steel and aluminium, and penetrate a distance of the order of millimetres into the sample, allowing analysis of bulk materials. The corollary of this is

that the neutrons, when they are scattered, only do so weakly, and the magnitude of this depends on the element it is scattered by.

There are two types of neutron scattering; *coherent* and *incoherent*. Coherent scattering occurs when the neutrons (treated as neutron waves) are scattered by different nuclei of the same type and interfere. When a neutron is scattered by a sample with no loss of energy then the scattering is said to be *elastic*. In wave vector terms, the direction of the vector changes but not its magnitude. Coherent elastic scattering is measured in diffraction experiments, providing information on the equilibrium structure, including the relative positions of atoms, etc. Incoherent scattering arises when the scattered neutron waves do not interfere. This occurs when the natural isotopic and spin mixture of the sample destroys local order so that the incoming neutron wave interacts independently with each nucleus.

The scattering utilised in this work is incoherent *inelastic neutron scattering* (hereafter referred to as INS). In inelastic scattering, the incoming neutron exchanges energy and momentum with the sample; i.e. the direction and magnitude of the neutron's wave vector both change.

4.2 The Theory of Inelastic Neutron Scattering (INS)

INS is a technique used to measure atomic and molecular vibrations of condensed matter. The neutrons collide inelastically with the scattering material; losing energy by exciting vibrational modes. INS, therefore, is a spectroscopic technique yielding similar results to those found with the optical techniques of Raman and infrared. An advantage of using INS over Raman and IR is that, unlike these techniques, INS is not subject to the same optical selection rules. This means that all vibrations are active and will appear in the spectrum. Furthermore, the measured intensities are proportional to the concentration of the elements in the sample. X-ray techniques are generally better suited to the study of heavier elements; being more sensitive to the vibrations of these elements because of the larger number of electrons they possess. INS, on the other hand, is particularly sensitive to vibrations of hydrogen atoms as a result of their uniquely high neutron incoherent cross section, σ. In basic terms, the neutron cross

section can be described as the effective area presented by a nucleus to an incident neutron. Given units of m^2 or, more conventionally, barns (where 1 barn = 10^{-28} m^2), the neutron cross section can also be defined as the number of particles scattered per unit time divided by the incident number per unit flux density. The scattering cross section is related to another property of the scattering atom; that is, the scattering length, *b*. Given units of m, and used as a measure of the strength of the neutron-nucleus interaction, the scattering length can be used to calculate the scattering cross section according to the following equation:

$$\sigma = 4\pi b^2 \qquad \textbf{Eq. 32}$$

It is important to note at this point the existence of two different values of *b*; the coherent scattering length, b_{coh}, and the incoherent scattering length, b_{inc}. This, of course, gives rise to two corresponding scattering cross sections; σ_{coh} and σ_{inc}. Coherent scattering arises as a result of long range order present in a sample. By treating incoming neutrons as a series of in-phase wavefronts, the scattered neutron waves will remain in-phase as a result of the long range order of the sample leading to interference effects, which can be measured in neutron diffraction experiments. With incoherent scattering, the sample possesses no significant long range order so the incoming neutrons can be treated as individual particles, leading to scattered neutron waves in all directions and all out-of phase with each other.

Scattering lengths cannot be determined by any theoretical route and must be deduced experimentally. They show no clear pattern; often varying dramatically between neighbouring elements. Neutrons are also sensitive to isotopic variations; for instance, ^{35}Cl has a coherent scattering length of 11.8 x 10^{-15} m, compared with 2.60 x 10^{-15} m for ^{37}Cl. The average scattering length that gives rise to the coherent signal is calculated from these two values based on the isotopic fractions of the sample. The corresponding incoherent scattering length is calculated as the difference between the average of the squared lengths and the square of the average length. Finally, while equation 32 is invariably used to calculate the scattering cross sections from their corresponding scattering lengths, the values obtained for σ_{inc} are not always the true values. Adjustments are sometimes required to correct for the influence of spin incoherence. This factor is often significant in hydrogenous materials, arising as a consequence of the

interaction between neutrons and unbound protons. This results in the existence of two scattering lengths, b_+ and b_-, occurring for a triplet state (where the neutron and hydrogen spins are parallel) and a singlet state (where the neutron and hydrogen spins are antiparallel), respectively. The coherent and incoherent scattering lengths are then calculated using equations 33 and 34:

$$b_{\text{coh}} = \frac{P_+}{P_S} b_+ + \frac{P_-}{P_S} b_- \qquad \textbf{Eq. 33}$$

$$b_{\text{inc}} = \frac{P_+}{P_S} |b_+|^2 + \frac{P_-}{P_S} |b_-|^2 - (b_{\text{coh}})^2 \qquad \textbf{Eq. 34}$$

where $P_+ = 3$ (triplet), $P_- = 1$ (singlet) and P_S is the total spin. The values of b_{coh} and b_{inc} are then used in equation 32 to calculate the *free atom* coherent and incoherent scattering cross sections.

The final convention used for the calculated scattering cross sections is to represent them as *bound* values. A bound scattering length is what the scattering atom would possess if its mass were infinite. This allows the scattering atom to be placed at the origin of coordinates and removes the need to use reduced masses in all subsequent scattering calculations. The reduced mass of the incoming neutron is first calculated using equation 35:

$$\frac{1}{\mu_n} = \frac{1}{m} + \frac{1}{m_n} \qquad \textbf{Eq. 35}$$

where μ_n is the reduced mass of the incident neutron, m is the scattering atom mass and m_n is the rest mass of the neutron.

The bound cross section can then be calculated using equation 36:

$$\frac{\sigma_{\text{bound}}}{m_n^2} = \frac{\sigma_{\text{free}}}{\mu_n^2} \qquad \textbf{Eq. 36}$$

Bound neutron scattering lengths and cross sections for elements and their isotopes are available in the literature. The cross sections for hydrogen are shown here: σ_{coh} = 1.76 barn (where 1 barn = 10^{-28} m^2), σ_{inc} = 80.3 barn and σ_{total} = 82.0 barn. It can be seen from these values that the coherent cross section for hydrogen is very low, making neutron diffraction a poor technique for the study of hydrogen-containing materials. The incoherent cross section on the other hand is exceptionally high; the vast majority of the other elements having cross sections of between 5 and 10 barn, often lower (e.g. the cross section of carbon is 5.5 barn). This is why, in INS spectra, scattering intensity due to vibrations involving hydrogen tend to dominate.

Variations in cross sections between isotopes of the same element can be advantageous in structure determination using a process called isotopic labelling. By substituting one isotope for another, the scattering becomes different in those constituents containing the substitute, revealing their positions relative to other constituents. This technique is often used for the assignment of hydrogen modes by selective substitution of deuterium. The bands occur at the same energies, but those involving deuterium will be considerably weaker as a result of the decrease in scattering cross section from hydrogen to deuterium (82.0 barn becomes 7.64 barn).

By knowing the neutron scattering cross section, this allows the flux of neutrons scattered out of the beam to be calculated if the incident flux, J_i is known (see equation 37):

$$J_f = J_i \, exp(-d_s C \sigma) \qquad \textbf{Eq. 37}$$

where J_f is the unscattered flux after the sample, d_s is the thickness of the sample and C is its concentration. The scattered flux is therefore $(J_i - J_f)$.

In scattering experiments, the neutron can be described as a wave with all the corresponding properties this implies. This includes having an associated wavelength, λ, and velocity, v (with **v** being the corresponding vector quantity). When working with neutrons, it is often useful to do so in terms of the neutron *wave vector*, **k**, (where the magnitude of $k = 2\pi/\lambda$). This property is linearly related to the neutron's momentum as seen in equation 38, which also details the relationship between **v** and **k**:

$$\frac{h\mathbf{k}}{2\pi} = m\mathbf{v} \qquad \textbf{Eq. 38}$$

where h is Plank's constant, m is the mass of the neutron and $m\mathbf{v}$ is momentum of the neutron. The conventional wavelength units used with neutrons is angstroms. The wave vector, **k**, is denoted in units of $Å^{-1}$ as a result of the relationship expressed in the previous paragraph.

The incoming neutron wave is represented as a wavefunction, $e^{i\mathbf{k}\cdot\mathbf{r}}$ which is a plane wave of unit amplitude expressed in terms of the position vector, **r**. This wave is shown by the straight lines in figure 26, where the lines represent the nodes of the wave. The scattered neutron wave takes the form of the spherical wave fronts seen in figure 27. This occurs because the size of the scattering nucleus is so small compared to the wavelength of the neutron wave that it is effectively a point scatterer. Thus the radiation after collision with the nucleus is scattered isotropically; that is, with equal probability in any direction. The scattered neutron wave can be expressed by the wavefunction, $(-b/r)e^{i\mathbf{k}\cdot\mathbf{r}}$, where the spherical wavefronts have amplitudes of b/r.

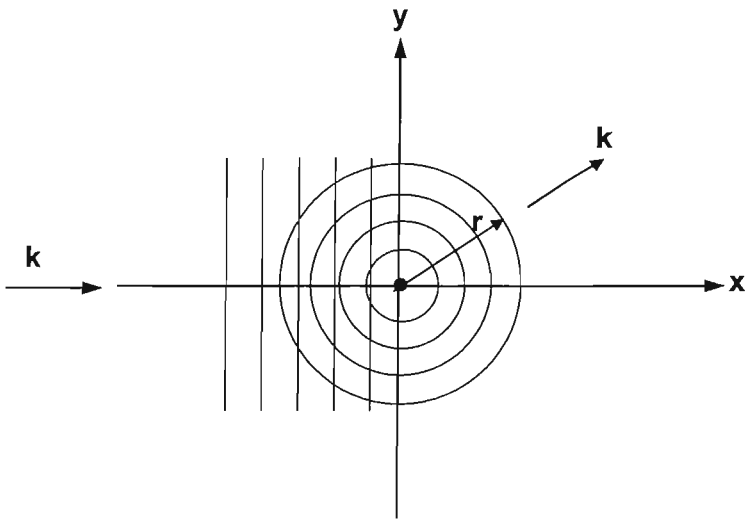

Figure 26 Diagram showing incoming plane wave being scattered by nucleus as spherical wavefronts

When measuring the scattering of neutrons by a sample, the total scattering is a sum of all the individual scattering from each of the nuclei. If the scattering is inelastic, then

there has been an exchange of energy and/or momentum between the neutrons and the atoms in the sample. If momentum can be calculated from equation 38, and the incoming and scattered neutron wave vectors are labelled $\mathbf{k_i}$ and $\mathbf{k_f}$ respectively, then the momentum transfer from the neutron to the sample can be represented as in equation 39:

$$\frac{h}{2\pi}\mathbf{Q} = \frac{h}{2\pi}(\mathbf{k}_i - \mathbf{k}_f) \qquad \textbf{Eq. 39}$$

where $\mathbf{Q}$ is the *scattering vector* (equivalent to $(\mathbf{k_i} - \mathbf{k_f})$). The relationship between these three quantities can be expressed graphically in a scattering triangle (as seen in figure 27).

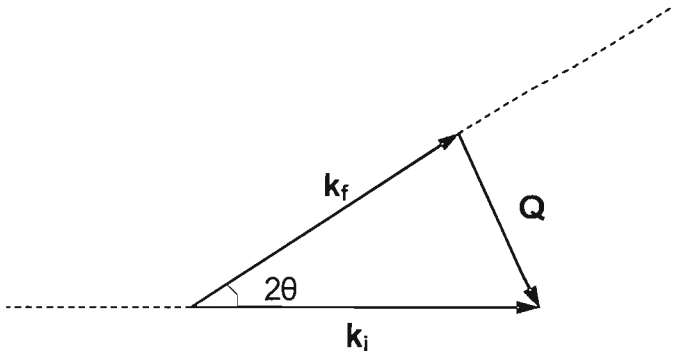

Figure 27 **Neutron scattering triangle for an inelastic collision where the incoming neutron loses energy ($\mathbf{k_f} < \mathbf{k_i}$)**

The scattering triangle depicted in figure 27 represents an inelastic collision in which the neutron loses energy; thereby $\mathbf{k_f} < \mathbf{k_i}$. The scattering vector, $\mathbf{Q}$, makes up the third side of the triangle. The magnitude and direction of $\mathbf{Q}$ are therefore dependent on the two wave vectors, along with the scattering angle, 2θ (the angle through which the neutron is deflected).

In a neutron scattering experiment, the energy spectrum of the sample is scanned and the scattered neutrons are measured by a detector as a function of time. This is the final, or detected, neutron flux, J_f. This is normalised to the number of neutrons reaching the sample per second (the incident flux, J_i). The intensity of scattered neutrons measured by the detector is related to the rate of change of the cross section with respect to the final energy, E_f, and solid angle, $d\Omega$. This is represented by the

double differential scattering cross section, $(d^2\sigma/dE_f\, d\Omega)$, with units of barn eV^{-1} sr^{-1}. The solid angle is calculated as in equation 40:

$$d\Omega = \frac{A}{d_f^2} \qquad \textbf{Eq. 40}$$

where A is the area of the detector, and d_f is the distance of the detector from the sample.

This double differential can be expressed in terms of a function, S, as shown in equation 41:

$$S(\boldsymbol{Q},\omega)_l = \frac{4\pi}{\sigma_l}\frac{\boldsymbol{k}_i}{\boldsymbol{k}_f}\left(\frac{d^2\sigma}{dE_f\, d\Omega}\right)_l \qquad \textbf{Eq. 41}$$

The subscript, l, refers to one specific atom of the molecule. This is one form of the *scattering law*, where S represents the observed intensity as a function of $\boldsymbol{Q}$, the momentum transfer, and ω, the oscillator frequency (corresponding to the energy transfer for a specific vibrational mode). The scattering law is directly related to the observed intensities when summed over all the atoms in the sample. When collecting INS data for incoherent systems such as isotropic powder samples where the vibrations along the three Cartesian axes are degenerate, the scattering law can be simplified and expressed as in equation 42:

$$S(\boldsymbol{Q},n\omega) = \left(\frac{Q^2u^2}{n!}\right)\exp\left(-Q^2u^2\right) \qquad \textbf{Eq. 42}$$

where n is an integer representing the order of the transition; 1 for the fundamental (1←0), 2 for the first overtone (2←0), etc. (n = 0 represents the elastic scattering of the neutrons where there is no exchange of energy). u is the atomic displacement vector where u^2 equals $\hbar/(2\mu\omega_0)$, with μ representing the oscillator reduced mass.

Overtones in neutron spectroscopy are commonly observed and should always be included in the calculations; at least up to $n = 10$. The total intensity is therefore expressed as in equation 43:

$$S(\boldsymbol{Q},\omega)_{\text{total}} = Q^2 u^2 \exp\left(-Q^2 u^2\right) \qquad \textbf{Eq. 43}$$

The pre-exponential term, Q^2u^2, increases as either the momentum transferred or the atomic displacement increases. However, the momentum transfer, Q, is fixed by the spectrometer being used, allowing the atomic displacement data to be extracted. The exponential term is the Debye-Waller factor corresponding to atomic disorder in the system (random fluctuations of atoms around their lattice sites). This factor decreases more rapidly with Q^2u^2 than the pre-exponential term increases. The exponential term is temperature dependent requiring the use of cryogenic temperatures in order to yield increased intensities (see section 4.3.2).

4.3 Experimental Aspects of Inelastic Neutron Scattering (INS)

4.3.1 The Neutron Source

Modern sources of strong neutrons are produced by two possible methods. The first of these is a reactor source. Neutrons are produced in a nuclear reactor by fission of a critical mass of uranium. These fast (or hot) neutrons that are emitted have energies greater than 1 MeV, making the corresponding wavelengths too short for the study of condensed matter. Furthermore, these high-energy neutrons would be able to knock atoms out of their lattice sites producing vacancies and interstitials. These neutrons are 'cooled' down to more user-friendly energies with the use of a moderator. This is usually a cold material containing elements with a high neutron cross-section (i.e. water or liquid hydrogen) that the neutrons can interact with inelastically, thereby losing energy. The neutrons are emitted with similar energies to those of the moderating material and are known as cold (or thermal) neutrons. The resulting neutron beam must then be reduced to a monochromatic beam in order to be used for scattering experiments. This is achieved by utilising a crystal monochromator and positioning it

such that only those neutrons with a wavelength satisfying the Bragg equation are transmitted in the direction of the experiment.

The second method used in the manufacture of strong neutrons (and the one of most interest here) is the spallation source. The following information presented is specific to the ISIS facility at the CCLRC's Rutherford Appleton Laboratory near Oxford, England where the experiments described in this project were undertaken. The ISIS facility is shown schematically in figure 28 [37].

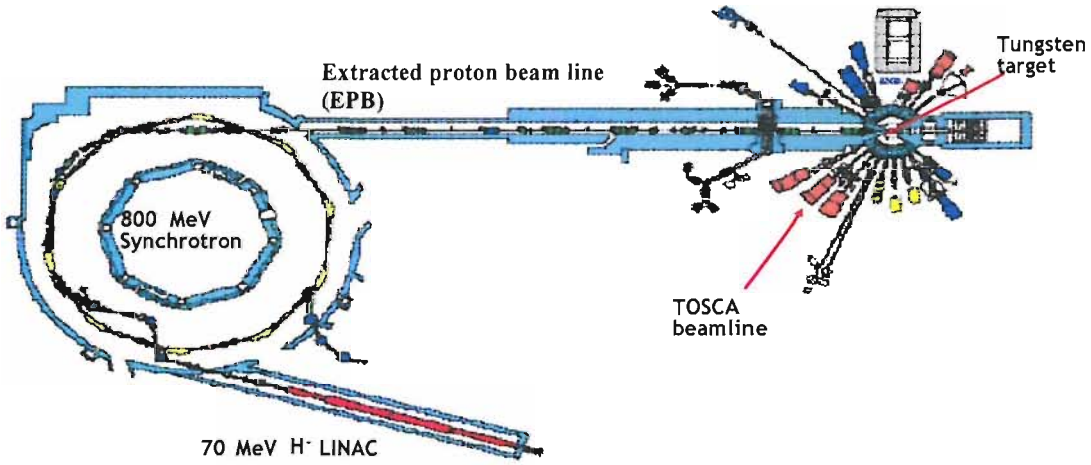

Figure 28 Plan of the ISIS facility (Chilton, UK) [37]

The spallation process occurs when a highly energetic beam of protons collides with a heavy metal target, knocking neutrons loose from the nuclei of the target atoms. One of the advantages of the spallation process over that of fission is the reduced amount of heat production by the spallation target than occurs in a nuclear reactor.

The production of highly energetic protons begins first with the generation of H^- ions by the dissociation of hydrogen followed by electron transfer from a caesium-coated cathode. These ions are then extracted by an electric field into a radio frequency quadrupole accelerator that injects the ions into a linear accelerator (LINAC), where the beam is accelerated to 70 MeV. At the end of the LINAC, the H^- ions pass through a 0.3 μm thick alumina foil that strips both electrons, converting the ions into protons. The beam is then injected into the synchrotron ring where the protons are trapped into two bunches and accelerated to 800 MeV with the use of ten ferrite-tuned radio

frequency cavities. After approximately 10,000 cycles of acceleration around the synchrotron, a 'kicker' magnet deflects the beam into the extracted proton beam line (EPB) – a straight section, at the end of which sits a heavy metal target. In the case of ISIS, this consists of a set of tungsten plates surrounded by a D_2O moderator. When the protons collide with the tungsten nuclei, an intra-nuclear process is triggered, whereby energy is passed between the individual nucleons creating a series of highly excited nuclei. These then lose this excess energy by an 'evaporation' process with the emission of high energy neutrons. Figure 39 shows this *spallation* process pictorially. In addition some protons and other secondary particles, such as alpha-particles, are emitted. Some of these high energy nucleons go on to trigger further reactions, while the majority of the neutrons leave the sample, passing through the moderator material. Those that emerge in the direction of the open neutron port can be used in experiments while others are simply reflected back into the sample by a beryllium reflector assembly. For every high-energy proton that collides with the target, approximately 15 neutrons are produced. These neutrons take the form of a very intense neutron pulse.

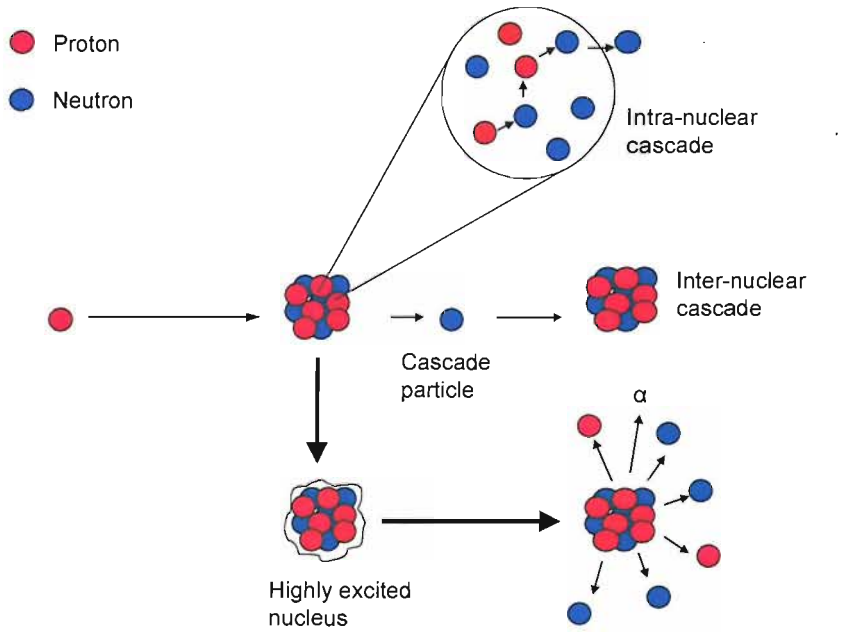

Figure 29 Diagrammatic representation of the spallation process

The production of neutrons in pulses rather than as a continuous stream means that a monochromator crystal is no longer needed to select a narrow energy range of neutrons. Essentially, all of the neutrons that are directed towards the sample can be used by virtue of the *time-of-flight* technique. The velocity and kinetic energy of the neutrons

can be calculated by measuring the time taken to reach the detectors (via the sample) as this is over a fixed distance. The faster (energetic) neutrons arrive early, while the slower neutrons arrive later. The information required is the energy transfer, E_{trans}, occurring between the incident neutrons and the sample. This is clearly the difference between the energy of the incident neutrons (E_i) and that of the scattered neutrons reaching the detector (E_f).

$$E_{trans} = E_i - E_f \qquad \textbf{Eq. 44}$$

The final energy is defined by the use of a crystal analyser. This is a highly orientated pyrolytic graphite (002) crystal, where the angle of the planes is set so that a final neutron energy of ~32 cm^{-1} (4 meV) is selected. These neutrons are then Bragg diffracted onto a cooled beryllium filter to remove high order harmonics before the neutrons arrive at a detector assembly consisting of 13 ^{3}He detectors. There are two such set-ups of crystal analyser; one for neutrons that are Bragg scattered at 45° (forward scattering) and another for those that are scattered at 135° (back scattered). The latter neutrons are those which have sufficient energy to promote an internal transition in the sample. Figure 30 illustrates how an analyser module may be arranged:

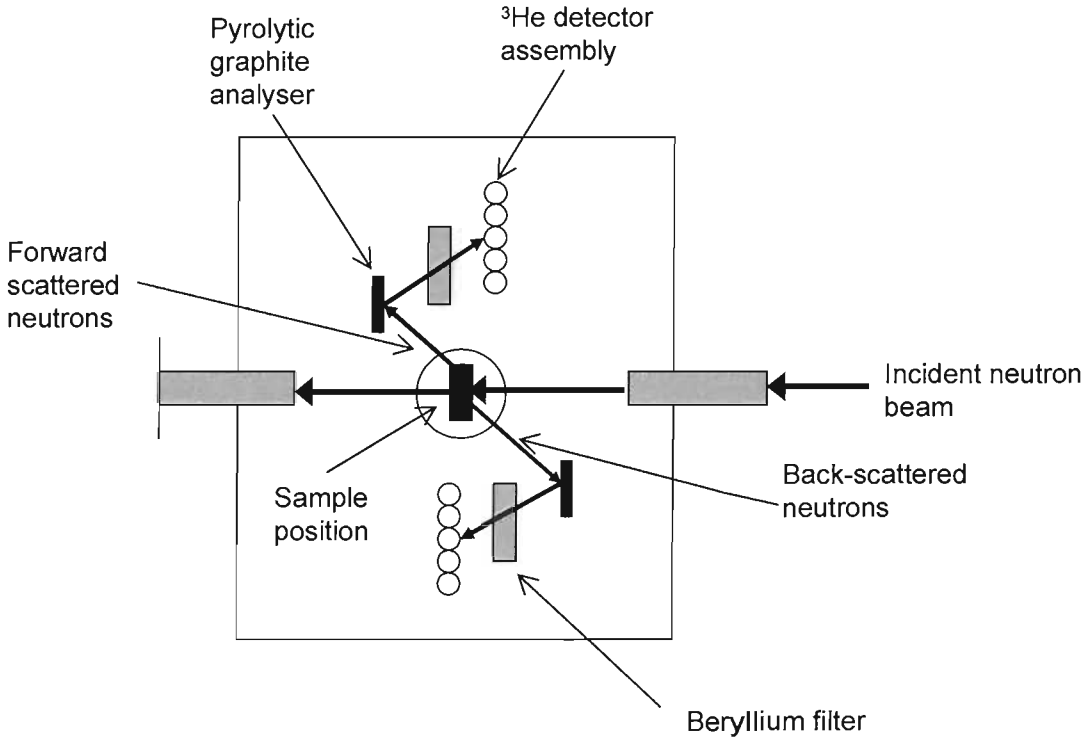

Figure 30 **Overhead view through the analyser module for a indirect geometry time-of-flight spectrometer at a pulsed spallation neutron source**

The incident energy of the neutrons can be determined from the velocity as shown in equation 45:

$$E_i = \frac{m_n v_i^2}{2} \qquad \textbf{Eq. 45}$$

where m_n is the mass of the neutron and v_i is the incident neutron velocity.

Both the travel time and distance travelled by the neutrons are known. The incident travel time, t_i, can be expressed as shown in equation 46:

$$t_i = \frac{d_i}{\sqrt{\frac{2E_i}{m_n}}} \qquad \textbf{Eq. 46}$$

where d_i is the distance from the moderator to the sample.

The time that is actually measured, t_t, is the total travel time of the neutrons from the moderator to the sample, and from the sample through the analyser to the detectors. The total time is therefore:

$$t_t = t_i + t_f = \frac{d_i}{v_i} + \frac{d_f}{v_f} = \frac{d_i}{\sqrt{\frac{2E_i}{m_n}}} + \frac{d_f}{\sqrt{\frac{2E_f}{m_n}}} \qquad \textbf{Eq. 47}$$

where t_f is the time that the neutrons take to travel from the sample to the detectors, d_f is the distance of the path the neutrons take travelling from the sample to the analyser crystal to the detectors, v_f is the final velocity of the neutrons reaching the detectors and E_f is the final energy of the neutrons. By rearranging equation 47 and substituting E_i with $(E_t + E_f)$ where E_t is the energy transferred between the neutrons and the sample (i.e. the desired quantity), it follows that:

$$t_t = \sqrt{\frac{m_n d_i^2}{2(E_t + E_f)}} + \sqrt{\frac{m_n d_f^2}{2E_f}} \qquad \textbf{Eq. 48}$$

It can be seen from equation 48 that, as long as the distances, d_i and d_f, are known along with the final energy and total travel time of the neutrons, then the energy transferred can be calculated.

4.3.2 Experimental set-up

The ISIS facility has a number of beamlines that utilise the spallation neutrons produced there. The work for this project was undertaken on the TOSCA beamline; a time-of-flight spectrometer operating on the same basic principles as described in the previous section. The analyser module works in essentially the same way as that shown in figure 30. The TOSCA set-up is also known as an indirect geometry instrument. This refers to the fact that the neutrons used have a range of energies, so instead the wavelength of the scattered neutrons is fixed by Bragg reflecting them from the pyrolitic graphite crystal into the detector. On TOSCA, the momentum transfer, Q, is fixed for each energy ($Q^2 \sim E_t/16$).

A Nimonic chopper is situated between the moderator and the sample, which can be in either an open or a closed position. This is used to determine the range of energies reaching the sample. The TOSCA chopper is used to remove the gamma flash and improve the background. Also present on the chopper is a tailcutter (a sheet of B_4C) on the leading edge, which removes the slowest 'low-energy' neutrons from the moderated pulse that would otherwise result in frame overlap. The end result is that the TOSCA station constitutes a spectrometer with no moving parts, that can record spectra from 0 to 8000 cm^{-1}; optimal between 30 and 4000 cm^{-1} (0-500 meV) with the best results below 2000 cm^{-1} (250 meV). Neutron energy in INS is conventionally expressed in meV; however, chemists often prefer to use the more recognisable unit of cm^{-1}. These two sets of units are easily convertible using the following relationship:
1 meV = 8.066 cm^{-1}.

It is not feasible to study catalyst materials with INS as *in-situ* electrodes so samples are run on the catalysts in powder form. The samples were loaded into a thin-walled aluminium can, which was then sealed using an indium strip. Due to the low scattering intensity with neutrons, the cells are designed to hold a relatively large quantity of

sample; commonly around 20 g. The cell was attached to the base of a 1.40 m long pole, or *centrestick*, so that the cell can be positioned below-ground in the path of the neutron beam. Heated gas lines run down the centrestick into the cell, where temperature and pressure sensors are also situated. As previously stated, the Debye-Waller factor is responsible for dampening the INS intensity. For this reason the sample needs to be cooled to below 20 K during data collection. To this end, the sample is situated within a *Closed Cycle Refrigerator* (CCR) and cooled with the aid of helium exchange gas. The sample can be placed under vacuum using a turbomolecular pump (Leybold). A typical spectrum is presented as the sum of 3 - 4 scans run successively over about 12 hours.

Specific details relating to the individual experiments can be found in chapter 5.

4.4 Analysis of INS spectra

Once an INS spectrum has been obtained, the observed vibrations can be assigned. This is achieved using computational chemistry programs to calculate the vibrational modes for a given sample and compare these with the results obtained. Modelling calculations and generation of theoretical spectra were undertaken by Dr. Ramirez-Cuesta at the ISIS facility at the Rutherford Appleton Laboratory.

4.4.1 Molecular Modelling of INS spectra

The systems under investigation in this project involve the dosing of molecular hydrogen onto carbon-supported Platinum or Platinum-Molybdenum catalysts. With this in mind, the vibrational modes of hydrogen on different Pt surfaces were calculated. This was achieved using the DMol^3 program from Accelerys [38], which performs *ab initio* calculations based on density functional theory (DFT). This is preferred over the older Hartree-Fock methods due to the relatively lower computing power required when dealing with larger systems. It does this by replacing the complicated many-body electronic wavefunction with the electron probability density, $\rho(\mathbf{r})$. The consequence of this is that the function is now dependent on only three spatial variables as opposed to the $3N$ coordinates that are used to describe the Schrödinger wavefunction. DFT also takes into account some of the effects of electron correlation; that is, how electrons in a

molecular system react to the motion of all the other electrons. Whereas Hartree-Fock methods have each electron reacting to an averaged electron density, DFT methods account for the instantaneous interactions of pairs of electrons with opposite spin.

Extensions to the DFT method used in DMol[3] have made it possible to go from performing calculations on molecules to being able to deal with larger extended systems, i.e. solids. In order to cope with the infinite number of eigenstates, the solid is represented as a periodic array of atoms; idealised as a unit cell with perfect translational symmetry. Three Pt surfaces were generated: Pt(111), Pt(110) and Pt(100) (as shown in figure 31).

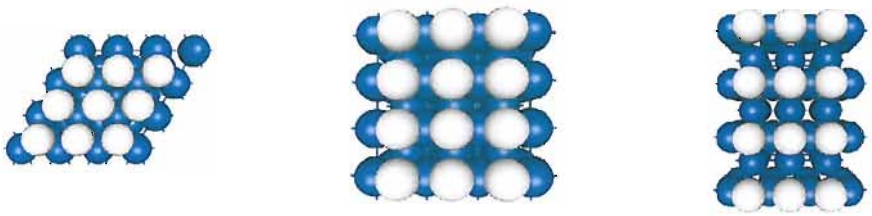

Figure 31 **Model surfaces of Pt(111) [left], Pt(100) [middle], and Pt(110) [right]. Pt atoms shown in blue, while H atoms riding on the surface in the energy minimized geometry are shown in white.**

Each surface was modelled as a slab containing five layers of Pt atoms. The periodicity was accounted for by generating a supercell of 3x3 in the *xy* plane. A vacuum gap was introduced to simulate the open surface and ensure that periodic images do not interact. Sampling of the first Brillouin zone was then performed using the local density approximation (Perdew-Wang) with a localised basis set represented as a numerical tabulation to find the energy minimized geometry of the H atoms riding on the Pt sites. A finite displacement technique was then used to obtain the dynamical matrix, which involved displacing each of the atoms in the unit cell by 0.005 Å in turn along the three Cartesian directions and a single-point calculation used to derive the force constants. Diagonalization of the dynamical matrix was then used to yield the desired eigenvalues; in this instance, the vibrational frequencies as well as the atomic displacement eigenvectors.

4.4.2 The aCLIMAX program

The output from DMol[3] and indeed other *ab initio* packages such as GAUSSIAN98 can be entered into the aCLIMAX program [39]. The vibrational frequencies and atomic displacements are used in order to calculate $S(\boldsymbol{Q},\omega)$. The aCLIMAX program will then use the results of these calculations to generate an INS spectrum that can be compared with the actual experimental data obtained. aCLIMAX was compiled using Visual Basic and has been released as 'freeware'.

5 REFERENCES

1. Keck, L.; Buchanan, J. S.; Hards, G. A. U.S. Patent 5,067,161, 1991.
2. Hoogers, G.; Thompsett, D. *Cattech* **2000**, *3*, 106.
3. Ralph, T. R.; Hogarth, M. P. *Platinum metals Rev.* **2002**, *46*, 3.
4. Crabb, E. M.; Ravikumar, M. K.; Qian, Y.; Russell, A. E.; Maniguet, S.; Yao, J.; Thompsett, D.; Hurford, M.; Ball, S. C. *Electrochemical and Solid State Letters* **2002**, *5*, A5.
5. Cotton, F. A.; Pipal, J. R. *Journal of the American Chemical Society* **1971**, *93*, 5441.
6. Hogarth, M. P. The Development of the Direct Methanol Fuel Cell. PhD. Thesis, University of Newcastle, 1995.
7. Fisher, A. C. *Electrode Dynamics*; Oxford University Press, 1996.
8. Bett, J.; Kinoshita.K; Routsis, K.; Stonehart.P. *Journal of Catalysis* **1973**, *29*, 160.
9. Gasteiger, H. A.; Kocha, S. S.; Sompalli, B.; Wagner, F. T. *Applied Catalysis B-Environmental* **2005**, *56*, 9.
10. van Dorssen, G. E. *New developments in XAFS spectroscopy*, 1999.
11. Rehr, J. J.; Albers, R. C. *Reviews of Modern Physics* **2000**, *72*, 621.
12. Brown, M.; Peierls, R. E.; Stern, A. *Physical Review B* **1977**, *15*, 738.
13. Mansour, A. N.; Cook, J. W.; Sayers, D. E. *Journal of Physical Chemistry* **1984**, *88*, 2330.
14. Lytle, F. W. *Journal of Synchrotron Radiation* **1999**, *6*, 123.
15. Sayers, D. E.; Stern, E. A.; Lytle, F. W. *Physical Review Letters* **1971**, *27*, 1204.
16. Lee, P. A.; Pendry, J. B. *Physical Review B* **1975**, *11*, 2795.
17. Zabinsky, S. I.; Rehr, J. J.; Ankudinov, A.; Albers, R. C.; Eller, M. J. *Physical Review B* **1995**, *52*, 2995.
18. Russell, A. E.; Rose, A. *Chemical Reviews* **2004**, *104*, 4613.
19. Cook, J. W.; Sayers, D. E. *Journal of Applied Physics* **1981**, *52*, 5024.
20. Binsted, N. EXCURV98: CCLRC Daresbury Laboratory computer program, 1998.
21. Gurman, S. J.; Binsted, N.; Ross, I. *Journal of Physics C-Solid State Physics* **1984**, *17*, 143.

22. Rehr, J. J.; Albers, R. C. *Physical Review B* **1990**, *41*, 8139.
23. Rehr, J. J.; Albers, R. C.; Zabinsky, S. I. *Physical Review Letters* **1992**, *69*, 3397.
24. Rose, A. Structural Effects in Fuel Cell Electrocatalysts. PhD Thesis, University of Southampton, 2004.
25. Kampers, F. W. H. *EXAFS in Catalysis: Instrumentation and Applications*; Technical University of Eindhoven, 1998.
26. McMaster, W. H. Compilation of X-ray Cross-Sections, National Bureau of Standards, for calculation of X-ray cross sections.
27. O'Grady, W. E.; Hagans, P. L.; Pandya, K. I.; Maricle, D. L. *Langmuir* **2001**, *17*, 3047.
28. Herron, M. E.; Doyle, S. E.; Pizzini, S.; Roberts, K. J.; Robinson, J.; Hards, G.; Walsh, F. C. *Journal of Electroanalytical Chemistry* **1992**, *324*, 243.
29. Maniguet, S.; Mathew, R. J.; Russell, A. E. *Journal of Physical Chemistry B* **2000**, *104*, 1998.
30. Viswanathan, R.; Hou, G. Y.; Liu, R. X.; Bare, S. R.; Modica, F.; Mickelson, G.; Segre, C. U.; Leyarovska, N.; Smotkin, E. S. *Journal of Physical Chemistry B* **2002**, *106*, 3458.
31. Roth, C.; Martz, N.; Buhrmester, T.; Scherer, J.; Fuess, H. *Physical Chemistry Chemical Physics* **2002**, *4*, 3555.
32. Wiltshire, R. J. K.; King, C. R.; Rose, A.; Wells, P. P.; Hogarth, M. P.; Thompsett, D.; Russell, A. E. *Electrochimica Acta* **2005**, *50*, 5208.
33. Mepsted, G. O.; Moore, J. M. Performance and durability of bipolar plate materials. In *Handbook of Fuel Cells - Volume 3: Fuel Cell Technology and Applications Part 1*; Vielstich, W., Lamm, A., Gasteiger, H. A., Eds.; Wiley, 2003; Vol. 3.
34. Wiltshire, R. J. K. Extending *in situ* XAS of PEM fuel cells to more Realistic Conditions. PhD Thesis, University of Southampton, 2005.
35. Lin, J.-C.; Kiunz, H. R.; Fenton, J. M. Membrane/electrode additives for low-humidification operation. In *Handbook of Fuel Cells - Volume 3: Fuel Cell Technology and Applications Part 1*; Vielstich, W., Lamm, A., Gasteiger, H. A., Eds., 2003; Vol. 3.
36. Chadwick, J. *Nature* **1932**, *120*, 312.
37. www.isis.ac.uk.
38. Delley, B. *Journal of Chemical Physics* **2000**, *113*, 7756.

39. Ramirez-Cuesta, A. J. *Computer Physics Communications* **2004**, *157*, 226.

Chapter Three: Platinum-Molybdenum Anode Catalyst

1 Introduction

Proton Exchange Membrane (PEM) fuel cells are currently at the forefront of research intended to develop clean and plentiful sources of power to counter increasing environmental concerns and the depletion of fossil fuels. The simplest system utilises pure hydrogen as a fuel, which is then oxidised by a Pt-based catalyst at the anode. It is unlikely that such systems will become fully commercial, however, due to the inherent difficulties with the storage of pure hydrogen. The size and complexity of such hydrogen storage systems make them especially inappropriate for use on-board of cars, which is a problem because the automotive industry is intended to be a major end market for fuel cell systems. In addition, there is not an existing storage and distribution infrastructure in place for a large scale hydrogen economy, as there is for liquid fuels such as petrol. This also makes it unsuitable for use in larger stationary power applications.

The current preferred option is to use an alternative source of hydrogen; commonly a liquid hydrocarbon, such as methanol. This can then be converted into hydrogen via an on-board reformer. This process also leads to significant quantities of CO_2 (15-20 %) and CO (1-2 %) being present in the fuel stream [1]. CO acts as a poisoning species by strongly binding to Pt catalytic sites, effectively preventing the dissociative adsorption and oxidation of hydrogen. The concentration of CO can be lowered to less than 100 ppm by the use of a water gas shift reactor to convert CO back into CO_2 and more hydrogen [2]. Selective catalytic oxidation methods can also be used to lower the CO concentration further. These extra components understandably add extra size and complexity to the overall system, meaning that reformer-based fuel cells are currently in use for larger stationary power applications only and not in automotive systems.

An alternative approach is the development of Pt-based anode catalysts that have increased tolerance to the presence of CO. These are often bimetallic alloys, such as PtRu and PtCo [2]. The bifunctional mechanism for the CO tolerance of PtRu was first postulated by Watanabe *et al* [3] and involves water activation by Ru, leading to OH species, which are then involved in the promotion of CO to CO_2 on neighbouring Pt sites. These alloy catalysts are also thought to operate via an intrinsic mechanism, whereby the addition of a secondary metal alters the chemisorption properties of the catalyst so that the CO coverage is lowered with respect to H_2 oxidation sites. Pt-based catalysts that have been promoted by the addition of a second metal oxide have also been shown to have some tolerance to CO compared with Pt alone. Examples of these types of catalyst include Pt-WO_3 and Pt-SnO_2 [4,5], and operate via the promoted mechanism only.

In 1965, Niedrach and Weinstock first showed that Mo oxides were active towards the electrooxidation of carbon monoxide when mixed with platinum black [6]. More recently, Grgur *et al* have investigated electrooxidation of H_2/CO mixtures on bulk PtMo alloys prepared by arc-melting of the pure elements in an argon atmosphere and a homogenising heat treatment [7,8]. They determined that their PtMo catalysts produced similar polarisation curves and comparable current densities when operating with 100 ppm CO in H_2 to a PtRu bulk alloy. It was also shown that although the anodic stripping process of CO electrooxidation varied between the two catalysts with most of the CO being oxidised above 0.6 V vs. RHE on the PtMo, there was also evidence of small amounts being oxidised at very low potential (0.05 to 0.5 V). The enhancement of H_2 oxidation in both cases was determined to be similar, with a reduction in the steady-state coverage of CO_{ads} by oxidative removal, freeing up Pt sites for H_2 oxidation.

Later work by the same group [9] and also by Mukerjee *et al* [10,11] extended this work into the study of carbon-supported PtMo catalysts supplied by E-TEK that would have more practical applications as possible anode catalysts in PEM fuel cells due to their lower precious metal loadings. These catalysts were all shown to have enhanced CO tolerance properties compared to carbon-supported PtRu catalysts. In one instance, a PtMo/C catalyst with a Pt: Mo ratio of 4: 1, operating with a 100 ppm CO in hydrogen gas mixture in a PEMFC single cell at 85 °C, showed only a 50 mV loss in

cell potential, compared with a loss of 160 mV for a 1: 1 PtRu/C catalyst [9]. Johnson Matthey have also prepared PtMo/C catalysts by sequentially depositing Pt oxide and Mo oxide followed by thermal reduction at high temperature, which were then tested in a PEMFC [1,12]. A 3:1 PtMo/C catalyst, when operating with a hydrogen feed containing 46 ppm CO and current density of 1.0 A cm^{-2}, was found to be operating at up to 0.2 V above a 1: 1 Pt Ru catalyst under the same conditions. However, when the CO concentration was lowered to 10 ppm, the PtRu catalyst actually became more CO tolerant [1].

The enhanced mechanism for CO oxidation at low potentials has been attributed to oxygen transfer from Mo oxy-hydroxide species at the surface of the catalyst particles to CO adsorbed on neighbouring Pt sites, promoting oxidative removal by conversion to CO_2 [7,9]. This is believed to be possible due to the Mo (IV/VI) redox couple present for surface Mo atoms, whereby the more oxidised form (predominantly $MoO(OH)_2$) is reactive towards the oxidative removal of CO because it can easily be reduced to the +IV state by the donation of oxygen to neighbouring species. Surface Mo atoms readily form oxides in air, which can then become hydrated to form oxy-hydroxides (such as MoO(OH) and $MoO(OH)_2$). The promotional effect would be maximised by increasing the intimate contact between platinum and these oxidised molybdenum species. EXAFS studies on some of the supported PtMo systems previously mentioned have found that it is much harder to produce a well-mixed alloy than it is for equivalent PtRu catalysts [13-15]. A lack of molybdenum neighbours in the first coordination shell in the Pt EXAFS analysis implies that a small amount of platinum has been modified by molybdenum; however the majority of molybdenum is present as a separate oxide phase. In order to ensure that all of the molybdenum present is associated with the platinum Crabb *et al* developed a preparation method whereby an organometallic Mo precursor undergoes a controlled surface reaction with a reduced Pt surface to yield a modified Pt/C catalyst with sub-monolayer coverages of Mo [16] (see chapter 2, section 1.2.2). The precursor used in this instance was tetraallyldimolybdenum, which is highly air sensitive. EXAFS results obtained at the Mo K edge found that, at 0.65 V, the molybdenum was present on the surface as an oxide species associated with the platinum, while at 0.05 V, the molybdenum atoms are reduced and will become incorporated into the surface layer of the platinum nanoparticles. In addition, the onset of CO oxidation was found to occur at similar

overpotentials to conventionally prepared PtMo/C catalysts. The coverage of molybdenum on the catalysts was substantially less than expected as shown by the Inductively Coupled Plasma Emission Spectroscopy (ICP-ES) analysis; only a tenth of a monolayer was present as opposed to the expected half a monolayer.

The cocatalytic effect of molybdenum on the electrooxidation of methanol on platinum catalysts has also been investigated as part of current development of direct methanol fuel cells. Shropshire first reported an increase in the activity of platinum towards methanol electrooxidation in H_2SO_4 when Na_2MoO_4 was present as an adsorbate on the electrode in 1965 [17]. The enhanced catalysis was attributed to the presence of the Mo(VI)/Mo(V) redox couple, as seen in equations 1 and 2:

$$6[Mo^{6+}]_{ads} + CH_3OH + H_2O \longrightarrow 6[Mo^{5+}]_{ads} + CO_2 + 6H^+ \qquad \textbf{Eq. 1}$$

$$[Mo^{5+}]_{ads} \longleftrightarrow [Mo^{6+}]_{ads} + e^- \qquad \textbf{Eq. 2}$$

The reaction shown in equation 1 is very slow, however, leading to current densities for methanol oxidation that were too small for practical fuel cell applications. More recently, Zhang *et al* investigated the catalytic oxidation of methanol using an electrochemically codeposited platinum/molybdenum oxide catalyst supported on carbon [18]. They found enhanced activity for methanol oxidation in acidic media compared with a platinized carbon electrode. This was attributed to a surface redox mechanism involving the Mo(VI)/Mo(IV) couple in substoichiometric lower valence molybdenum oxides MoO_x ($2<x<3$) and a possible proton spillover effect from hydrogen molybdenum bronze. Li *et al* carried out research of methanol oxidation on Pt in acidic media using adsorbed molybdates that had been reduced at very negative potentials in H_2SO_4 to form a variety of hydrogen molybdenum bronzes (H_xMoO_3, $0<x<2$). The concentration of the acid affected the form of the bronze that was present, with an optimum concentration of 3.7 M H_2SO_4 solution giving rise to a bronze form that yielded the strongest catalysis of methanol oxidation [19]. Other groups researching the cocatalytic effect of molybdenum on methanol oxidation by platinum have found that PtMo catalysts are not as effective as the current PtRu alloy catalysts

available, however, ternary Pt-Ru-Mo catalysts have shown promising improvements in performance [20-22].

This chapter will present results obtained for a series of codeposited PtMo/C catalysts produced by a variety of preparation methods supplied by Johnson Matthey. In addition, a surface modified PtMo/C catalyst prepared by a variation on the controlled surface reaction (CSR) method described earlier was also investigated. The CO tolerance and methanol oxidation properties have been tested electrochemically and XAS results obtained in order to yield structural parameters of the catalysts. The XAS results reported here represent the first *in-situ* single cell data for these types of catalysts allowing the properties of the catalysts within actual fuel cell environments to be probed.

2 Experimental Details

2.1 Catalysts

A series of PtMo/C catalysts supported on XC72R carbon was supplied by Johnson Matthey along with 20 wt. % and 40 wt. % Pt/C catalysts for comparison. These catalysts were prepared by proprietary methods [23] and described further in chapter 2, section 1.2.1. Mean particle sizes determined by XRD for the catalysts in Table 1 were provided by Johnson Matthey.

Table 1 Composition of Pt/C and PtMo/C catalysts by weight and atomic ratio

Pt wt. %	Mo wt. %	Preparation route (see text)	Heat treatment / °C (environment)	Atomic ratio Pt: Mo	Mean particle size determined by XRD / nm
20	0	-	-	100: 0	2.9
40	0	-	-	100: 0	4
26.8	10.1	1	620 (N_2)	57: 43	-
29.7	11.4	1	900 (N_2)	56: 44	2.4
35.4	5.3	2	620 (N_2)	77: 23	2.9
36.9	5.7	2	900 (N_2)	76: 24	3.3
34.5	8.6	3	1000 (N_2)	66: 34	-
19.9	1.8	3	1000 (Ar)	84: 16	3.7
20.3	3.5	3	1000 (Ar)	74: 26	3.1
19.3	3.6	3	650 (N_2)	73: 27	1.8
19.3	3.6	3	1000 (Ar)	73: 27	-
18.0	4.3	3	1000 (Ar)	67: 33	2.9
17.0	7.6	3	1000 (Ar)	52: 48	-

The first five PtMo catalysts in Table 1 were prepared with a high total metal content (~ 40 wt. %) using three different preparation methods. The details of the methods are proprietary, but may be summarised briefly as follows. Preparation routes 1 and 2 follow a similar method involving the reaction of a 40 wt. % Pt/XC-72R catalyst with a Mo oxide precursor compound in an organic solvent followed by a subsequent heat treatment; method 2 being altered slightly in an effort to improve the yield by dissolving the precursor in an aqueous acidic solution. Preparation route 3 was an attempt to improve the amount of mixing of the Pt and Mo and involved the sequential deposition of Pt oxide and Mo oxide onto the carbon support followed by thermal reduction at high temperatures, and was first attempted to create a high metal content catalyst similar to the previous PtMo catalysts. This method was then used to create a range of catalysts with closer to 20 wt. % total metal content.

A surface modified PtMo/C catalyst was prepared using the controlled surface reaction as described in chapter 2, section 1.2.2.

Table 2 Composition of CSR PtMo catalyst

Pt wt. %	Mo wt. %	Heat treatment (under hydrogen) / °C	Atomic ratio Pt: Mo
19.5	2.3	200	81: 19

2.2 Electrode preparation

The catalysts were fabricated into electrodes by first making inks using Nafion® as described in chapter 2, section 1.3. Preliminary cyclic voltammetry measurements were obtained using electrodes prepared via the pasting method. However, for the majority of half-cell work involving cyclic voltammetry and steady state polarisation measurements, the inks were painted onto carbon paper electrodes to give loadings of between 0.2 and 1.0 mg Pt cm^{-2}. Electrodes of area 1.32 cm^2 were cut from the resulting sheet. For half cell XAS measurements, the inks were thickened to give a paste and spread manually onto carbon paper in a 3 x 3 cm template to give a loading of 1.5 to 3.0 mg Pt cm^{-2} and larger electrodes with an area of 2.54 cm^2 were punched out and used. The electrodes were then placed in boiling water for 20 minutes to ensure that they were fully hydrated.

2.3 MEA preparation

MEAs of the catalyst samples were prepared as described in chapter 2, section 1.3. For XAS measurements, the anodes were produced by painting catalyst inks onto carbon paper electrodes to give loadings of 1 mg Pt cm^{-2}. 20 wt. % Pd/C was used for the cathodes. MEAs for work involving cyclic voltammetry and steady state polarisation measurements in the mini cell used anodes with catalyst inks painted on to give loadings of 0.22 mg Pt cm^{-2}. The cathodes consisted of carbon paper with a screen printed catalyst layer of 60 wt. % Pt/Ketjen with a loading of 0.38 mg Pt cm^{-2}. Electrodes with an area of 12.56 cm^2 for use in the modified XAS mini cell, or 3.14 cm^2 for use in the unmodified mini cell, were then cut out in preparation for hot pressing. A Flemion® membrane, 30 μm, was used to make the MEAs.

2.4 Electrochemistry

2.4.1 Cyclic Voltammetry

CVs were carried out on the catalysts as working electrodes in a three-electrode half cell. A platinum gauze was used as the counter electrode and all potentials were measured with respect to a MMS reference electrode. All potentials have been converted to the RHE scale, as determined by calibrating with respect to a dynamic hydrogen/Pt electrode. 2.5 M $H_2SO_{4(aq)}$ purged with nitrogen was the electrolyte. CO stripping experiments were performed by holding at 0.05 V vs. RHE while first CO, then N_2, were purged through the electrolyte for 30 minutes each. The electrode was then cycled between 0 and 1 V vs. RHE. The practical procedure is described in more detail in chapter 2, section 2.2.

2.4.2 Methanol Oxidation

Again a three-electrode cell was used. After determining the metal area using CO stripping in 1 M H_2SO_4, the electrode was transferred to a cell with 2 M methanol in 1 M $H_2SO_{4(aq)}$. The electrode was then conditioned by cycling between 0.05 and 0.8 V vs. RHE with a scan rate of 10 mV s^{-1}. The electrode was then polarised using the same potential range and a step potential of 0.05 V. The current was recorded after a stabilisation time of 30 seconds. Current interrupt measurements were taken at 0.65, 0.7 and 0.75 V vs. RHE to correct the data for cell resistance. The temperature was controlled by connecting the cell to a water bath which pumped water through the outer jacket of the cell allowing the procedure to be carried out at 30 °C and 80 °C.

2.4.3 Mini Cell electrochemical measurements

The MEA under investigation was assembled in the mini cell and compressed to 70 % thickness. A water bath was used to pump water through the gas humidifiers and the water channel of the cell; keeping it at a temperature of 80 °C. Gas flow rates of 60 and 40 ml min^{-1} were used for the cathode and anode respectively, and the cell pressure regulators adjusted to keep both sides of the mini cell pressurised to 14 psi-gauge. The system was first flushed with nitrogen gas. Setting the cathode as the working

electrode, and the anode as the counter/reference electrode, the anode gas was switched to hydrogen, with nitrogen as the cathode gas. Once a stable open circuit potential had been reached, the cell was polarised to 0.5 V vs. RHE and the current measured. This current quantifies the hydrogen crossover from the anode to the cathode, and was usually found to be below 20 mA. CO stripping measurements were collected at the cathode using cyclic voltammetry. The potential was held at 0.125 V vs. RHE with CO flowed over the cathode for two mins, followed by 43 mins with the cathode gas switched back to nitrogen. CVs were then measured by cycling from a lower limit of 0.075 V to an upper limit of 1.0 V vs. RHE, with a scan rate of 10 mV s^{-1}. Successive scans were recorded until no CO was present.

Steady state polarisation measurements were recorded when operating the cell under fuel cell conditions. Oxygen gas was flowed to the cathode, while polarisation curves were measured with hydrogen to the anode. Ten fast polarisation curves were recorded first in order to condition the cell. The potential was first held at 0.65 V vs. RHE for 3 min before measuring between 0.95 and 0.65 V vs. RHE, using a step potential of 0.05 V and a maximum time interval of 5 s. Two normal polarisation curves were then recorded in the same manner, with the maximum time interval increased to 60 s. Current interrupt measurements were taken at 0.05 V intervals from 0.9 to 0.6 V vs. RHE and back again, to correct the potential for cell resistance. Further polarisation curves were then obtained in the same way with the anode gas switched first to 100 ppm CO in H_2; followed by 1 % CO in H_2.

CO stripping measurements were then collected at the anode using cyclic voltammetry, after switching the connections so that the anode was now the working electrode. With the cathode gas now switched to hydrogen, CO stripping CVs were obtained for the anode using the same procedure described above for the cathode.

2.5 XAS measurements

All XAS measurements were carried out on station 16.5 at the Synchrotron Radiation Source (SRS) at the Daresbury Laboratory, UK. This station operates with a multipole wiggler source and double crystal Si (220) monochromator and is optimized for ultra-

dilute EXAFS between 9 and 40 keV. Measurements were taken at the Pt L_{III} edge (11.5637 keV) and the Mo K edge (19.9995 keV). The monochromator was detuned to 50% at the Pt L_{III} edge and 60% at the Mo K edge to minimise the higher harmonics.

2.5.1 Half-cell

The majority of the PtMo data were collected at the Mo K edge in the fluorescence XAS cell described previously in chapter 2, section 3.2.6. Data at the Pt L_{III} edge were collected in transmission for one of the samples requiring the use of the transmission XAS cell. In all half cell experiments, the electrode was placed against a gold wire current collector and an electrolyte of 1.0 M H_2SO_4 was flowed through the cell. A platinum gauze was used for the counter electrode and all potentials were measured with respect to a Hg/Hg_2SO_4 (MMS) reference electrode. All potentials shown have been corrected to the RHE scale. The fluorescence cell was positioned at 45° with respect to the incident beam and a 30-element solid state detector used to measure the X-ray fluorescence, I_f, while the transmission cell was aligned perpendicular to the incident beam. The majority of the XAS data were collected at two potentials: 0.05 and 0.85 V vs. RHE, although some results were also collected at 0.55 V and open circuit where noted. The electrode was polarised to these potentials and the experiment started once the current had decayed to a constant value.

2.5.2 Mini-cell

In situ XAS measurements were carried out using the mini cell modified for operation in fluorescence mode, as described in chapter 2, section 3.2.8. For safety reasons, a gas mix of 5% H_2 / N_2 was used as opposed to pure H_2. The gas was flowed to both sides of the MEA and the PtMo anode polarised at potentials between 0 and 0.8 V vs. RHE. The experiment was started once a stable current had been reached.

3 Results and Discussion

The performance of a series of PtMo/C anode catalysts has been investigated using a range of electrochemical techniques, including half cell cyclic voltammetry of CO

oxidation, and methanol oxidation polarisation curves, as well as *in-situ* performance data in the mini cell operating with varying amounts of CO present. The results will be discussed in relation to catalyst composition data obtained using XAS techniques.

3.1 Electrochemistry

3.1.1 Cyclic Voltammetry

Cyclic voltammetry measurements were obtained for the catalysts listed in Tables 1 and 2. Electrodes were prepared using both the pasted and painting methods described in chapter 2, section 1.3.1. The painting method is generally preferred because it allows the catalyst loading to be more accurately controlled and produces layers of more even thickness. Figure 1 below shows a direct comparison between electrodes for one of the catalysts prepared by the two different methods.

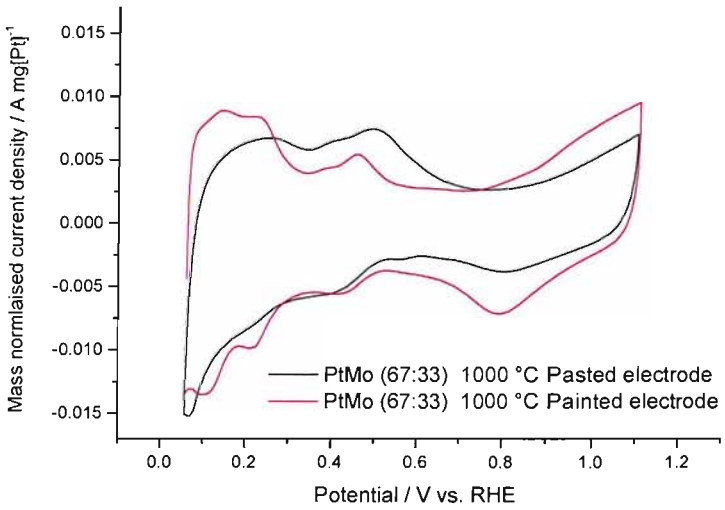

Figure 1 **Cyclic voltammograms of a 67: 33 PtMo / XC72R catalyst carried out in 2.5 M $H_2SO_{4\,(aq)}$ with a scan rate of 10 mV s^{-1}. Electrodes prepared using pasted method (black line) and painted method (red line)**

It is apparent from figure 1 that the CV for the painted electrode contains more definition. This is most evident in the hydrogen region where the peaks corresponding to weak and strong hydrogen adsorption are more resolved. While CVs are shown for all the catalysts using electrodes prepared by both methods for comparison in figures 2 and 4, the CO stripping CVs shown in figures 3 and 5, and all the electrochemical

parameters obtained, are derived solely from the painted electrodes. The inferior appearance of the pasted electrode CVs is likely a result of increased resistance/capacitance. This arises from the greater thickness of the electrodes due to the inability to control it to any great degree, as well as a higher catalyst: Nafion ratio (85: 15 as opposed to 70: 30 with the painted electrodes).

Figure 2 shows the cyclic voltammograms obtained for the high metal content catalysts prepared by the three varying preparation routes. The CVs for the 57:43 PtMo catalyst prepared by method 1 and heated to 620 °C are not shown as this catalyst was found to have degraded over time to such an extent that no significant current was passed.

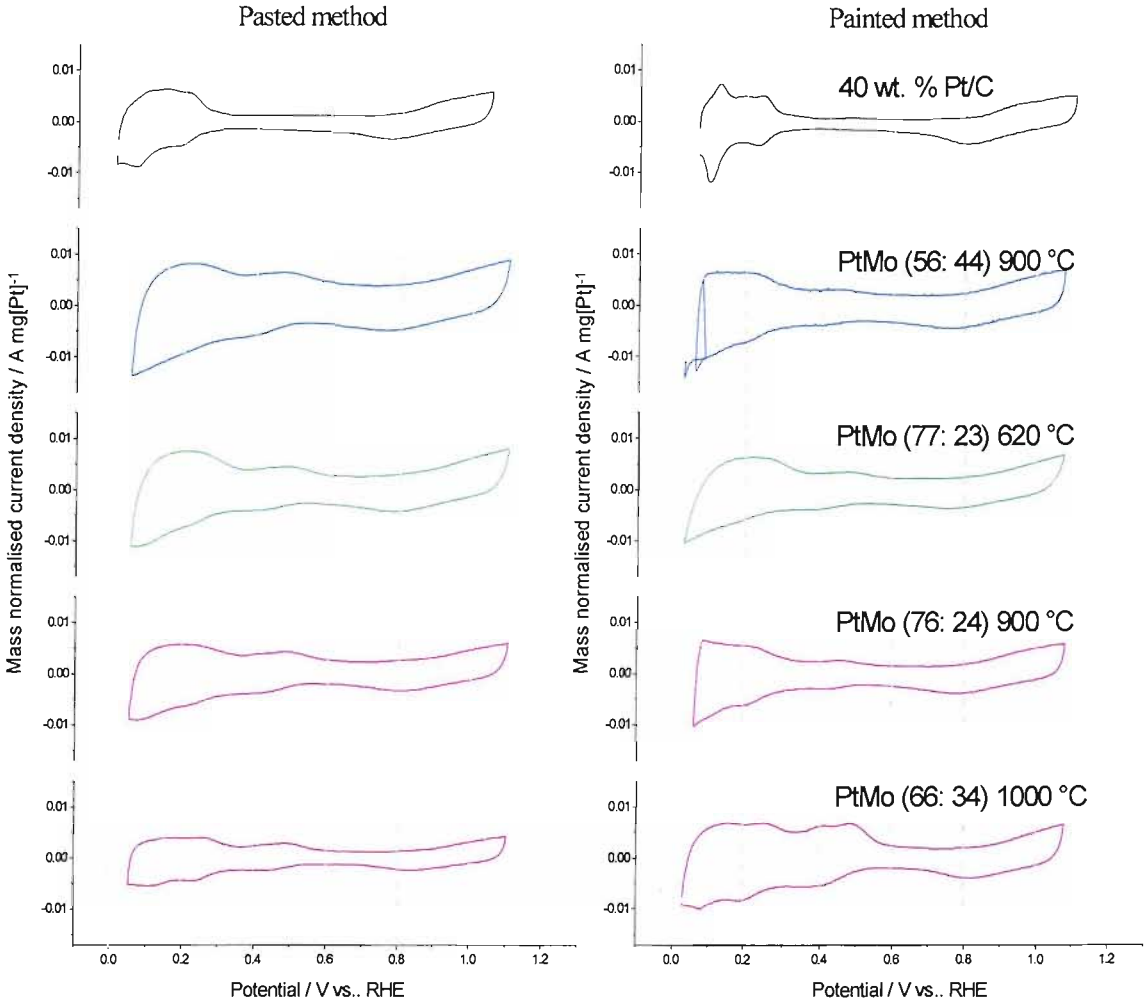

Figure 2 **Cyclic voltammograms for a series of PtMo catalysts prepared by preparation route 1 [56: 44 PtMo], preparation route 2 [77: 23 and 76: 24 PtMo] and preparation route 3 [66: 34 PtMo]. A 40 wt. % Pt/C catalyst CV is shown for comparison. Electrodes prepared by pasted method (left) or painted method (right) and run in 2.5 M $H_2SO_{4\,(aq)}$ at 10 mV s^{-1}. Currents normalised to the Pt loading.**

With the exception of the 40 wt. % Pt/C catalyst, the features in these CVs show no great improvement between the pasted and painted electrodes. The catalysts prepared using routes 1 and 2 have poorly defined features in the hydrogen region, indicating that the catalyst surface is quite heterogeneous, leading to a diverse range of adsorption sites. However, the origins of this heterogeneity are not known. They may arise because of the inferior preparation methods used, or simply because they are the oldest catalysts, having been prepared three years earlier than the codeposited catalysts, and have degraded over time. The 66: 34 PtMo catalyst prepared by preparation route 3 clearly shows peaks due to weak and strong hydrogen adsorption sites. In addition, the

painted electrode of this catalyst gives rise to better catalyst utilisation as evidenced by larger mass normalised currents being passed. Features in the 0.3 to 0.5 V region on both the forward and reverse sweep have been attributed to a Mo (IV/VI) redox couple [9,10,18]. It is believed that Mo on the surface of these catalysts exists in a (+IV) state as an oxyhydroxide, $-O(OH)_2$, and is oxidised to the (+VI) state above 0.4 V [9]. In the pure metal this would result in dissolution, however the presence of Pt seems to stabilise this oxidation state by intermetallic bonding. Mukerjee *et al* have since used *in situ* XANES spectroscopy at the Mo K-edge to suggest that the oxidation change is actually +V to +VI [13].

CO stripping voltammograms for these catalysts are shown in figure 3. In every instance, it can be seen that during the forward sweep after bubbling CO through the electrolyte and holding the potential at 0.05 V, the region corresponding to hydrogen desorption has been suppressed due to a nearly complete surface layer of adsorbed CO. After one complete sweep, the hydrogen desorption peaks are in evidence indicating complete removal of the adsorbed CO. In the case of the 40 wt. % Pt/C catalyst, a small "prewave" peak is observed around 0.5 V. This was first reported by Grambow and Bruckenstein [24] and discussed in a paper by Couto *et al* [25] and was described as the electrooxidation of dissolved CO on the small amount of CO-free Pt sites. The charge passed is very low and is typically < 10 % of the charge under the main stripping peak.

The PtMo catalysts also show similar "prewave" peaks; although these appear between the lower potentials of 0.2 to 0.4 V. These peaks are similar in size and position to the Mo redox peak on the forward scan, and are believed to be the result of a small amount of CO being oxidised at lower potentials than is seen on pure Pt catalysts [15,16]. The main CO stripping peak is observed at potentials similar to that of the 40 wt. % Pt/C catalyst (0.85 V), however the peak is broader and the peak position occurs anywhere between 0.75 and 0.83 V. This has led to suggestions that the surface of these PtMo catalysts is highly heterogeneous, unlike that of PtRu where good mixing of Pt and Ru sites is apparent [12]. Indeed, with PtRu the main oxidation peak is shifted to lower potentials (~0.5 V); although these catalysts show none of the CO oxidation occurring at even lower potentials, as with the PtMo "prewave" peaks. Mukerjee *et al* have

attributed the two stripping peaks seen with PtMo catalysts to the activity of both Pt and Mo for CO oxidation. The peaks on the first forward sweeps beginning around 0.1 V and continuing to around 0.4 V are the result of oxygenated species on the Mo surface initiating CO oxidation on neighbouring Pt sites, while the second peak is due to CO oxidation by oxides of Pt, occurring after water activation and oxide formation has occurred [10,11,13].

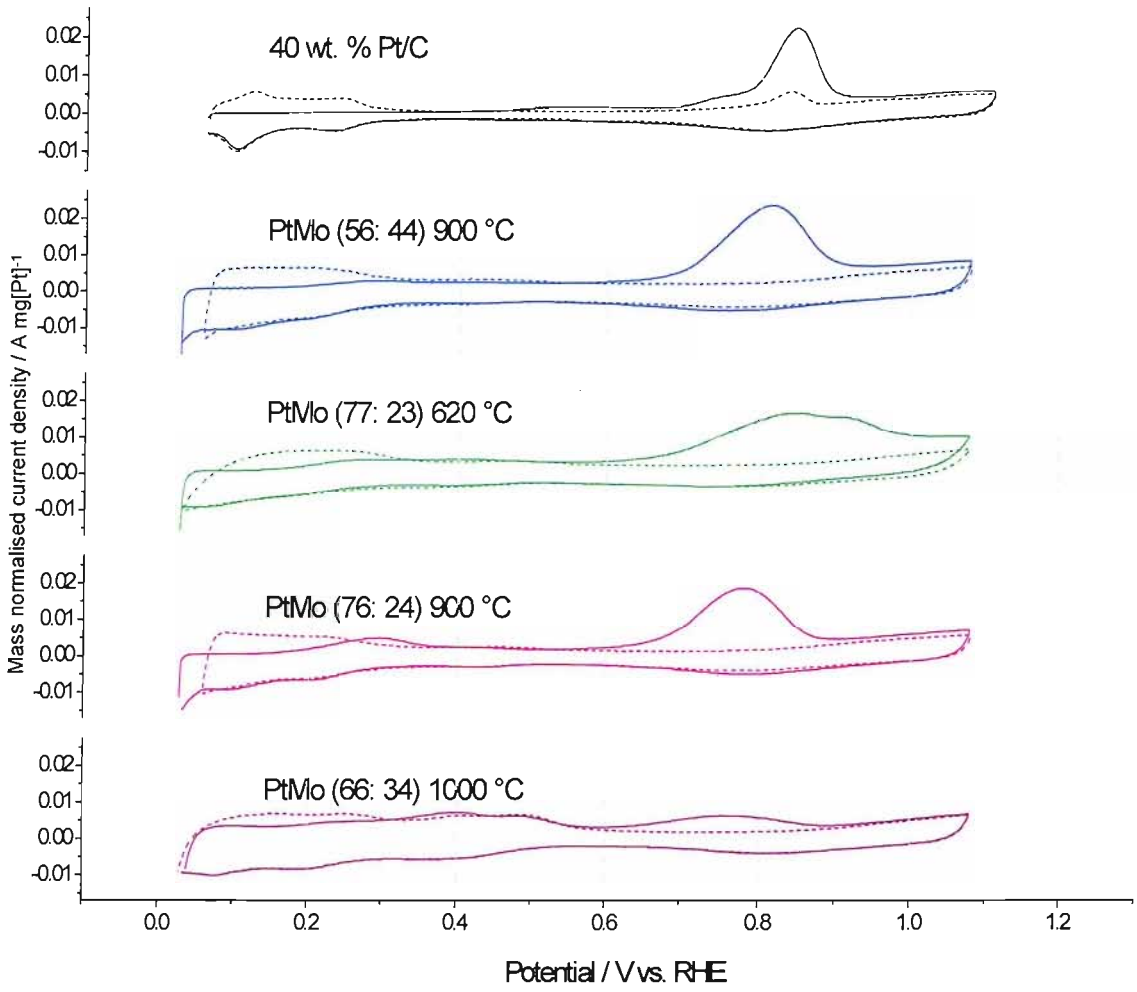

Figure 3 **CO stripping voltammetry for a series of PtMo catalysts prepared by preparation route 1 [56: 44 PtMo], preparation route 2 [77: 23 and 76: 24 PtMo] and preparation route 3 [66: 34 PtMo]. A 40 wt. % Pt/C catalyst CV is shown for comparison. Electrodes prepared by painted method and run in 2.5 M $H_2SO_{4\,(aq)}$ at 10 mV s^{-1}. Currents normalised to the Pt loading. Solid line indicates the first cycle; the dotted line indicates the second cycle.**

Table 3 summarises the electrochemical parameters obtained from the CVs shown in figures 2 and 3.

Table 3 Table of electrochemical parameters for the Pt/C and PtMo/C catalysts in figures 2 and 3

Catalyst	Preparation route	Heat treatment / °C	Pt loading / mg cm^{-2}	Hydrogen adsorption charge / C	Mo IV/VI redox peak charge / C	Mo redox peak positions / V vs. RHE (IV/VI; VI/IV)	CO pre-wave peak position / V vs. RHE	CO pre-wave charge / C	CO stripping peak position / V vs. RHE	CO stripping peak charge / C	Mass normalised Pt surface area ($Pt_{area.m}$) / m^2 Pt g^{-1} Pt
40 wt. % Pt/C	-	-	0.32	4.34×10^{-2}	-	-	-	-	0.845	8.73×10^{-2}	49
29.7 wt. % Pt / 11.4 wt. % Mo (56: 44 PtMo)	1	900	0.24	3.75×10^{-2}	1.89×10^{-3}	0.452; 0.426	0.287	4.86×10^{-3}	0.814	8.57×10^{-2}	73
35.4 wt. % Pt / 5.3 wt. % Mo (77: 23 PtMo)	2	620	0.30	4.83×10^{-2}	6.11×10^{-3}	0.481; 0.372	0.301	3.56×10^{-3}	0.834	1.38×10^{-1}	85
36.9 wt. % Pt / 5.7 wt. % Mo (76: 24 PtMo)	2	900	0.25	3.34×10^{-2}	5.50×10^{-3}	0.460; 0.425	0.294	1.24×10^{-2}	0.781	7.70×10^{-2}	59
34.5 wt. % Pt / 8.6 wt. % Mo (66: 34 PtMo)	3	1000	0.56	1.28×10^{-1}	7.65×10^{-2}	0.488; 0.401	0.397	2.13×10^{-2}	0.753	6.71×10^{-2}	21

The charges under the hydrogen adsorption peaks were measured by visually estimating where the adsorption process would begin in the absence of the Mo redox peaks. These values have inherently larger errors than for measurements of the CO oxidation peak and are included for completeness only. The charges passed under the main CO stripping peak are used to calculate the mass normalised Pt surface area. It is interesting to note that the Pt surface area for the 40 wt. % Pt/C catalyst is lower than for the catalysts prepared using preparation routes 1 and 2 involving heat treatments to either 620 or 900 °C. This indicates that the process of adding Mo not only reduces the degree of sintering during the electrocatalyst manufacturing process, but seems to have led to smaller particle sizes, despite the subsequent heat treatments, as seen by the XRD results seen in Table 1. The mass normalised area is greatest for the 77: 23 PtMo catalyst prepared by route 2 and heated to 620 °C with a value of 85 m^2 Pt g^{-1} Pt, presumably due to the lower temperature used in comparison to the other catalysts. The same catalyst heated to 900 °C has a lower Pt area of 59 m^2 Pt g^{-1} Pt. The CO stripping peaks for these two catalysts appear at 0.834 and 0.781 V respectively. The stripping peak for the 620 °C catalyst is also broader which suggests that this catalyst's surface is very inhomogenous in nature. The peak for the same catalyst heated to 900 °C is less broad (although still broader than pure Pt/C) and the lowering of the peak potential by 0.05 V indicates better contact and improved mixing of the Pt and Mo atoms. The "prewave" charge is significantly higher meaning a larger number of poisoned Pt sites have neighbouring Mo oxides to promote the oxidation of CO. The increased number of free Pt sites then allows for an improvement in the efficiency of subsequent water activation allowing for the remaining CO to be oxidized by Pt oxides. Comparing this catalyst with the 56: 44 PtMo catalyst prepared by route 1 and also heated to 900 °C, it can be seen that while the larger ratio of Mo in the catalyst yields an increase in Pt area (73 compared with 59 m^2 Pt g^{-1} Pt), the CO "prewave" charge and main CO stripping peak position are less favourable. This may indicate that a 1: 1 PtMo ratio is too high, with the increase in Mo possibly infringing on the active Pt sites and decreasing the overall performance. This is unlike PtRu/C catalysts where a 1: 1 ratio is often found to be the optimum ratio.

The 66: 34 PtMo prepared by route 3 and heated to 1000 °C has the lowest peak position for the main CO stripping peak, although the relative charge passed is lower than for the other catalysts giving rise to a much smaller Pt area value of

21 m^2 Pt g^{-1} Pt. This is not a result of a larger amount of CO being oxidised in the "prewave" peak because the charge passed is no greater than that for the 76: 24 PtMo catalyst heated to 900 °C, once catalyst loading is taken into account. Indeed, if the "prewave" charge was included, the total mass normalised area would still only be as high as 28 m^2 Pt g^{-1} Pt. The charge passed under the "prewave" peak is roughly 30% of that passed under the main stripping peak. The fact that the approximated hydrogen adsorption charge is double the value of the CO oxidation charge (as opposed to the expected half), indicates that, in this instance, a full monolayer of CO was not present on this catalyst and this experiment should be repeated.

The hydrogen adsorption charges and Mo redox charges were used to compare the relative surface ratios of Pt and Mo to determine the degree of mixing. This is not without difficulty as there tends to be a small amount of overlap between the hydrogen peaks and the Mo redox peaks, and there is uncertainty as to whether the redox couple is in fact due to IV/VI or V/VI transitions, as these denote either a $2e^-$ or a $1e^-$ process. The calculated atomic ratios are shown in Table 4. It should be noted that the peak areas can usually be measured to an accuracy of about 5 %; although the presence of overlapping peaks puts this closer to 15 %.

Table 4 **Approximate Pt: Mo surface ratios calculated from the hydrogen adsorption peaks and the Mo oxidation peaks**

Catalyst	Preparation route	Heat treatment / °C	Ratio based on IV/VI couple	Ratio based on V/VI couple
29.7 wt. % Pt / 11.4 wt. % Mo (56: 44 PtMo)	1	900	98: 2	95: 5
35.4 wt. % Pt / 5.3 wt. % Mo (77: 23 PtMo)	2	620	94: 6	89: 11
36.9 wt. % Pt / 5.7 wt. % Mo (76: 24 PtMo)	2	900	93: 7	86: 14
34.5 wt. % Pt / 8.6 wt. % Mo (66: 34 PtMo)	3	1000	77: 23	63: 37

The PtMo ratios calculated for the catalysts prepared using routes 1 and 2 all show considerably less Mo than is expected for a well-mixed sample. A possible explanation is that not all of the Mo atoms are available to be oxidized; either because the concentration of Mo atoms inside the nanoparticle is greater than the concentration on the surface or, more likely, that the Mo forms clusters on the surface, with Mo inside the clusters essentially being metallic in character, and not undergoing any redox change. The ratio for the catalyst prepared using route 3 is more similar to the expected ratio. This suggests a much better mixed sample; although it doesn't rule out the possibility that the majority of Mo is on the surface in clusters, albeit to less of an extent than seen with the other catalysts. XAS techniques will be used later to determine which of these models is most accurate by fitting the average coordination shells at the Mo K-edge.

Figure 4 shows the cyclic voltammograms obtained for the low metal content catalysts obtained by a co-deposition technique (preparation route 3) and supplied by Johnson Matthey, along with the CSR catalyst prepared by the surface modification technique. Figure 5 shows the CO stripping voltammograms for these catalysts, while Table 5 summarises the electrochemical parameters obtained from the CVs shown in figures 4 and 5. Visual inspection of the cyclic voltammograms in figure 4 show an improvement in definition for all painted electrodes of the PtMo catalysts prepared by route 3, when compared with pasted electrodes. This is likely to be due to increased capacitance/resistance. The presence of weak and strong adsorption peaks in the hydrogen region, which were not as clearly defined for the catalysts prepared by routes 1 and 2, indicate that the surface of the route 3 catalysts is not so far removed from the surface Pt sites on the 20 wt. % Pt/C catalyst. The catalyst utilisation is also improved for some of the catalysts using painted electrodes; most notably for the 77: 23 PtMo catalyst. All of the catalysts show evidence of the Mo redox peaks between 0.3 and 0.5 V in the forward and reverse scans, proving that there is Mo at the surface of the catalyst nanoparticles that is capable of undergoing changes in oxidation state.

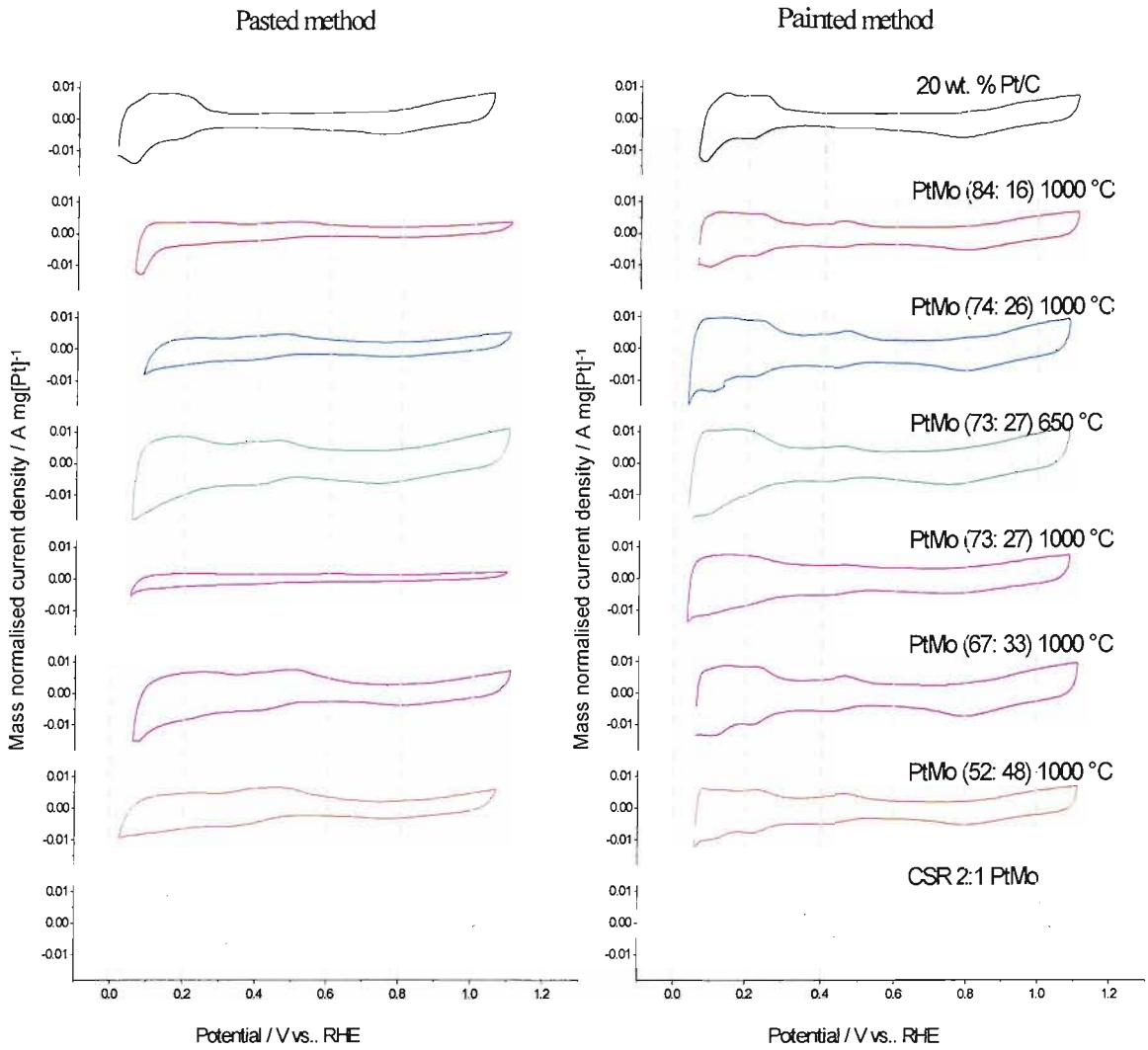

Figure 4 **Cyclic voltammograms for a series of PtMo catalysts prepared by preparation route 3. A 20 wt. % Pt/C catalyst CV is shown for comparison. Electrodes prepared by pasted method (left) or painted method (right) and run in 2.5 M $H_2SO_{4\,(aq)}$ at 10 mV s^{-1}. Currents normalised to the Pt loading.**

CO stripping voltammograms for these catalysts are shown in figure 5. In every instance, it can be seen that during the forward sweep after bubbling CO through the electrolyte and holding the potential at 0.05 V, the region corresponding to hydrogen desorption has been suppressed due to a nearly complete surface layer of adsorbed CO. After one complete sweep, the hydrogen desorption peaks are in evidence indicating complete removal of the adsorbed CO from the Pt sites on the surface of the catalyst. The main CO stripping peaks are all seen to be shifted to lower potentials compared with the 20 wt. % Pt/C, as was found for the previous higher metal content PtMo catalysts shown in figure 3, where the peak positions were found between 0.01 and 0.09 V lower than for a 40 wt. % Pt/C catalyst. In the case of the CVs shown in figure

5, the CO stripping peak positions are lowered by between 0.09 and 0.13 V. Small "prewave" peaks attributed to the oxidation of CO on Pt sites promoted by oxygenated Mo neighbours are again present, although the charge passed under these peaks was found to be between only 8 and 15% of the charge passed under the main stripping peak.

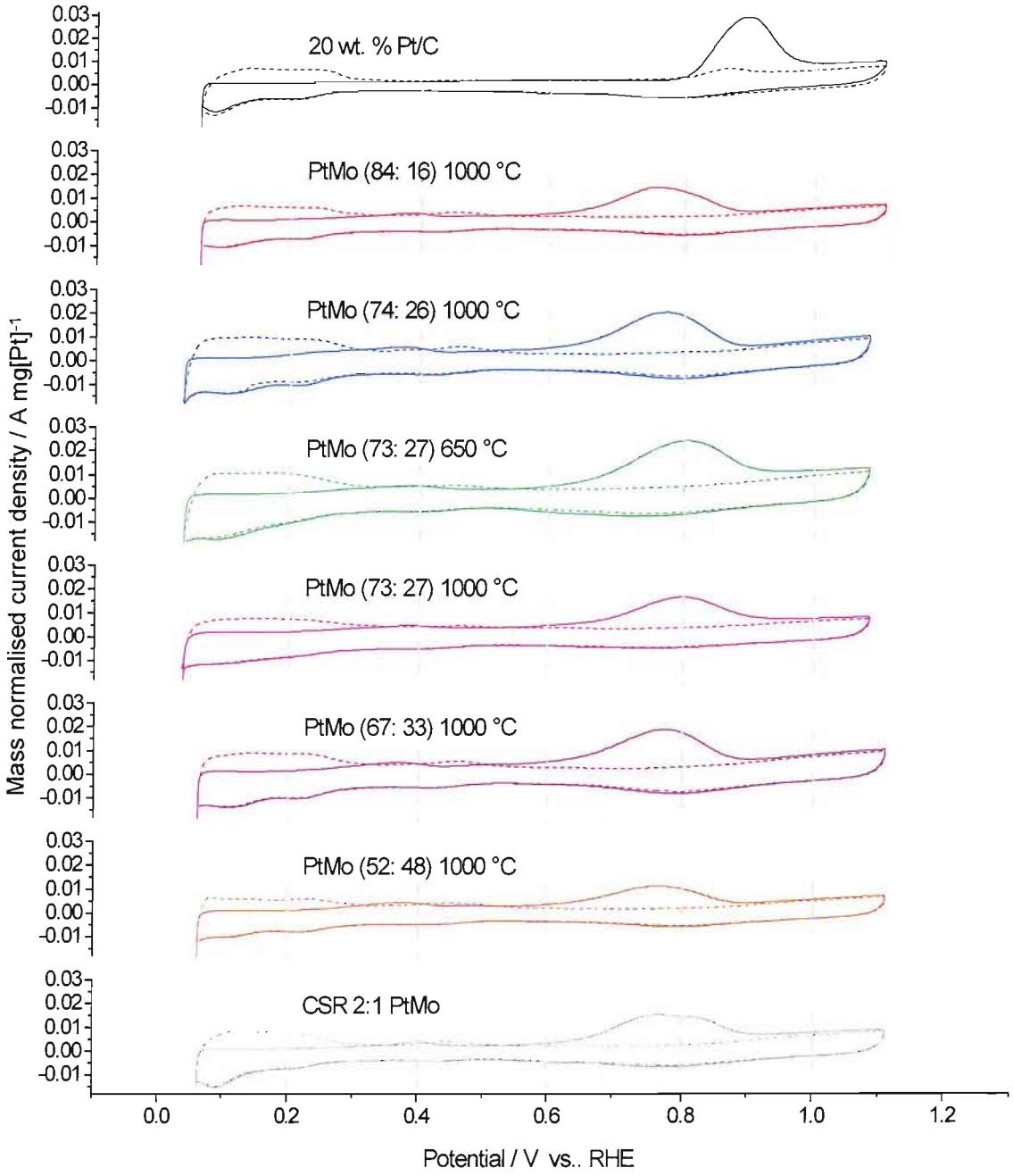

Figure 5 **CO stripping voltammetry for a series of PtMo catalysts prepared by preparation route 3. A 20 wt. % Pt/C catalyst CV is shown for comparison. Electrodes prepared by painted method and run in 2.5 M $H_2SO_{4\,(aq)}$ at 10 mV s^{-1}. Currents normalised to the Pt loading. Solid line indicates the first cycle; the dotted line indicates the second.**

Table 5 Table of electrochemical parameters for the Pt/C and PtMo/C catalysts in figures 4 and 5

Catalyst	Preparation route	Heat treatment / °C	Pt loading / mg cm^{-2}	Hydrogen adsorption charge / C	Mo IV/VI redox peak charge / C	Mo redox peak positions / V vs. RHE (IV/VI; VI/IV)	CO pre-wave peak position / V vs. RHE	CO pre-wave charge / C	CO stripping peak position / V vs. RHE	CO stripping peak charge / C	Mass normalised Pt surface area ($Pt_{area.m}$) / m^2 Pt g^{-1} Pt
20 wt. % Pt/C	-	-	0.27	3.65×10^{-2}	-	-	-	-	0.895	1.07×10^{-1}	71
19.9 wt. % Pt 1.8 wt. % Mo (84: 16 PtMo)	3	1000	0.22	2.88×10^{-2}	7.21×10^{-3}	0.455; 0.437	0.380	5.20×10^{-3}	0.763	5.98×10^{-2}	48
20.3 wt. % Pt 3.5 wt. % Mo (74: 26 PtMo)	3	1000	0.22	4.84×10^{-2}	2.12×10^{-2}	0.463; 0.431	0.378	1.27×10^{-2}	0.773	8.27×10^{-2}	68
19.3 wt. % Pt 3.6 wt. % Mo (73: 27 PtMo)	3	650	0.24	5.04×10^{-2}	1.69×10^{-2}	0.462; 0.408	0.378	1.26×10^{-2}	0.801	1.24×10^{-1}	92
19.3 wt. % Pt 3.6 wt. % Mo (73: 27 PtMo)	3	1000	0.23	4.14×10^{-2}	1.26×10^{-2}	0.469; 0.419	0.374	7.51×10^{-3}	0.797	7.46×10^{-2}	58
18.0 wt. % Pt 4.3 wt. % Mo (67: 33 PtMo)	3	1000	0.23	4.44×10^{-2}	1.89×10^{-2}	0.465; 0.427	0.364	7.99×10^{-3}	0.774	8.52×10^{-2}	67
17.0 wt.% Pt 7.6 wt. % Mo (52: 48 PtMo)	3	1000	0.23	3.21×10^{-2}	2.21×10^{-2}	0.463; 0.420	0.370	7.03×10^{-3}	0.763	5.35×10^{-2}	41
19.5 wt. % Pt 2.3 wt. % Mo CSR (½ monolayer)	CSR	250	0.27	3.82×10^{-2}	1.15×10^{-2}	0.446; 0.419	0.398	6.54×10^{-3}	0.764	8.95×10^{-2}	60

The charges passed under the main CO stripping peak are used to calculate the mass normalised Pt surface area. All of the PtMo catalysts prepared by route 3 have lower Pt surface areas than the standard 20 wt. % Pt/C catalyst having undergone no heat treatment (71 m^2 Pt g^{-1} Pt), with the exception of the 73: 27 PtMo sample, heated to only 650 °C, which has an area of 92 m^2 Pt g^{-1} Pt. The values for the other catalysts heated to 1000 °C range between 41 and 68 m^2 Pt g^{-1} of Pt. These values are all larger than expected for a 20 wt. % Pt/C catalyst heated to the same temperature, which has displayed as much as a four-fold increase in particle size and corresponding 70% drop in Pt area when measured by CO chemisorption testing. The addition of Mo is again found to be limiting the sintering effect of the heat treatments. Looking at the Pt area values for the samples heated to 1000 °C, the lowest values are obtained for the catalysts with the lowest amount of Mo present (84: 16 PtMo) and the highest amount (52: 48 PtMo). It can be inferred from this that there is an optimum amount of Mo required to maximise the Pt surface area. Not enough molybdenum and the limiting effect on particle sintering is less, whereas too many Mo atoms at the surface and forming oxides must impinge onto the Pt sites, causing a lowering of the catalytic area. The optimum amount appears to be between a 3: 1 and 2: 1 ratio of Pt to Mo.

The CO stripping peak for the CSR catalyst is very similar to that obtained for the other PtMo catalysts. In this instance, the Mo is purely on the surface of the catalyst and only a very low heat treatment has been attempted, (i.e. in the bulk, the Pt and Mo should not be alloyed at all). This suggests that only the surface promotion effects are playing any part in the lowering of the potential for CO oxidation, and that no additional chemisorption effects due to alloying are achieved for the route 3 catalysts. Either the Pt and Mo are not mixing/alloying enough at 1000 °C or, if they are, it doesn't achieve an appreciable effect as is seen with PtRu alloys. The main CO stripping peak for the CSR catalyst also has a shoulder at around 0.85 V, indicating the oxidation of CO from weak and strong adsorption sites on the Pt.

The hydrogen adsorption charges and Mo redox charges were used to compare the relative surface ratios of Pt and Mo to determine the degree of mixing. These are shown in Table 6:

Table 6 Approximate Pt: Mo surface ratios calculated from the hydrogen adsorption peaks and the Mo oxidation peaks

Catalyst	Preparation route	Heat treatment / °C	Ratio based on IV/VI couple	Ratio based on V/VI couple
19.9 wt. % Pt 1.8 wt. % Mo (84: 16 PtMo)	3	1000	89: 11	80: 20
20.3 wt. % Pt 3.5 wt. % Mo (74: 26 PtMo)	3	1000	82: 18	70: 30
19.3 wt. % Pt 3.6 wt. % Mo (73: 27 PtMo)	3	650	86: 14	75: 25
19.3 wt. % Pt 3.6 wt. % Mo (73: 27 PtMo)	3	1000	87: 13	77: 23
18.0 wt. % Pt 4.3 wt. % Mo (67: 33 PtMo)	3	1000	82: 18	70: 30
17.0 wt.% Pt 7.6 wt. % Mo (52: 48 PtMo)	3	1000	74: 26	59: 41
19.5 wt. % Pt 2.3 wt. % Mo CSR (½ monolayer)	CSR	250	87: 13	77: 23

Unlike the values for the route 1 and 2 catalysts as seen in Table 4, the ratios obtained are much closer to the expected values for a well-mixed sample. In any event, even if the Mo is mostly restricted to the surface, and has formed clusters, it is clear that the effect would be much reduced from the severe clustering observed for the previous catalysts. For the CSR catalyst where all of the Mo should be present on the surface, the 2: 1 Pt to Mo ratio expected is not observed. It would appear, therefore, that small

clusters of Mo are present on this catalyst, such that approximately a third of the Mo atoms present must be within such cluster and unable to undergo the expected redox transitions.

3.2 XAS measurements

3.2.1 XANES

The near edge region (XANES) of the XAS data collected at the Mo K-edge can be used to initially assess the effects of changes in catalyst environment and of polarisation. A shift in edge position to more positive values indicates an increase in the average oxidation state of the absorbing element in the sample. In addition, the area under the white line is seen to grow with increased valency; the white line being an indication of the number of empty d states that exist. The white line in Mo K-edge spectra, however, is very small as this probes transitions from the 1s orbital to a *p*-symmetric final state, which tend to be small and spread out over a wide energy range, unlike the transitions observed at the Pt L_{III} and L_{II} edges. Figure 6 below shows the XANES region obtained at the Mo K-edge for the CSR PtMo catalyst in the fluorescence XAS half cell polarised to 0.15 and 0.65 V vs. RHE, compared with the data for a Mo foil.

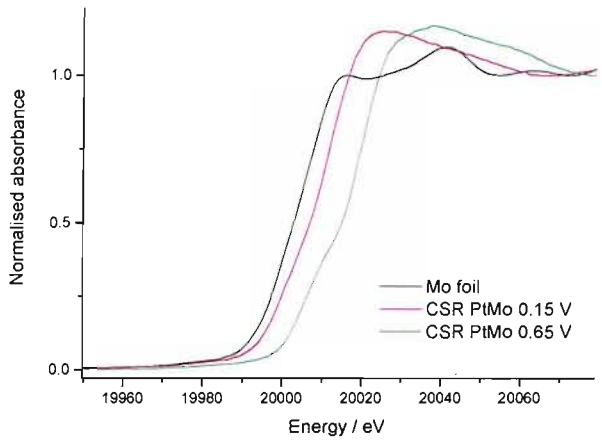

Figure 6 **XANES region at the Mo K-edge for Mo foil (black), and the CSR PtMo catalyst in the fluorescence XAS half cell polarised to 0.15 (red) and 0.65 V vs. RHE (green).**

The positive shifts in edge position observed for the CSR catalyst indicate that the Mo is oxidised even at potentials as low as 0.15 V, and a larger shift is observed upon increasing the potential to 0.65 V. A pre-edge feature is observed in all three XANES spectra as a shoulder on the absorption edge, which is seen to grow as the sample becomes more oxidised. The pre-edge is dependant on the oxidation state of the absorbing atom, as is the edge; although the pre-edge is caused by transitions to empty bound states, whereas the edge represents the ionisation threshold for transitions to the continuum. In addition, the pre-edge can provide information on the local geometry of the absorbing atom; for instance, tetrahedral geometries give rise to larger pre-edge features than octahedral geometries due to p-d mixing. A slight increase in amplitude just beyond the edge is also observed. All these features indicate that the Mo in this catalyst sample becomes more oxidised upon increasing the potential to 0.65 V.

A more quantitative analysis of the XANES region is also possible. The relationship between the valence state and edge position can be used to determine unknown oxidation states based on their corresponding edge shift. Mansour *et al* have shown a quadratic dependence between oxidation state and edge position for manganese samples [26], while a linear relationship has been observed for a series of nickel samples [27]. This linear relationship is only strictly accurate for samples where the absorbing element is in a similar coordination environment; however, this technique has been reported in the literature for Mo samples. Cramer *et al* used reference compounds to determine the charge on the Mo in nitrogenase [28], while more recently Mukerjee *et al* attempted to ascertain the likely oxidation state and hence possible composition of Mo in a 3: 1 PtMo carbon supported catalyst [13] and reported a linear relationship between edge position and oxidation state of Mo.

XANES data for Mo compounds of known oxidation state were obtained; these being Mo foil (0), cyclopentadienylmolybdenum (II) tricarbonyl chloride, MoO_2 (+4) and MoO_3 (+6). Edge positions are usually taken as the maximum slope point on the edge, corresponding to the peak position of the differentiated spectrum. The appearance of a pre-edge in the spectrum can lead to the appearance of two inflection points; neither of which represents the true edge position. For the purposes of consistency, the edge positions were taken as the energy value halfway up the absorption edge of the XAS

spectrum normalised to an edge jump of 1 based on the previous Mo edge work reported [13].

A plot of the edge positions obtained versus the Mo oxidation state is shown in figure 7, along with the corresponding line of best fit.

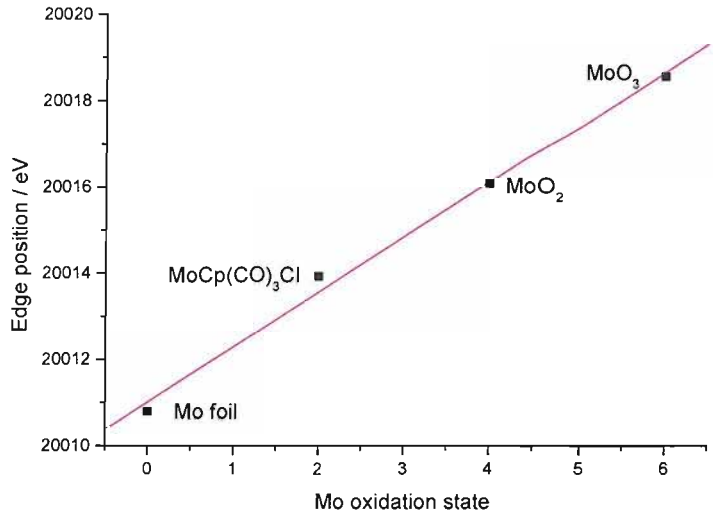

Figure 7 **Comparison of the edge positions and corresponding oxidation states for the series of Mo reference compounds**

Edge positions were recorded for the series of PtMo catalysts in the XAS half cell and mini cell as described in section 2.5. The Mo oxidation states were then calculated based on the line of best fit. Based on the step size used for measuring the data points during the edge (0.64 eV for the Mo K-edge data reported here), and the fitting of the measured edge positions to a line of best fit, it is estimated that the errors induced lead to average oxidation state values accurate to ± 0.3 using this method. Table 7 lists the average oxidation states for the series of PtMo catalysts in the XAS half cell.

Table 7 **Calculated values of average Mo oxidation states for PtMo catalysts in the XAS half cell based upon the line of best fit for Mo reference compounds**

Catalyst	Preparation route	Heat treatment / °C	Average Mo oxidation state	
			0.05 V	0.85 V
26.8 wt. % Pt 10.1 wt. % Mo (57: 43 PtMo)	1	620	1.5	3.1
29.7 wt. % Pt 11.4 wt. % Mo (56: 44 PtMo)	1	900	1.1	1.4
35.4 wt. % Pt 5.3 wt. % Mo (77: 23 PtMo)	2	620	1.3	2.1
36.9 wt. % Pt 5.7 wt. % Mo (76: 24 PtMo)	2	900	0.8	1.6
34.5 wt. % Pt 8.6 wt. % Mo (66: 34 PtMo)	3	1000	0.5	0.9
19.9 wt. % Pt 1.8 wt. % Mo (84: 16 PtMo)	3	1000	0	1.2
20.3 wt. % Pt 3.5 wt. % Mo (74: 26 PtMo)	3	1000	0.7	1.7
19.3 wt. % Pt 3.6 wt. % Mo (73: 27 PtMo)	3	650	2.4	4.0
19.3 wt. % Pt 3.6 wt. % Mo (73: 27 PtMo)	3	1000	3.1	4.0
18.0 wt. % Pt 4.3 wt. % Mo (67: 33 PtMo)	3	1000	1.6	2.0
17.0 wt.% Pt 7.6 wt. % Mo (52: 48 PtMo)	3	1000	0.7	0.8
19.5 wt. % Pt 2.3 wt. % Mo (½ monolayer)	CSR	250	3.0	5.3

The catalysts heated to 620 °C are seen to correspond to the largest average oxidation state of the Mo for catalysts prepared by methods 1 and 2. Heating the samples to 900 °C results in a lowering of the oxidation state; while the 66: 34 PtMo sample prepared by the codeposition method (route 3) and heated to 1000 °C has the lowest average oxidation states at both potentials. It appears that heating of the samples to greater temperatures increases the amount of particle sintering, causing a lower

proportion of the overall Mo to be present at the surface, or the heating effect may be to simply drive Mo into the bulk, or both. Certainly the lowering of the oxidation state when the catalysts are polarised to 0.05 V must involve a loss of oxygen neighbours; possibly prompted by surface Mo atoms being relatively mobile and moving deeper inside the surface layer. If true, this will be observed upon analysing the EXAFS data, as this would result in a corresponding increase in first shell metal neighbours.

For the remaining catalysts prepared by the codeposition method, the largest oxidation states are observed for those with an approximate 3: 1 or 2: 1 PtMo ratio. With a higher Mo content the average oxidation state drops, most likely due to a higher proportion of metallic Mo within clusters and not able to be oxidised. The CSR catalyst where the deposition of Mo on the surface was controlled to a greater extent and no high temperature annealing process was attempted, evidently has a high proportion of surface Mo oxides and, correspondingly, the highest Mo oxidation states as expected.

The derivation of the average Mo oxidation state should, in theory, allow for an estimation of the amount of Mo at the surface of the catalyst particle (and capable of being oxidised), and that within the bulk of the particle. This requires some assumptions to be made regarding the oxidation state of the Mo in the different environments. The presence of the redox couple in the cyclic voltammograms has been attributed in the literature to a IV/VI transition, while Mukerjee *et al* have concluded that Mo on the surface of a PtMo/C catalyst at 0.0 V will be in a +5 oxidation state. The calculations of the fraction of the Mo at the surface of the catalyst reported here will be done using both the IV/VI and V/VI couples. Thus we will assume that Mo at the surface may exist in only the IV or V oxidation state at 0.05 V and in the VI oxidation state at 0.85 V vs. RHE. Mo inside the bulk of the particle (or within large surface clusters of Mo) is assumed to be metallic in character with an oxidation state of zero. It is also assumed that no changes in particle size are occurring with change in potential.

The details of the calculation are shown below. The 29.7 wt. % Pt; 11.4 wt. % Mo [56: 44 atomic ratio] catalyst prepared by route 1 and heat treated to 900 °C is used as an example.

At 0.05 V vs. RHE, the molybdenum present on the surface is believed to be in a +4 oxidation state (for the purposes of this example). By taking the absorption edge position from the XAS data and using the line of best fit for the Mo reference compounds in figure 7, the average Mo oxidation state was estimated to be 1.1.

1.1 = (fraction of Mo at surface)(+4) + (fraction of Mo inside particle)(0)

The fraction of Mo at the surface, therefore, = 1.1/4 = 0.27
At 0.85 V vs. RHE, the molybdenum present on the surface is believed to be in a +6 oxidation state. Based on the edge position, the average Mo oxidation state was found to be 1.4. The fraction of Mo at the surface is then taken as 1.4/6 = 0.24
The fraction of Mo at the surface of the nanoparticle does not appear to change significantly with potential.

Taking the average of these two results gives 0.255 (the average fraction of total Mo in the sample found at the surface). Multiplying this value by the total number of molybdenum atoms per gram of catalyst gives the total number of surface Mo atoms per gram of catalyst:

$0.255 \times (7.17 \times 10^{20}) = 1.83 \times 10^{20}$ surface Mo atoms per gram of catalyst.

The number of platinum surface atoms is then calculated based on the mass normalised Pt areas seen earlier in Tables 3 and 5. This is the surface area of Pt available for the CO to bind to. It is assumed that the CO will form a complete monolayer with one CO molecule binding to each surface Pt atom. It is also estimated that there will be 1.31×10^{19} molecules of CO per m^2 of catalytic surface area calculated by using the charge associated with a monolayer of CO (420 $\mu C\ cm^{-2}$) [29]. Multiplying this constant by the mass normalised Pt area value (73 m^2 Pt g^{-1} Pt for this sample) should give the number of CO molecules (hence number of Pt surface atoms) per gram of platinum, while multiplying again by the fractional wt.% of Pt in the catalyst should give the number of Pt surface atoms per gram total catalyst:

$(1.31 \times 10^{19}$ CO molecules $m^{-2}) \times (73\ m^2\ Pt^{-1}\ g^{-1}$ Pt) $\times\ 0.297$

$= 2.84 \times 10^{20}$ Pt atoms g^{-1} catalyst

The ratio of Mo atoms to Pt atoms at the surface can then be calculated and reported in a manner which enables easy comparison with the atomic ratio of the species in the as-prepared catalyst and those based on the voltammetry as seen in tables 4 and 6:

$$\frac{2.84 \times 10^{20}}{\left(2.84 \times 10^{20}\right)+\left(1.83 \times 10^{20}\right)} \times 100 : \frac{1.83 \times 10^{20}}{\left(2.84 \times 10^{20}\right)+\left(1.83 \times 10^{20}\right)} \times 100 = 61:39 \text{ Pt} : \text{Mo}$$

Comparison with the atomic ratio for the as-prepared sample (56: 44 Pt: Mo) shows that for this particular catalyst the amount of Mo atoms on the surface is less than would be expected if the Mo and Pt were distributed evenly throughout the sample. Table 8 shows the results obtained for the series of PtMo catalysts based on XAS results obtained in the half cell environment for both the IV/VI and V/VI models.

The values for the Mo: Pt ratios appear to be slightly lower than expected for the route 1 and 2 catalysts. This could indicate that less Mo is present at the surface than is expected in a well-mixed sample, which would confirm the results seen by cyclic voltammetry where the redox peak areas were used to determine the surface ratio; however, the results here are much closer to the expected values than those determined by voltammetry. Again this assumes that all Mo at the surface is present in an oxidised form, and not in metallic Mo clusters. Determination of the number of metal neighbours by analysis of the corresponding EXAFS results should give a more definite answer. The values for the codeposited route 3 catalysts are, for the most part, larger than expected indicating more Mo on the surface than in a well-mixed sample. This must mean that more Mo is definitely oxidised on the surface, and may actually indicate better mixed samples with less Mo surface clustering taking place. The Pt: Mo ratios obtained based on either the IV/VI or V/VI redox couples are very close, meaning that, based on this method, it is not possible to establish whether Mo at the surface of the catalyst nanoparticles is present in a +4 or +5 oxidation state at 0.05 V vs. RHE. The CSR surface modified PtMo/C sample, where all the Mo is expected to be at the surface of the nanoparticles, was determined to have average Mo oxidation states of 3.0 and 5.3 at 0.15 V and 0.55 V respectively, which would tend to support the presence of a +4/+6 redox couple as opposed to a +5/+6 couple although this cannot be proven conclusively.

Table 8 **Calculated ratios of Mo/Pt atoms at the catalyst surface based on fitting edge positions from XAS Mo K-edge data in the half cell to Mo reference line and comparison with expected results for a well-mixed sample (value for CSR catalyst in brackets is the expected surface ratio based on ½ monolayer deposition).**

Catalyst	Route and heat treatment	Pt: Mo atomic ratio for as-prepared sample	Calculated ratio derived using IV/VI redox couple	Calculated ratio derived using V/VI redox couple
29.7 wt. % Pt 11.4 wt. % Mo	1 (900 °C)	56: 44	61: 39	63: 37
35.4 wt. % Pt 5.3 wt. % Mo	2 (620 °C)	77: 23	78: 22	80: 20
36.9 wt. % Pt 5.7 wt. % Mo	2 (900 °C)	76: 24	77: 23	78: 22
34.5 wt. % Pt 8.6 wt. % Mo	3 (1000°C)	66: 34	58: 42	60: 40
19.9 wt. % Pt 1.8 wt. % Mo	3 (1000 °C)	84: 16	91: 9	91: 9
20.3 wt. % Pt 3.5 wt. % Mo	3 (1000 °C)	74: 26	79: 21	80: 20
19.3 wt. % Pt 3.6 wt. % Mo	3 (650 °C)	73: 27	63: 37	65: 35
19.3 wt. % Pt 3.6 wt. % Mo	3 (1000 °C)	73: 27	47: 53	50: 50
18.0 wt. % Pt 4.3 wt. % Mo	3 (1000 °C)	67: 33	62: 38	65: 35
17.0 wt.% Pt 7.6 wt. % Mo	3 (1000 °C)	52: 48	55: 45	58: 42
19.5 wt. % Pt 2.3 wt. % Mo	CSR (250 °C)	81: 19 *(50: 50)*	56: 44	59: 41

Table 9 lists the average oxidation states for five of the PtMo catalysts in the XAS mini cell determined using the line of best fit in figure 7.

Table 9 **Calculated values of average Mo oxidation states for PtMo catalysts in the XAS mini cell based upon the line of best fit for Mo reference compounds**

Catalyst	Preparation route	Heat treatment / °C	Average Mo oxidation state	
			0.1 V	0.5 V
35.4 wt. % Pt 5.3 wt. % Mo (77: 23 PtMo)	2	620	2.6	3.3
36.9 wt. % Pt 5.7 wt. % Mo (76: 24 PtMo)	2	900	0.3	0.8
19.3 wt. % Pt 3.6 wt. % Mo (73: 27 PtMo)	3	650	3.0	4.6
19.3 wt. % Pt 3.6 wt. % Mo (73: 27 PtMo)	3	1000	2.1	3.1
18.0 wt. % Pt 4.3 wt. % Mo (67: 33 PtMo)	3	1000	1.8	2.6

This shows the very metallic-like nature of the Mo found for the route 2 catalyst heated to the higher temperature of 900 °C, with a corresponding very small increase in oxidation state with potential compared to the other catalysts. The route 3 catalysts heated to 1000 °C are more comparable to the route 2 catalyst only heated to 620 °C, indicating increased ability to oxidise the Mo at the surface of samples prepared by the codeposition method. The route 3 catalyst only heated to 650 °C has the larger oxidation values and the greatest increase with potential. The values obtained for this catalyst are similar to that found for the CSR surface modified catalyst indicating that this sample has a high proportion of Mo at the surface in the form of an oxide. These results indicate that under realistic operating conditions in a fuel (i.e. presence of hydrogen gas in the fuel stream, 80 °C cell operation and full humidification) the Mo remains oxidised for most of the samples and will undergo a change with potential; the largest change observed for the route 3 catalysts.

Table 10 shows the Mo surface fraction results obtained for the series of PtMo catalysts based on XAS results obtained in the mini cell environment.

Table 10 **Calculated ratios of Mo/Pt atoms at the catalyst surface based on fitting edge positions from XAS Mo K-edge data in the mini cell to Mo reference line and comparison with expected results for a well-mixed sample**

Catalyst	Route and heat treatment	Pt: Mo atomic ratio for as-prepared sample	Calculated ratio derived using IV/VI redox couple	Calculated ratio derived using V/VI redox couple
35.4 wt. % Pt 5.3 wt. % Mo	2 (620 °C)	77: 23	67: 33	69: 31
36.9 wt. % Pt 5.7 wt. % Mo	2 (900 °C)	76: 24	88: 12	89: 11
19.3 wt. % Pt 3.6 wt. % Mo	3 (650 °C)	73: 27	58: 42	61:39
19.3 wt. % Pt 3.6 wt. % Mo	3 (1000 °C)	73: 27	56: 44	58: 42
18.0 wt. % Pt 4.3 wt. % Mo	3 (1000 °C)	67: 33	57: 43	60: 40

With the exception of the route 2 catalyst heated to 900 °C, the surface fractions obtained are greater than for a well-mixed sample, indicating that the Mo prefers to be at the surface of the particles, rather than in the bulk, and that the Mo is well distributed at the surface and not clustered together. The values obtained are again essentially the same for both the IV/VI and V/VI models within error, so it is still not possible to accurately determine the oxidation state of the surface Mo atoms at reduced potentials by this method.

3.2.2 EXAFS - Half Cell

EXAFS data were collected for the majority of the PtMo catalysts in the series. Figure 8 shows the k^2-weighted data and corresponding fit for the catalysts prepared by preparation route 1 as electrodes in the XAS fluorescence half cell at the Mo K edge.

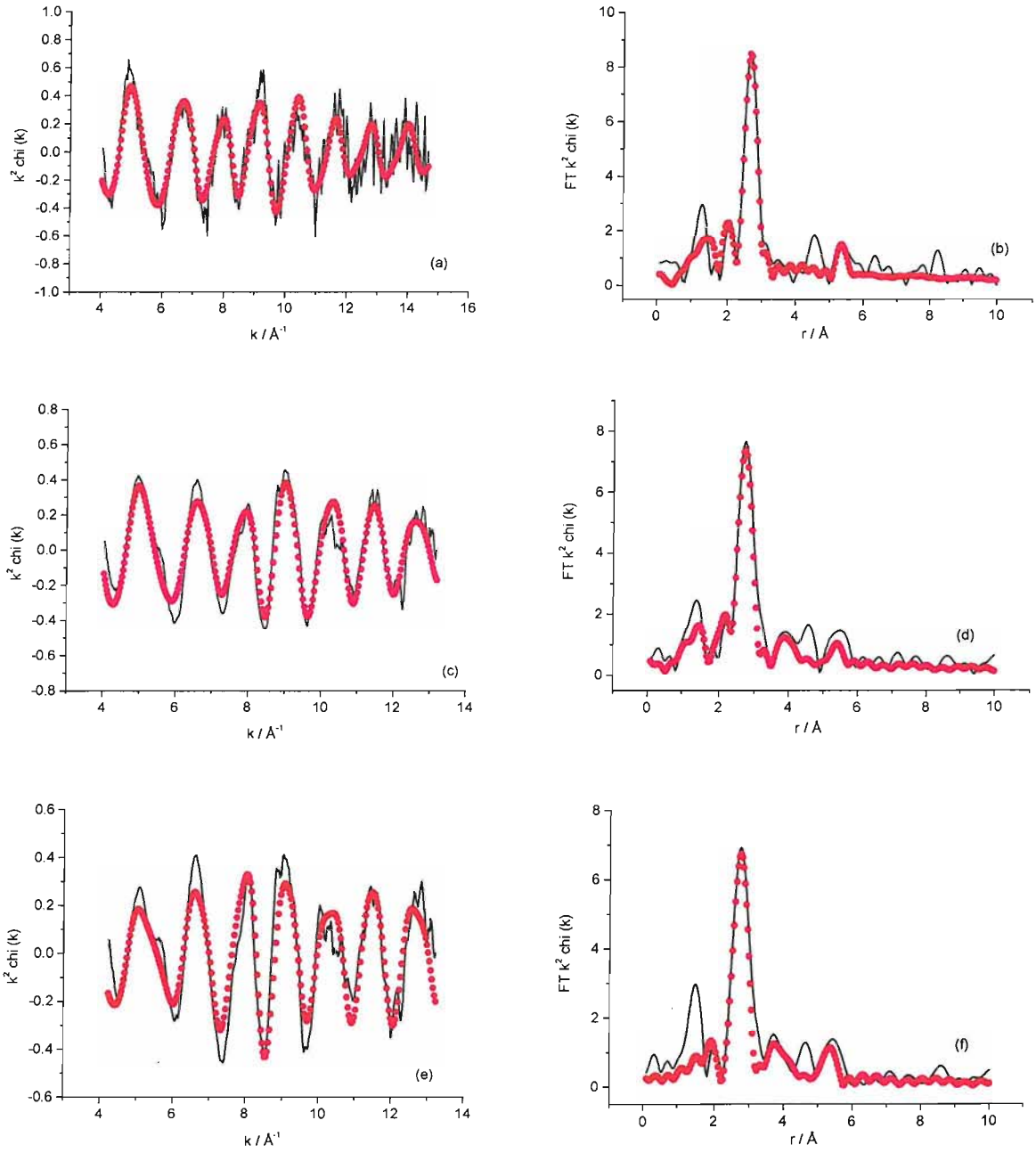

Figure 8 **k^2-weighted Mo K-edge experimental data (solid lines) and fit (dots) [left] and corresponding Fourier transform [right] for the 26.8 wt. % Pt/ 10.1 wt. % Mo route 1 catalyst in the half cell at 0.05 V vs. RHE (a and b); and the 29.7 wt. % Pt/ 11.4 wt. % Mo route 1 catalyst in the half cell at 0.05 V vs. RHE (c and d) and 0.55 V vs. RHE (e and f). Phase corrected for backscattering from Pt.**

Data is shown for the 26.8 wt. % Pt / 10.1 wt. % Mo catalyst at 0.05 V vs. RHE, and for the 29.7 wt. % Pt / 11.4 wt. % Mo catalyst at 0.05 and 0.55 V vs. RHE, both prepared by route 1. These samples essentially comprise the same atomic ratio of Pt to Mo, with the main difference being the heat treatments performed on the catalysts as the final step in the catalyst preparation. The temperatures used were 620 and 900 °C respectively.

The chi plots show oscillations occurring at the same points in k space in all instances, with the only noticeable difference being a small decrease in the amplitude of the oscillation at approximately 5 $Å^{-1}$ for the sample with the higher heat treatment. This region, occurring at low *k* space, contains the greatest contribution from low z neighbours, such as oxygen. Less average oxygen neighbours means that a lower fraction of Mo is present on the surface of the catalyst nanoparticle and present as an oxide, presumably by Mo being driven into the bulk of the particle by the heat treatment. The parameters obtained from fitting the data are shown in tables 11 and 12.

Table 11 Structural parameters for the 26.8 wt. % Pt / 10.1 wt. % Mo route 1 catalyst by fitting the Mo K edge EXAFS data

Condition	Shell	*N*	*R* / Å	$2\sigma^2$ / $Å^2$	E_f / eV	R_{exafs}
0.05 V vs. RHE in half cell	Mo-Pt	2.5 ± 0.3	2.73 ± 0.01	0.012 ± 0.001	-4.1 ± 2.1	49.07
	Mo-O	1.3 ± 0.2	2.08 ± 0.02	0.013 ± 0.004		
	Mo-Mo	0.5 ± 0.2	2.55 ± 0.02	0.010 ± 0.003		
	Mo-Pt (MS)	2.5 ± 0.3	5.41 ± 0.04	0.014 ± 0.007		

Table 12 Structural parameters for the 29.7 wt. % Pt / 11.4 wt. % Mo route 1 catalyst under various conditions by fitting the Mo K edge EXAFS data

Condition	Shell	*N*	*R* / Å	$2\sigma^2$ / $Å^2$	E_f / eV	R_{exafs}
0.05 V vs. RHE in half cell	Mo-Pt	2.8 ± 0.2	2.76 ± 0.01	0.012 ± 0.001	-3.6 ± 1.4	37.16
	Mo-O	0.7 ± 0.1	2.06 ± 0.02	0.010 ± 0.004		
	Mo-Mo	0.3 ± 0.1	2.58 ± 0.02	0.009 ± 0.004		
	Mo-Pt	1.1 ± 0.4	3.87 ± 0.02	0.011 ± 0.004		
	Mo-Pt (MS)	2.8 ± 0.2	5.40 ± 0.02	0.017 ± 0.007		
0.55 V vs. RHE in half cell	Mo-Pt	3.1 ± 0.2	2.76 ± 0.01	0.011 ± 0.001	-1.8 ± 1.4	43.41
	Mo-Pt	1.8 ± 0.6	3.87 ± 0.02	0.013 ± 0.004		
	Mo-Pt (MS)	3.1 ± 0.2	5.39 ± 0.03	0.012 ± 0.005		

It can be seen from comparing the two sets of data at 0.05 V vs. RHE that increasing the temperature of the heat treatment leads to a drop of first shell O neighbours from 1.3 to 0.7. While a small increase in first shell Pt neighbours from 2.5 to 2.8 is seen, these are the same within the errors shown. The Mo-Pt bond distance increases from 2.73 to 2.76 Å. The Mo-Mo distances of 2.55 and 2.58 Å are similar to those fitted for a monoclinic MoO_2 structure [30] and that for Mo_2O_4(dtc pro)$_2$ [31] by Ressler and Macias respectively.

No attempt was made to fit carbon neighbours for the purposes of this work. Fitting carbon neighbours can be done to determine carbon contributions from adsorbed CO, or from the carbon support. Including contributions from carbon can make fitting the data more complicated because it can be hard to differentiate between backscattering from oxygen or carbon neighbours because of their similar atomic weights. The oxygen neighbours fitted in tables 11 and 12 are not believed to be interchangeable with carbon neighbours for two reasons. Firstly, any carbon contributions from the support would occur at greater bond distances (typically 2.6 -3.7 Å) [32]. Metal-carbon neighbours could occur between 1.7 and 2.0 Å if there was adsorbed CO or metal carbides present. However, no carbon monoxide was introduced to the sample during the experiments, while TEM results provided by Johnson Matthey has shown no evidence for the presence of Mo carbides, even with the high heat treatments used during catalyst preparation.

Figure 9 shows the EXAFS data obtained for the 36.9 wt. % Pt / 5.7 wt. % Mo sample prepared by route 2 and heat treated to 900 °C, at both the Mo K and Pt L_{III} edges in the XAS fluorescence half cell. The data at the Mo K edge was obtained at 0.05 V vs. RHE and at open circuit (O.C. ~ 0.95 V vs. RHE). The most significant change is the increased splitting and dampened oscillation occurring between 5 and 6 $Å^{-1}$ in the data at open circuit, compared with the reduced sample at 0.05 V vs. RHE. This is coupled with some splitting of the main peak in the corresponding Fourier Transform.

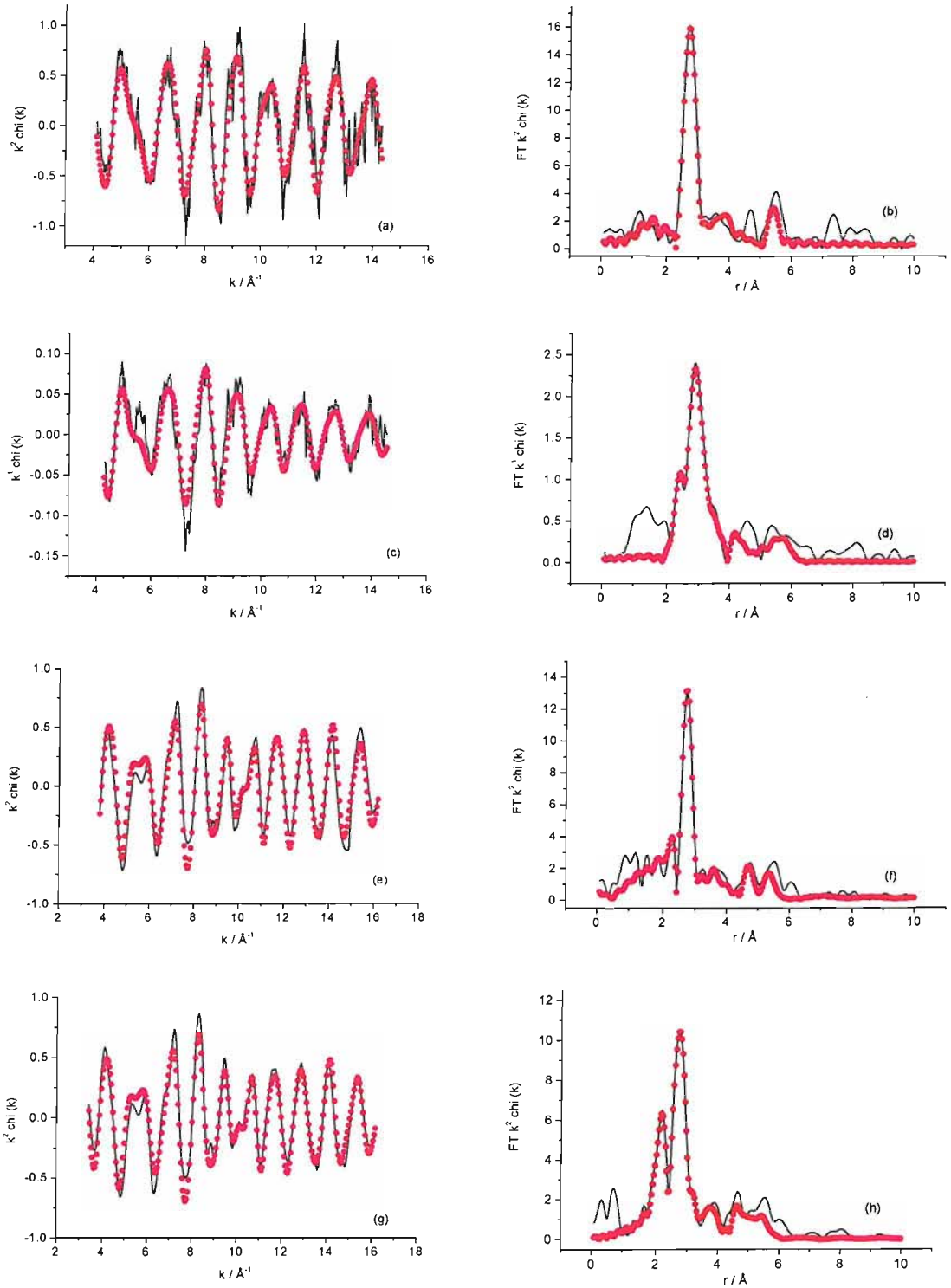

Figure 9 **Experimental data (solid lines) and fit (dots) [left] and corresponding Fourier transform [right] for the 36.9 wt. % Pt/ 5.7 wt. % Mo route 2 catalyst in the half cell at the Mo K-edge at 0.05 V vs. RHE (a and b); open circuit (c and d); and at the Pt L_{III} edge at 0.05 V vs. RHE (e and f); 0.55 V vs. RHE (g and h). Data is k^2-weighted apart from c and d, which is k^1-weighted. Phase corrected for back scattering from Pt.**

The parameters obtained from the fitting of the experimental data shown in figure 9 can be found in table 13.

Table 13 **Structural parameters for the 36.9 wt. % Pt / 5.7 wt. % Mo route 2 catalyst under various conditions by fitting both the Mo K edge and the Pt L_{III} edge EXAFS data**

Condition	Shell	N	R / Å	$2\sigma^2$ / Å^2	E_f / eV	R_{exafs}
Open circuit in half cell Mo K edge	Mo-Pt	5.2 ± 0.4	2.76 ± 0.01	0.012 ± 0.001	-2.2 ± 1.5	42.35
	Mo-O	0.7 ± 0.2	2.27 ± 0.03	0.012 ± 0.009		
	Mo-Mo	1.2 ± 0.6	4.02 ± 0.03	0.015 ± 0.008		
	Mo-Pt (MS)	5.2 ± 0.4	5.42 ± 0.03	0.012 ± 0.005		
0.05 V vs. RHE in half cell Mo K edge	Mo-Pt	5.9 ± 0.4	2.76 ± 0.01	0.011 ± 0.001	-4.6 ± 1.0	38.20
	Mo-O	0.8 ± 0.2	2.10 ± 0.02	0.015 ± 0.009		
	Mo-Mo	2.7 ± 0.8	3.98 ± 0.02	0.014 ± 0.004		
	Mo-Pt (MS)	5.9 ± 0.4	5.42 ± 0.02	0.010 ± 0.004		
0.05 V vs. RHE in half cell Pt L_{III} edge	Pt-Pt	6.3 ± 0.3	2.74 ± 0.00	0.011 ± 0.000	-11.9 ± 0.8	31.24
	Pt-Mo	1.2 ± 0.2	2.73± 0.01	0.010 ± 0.002		
	Pt-Mo	1.3 ± 0.4	3.99 ± 0.02	0.012 ± 0.003		
	Pt-Pt	3.6 ± 1.1	4.75 ± 0.02	0.013 ± 0.003		
	Pt-Pt (MS)	6.1 ± 0.3	5.36 ± 0.02	0.017 ± 0.004		
0.55 V vs. RHE in half cell Pt L_{III} edge	Pt-Pt	6.0 ± 0.2	2.75 ± 0.00	0.011 ± 0.000	-13.6 ± 0.6	28.17
	Pt-Mo	1.3 ± 0.2	2.75 ± 0.01	0.011 ± 0.001		
	Pt-Mo	1.3 ± 0.4	4.00 ± 0.02	0.012 ± 0.003		
	Pt-Pt	3.1 ± 0.9	4.77 ± 0.01	0.011 ± 0.002		
	Pt-Pt (MS)	6.0 ± 0.2	5.38 ± 0.02	0.017 ± 0.004		

When fitting the Mo K edge data, the number of first shell Mo-Pt neighbours was found to be roughly double that of the previous route 1 catalysts. The atomic ratio of Mo to Pt in this sample is approximately half that of the route 1 catalysts. This suggests that the proportion of Mo going into the bulk of the particle has been increased. No Mo-Mo neighbours could be fitted in the first coordination shell, while the number of oxygen neighbours was found to be the same as that for the route 1 catalyst heated to 900 °C at 0.05 V vs. RHE. This indicates that the Mo atoms on the route 1 catalysts are largely present as clusters on the surface, while the degree of

mixing has been improved for the route 2 catalyst. This complements the results shown in table 4, which attempted to deduce how well-mixed the samples were by measuring the Mo redox peaks. This found that, while the amount of Mo at the surface capable of being oxidised was less than expected for an evenly-mixed sample, possibly due to a clustering effect; the results for the route 2 catalysts were closer to the expected values.

The chi plots for the Pt L_{III} data in figure 9 (e and g) show a region of low amplitude oscillation at approximately 6 $Å^{-1}$. This is an area of destructive interference between the backscattered photoelectron wave from the Pt and Mo neighbours, as has been reported previously for Pt and Ru neighbours in a PtRu sample [15,33]. This occurs when the backscattering is 180 ° out of phase and leads to peak splitting in the Fourier transform. In the case of 1: 1 Pt: Ru, the presence of such splitting was shown to be a good indication of intermixing of the species. For the data shown in figure 9, the coordination numbers obtained at the Pt L_{III} edge remain consistent between 0.05 and 0.55 V vs. RHE. At 0.05 V vs. RHE, the number of Pt-Pt neighbours in the first coordination shell is 6.3 compared with 1.2 Pt-Mo neighbours. The atomic ratio of Pt: Mo in this sample is close to 3: 1 so the number of Mo neighbours is less than expected, although closer to the expected value than has been reported for other PtMo catalysts in the literature [13,15]. This demonstrates the difficulty inherent in attempting to produce a well-mixed PtMo alloy, when compared with PtRu. Comparison with the data at the Mo K edge allows for an estimation of the extent of mixing in the sample. The ratio of Pt-Mo neighbours to Mo-Pt neighbours is 1.2/5.2 = 0.23, which is not equal to the ratio of Pt atoms to Mo atoms in the sample (0.32). While some mixing of Pt and Mo is apparent, it is not an evenly-mixed alloy. No Pt-O neighbours are fitted, which is consistent with results obtained of a CV for Pt in acid, where oxide formation is seen to occur only above 0.8 V vs RHE (see figure 6, chapter 2).

The number of metal atoms in the first coordination shell at the Pt L_{III} edge can also be used to deduce the particle size of the catalyst. A bulk Pt foil is known to have an fcc structure with a first shell coordination number of 12. However, for catalyst nanoparticles with a diameter of less than 5 nm, the fraction of Pt atoms at the surface is approximately 0.5. The atoms at or near the surface of the particle do not have the

full complement of neighbours and, as EXAFS is an averaging technique, the corresponding first shell coordination number values are lower than in a bulk Pt foil. Benfield [34] has derived equations to calculate particle size based on number of neighbours using either icosahedral or cuboctahedral geometries. These are modelled as concentric shells of atoms where, if the central atom is counted as the first shell, a cluster of *m* complete shells has edge length of *m* atoms. Equations 3 and 4 show the relationship between the coordination number, *N*, and the number of complete shells, *m*, for the icosahedral and cuboctahedral cases respectively.

$$N_{total} = \frac{6(m-1)(20m^2 - 25m + 12)}{(2m-1)(5m^2 - 5m + 3)} \qquad \textbf{Eq. 3}$$

$$N_{total} = \frac{12(m-1)(10m^2 - 14m + 6)}{(2m-1)(5m^2 - 5m + 3)} \qquad \textbf{Eq. 4}$$

These two geometries are shown pictorially in figure 10 below.

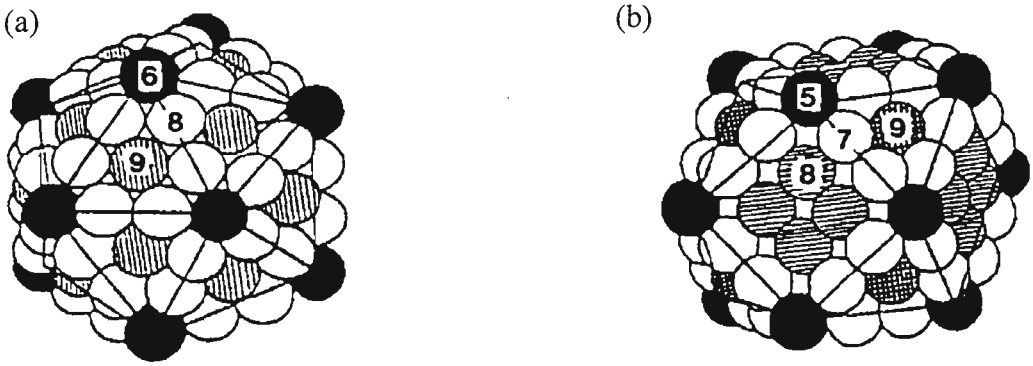

Figure 10 **Particle geometries for a) icosahedron and b) cuboctahedron using 147 atoms corresponding to four complete shells. Numbers on surface atoms indicate varying coordination numbers [34].**

The cuboctahedron is the most widely used cluster model [35], however the icosahedron is favoured thermodynamically for smaller particles as it possesses a higher value of *N* than the cuboctahedron for a particle the same size because of the higher coordination of some of the surface atoms. The total number of first shell metal neighbours (N_{total}) for the 36.9 wt. % Pt / 5.7 wt. % Mo route 2 catalyst is 7.5. The values of m calculated using equations 3 and 4 are 2.4 and 2.8 respectively, giving rise

to particle sizes of 1.10 and 1.28 nm. These values are considerably lower than the value of 3.26 nm obtained using XRD. Neither model correctly correlates with the XRD data obtained. This is likely due to the EXAFS data including contributions from all Pt atoms present, including those in particles too small to be detected by XRD, and the limitation in assuming particle geometries with complete shells. For incomplete shells, the average coordination number will be significantly lower.

EXAFS data for the series of PtMo catalysts prepared via the co-deposition method (route 3) with a lower total metal content are shown in figures 11 and 12. The data shown was collected at 0.05 and 0.85 V vs. RHE in the XAS fluorescence half cell at the Mo K edge. The potentials chosen are situated before and after the Mo redox couple as seen in the cyclic voltammetry experiments.

Figure 11 shows the EXAFS data collected with the potential held at 0.05 V vs. RHE. The data shown is in order of increasing Mo content. Neither the chi nor FT plots display any noticeable differences as the total Mo content is increased. The oscillation at low *k* space (between 5 and 6 $Å^{-1}$) has a small shoulder as was seen with the route 1 and 2 catalysts at 0.05 V vs. RHE. This is not to the extent of the 36.9 wt. % Pt / 5.7 wt. % Mo catalyst at open circuit, where this increased shoulder was coupled with dampening of the oscillation at 6 $Å^{-1}$, leading to splitting of the main peak in the Fourier Transform.

The parameters obtained from fitting of the experimental data in figure 11 can be found in table 14.

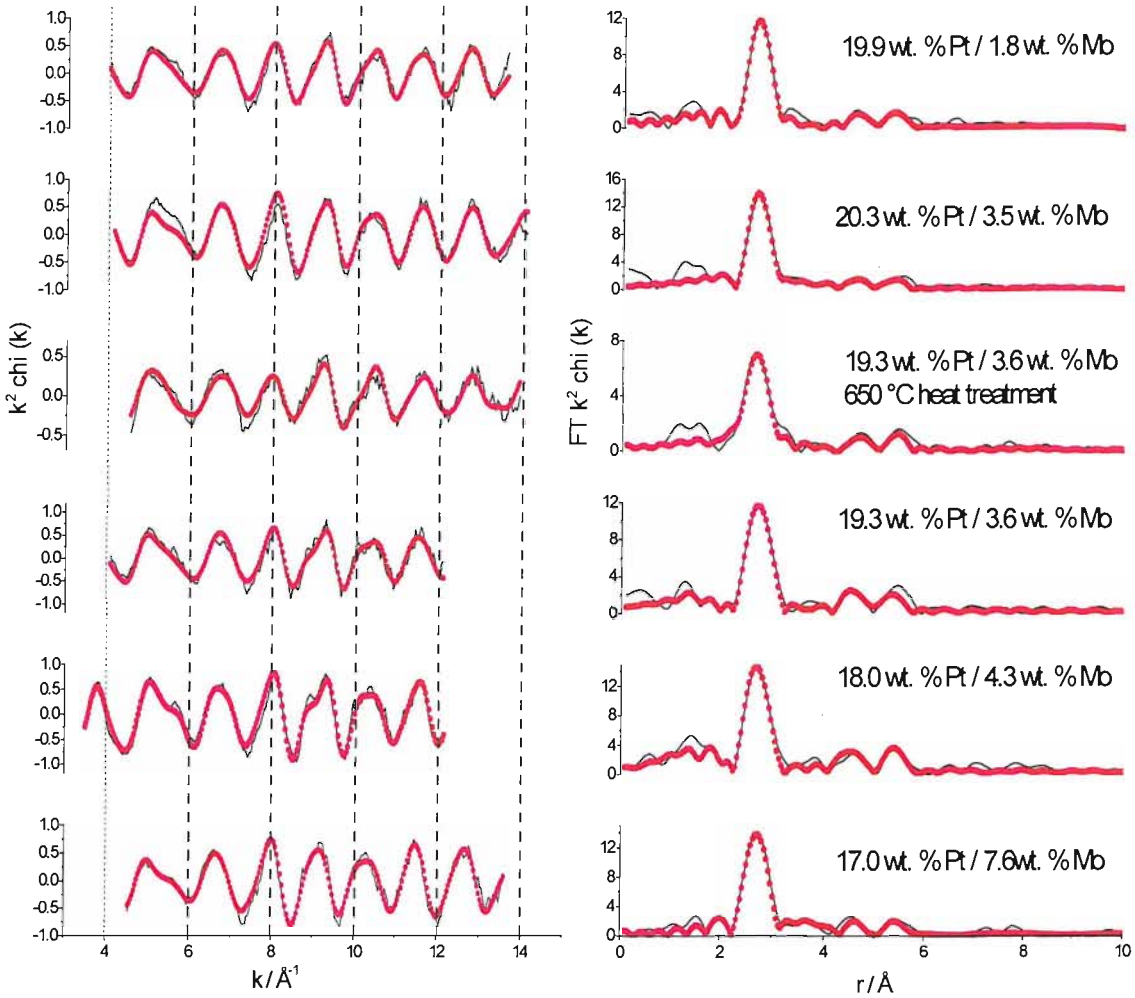

Figure 11 **Experimental data (solid lines) and fit (dots) [left] and corresponding Fourier transform [right] for the series of route 3 PtMo catalysts prepared with close to 20 wt. % Pt. Data obtained at the Mo K edge for catalysts in the half cell at 0.05 V vs. RHE. Data is k^2-weighted and the Fourier transforms are phase corrected to Pt.**

Table 14 **Structural parameters for the series of route 3 PtMo catalysts prepared with close to 20 wt. % Pt. Data obtained at the Mo K edge for catalysts in the half cell at 0.05 V vs. RHE. Catalysts heat treated at 1000 °C unless otherwise stated.**

Sample	Shell	N	R / Å	$2\sigma^2$ / Å^2	E_f / eV	R_{exafs}
19.9 wt. % Pt / 1.8 wt. % Mo	Mo-Pt	3.8 ± 0.2	2.74 ± 0.00	0.009 ± 0.001	-7.1 ± 1.1	29.54
	Mo-O	0.5 ± 0.3	2.02 ± 0.03	0.012 ± 0.007		
	Mo-Mo	0.7 ± 0.2	3.65 ± 0.02	0.008 ± 0.004		
	Mo-Pt	2.6 ± 1.0	4.75 ± 0.02	0.011 ± 0.004		
	Mo-Pt (MS)	3.8 ± 0.2	5.40 ± 0.02	0.010 ± 0.003		
20.3 wt. % Pt / 3.5 wt. % Mo	Mo-Pt	5.6 ± 0.3	2.73 ± 0.00	0.012 ± 0.001	-4.3 ± 1.1	32.45
	Mo-Mo	1.1 ± 0.6	3.95 ± 0.03	0.013 ± 0.006		
	Mo-Pt	2.9 ± 1.4	4.71 ± 0.03	0.013 ± 0.005		
	Mo-Pt (MS)	5.6 ± 0.3	5.38 ± 0.03	0.016 ± 0.005		
19.3 wt. % Pt / 3.6 wt. % Mo (650 ° C heat treatment)	Mo-Pt	2.7 ± 0.2	2.73 ± 0.01	0.012 ± 0.001	-6.3 ± 1.9	40.06
	Mo-O	0.5 ± 0.1	2.03 ± 0.03	0.007 ± 0.005		
	Mo-Mo	0.4 ± 0.1	2.57 ± 0.02	0.009 ± 0.003		
	Mo-Mo	1.1 ± 0.6	4.90 ± 0.03	0.009 ± 0.006		
	Mo-Pt (MS)	2.5 ± 0.3	5.42 ± 0.03	0.010 ± 0.004		
19.3 wt. % Pt / 3.6 wt. % Mo	Mo-Pt	4.8 ± 0.3	2.74 ± 0.01	0.011 ± 0.001	-5.6 ± 1.7	34.14
	Mo-O	0.6 ± 0.2	2.01 ± 0.03	0.010 ± 0.001		
	Mo-Pt	5.1 ± 1.5	4.71 ± 0.02	0.012 ± 0.003		
	Mo-Pt (MS)	4.8 ± 0.3	5.39 ± 0.03	0.012 ± 0.003		
18.0 wt. % Pt / 4.3 wt. % Mo	Mo-Pt	6.1 ± 0.3	2.74 ± 0.01	0.011 ± 0.001	-0.1 ± 0.6	25.49
	Mo-O	0.9 ± 0.1	1.97 ± 0.01	0.018 ± 0.005		
	Mo-Pt	11.6 ± 3.0	4.71 ± 0.02	0.010 ± 0.004		
	Mo-Mo	5.2 ± 2.4	5.02 ± 0.03	0.009 ± 0.007		
	Mo-Pt (MS)	6.1 ± 0.3	5.38 ± 0.02	0.006 ± 0.003		
17.0 wt. % Pt / 7.6 wt. % Mo	Mo-Pt	5.7 ± 0.2	2.76 ± 0.00	0.011 ± 0.000	-8.0 ± 0.7	25.31
	Mo-Mo	1.3 ± 0.4	3.98 ± 0.02	0.010 ± 0.004		
	Mo-Pt	2.7 ± 1.1	4.73 ± 0.02	0.011 ± 0.004		
	Mo-Pt (MS)	5.7 ± 0.2	5.42 ± 0.02	0.013 ± 0.004		

The number of Pt neighbours in the first coordination shell is between 4.8 and 6.1, with the exception of the very low Mo content catalyst (1.8 wt. % Mo corresponding to a Pt: Mo ratio greater than 5 to 1), and the catalyst that was only heated to 650 °C as opposed to 1000 °C. This latter catalyst only had 2.7 Mo-Pt neighbours in the first coordination shell; a number that increases to 4.8 for the same catalyst heated to the higher temperature. At the lower temperature, less Mo is driven into the bulk of the catalyst particle and associated with the Pt. The number of oxygen neighbours for both catalysts remains unchanged (approximately 0.5 - 0.7). This suggests that some of the Mo at the surface for the lower heat treatment sample must have been present in small clusters and therefore prevented from being fully oxidised, because if all Mo on the surface was fully oxidised and heating drove a larger amount of Mo inside the catalyst, the number of O neighbours would be expected to drop. The fact that the catalyst heated to 650 °C is the only one to which Mo-Mo neighbours in the first coordination shell could be fitted backs up this claim. This clustering at the surface may not be a disadvantage of the general preparation method but rather the result of the small particle sizes meaning Mo at the surface may be forced to have Mo neighbours due to the lack of available space. The fact that the number of Mo-O neighbours doesn't always correlate with the calculated average Mo oxidation states as shown in Table 7 can be attributed to particle size effects and the larger errors associated with the XANES analysis method.

The majority of the catalysts also had oxygen neighbours at close to 2.0 Å, indicating that Mo at the surface of the nanoparticles remain oxidised even when the potential is lowered to 0.05 V vs. RHE in the presence of an acidic electrolyte. The bond distance for Mo-O neighbours is lower than found previously with the route 1 and 2 catalysts indicating a change in the structure of the Mo oxides at the surface. The oxides on the route 1 and 2 catalysts are believed to be the result of O neighbours on Mo clusters that have little association with Pt. The change in Mo-O bond length for the route 3 catalysts should be because the O neighbours are now bonded to well-mixed Mo atoms present in the surface layer of the nanoparticle and having a greater association with neighbouring Pt atoms.

The EXAFS data for the same series of catalysts when a potential of 0.85 V vs. RHE is applied in the XAS fluorescence half cell are shown in figure 12, with corresponding

structural parameters in table 15.

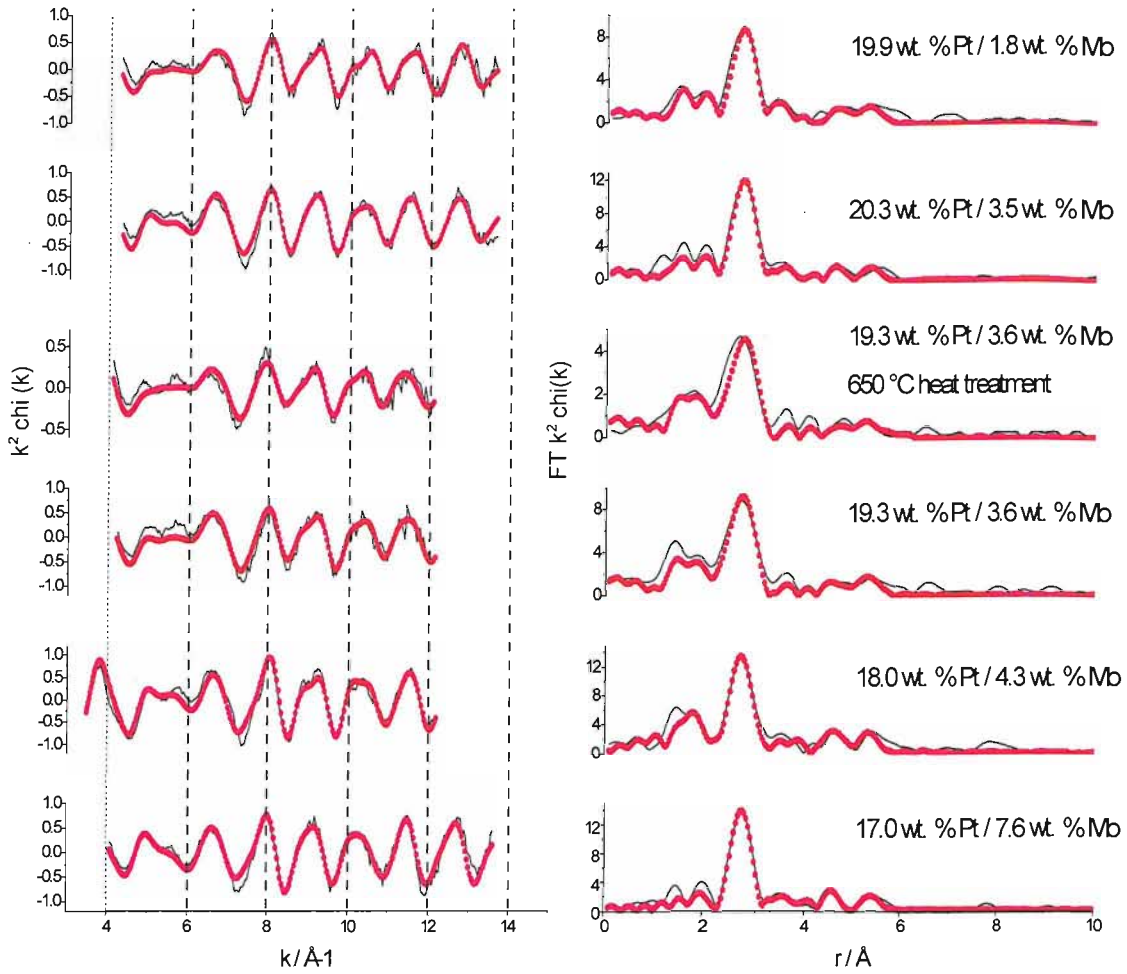

Figure 12 **Experimental data (solid lines) and fit (dots) [left] and corresponding Fourier transform [right] for the series of route 3 PtMo catalysts prepared with close to 20 wt. % Pt. Data obtained at the Mo K edge for catalysts in the half cell at 0.85 V vs. RHE. Data is k^2-weighted and the Fourier transforms are phase corrected to Pt.**

Table 15 **Structural parameters for the series of route 3 PtMo catalysts prepared with close to 20 wt. % Pt. Data obtained at the Mo K edge for catalysts in the half cell at 0.85 V vs. RHE. Catalysts heat treated at 1000 °C unless otherwise stated.**

Sample	Shell	N	R / Å	$2\sigma^2$ / Å^2	E_f / eV	R_{exafs}
19.9 wt. % Pt / 1.8 wt. % Mo	Mo-Pt	3.3 ± 0.2	2.74 ± 0.01	0.010 ± 0.001	-3.0 ± 1.6	43.10
	Mo-O	0.6 ± 0.1	1.72 ± 0.02	0.006 ± 0.004		
	Mo-Mo	0.7 ± 0.3	3.65 ± 0.02	0.010 ± 0.004		
	Mo-Pt	3.2 ± 1.2	4.75 ± 0.02	0.012 ± 0.004		
	Mo-Pt (MS)	3.3 ± 0.2	5.39 ± 0.03	0.008 ± 0.005		
20.3 wt. % Pt / 3.5 wt. % Mo	Mo-Pt	5.1 ± 0.3	2.74 ± 0.01	0.011 ± 0.001	-3.6 ± 1.2	35.31
	Mo-O	0.5 ± 0.1	1.71 ± 0.02	0.009 ± 0.006		
	Mo-Mo	0.9 ± 0.5	3.96 ± 0.04	0.011 ± 0.008		
	Mo-Pt	2.5 ± 1.2	4.73 ± 0.04	0.012 ± 0.007		
	Mo-Pt (MS)	5.1 ± 0.3	5.40 ± 0.03	0.015 ± 0.007		
19.3 wt. % Pt / 3.6 wt. % Mo (650 ° C heat treatment)	Mo-Pt	2.3 ± 0.2	2.77 ± 0.01	0.011 ± 0.001	-5.9 ± 1.7	49.69
	Mo-O	0.5 ± 0.1	1.75 ± 0.02	0.008 ± 0.004		
	Mo-Mo	1.0 ± 0.6	4.93 ± 0.04	0.010 ± 0.007		
	Mo-Pt (MS)	2.3 ± 0.2	5.45 ± 0.03	0.011 ± 0.007		
19.3 wt. % Pt / 3.6 wt. % Mo	Mo-Pt	4.3 ± 0.3	2.75 ± 0.01	0.011 ± 0.001	-2.6 ± 1.9	47.56
	Mo-O	0.7 ± 0.2	1.72 ± 0.02	0.006 ± 0.004		
	Mo-Pt	3.5 ± 1.9	4.73 ± 0.04	0.014 ± 0.007		
	Mo-Pt (MS)	4.3 ± 0.3	5.40 ± 0.03	0.010 ± 0.005		
18.0 wt. % Pt / 4.3 wt. % Mo	Mo-Pt	5.7 ± 0.3	2.74 ± 0.00	0.010 ± 0.001	1.1 ± 0.7	34.21
	Mo-O	0.6 ± 0.1	1.76 ± 0.02	0.008 ± 0.005		
	Mo-Mo	1.1 ± 0.6	3.96 ± 0.03	0.011 ± 0.006		
	Mo-Pt	5.5 ± 1.5	4.69 ± 0.02	0.011 ± 0.003		
	Mo-Pt (MS)	5.7 ± 0.3	5.39 ± 0.02	0.008 ± 0.004		
17.0 wt. % Pt / 7.6 wt. % Mo	Mo-Pt	4.7 ± 0.2	2.76 ± 0.01	0.009 ± 0.000	-6.3 ± 1.1	32.40
	Mo-Mo	1.3 ± 0.5	3.98 ± 0.02	0.010 ± 0.004		
	Mo-Pt	3.0 ± 1.0	4.70 ± 0.02	0.009 ± 0.003		
	Mo-Pt (MS)	4.7 ± 0.2	5.43 ± 0.02	0.011 ± 0.004		

Upon increasing the potential to 0.85 V vs. RHE, a region of destructive interference is observed in the low *k* space region in the 5 – 6 $Å^{-1}$ region, with corresponding features appearing between 1 and 2 Å in the Fourier Transforms. The exception to this is the 17.0 wt. % Pt / 7.6 wt. % Mo (the highest Mo content) catalyst, which appears unchanged from the data seen at 0.05 V vs. RHE. The number of Mo-Pt neighbours in the first coordination shell has dropped for all six catalysts in the series, generally by between 0.5 and 1. The number of Mo-O neighbours remains fairly consistent between potentials, although the bond length decreases from around 2.0 Å to between 1.72 and 1.76 Å. This shortened bond length is consistent with that found for Mo-O neighbours with a surface modified PtMo catalyst at 0.65 V vs. RHE with previous XAS studies[16]. This indicates that the Mo atoms that form the oxides are no longer fully integrated into the surface layer of the nanoparticle and actually possess some potential dependent mobility, being able to come out of the surface layer to some extent. This explains the drop in Mo-Pt neighbours observed, although they still remain significantly higher than found with the route 1 and 2 catalysts. This indicates that, even when oxidised, the Mo atoms at the surface do not completely come out of the surface layer to sit on top of the particles. The shortening of the Mo-O bond also appears to be the cause of the destructive interference seen in the chi plot; presumably as it leads to the back scattering from the Pt and O neighbours being 180° out of phase. It would be expected that the number of Mo-O neighbours would increase when changing potential from 0.05 to 0.85 V as seen with the increasing average Mo oxidation states as calculated from the edge positions. It is unclear why this isn't observed in the EXAFS fitting.

The fit of the highest Mo content catalyst does not acquire any first shell oxygen neighbours at both potentials, presumably as a result of the much larger particle size.

The EXAFS data for the CSR PtMo catalyst obtained in the XAS fluorescence half cell at 0.15 and 0.65 V vs. RHE at the Mo K edge are shown in figure 13 with the corresponding parameters derived to be found in table 16.

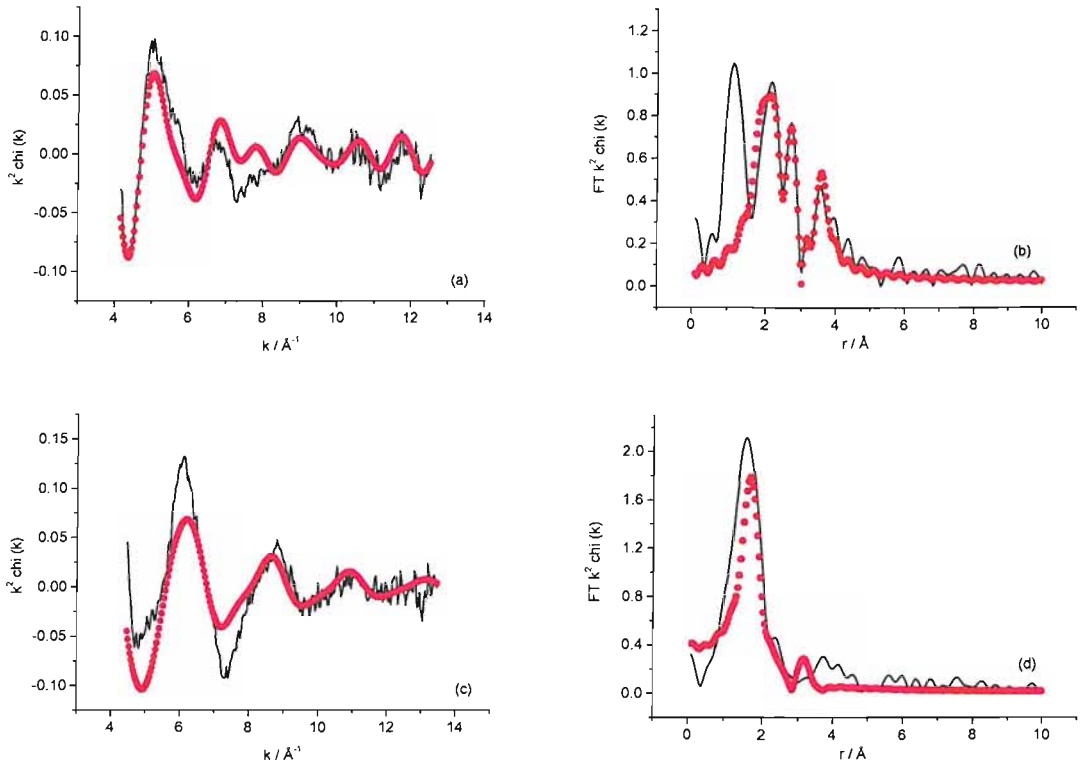

Figure 13 **Experimental data (solid lines) and fit (dots) [left] and corresponding Fourier transform [right] for the CSR PtMo catalyst at 0.15 V vs. RHE in the half cell (a and b) and at 0.65 V vs. RHE in the half cell (c and d). Data collected at the Mo K-edge and is k^2-weighted. Phase corrected to O neighbours.**

Table 16 **Structural parameters for the CSR PtMo catalyst in the half cell. Data collected at the Mo K edge**

Condition	Shell	N	R / Å	$2\sigma^2$ / Å^2	E_f / eV	R_{exafs}
0.15 V vs. RHE in half cell	Mo-Pt	1.3 ± 0.4	2.70 ± 0.02	0.011 ± 0.004	-3.6 ± 2.0	59.14
	Mo-O	1.0 ± 0.2	2.00 ± 0.02	0.014 ± 0.005		
	Mo-Mo	0.4 ± 0.2	2.60 ± 0.03	0.012 ± 0.007		
0.65 V vs. RHE in half cell	Mo-O	1.2 ± 0.1	1.72 ± 0.02	0.005 ± 0.003	4.3 ± 5.1	68.42

The data at 0.65 V can only be fitted as an oxide with 1.2 Mo-O neighbours in the first coordination shell at a bond length of 1.72 Å. Reducing the potential to 0.15 V leads to some association with the Pt present. This can be seen by a shift in the low k space oscillation from 5 Å^{-1} to 6 Å^{-1} and an increase in overall number of oscillations present

in the chi plot. The main peak in the Fourier transform is also split when the potential is reduced, giving rise to a peak at 2.7 Å. There is also a small drop in number of Mo-O neighbours (from 1.2 to 1.0), with an increase in bond length from 1.72 to 2.00 Å, as was observed with the co-deposited route 3 catalysts.

These results are in contrast to the previous CSR PtMo catalyst prepared by Crabb *et al* [16], which was determined to only have an approximate 0.1 monolayer (as opposed to the 0.5 monolayer for the catalyst reported here), but which displayed a much increased association with Pt when reduced at 0.05 V vs. RHE, with 4.5 Mo-Pt neighbours at 2.63 Å reported. The overall coordination number of Pt neighbours is likely lowered because with such a high Mo content at the surface, a larger proportion of Mo atoms are likely to be present within large Mo oxide clusters at the surface and prevented from associating with the Pt. The fitting of 0.4 Mo-Mo neighbours at 2.60 Å, compared with no Mo-Mo neighbours fitted with the 0.1 monolayer catalyst [16], supports this.

3.2.3 EXAFS - Mini Cell

XAS data were obtained for five of the PtMo catalysts at the Mo K and Pt L_{III} edges, using the PEM mini cell operating at 80 °C, with the MSA humidifiers, and a 5 % H_2/N_2 gas feed to both the anode and cathode sides of the cell. The measured open circuit potential was 0.0 V. The k^2 weighted EXAFS data and corresponding Fourier transforms for the 35.4 wt. % Pt / 5.3 wt. % Mo and 36.9 wt. % Pt / 5.7 wt. % Mo samples (prepared by route 2 with subsequent heat treatments to 620 and 900 °C respectively) are shown in figure 14. Data were collected at 0.1 V and 0.5 V vs. RHE, and EXAFS data of the 900 °C catalyst obtained as an MEA in air is also shown for comparison. The structural parameters obtained can be found in table 17.

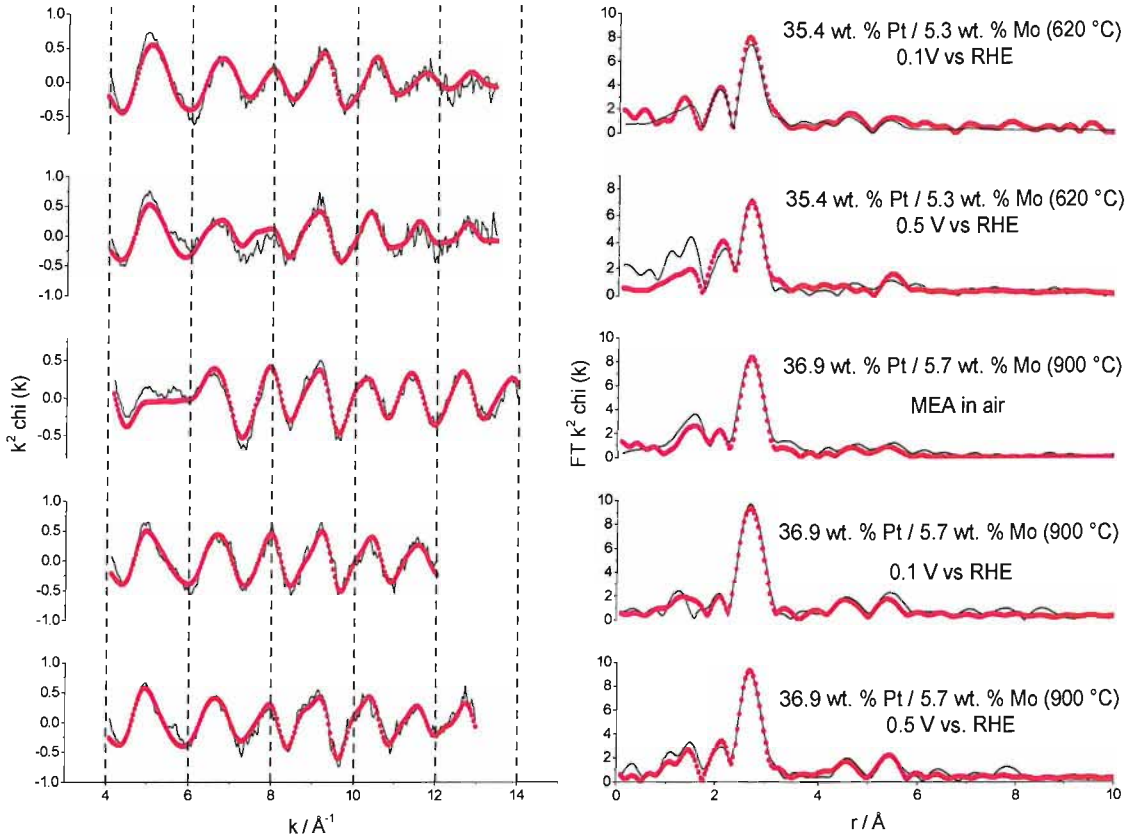

Figure 14 **Experimental data (solid lines) and fit (dots) [left] and corresponding Fourier transform [right] for a series of PtMo catalysts prepared by preparation route 2. Data obtained at the Mo K edge for catalysts either as an MEA in air or polarised in the mini cell with a 5 % H_2 in nitrogen gas mixture to both electrodes. Data is k^2-weighted and the Fourier transforms are phase corrected to Pt.**

Table 17 **Structural parameters for a series of PtMo catalysts prepared by preparation route 2. Data obtained at the Mo K edge for catalysts either as an MEA in air or polarised in the mini cell with a 5 % H_2 in nitrogen gas mixture to both electrodes.**

Sample	Shell	N	R / Å	$2\sigma^2$ / Å^2	E_f / eV	R_{exafs}
35.4 wt. % Pt / 5.3 wt. % Mo 0.1 V vs. RHE	Mo-Pt	2.5 ± 0.3	2.73 ± 0.01	0.014 ± 0.001	-2.6 ± 1.8	39.14
	Mo-O	1.6 ± 0.2	2.04 ± 0.01	0.011 ± 0.002		
	Mo-Mo	0.6 ± 0.1	2.54 ± 0.01	0.010 ± 0.002		
	Mo-Mo	1.4 ± 0.8	4.90 ± 0.04	0.013 ± 0.007		
	Mo-Pt (MS)	2.5 ± 0.3	5.42 ± 0.04	0.015 ± 0.008		
35.4 wt. % Pt / 5.3 wt. % Mo 0.5 V vs. RHE	Mo-Pt	2.2 ± 0.3	2.75 ± 0.01	0.012 ± 0.002	-3.5 ± 2.2	52.18
	Mo-O	1.3 ± 0.2	2.04 ± 0.02	0.010 ± 0.004		
	Mo-Mo	0.7 ± 0.2	2.57 ± 0.01	0.011 ± 0.003		
	Mo-Pt	3.5 ± 2.0	5.46 ± 0.03	0.012 ± 0.006		
36.9 wt. % Pt / 5.7 wt. % Mo MEA in air	Mo-Pt	3.4 ± 0.2	2.76 ± 0.01	0.011 ± 0.001	-6.5 ± 1.2	37.98
	Mo-O	0.6 ± 0.1	1.71 ± 0.01	0.005 ± 0.003		
	Mo-Mo	1.0 ± 0.6	4.89 ± 0.03	0.011 ± 0.006		
	Mo-Pt (MS)	3.4 ± 0.2	5.44 ± 0.03	0.015 ± 0.005		
36.9 wt. % Pt / 5.7 wt. % Mo 0.1 V vs. RHE	Mo-Pt	3.7 ± 0.3	2.74 ± 0.01	0.012 ± 0.001	-4.1 ± 1.9	32.72
	Mo-O	1.0 ± 0.2	2.06 ± 0.02	0.013 ± 0.004		
	Mo-Mo	0.3 ± 0.1	2.54 ± 0.02	0.011 ± 0.005		
	Mo-Pt	2.8 ± 1.1	4.75 ± 0.03	0.012 ± 0.005		
	Mo-Pt (MS)	3.7 ± 0.3	5.42 ± 0.03	0.011 ± 0.008		
36.9 wt. % Pt / 5.7 wt. % Mo 0.5 V vs. RHE	Mo-Pt	3.3 ± 0.3	2.75 ± 0.01	0.012 ± 0.001	-3.2 ± 1.3	33.16
	Mo-O	1.2 ± 0.2	2.07 ± 0.01	0.008 ± 0.003		
	Mo-Mo	0.6 ± 0.2	2.58 ± 0.01	0.011 ± 0.002		
	Mo-Pt	2.8 ± 1.1	4.75 ± 0.03	0.013 ± 0.005		
	Mo-Pt (MS)	3.3 ± 0.3	5.43 ± 0.03	0.007 ± 0.003		

The data for the 35.4 wt. % Pt / 5.3 wt. % Mo catalyst heat treated to the lower temperature is very similar at the reducing and oxidising potentials. The number of Mo-Pt neighbours in the first coordination shell is very low (between 2.2 and 2.5) indicating little association with the Pt. The large number of oxygen neighbours (1.6) at 2.04 Å and fitting of Mo-Mo neighbours in the first shell when held at 0.1 V vs. RHE also suggests that the majority of the Mo atoms are present grouped together on the surface of the particle, rather than being integrated into the bulk of the nanoparticle. Upon increasing the potential to 0.5 V (a point at, or just after, the Mo redox couple peak seen in the forward sweep of a CV) no real changes are observed, most notably the Mo-O bond length remains at 2.04 Å.

Data for the 36.9 wt. % Pt / 5.7 wt. % Mo catalyst shows that, while the overall composition is almost identical, the increased heat treatment during preparation to 900°C leads to an increase in first shell Mo-Pt neighbours by 1 and a small drop in number Mo-O neighbours when measured in the mini cell at the same potentials. Again there is very little difference in the data when the potential is increased from 0.1 to 0.5 V, as seen by the small edge change seen in the XANES analysis. There is a small drop in Mo-Pt neighbours, but the Mo-O bond length remains above 2 Å, not decreasing to the ~1.7 Å value found for the oxidised route 3 catalysts in the half cell. This was also not observed for any of the route 1 and 2 catalysts in the half cell at oxidising potentials. Data for this catalyst as an MEA in air, on the other hand, shows a region of destructive interference in the chi plot between 5 and 6 $Å^{-1}$ and corresponding drop in Mo-O bond length to 1.71 Å. This says that the catalysts prepared by routes 1 and 2 can only be fully oxidised when in air; the environments found in the half cell and mini cell lead to a reduced form of the catalyst that cannot be significantly altered with potential.

The data for the 36.9 wt. % Pt / 5.7 wt. % Mo catalyst in the mini cell can also be compared with that for the same catalyst in the half cell in 1 M H_2SO_4 at open circuit and 0.05 V vs. RHE found in table 13. In the half cell at 0.05 V, the number of Mo-Pt neighbours in the first coordination shell is 5.9, compared with 3.7 in the mini cell at 0.1 V. The increase in neighbours in the half cell is possibly due to dissolution of Mo oxide from the surface leading to increased contributions to the EXAFS from Mo inside the nanoparticle. There may also be increased migration of some of the

remaining Mo at the surface into the bulk of the particle. The loss of Mo from the surface of carbon supported PtMo catalysts has been discussed by Lebedeva *et al* [36]. They suggested that water-soluble Mo compounds were formed by the electrochemical reduction of stable MoO_3 surface species. The rate of dissolution was found to increase for catalysts where the Mo was less well-associated with the Pt, and also the rate of dissolution was slower from catalysts in MEAs using solid electrolytes than in aqueous acidic environments. After cycling of the catalyst, the presence of Mo was detected on the cathode side of the MEA, which began as just a Pt/C electrode. The increased dissolution in aqueous acidic environments is likely a volume effect due to the greater amount of relative electrolyte and the fact that, being liquid, it is mobile so will pick up more Mo as it comes into contact with the catalyst.

EXAFS data for three of the PtMo catalysts prepared by the codeposition method (route 3) at the Mo K edge in the mini cell at 0.1 V and 0.5 V vs. RHE are shown in figure 15, along with data from one of the catalysts as an MEA in air for comparison. Structural parameters obtained are shown in table 18.

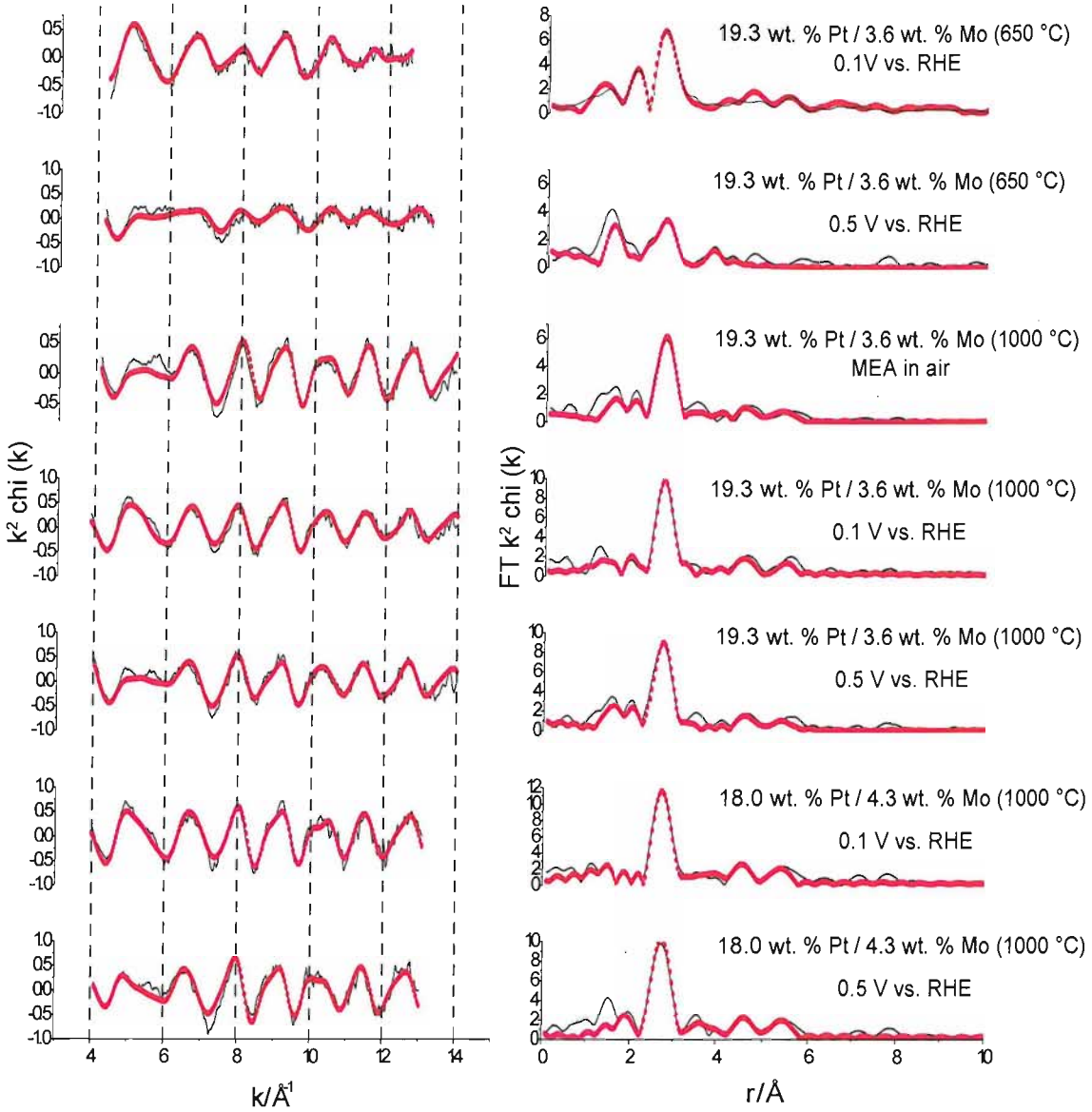

Figure 15 **Experimental data (solid lines) and fit (dots) [left] and corresponding Fourier transform [right] for a series of PtMo catalysts prepared by preparation route 3. Data obtained at the Mo K edge for catalysts either as an MEA in air or polarised in the mini cell with a 5 % H_2 in nitrogen gas mixture to both electrodes. Data is k^2-weighted and the Fourier transforms are phase corrected to Pt.**

Table 18 **Structural parameters for a series of PtMo catalysts prepared by preparation route 3. Data obtained at the Mo K edge for catalysts either as an MEA in air or polarised in the mini cell with a 5 % H_2 in nitrogen gas mixture to both electrodes.**

Sample	Shell	N	R / Å	$2\sigma^2$ / Å^2	E_f / eV	R_{exafs}
19.3 wt. % Pt / 3.6 wt. % Mo (650 °C) 0.1 V vs. RHE	Mo-Pt	2.2 ± 0.3	2.75 ± 0.01	0.013 ± 0.001	-7.6 ± 1.6	33.05
	Mo-O	1.7 ± 0.1	2.05 ± 0.01	0.011 ± 0.001		
	Mo-Mo	0.5 ± 0.1	2.54 ± 0.01	0.009 ± 0.002		
	Mo-Pt (MS)	2.2 ± 0.3	5.46 ± 0.04	0.009 ± 0.007		
19.3 wt. % Pt / 3.6 wt. % Mo (650 °C) 0.5 V vs. RHE	Mo-Pt	2.5 ± 0.4	2.72 ± 0.01	0.017 ± 0.002	2.7 ± 2.2	60.21
	Mo-O	0.5 ± 0.1	1.72 ± 0.02	0.006 ± 0.004		
	Mo-Mo	0.4 ± 0.2	2.60 ± 0.03	0.014 ± 0.005		
	Mo-Pt	1.1 ± 0.8	3.95 ± 0.04	0.016 ± 0.010		
19.3 wt. % Pt / 3.6 wt. % Mo (1000 °C) MEA in air	Mo-Pt	3.7 ± 0.2	2.75 ± 0.01	0.010 ± 0.001	-2.8 ± 1.5	43.80
	Mo-O	0.5 ± 0.1	1.72 ± 0.02	0.006 ± 0.004		
	Mo-Mo	1.3 ± 0.6	4.84 ± 0.02	0.007 ± 0.004		
	Mo-Pt (MS)	3.7 ± 0.2	5.40 ± 0.03	0.012 ± 0.005		
19.3 wt. % Pt / 3.6 wt. % Mo (1000 °C) 0.1 V vs. RHE	Mo-Pt	3.7 ± 0.2	2.75 ± 0.01	0.012 ± 0.001	-4.7 ± 1.3	34.80
	Mo-O	0.9 ± 0.1	2.03 ± 0.02	0.011 ± 0.004		
	Mo-Mo	0.3 ± 0.1	2.54 ± 0.02	0.010 ± 0.004		
	Mo-Mo	1.7 ± 0.7	4.88 ± 0.02	0.011 ± 0.004		
	Mo-Pt (MS)	3.7 ± 0.2	5.44 ± 0.03	0.014 ± 0.005		
19.3 wt. % Pt / 3.6 wt. % Mo (1000 °C) 0.5 V vs. RHE	Mo-Pt	3.8 ± 0.2	2.76 ± 0.01	0.011 ± 0.001	-3.8 ± 1.2	41.69
	Mo-O	0.4 ± 0.1	1.74 ± 0.02	0.006 ± 0.005		
	Mo-Mo	1.4 ± 0.6	4.86 ± 0.02	0.009 ± 0.005		
	Mo-Pt (MS)	3.8 ± 0.2	5.44 ± 0.04	0.016 ± 0.005		
18.0 wt. % Pt / 4.3 wt. % Mo (1000 °C) 0.1 V vs. RHE	Mo-Pt	4.6 ± 0.2	2.74 ± 0.01	0.011 ± 0.001	-4.0 ± 1.0	31.57
	Mo-O	0.7 ± 0.2	2.02 ± 0.02	0.009 ± 0.005		
	Mo-Mo	1.3 ± 0.5	3.99 ± 0.02	0.012 ± 0.004		
	Mo-Mo	2.5 ± 0.8	4.85 ± 0.02	0.011 ± 0.003		
	Mo-Pt	5.5 ± 1.6	5.39 ± 0.02	0.012 ± 0.003		
18.0 wt. % Pt / 4.3 wt. % Mo (1000 °C) 0.5 V vs. RHE	Mo-Pt	4.4 ± 0.3	2.74 ± 0.01	0.010 ± 0.001	-3.1 ± 1.5	44.81
	Mo-Mo	2.1 ± 0.8	4.85 ± 0.02	0.011 ± 0.005		
	Mo-Pt	6.5 ± 2.2	5.41 ± 0.02	0.012 ± 0.004		

For all three samples polarised in the mini cell, the chi plots show the region of destructive interference between 5 and 6 $Å^{-1}$ upon increasing the potential from 0.1 to 0.5 V, as was observed for the same catalysts when tested in the half cell. Looking at the parameters obtained, it can be seen that this again corresponds to a shortening of the Mo-O bond length in the first coordination shell from just above 2.0 Å to 1.72 Å (with the exception of the 18.0 wt. % Pt / 4.3 wt. % Mo catalyst where O neighbours could not be successfully fitted). Comparison of the data for the 19.3 wt. % Pt / 3.6 wt. % Mo catalysts heated to 650 and 1000 °C shows an increase in first shell Mo-Pt neighbours from 2.2 to 3.7 (at 0.1 V vs. RHE). This result is the same as seen previously, in that heating to higher temperatures is required to improve the amount of mixing and association of the Mo with the Pt as the Mo atoms tend to preferentially group together at the surface of the nanoparticles. The increased incorporation and mixing of the Mo into the particle is also inferred by the loss of Mo-Mo neighbours in the first shell for the higher heat treated sample.

EXAFS data is also shown for the 19.3 wt. % Pt / 3.6 wt. % Mo sample heated to 1000 °C as an MEA in air. The data shown is essentially identical to that for the same catalyst in the mini cell at 0.5 V vs. RHE. This shows that for the codeposited samples it is actually possible to oxidise the Mo to the same degree as the sample just in air. The fact that, for two of the catalysts at least, the Mo remains oxygenated when operating in the mini cell with a hydrogen-containing gas stream should allow for the desired promotion effect to take place when the neighbouring Pt sites are poisoned by CO. The redox behaviour remains intact as witnessed by the smaller Mo-O bond length at potentials above that where the redox peak is observed. This indicates a change in structure of the oxygenated Mo at the surface and may also correspond to the increased mobility of the surface Mo atoms; being able to move out of the surface layer to some degree. The Mo oxides at this potential should be the Mo (VI) species that are believed to play the key role in the promotional effect.

Higher numbers of metal neighbours are also observed for the same catalysts in the half cell as seen in tables 14 and 15. For instance, at 0.1 V the 18.0 wt. % Pt / 4.3 wt. % Mo catalyst (heat treated to 1000 °C) has 4.6 Mo-Pt neighbours in the mini cell compared with 6.1 neighbours in the half cell (measured at 0.05 V). Again, this could be explained by the dissolution of Mo oxide into the acid electrolyte, leading to increased

contributions from Mo inside the nanoparticle. The 19.3 wt. % Pt / 3.6 % Mo catalyst heated to 650 °C only shows an increase from 2.2 to 2.7 Mo-Pt neighbours at reducing potentials between the mini cell and half cell respectively, and a change of 2.5 to 2.3 neighbours (essentially the same within errors) when the potential is increased beyond the redox couple position. This is likely because, for the lower heat treated sample, the majority of the Mo is on the surface so when a small amount of dissolution does occur, the contribution from Mo surface atoms still outweighs that from Mo inside the nanoparticles.

EXAFS data were also collected for the same series of five PtMo catalysts at the Pt L_{III} edge when polarised to 0.1 and 0.5 V vs. RHE in the XAS mini cell operating at 80 °C with humidification and 5% H_2/N_2 fed to both the anode and cathode sides of the cell. Data were also collected for the samples as MEAs in air for comparison. The k^2 weighted EXAFS data and corresponding Fourier transforms for the 35.4 wt. % Pt / 5.3 wt. % Mo and 36.9 wt. % Pt / 5.7 wt. % Mo samples (prepared by route 2 with subsequent heat treatments to 620 and 900 °C respectively) are shown in figure 16. The structural parameters obtained can be found in table 19. The k^2 weighted EXAFS data and corresponding Fourier transforms for the 19.3 wt. % Pt / 3.6 wt. % Mo sample (heat treated to both 650 and 1000 °C) and 18.0 wt. % Pt / 4.3 wt. % Mo sample (also heat treated to 1000 °C) prepared by the codeposition route 3 are shown in figure 17, while the resulting structural parameters obtained can be found in tables 20 and 21.

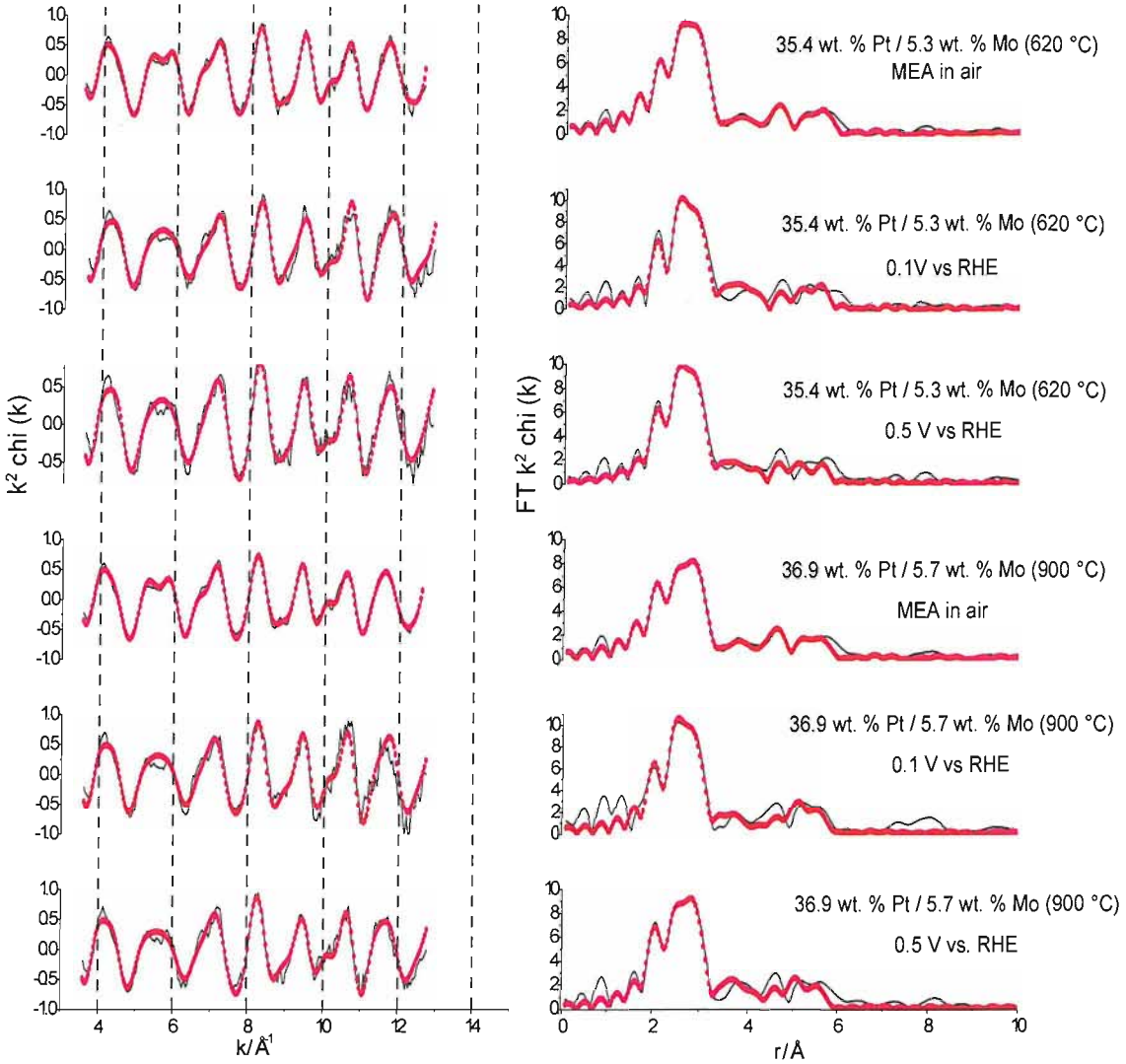

Figure 16 **Experimental data (solid lines) and fit (dots) [left] and corresponding Fourier transform [right] for a series of PtMo catalysts prepared by preparation route 2. Data obtained at the Pt L_{III} edge for catalysts either as an MEA in air or polarised in the mini cell with a 5 % H_2 in nitrogen gas mixture to both electrodes. Data is k^2-weighted and the Fourier transforms are phase corrected to Pt.**

Table 19 **Structural parameters for a series of PtMo catalysts prepared by preparation route 2. Data obtained at the Pt L_{III} edge for catalysts either as an MEA in air or polarised in the mini cell with a 5 % H_2 in nitrogen gas mixture to both electrodes. (Not all higher shells fitted are shown)**

Sample	Shell	N	R / Å	$2\sigma^2$ / Å^2	E_f / eV	R_{exafs}
35.4 wt. % Pt / 5.3 wt. % Mo MEA in air	Pt-Pt	6.7 ± 0.2	2.76 ± 0.00	0.011 ± 0.000	-13.8 ± 0.5	16.93
	Pt-O	0.5 ± 0.1	2.01 ± 0.02	0.017 ± 0.007		
	Pt-Mo	0.5 ± 0.1	2.75 ± 0.02	0.010 ± 0.003		
	Pt-Pt (MS)	6.7 ± 0.2	5.43 ± 0.01	0.008 ± 0.002		
35.4 wt. % Pt / 5.3 wt. % Mo 0.1 V vs. RHE	Pt-Pt	7.3 ± 0.4	2.74 ± 0.01	0.012 ± 0.001	-8.7 ± 0.9	29.60
	Pt-Mo	0.6 ± 0.2	2.66 ± 0.02	0.008 ± 0.004		
	Pt-Pt	2.3 ± 0.6	3.90 ± 0.01	0.007 ± 0.002		
	Pt-Pt (MS)	7.3 ± 0.4	5.39 ± 0.01	0.010 ± 0.003		
35.4 wt. % Pt / 5.3 wt. % Mo 0.5 V vs. RHE	Pt-Pt	7.5 ± 0.4	2.74 ± 0.01	0.012 ± 0.001	-11.7 ± 0.9	29.05
	Pt-Mo	0.5 ± 0.2	2.70 ± 0.03	0.012 ± 0.005		
	Pt-Pt	2.4 ± 0.7	3.90 ± 0.02	0.010 ± 0.003		
	Pt-Pt (MS)	7.5 ± 0.4	5.40 ± 0.02	0.014 ± 0.003		
36.9 wt. % Pt / 5.7 wt. % Mo MEA in air	Pt-Pt	6.4 ± 0.2	2.76 ± 0.00	0.011 ± 0.000	-13.6 ± 0.4	14.46
	Pt-O	0.4 ± 0.1	2.02 ± 0.02	0.016 ± 0.006		
	Pt-Mo	0.8 ± 0.1	2.74 ± 0.01	0.009 ± 0.001		
	Pt-Pt	2.4 ± 0.4	3.88 ± 0.01	0.015 ± 0.002		
	Pt-Pt (MS)	6.4 ± 0.2	5.42 ± 0.01	0.009 ± 0.001		
36.9 wt. % Pt / 5.7 wt. % Mo 0.1 V vs. RHE	Pt-Pt	7.3 ± 0.4	2.75 ± 0.01	0.011 ± 0.001	-9.8 ± 1.1	35.49
	Pt-Mo	0.7 ± 0.3	2.69 ± 0.03	0.012 ± 0.005		
	Pt-Pt	1.9 ± 1.0	3.89 ± 0.03	0.011 ± 0.006		
	Pt-Pt (MS)	7.3 ± 0.4	5.39 ± 0.02	0.009 ± 0.003		
36.9 wt. % Pt / 5.7 wt. % Mo 0.5 V vs. RHE	Pt-Pt	7.2 ± 0.3	2.75 ± 0.01	0.011 ± 0.001	-10.5 ± 0.8	28.32
	Pt-Mo	1.0 ± 0.2	2.72 ± 0.01	0.012 ± 0.003		
	Pt-Pt	2.8 ± 0.7	3.90 ± 0.01	0.010 ± 0.003		
	Pt-Pt (MS)	7.2 ± 0.3	5.39 ± 0.01	0.011 ± 0.002		

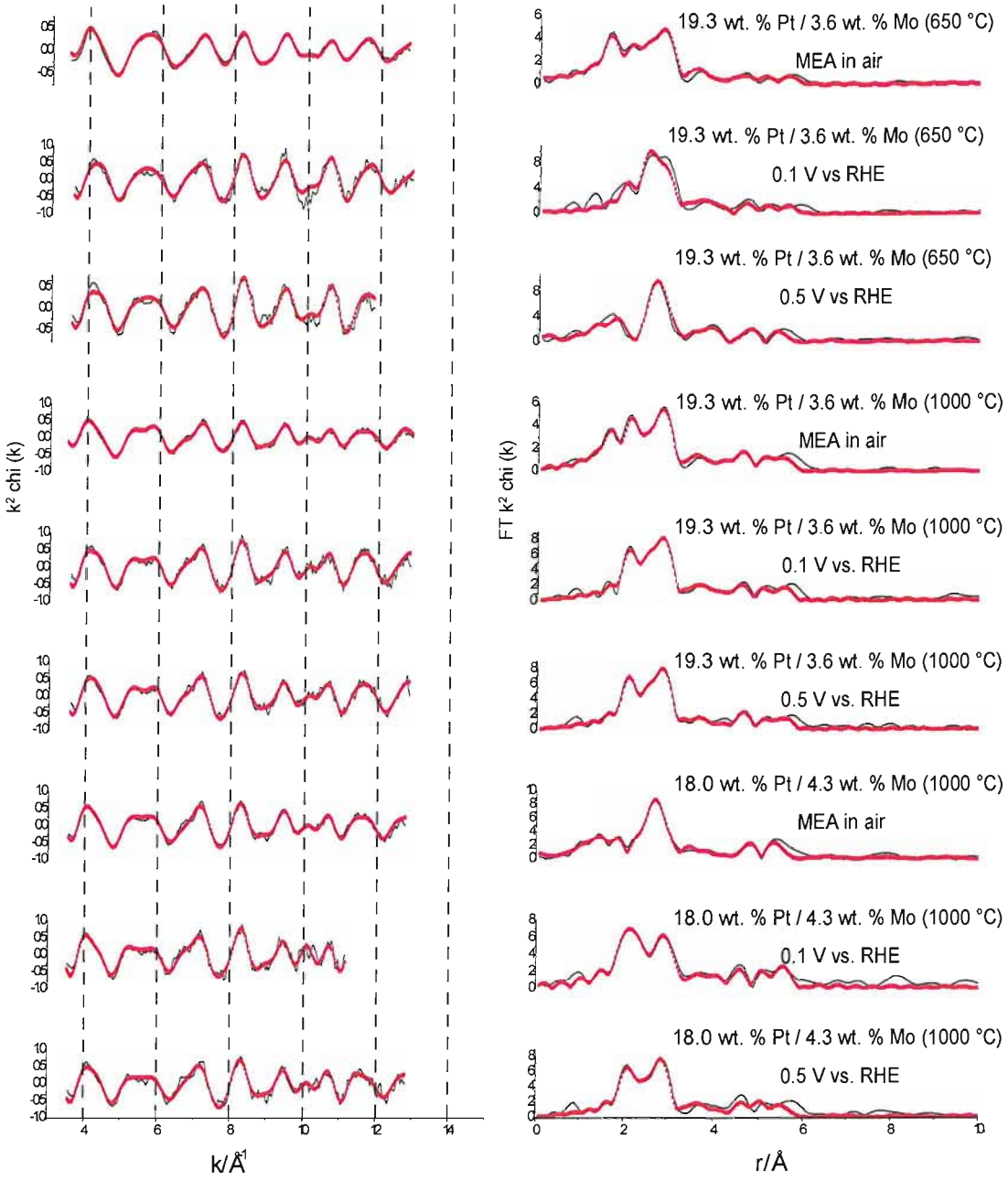

Figure 17 **Experimental data (solid lines) and fit (dots) [left] and corresponding Fourier transform [right] for a series of PtMo catalysts prepared by preparation route 3. Data obtained at the Pt L_{III} edge for catalysts either as an MEA in air or polarised in the mini cell with a 5 % H_2 in nitrogen gas mixture to both electrodes. Data is k^2-weighted and the Fourier transforms are phase corrected to Pt.**

Table 20 **Structural parameters for the 19.3 wt. % Pt / 3.6 wt. % Mo catalysts prepared by preparation route 3 and heated to either 650 or 1000 °C. Data obtained at the Pt L_{III} edge for catalysts either as an MEA in air or polarised in the mini cell with a 5 % H_2 in nitrogen gas mixture to both electrodes. (Not all higher shells fitted are shown)**

Sample	Shell	N	R / Å	$2\sigma^2$ / Å^2	E_f / eV	R_{exafs}
19.3 wt. % Pt / 3.6 wt. % Mo (650 °C) MEA in air	Pt-Pt	3.7 ± 0.2	2.76 ± 0.01	0.013 ± 0.001	-11.9 ± 0.7	18.18
	Pt-O	0.9 ± 0.1	2.00 ± 0.01	0.009 ± 0.002		
	Pt-Mo	0.8 ± 0.1	2.77 ± 0.02	0.016 ± 0.003		
	Pt-Pt	1.7 ± 0.3	3.89 ± 0.01	0.012 ± 0.002		
	Pt-Pt (MS)	3.7 ± 0.2	5.42 ± 0.02	0.015 ± 0.002		
19.3 wt. % Pt / 3.6 wt. % Mo (650 °C) 0.1 V vs. RHE	Pt-Pt	7.8 ± 0.5	2.74 ± 0.01	0.015 ± 0.001	-9.3 ± 1.0	32.87
	Pt-Mo	0.4 ± 0.2	2.62 ± 0.03	0.010 ± 0.006		
	Pt-Pt	2.0 ± 0.6	3.88 ± 0.02	0.008 ± 0.003		
	Pt-Pt (MS)	7.8 ± 0.5	5.39 ± 0.02	0.017 ± 0.005		
19.3 wt. % Pt / 3.6 wt. % Mo (650 °C) 0.5 V vs. RHE	Pt-Pt	6.2 ± 0.5	2.74 ± 0.01	0.013 ± 0.001	-10.4 ± 1.2	30.79
	Pt-Mo	0.7 ± 0.4	2.75 ± 0.05	0.017 ± 0.007		
	Pt-Pt	2.2 ± 0.6	3.89 ± 0.01	0.009 ± 0.004		
	Pt-Pt (MS)	6.2 ± 0.5	5.38 ± 0.03	0.017 ± 0.004		
19.3 wt. % Pt / 3.6 wt. % Mo (1000 °C) MEA in air	Pt-Pt	4.3 ± 0.2	2.76 ± 0.00	0.013 ± 0.001	-14.2 ± 0.5	19.59
	Pt-O	0.7 ± 0.1	2.01 ± 0.01	0.011 ± 0.002		
	Pt-Mo	1.2 ± 0.1	2.77 ± 0.01	0.014 ± 0.001		
	Pt-Pt	2.0 ± 0.3	3.87 ± 0.01	0.012 ± 0.002		
	Pt-Pt (MS)	4.3 ± 0.2	5.41 ± 0.01	0.011 ± 0.002		
19.3 wt. % Pt / 3.6 wt. % Mo (1000 °C) 0.1 V vs. RHE	Pt-Pt	6.6 ± 0.3	2.75 ± 0.01	0.012 ± 0.001	-9.9 ± 0.8	28.50
	Pt-Mo	1.2 ± 0.2	2.74 ± 0.01	0.011 ± 0.002		
	Pt-Pt	2.4 ± 0.6	3.87 ± 0.01	0.011 ± 0.003		
	Pt-Pt (MS)	6.6 ± 0.3	5.39 ± 0.02	0.012 ± 0.003		
19.3 wt. % Pt / 3.6 wt. % Mo (1000 °C) 0.5 V vs. RHE	Pt-Pt	6.8 ± 0.3	2.75 ± 0.01	0.012 ± 0.001	-9.7 ± 0.7	25.91
	Pt-Mo	1.3 ± 0.2	2.73 ± 0.01	0.011 ± 0.002		
	Pt-Pt	1.9 ± 0.6	3.87 ± 0.02	0.012 ± 0.004		
	Pt-Pt (MS)	6.8 ± 0.3	5.38 ± 0.01	0.013 ± 0.003		

Table 21 **Structural parameters for the 18.0 wt. % Pt / 4.3 wt. % Mo catalysts prepared by preparation route 3. Data obtained at the Pt L_{III} edge for catalysts either as an MEA in air or polarised in the mini cell with a 5 % H_2 in nitrogen gas mixture to both electrodes. (Not all higher shells fitted are shown)**

Sample	Shell	N	R / Å	$2\sigma^2$ / Å^2	E_f / eV	R_{exafs}
18.0 wt. % Pt / 4.3 wt. % Mo (1000 °C) MEA in air	Pt-Pt	6.0 ± 0.3	2.76 ± 0.00	0.013 ± 0.001	-11.1 ± 0.5	23.04
	Pt-O	0.4 ± 0.1	2.02 ± 0.02	0.010 ± 0.007		
	Pt-Mo	1.7 ± 0.2	2.76 ± 0.01	0.013 ± 0.001		
	Pt-Pt	2.1 ± 0.4	3.89 ± 0.01	0.012 ± 0.003		
	Pt-Pt (MS)	6.0 ± 0.3	5.38 ± 0.01	0.011 ± 0.002		
18.0 wt. % Pt / 4.3 wt. % Mo (1000 °C) 0.1 V vs. RHE	Pt-Pt	6.0 ± 0.4	2.78 ± 0.01	0.011 ± 0.001	-12.7 ± 0.8	31.33
	Pt-Mo	2.1 ± 0.3	2.76 ± 0.01	0.010 ± 0.002		
	Pt-Pt	2.9 ± 0.8	3.87 ± 0.02	0.011 ± 0.004		
	Pt-Pt	10.2 ± 2.0	5.37 ± 0.01	0.012 ± 0.003		
18.0 wt. % Pt / 4.3 wt. % Mo (1000 °C) 0.5 V vs. RHE	Pt-Pt	6.1 ± 0.3	2.75 ± 0.01	0.012 ± 0.001	-10.4 ± 0.8	32.95
	Pt-Mo	1.6 ± 0.2	2.75 ± 0.01	0.012 ± 0.002		
	Pt-Pt	2.2 ± 0.6	3.88 ± 0.02	0.011 ± 0.003		
	Pt-Pt (MS)	6.1 ± 0.3	5.37 ± 0.02	0.011 ± 0.003		

The data for all five of the samples confirms that the Pt component of the catalyst is completely reduced upon exposure to the hydrogen-containing fuel stream when polarised to potentials below that for oxide formation and stripping as seen with cyclic voltammetry in flooded cell conditions using an acid electrolyte. This is evidenced by the drop in first shell oxygen neighbours from between 0.4 and 0.9 to 0 and accompanied in all instances (apart from the 18.0 wt. % Pt / 4.3 wt. % Mo catalyst) by an increase in first shell Pt neighbours. For the route 2 catalysts, this is an average increase of 0.7 neighbours.

When comparing the parameters for the two route 2 samples in table 19, a small increase in number of first shell Mo neighbours for the sample heated to 900 °C is observed (e.g. $N_{Pt\text{-}Mo}$ increases from 0.5 to 1.0 between the samples for the data obtained at 0.5 V) indicating the increased mixing of Mo with the Pt as seen at the Mo K edge. The EXAFS data for the 36.9 wt. % Pt / 5.7 wt. % Mo catalyst can also be

compared with data from the flooded half cell as seen in table 13. The total number of first shell metal neighbours is larger when measured in the mini cell, which indicates that the Pt is more metallic in character, with less association with the Mo than is found in flooded cell conditions. This is seen by an increase in first shell Pt neighbours, along with a drop in first shell Mo neighbours.

The parameters for the codeposited route 3 catalysts in table 20 show that, for the 19.3 wt. % Pt / 3.6 wt. % sample heated to only 650 °C, there is a much larger difference between the results for the MEA in air and in the mini cell under more realistic operating conditions. Along with the loss of all Pt-O neighbours, there is a much larger increase in first shell Pt-Pt neighbours; notably from 3.7 in air to 7.8 at 0.1 V, and 6.2 at 0.5 V. The low number of first shell Pt neighbours and the highest number of Pt-O neighbours (0.9), when in air, is likely to be due to the low heat treatment and the almost half wt. % content of Pt compared with the route 2 catalysts. High metal content catalysts are known to result in increased particle sizes and lower dispersions so less Pt is at the surface as an oxide. The same sample with the higher heat treatment of 1000 °C has a higher number of total metal neighbours when comparing the two samples in air. The increase in Pt neighbours from 3.7 to 4.3 indicates an increase in particle size, while the number of Mo neighbours goes from 0.8 to 1.2 confirming the improved mixing of Pt and Mo in the sample. This sample also shows a large increase in Pt neighbours when polarised in the mini cell, going from 4.3 in air to 6.6 at 0.1 V. No real change is observed between potentials of 0.1 V and 0.5 V.

The 18.0 wt. % Pt / 4.3 wt. % Mo catalyst is dissimilar in that, even in air, the amount of oxide the Pt seems to form is much less with 6.0 Pt-Pt neighbours and only 0.4 Pt-O neighbours. In addition, it has a much larger number of Pt-Mo neighbours (1.7). When polarised in the mini cell, with the exception of the loss of Pt-O neighbours, the number of first shell Pt-Pt neighbours remains the same. The number of first shell Mo neighbours even increases to 2.1 when the sample is reduced to 0.1 V.

The EXAFS data reported in this chapter has shown that the codeposition method for the preparation of carbon-supported PtMo catalysts results in better mixing of the Pt and Mo than the earlier routes 1 and 2. Despite the improved preparation methods and heating as high as 1000 °C, true PtMo alloys are not formed. To varying extents, the

catalysts can all be thought of as a predominantly Pt-rich core with Mo oxide decorating the surface. The effect of increasing heat treatments is to force more Mo into the bulk of the particle. The most well-mixed catalysts are found to be those prepared by the codeposition method and heated to the greater temperature. However, as a real alloy is not found to form, it is unlikely that the presence of Mo is having any significant intrinsic effect on the Pt as is found with PtRu alloys where the electronic structure is altered such that the Pt-CO bond is weakened. If this effect is not obtainable, and supported PtMo catalysts only have increased CO tolerance by virtue of the promotional effect, then it stands to reason that the surface modified PtMo catalysts should be as good, assuming that the Mo will be deposited where desired, maximising the number of neighbouring Pt and Mo sites, and that a good enough association is achieved without having to use very high heat treatments. This will keep the particle sizes down, hopefully leading to increased Pt utilisation. The catalyst characterisation for the CSR PtMo catalyst has shown that the method used can be controlled quite accurately with the deposition of close to half a monolayer as desired. The EXAFS data for this catalyst in the half cell has shown that the Mo is mostly present as a surface oxide, but that a small amount of association with the Pt does occur under electrochemical reduction.

The inability of the Mo to alloy with the Pt in these supported catalysts is an unusual observation when looked at in relation to the calculations performed by Nørskov *et al* [37], who used DFT calculations to deduce segregation energies for alloying Pt with many other metals. The energies for Mo seemed to suggest that it would prefer to remain subsurface, whereas in reality it is always predominantly found at or near the surface. Despite the fact that alloys cannot be readily formed, it may still be beneficial to achieve very well-mixed catalysts with a significant amount of Mo within the bulk of the particle. If the amount of dissolution of Mo from the particle surface is significant, it may well be that Mo atoms in the bulk will act as a reservoir and come to the surface to replace those lost, thereby increasing the stability and overall lifetime of the catalysts.

The codeposited catalysts also show evidence of an increased ability to change the oxidation state of the Mo under operating conditions in a fuel cell, as seen by the

mobility of the surface Mo atoms when compared with the inferior early preparation routes.

3.3 Electrochemical performance testing

The results shown in this section are used to measure the performance of the series of PtMo catalysts, both for methanol oxidation in a flooded half cell, and operating in the mini cell with varying levels of CO in the anode gas stream (100 ppm and 1 % CO in H_2). The results obtained will be compared with performance loss data for some of the catalysts produced by Johnson Matthey.

3.3.1 Methanol oxidation

3.3.1.1 Low temperature methanol oxidation

Figures 18 and 19 present the anode half cell polarisation data for methanol oxidation of the PtMo catalysts and that of 20 and 40 wt. % Pt/C catalysts included for comparison, reported as mass activity and specific activity respectively. These measurements were recorded at 30 °C. The current was recorded after a maximum time interval of 30 s, which was found to be long enough for current stabilisation. Two successive polarisation curves were recorded in each instance. The data presented is the average of the two curves, as the data was found to overlay in all cases.

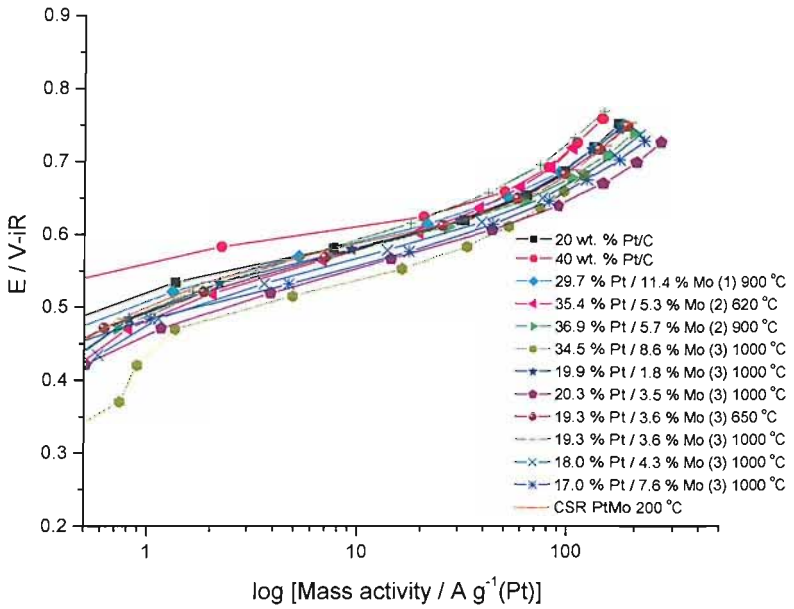

Figure 18 **Comparison of the mass activity of the PtMo catalysts and 20 and 40 wt. % Pt/C catalysts for comparison in 2 M MeOH / 1 M H_2SO_4 at 30 °C. Numbers in brackets indicate preparation route and temperature values denote subsequent heat treatments.**

Figure 18 shows a Tafel plot of the mass activities for the PtMo catalysts at 30 °C. In this plot, the data has been normalised with respect to the total mass of platinum in each catalyst. This allows the catalyst performances to be compared as a function of the platinum content. It can be seen that the 34.5 wt. % Pt / 8.6 wt. % Mo catalyst prepared by route 3 shows the best performance in the linear region (mainly seen between 0.5 and 0.6 V) as it has the highest current density at a given potential, while the catalysts prepared by routes 1 and 2 with the highest metal contents show the lowest performance; similar to or lower than that of the Pt/C control catalysts. Once mass transport effects begin to play a part (as evidenced by the tailing off of the current at potentials above 0.6 V), the 20.3 wt. % Pt / 3.5 wt. % Mo performs slightly better. The lowest performances in the linear region are for the 19.3 wt. % Pt / 3.6 wt. % Mo prepared by route 3 and heated to 1000 °C along with the 40 wt. % Pt/C catalyst. This result seems unusual in that the other route 3 catalysts are generally seen to perform better than the route 1 or 2 catalysts; while it is also seen, when comparing catalysts of similar Pt and Mo content, that the higher heat treated samples appear to outperform the lower heat treated samples; this is expected as higher heat treatments improve the

mixing of the Pt and Mo, presumably leading to an increased number of neighbouring Pt and Mo sites at the surface. This improved mixing has been confirmed by the EXAFS data reported earlier. At low potentials (below 0.5 V), the current response becomes non-linear as a result of the activation overpotential required to obtain significant current densities. However, an unusual current response is observed in this region for the 34.5 wt. % Pt / 8.6 wt. % Mo catalyst, which may be arising due to a competing reaction taken place from the presence of dissolved O_2 in the electrolyte. This may be occurring with the other catalysts to a lesser extent and, ultimately, makes a quantitative Tafel analysis by extrapolation of the linear regions problematic and so this is not attempted for this work.

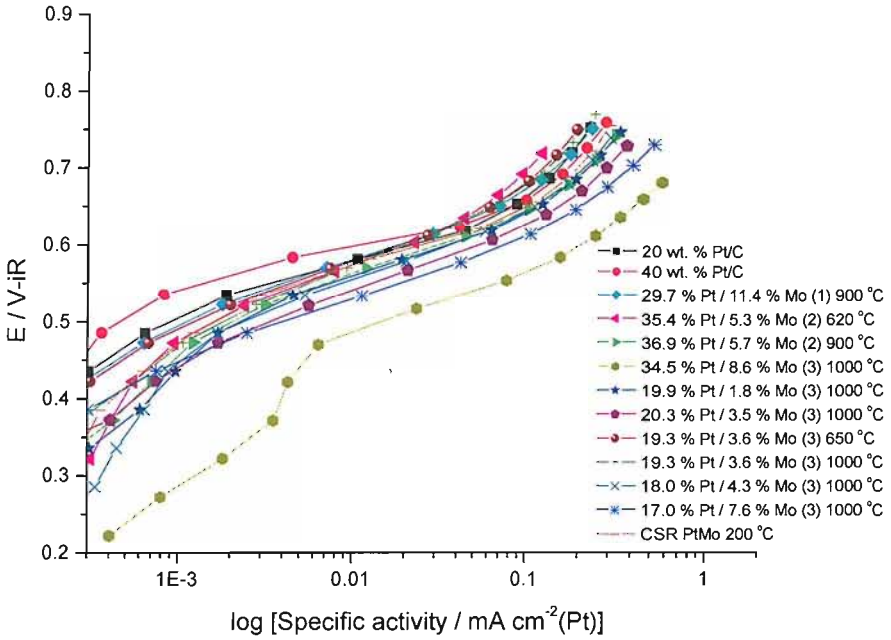

Figure 19 **Comparison of the specific activity of the PtMo catalysts and 20 and 40 wt. % Pt/C catalysts for comparison in 2 M MeOH / 1 M H_2SO_4 at 30 °C. Numbers in brackets indicate preparation route and temperature values denote subsequent heat treatments.**

Figure 19 shows the same data plotted as potential versus specific activity. This allows the intrinsic activity of the catalysts to be compared, independent of the surface area of the catalysts. It should be noted, however, that the active catalyst area measurements used to normalise the data are derived using the principal CO stripping peak only. In the linear region, the 34.5 wt. % Pt / 8.6 wt. % Mo catalyst prepared by route 3 has the greatest performance, with the 40 wt. % Pt/C having the lowest, with a difference of

120 mV at 0.01 mA cm^{-2}(Pt). The route 1 and 2 catalysts again show the lowest performances compared with the codeposited route 3 samples, with the 19.3 wt. % Pt / 3.6 wt. % Mo heated to 1000 °C showing the lowest performance out of the route 3 catalysts; especially once mass transport effects become significant.

3.3.1.2 High temperature methanol oxidation

Figures 20 and 21 present the anode half cell polarisation data for methanol oxidation for the series of PtMo and that of 20 and 40 wt. % catalysts for comparison. Results are presented as mass activity and specific activity respectively. These measurements were recorded at 80 °C. Two successive polarisation curves were recorded in each instance. The data presented is the average of the two curves, as the data was found to overlay in all cases. Measurements were recorded at 80 °C because satisfactory performances can only be achieved at such temperatures due to the low activity for methanol oxidation on typical platinum-based electrocatalysts.

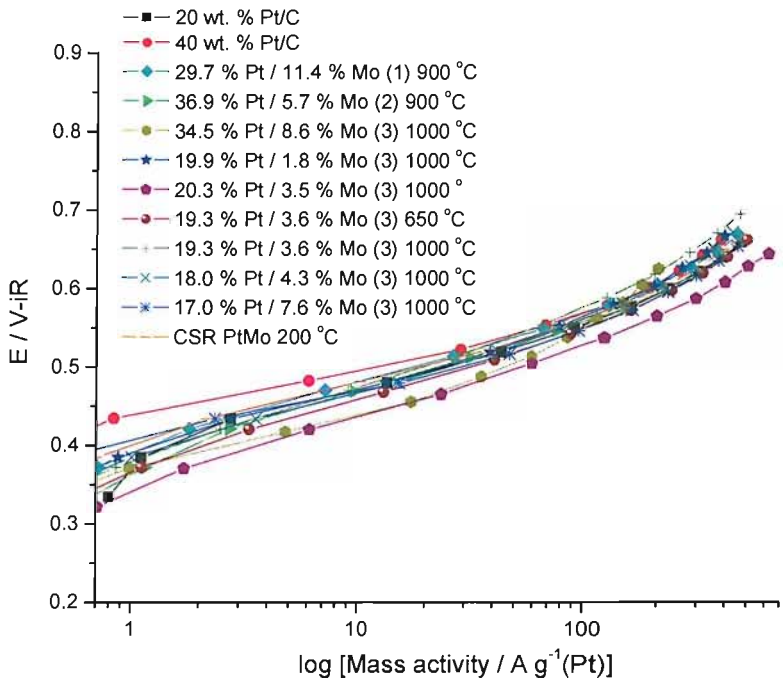

Figure 20 **Comparison of the mass activity of the PtMo catalysts and 20 and 40 wt. % Pt/C catalysts for comparison in 2 M MeOH / 1 M H_2SO_4 at 80 °C. Numbers in brackets indicate preparation route and temperature values denote subsequent heat treatments.**

Figure 20 shows a Tafel plot of the mass activities for the PtMo catalysts at 80 °C. All catalysts show an increase in performance compared with the results obtained at 30 °C as expected, confirming the unsuitability of operating such fuel cells systems at temperatures less than 80 °C. The performances are all grouped reasonably close together, with the majority of the route 3 catalysts again proving to be better for methanol oxidation than those samples prepared by the earlier routes. The 34.5 wt. % Pt / 8.6 wt. % Mo route 3 catalyst is one of the higher performing catalysts in the linear region, although mass transport effects appear to become more pronounced than for some of the other samples after 50 A g^{-1}(Pt), resulting in a significant drop in performance.

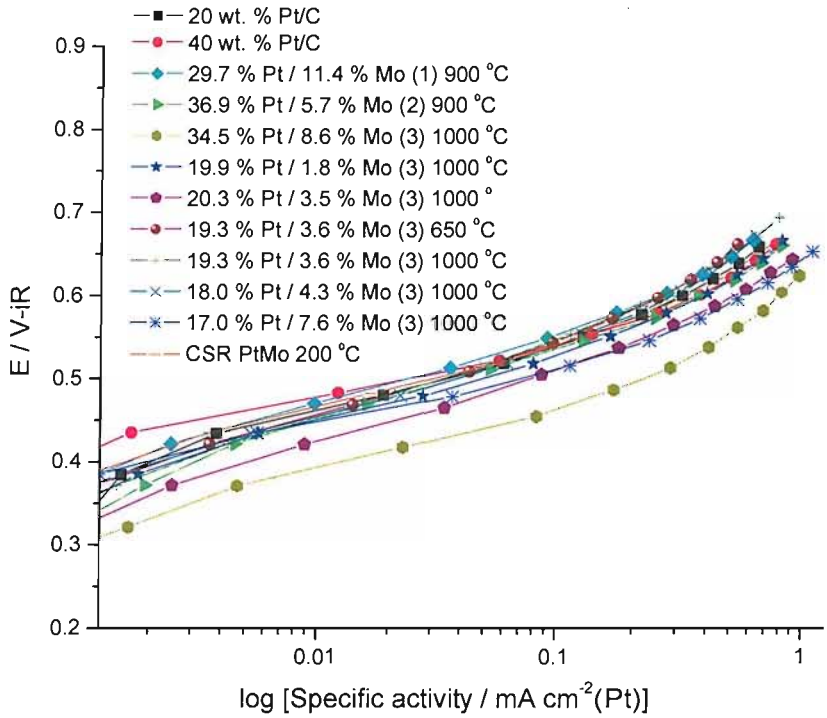

Figure 21 **Comparison of the specific activity of the PtMo catalysts and 20 and 40 wt. % Pt/C catalysts for comparison in 2 M MeOH / 1 M H_2SO_4 at 80 °C. Numbers in brackets indicate preparation route and temperature values denote subsequent heat treatments.**

Figure 21 shows the same data plotted as potential versus specific activity. This also shows much increased performances compared to the measurements recorded at 30 °C. For instance, the 20.3 wt. % Pt / 3.5 wt. % Mo codeposited catalyst, at 0.55 V vs. RHE, the specific activity has increased from 0.013 to 0.237 mA cm^{-2}. The 34.5 wt. % Pt / 8.6 wt. % Mo catalyst again demonstrates the highest performance; this arises due to

the low mass normalised Pt area obtained during the cyclic voltammetry experiments reported in section 3.1.1. Overall, the majority of the catalysts show some enhancement of the methanol oxidation reaction compared with the Pt/C reference compounds, although the effect is relatively small. It is unlikely that any of the catalysts reported here would be good enough for real DMFC applications.

3.3.2 Electrochemical mini cell testing

Figure 22 displays the polarisation data for a series of the PtMo catalysts obtained in an *in situ* single cell using pure hydrogen gas as the anode fuel. Gas flow rates were selected to ensure that there is no fuel deficit. The anode gas flow gave a fuel stoichiometry of 1.6 (based on the maximum mass activity of 5 A mg^{-1} (Pt)), while the cathode was operated at even greater stoichiometry in order to minimise flooding by removal of liquid water by evaporation and advection. The data was collected using the cathode connected as the working electrode and the anode as a combined counter/ reference electrode. The measured potential is actually the overall cell potential, however, as it includes any potential losses associated with the hydrogen oxidation reaction occurring at the anode. The cathode catalyst and oxygen fuel stream were the same in all instances, so any change in performance is the direct result of changing the anode catalyst and/or fuel stream. The data has been plotted as the logarithm of the mass activity.

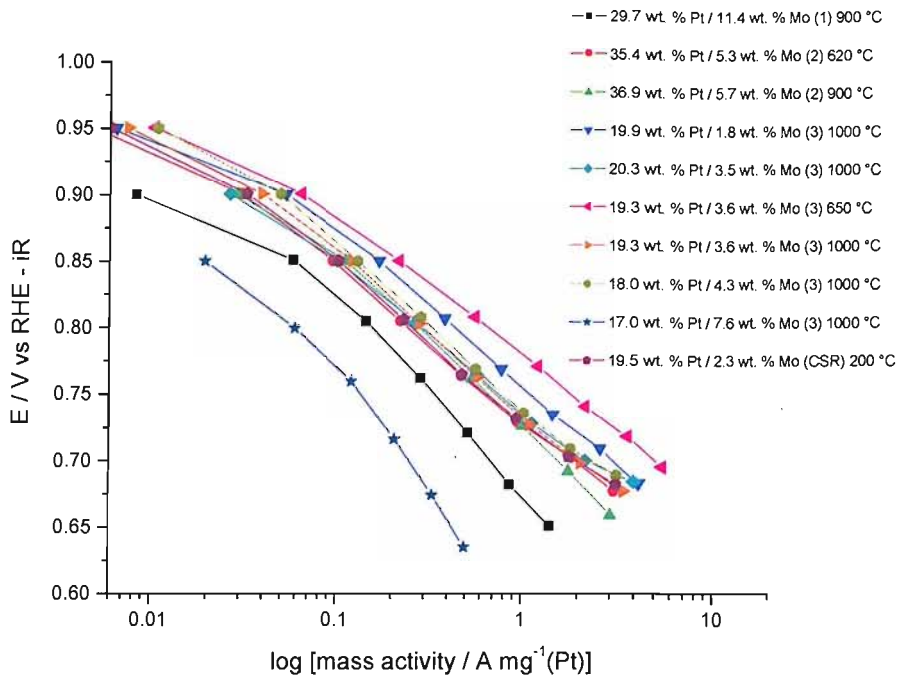

Figure 22 **Mass activity plots for single cell polarisation data in an *in-situ* mini PEM fuel cell for a series of PtMo anode catalysts as part of Flemion® bonded MEAs. Cathode catalyst is 60 wt. % Pt/Ketjen. Oxygen flowed to cathode (60 cm^3 min^{-1}) and hydrogen flowed to anode (40 cm^3 min^{-1}). Cell temperature of 80 °C. Currents normalised by the Pt loading at the anode and the magnitude of these currents plotted logarithmically.**

The highest performing catalyst is the 19.3 wt. % Pt / 3.6 wt. % Mo route 3 catalyst heated to only 650 °C. Of the catalysts tested this has the highest mass normalised Pt area value (92 m^2 Pt g^{-1} Pt), which correlates with having the smallest particle size of 1.8 nm obtained by XRD. The second highest performing catalyst is the 19.9 wt. % Pt/ 1.8 wt. % Mo catalyst route 3 catalyst heated to 1000 °C. This catalyst has the lowest content of Mo, leading to a larger average particle size (3.7 nm) and the lowest mass normalised Pt area (48 m^2 Pt g^{-1} Pt). The low level of Mo present means that there should be less surface Mo oxides on the particle surfaces than for many of the other catalysts. If increasing Mo oxides being present inhibit catalyst utilisation to some extent, then the effect should be weakest for this catalyst, which may explain the good performance. The weakest performing catalysts are the 29.7 wt. % Pt / 11.4 wt. % Mo route 2 catalyst and the 17.0 wt. % Pt / 7.6 wt. % Mo catalysts. This may be due to the increased amount of Mo oxides present on the surface which could be inhibiting

catalyst utilisation at the higher current densities. The performances of the remaining catalysts are very similar to each other.

Figure 23 shows the same data plotted as a function of specific activity. The currents were normalised by the electrochemically active Pt area at the anode calculated from the principal CO stripping peak of a cyclic voltammogram recorded beforehand and the magnitude of these currents plotted logarithmically.

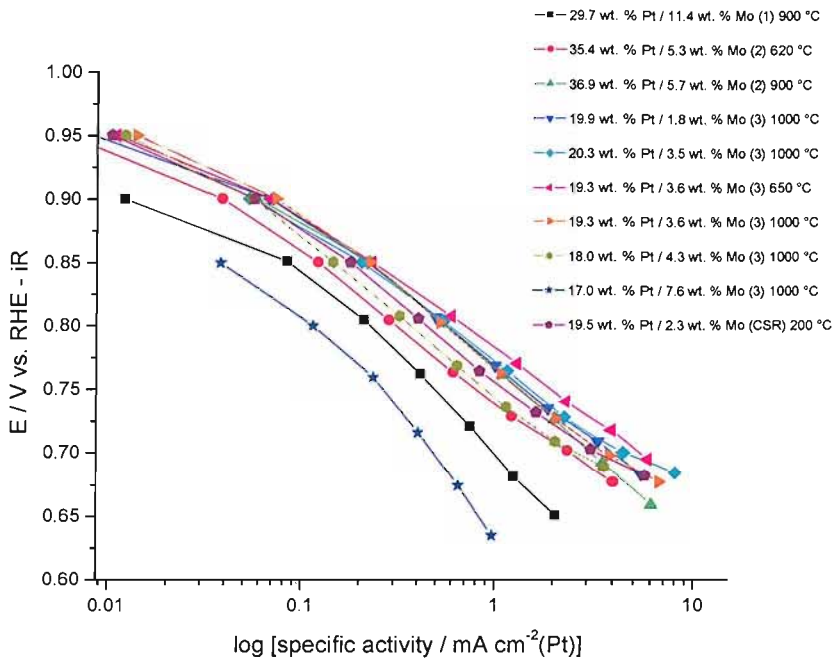

Figure 23 **Specific activity plots for single cell polarisation data in an *in-situ* mini PEM fuel cell for a series of PtMo anode catalysts as part of Flemion® bonded MEAs. Cathode catalyst is 60 wt. % Pt/Ketjen. Oxygen flowed to cathode (60 cm^3 min^{-1}) and hydrogen flowed to anode (40 cm^3 min^{-1}). Cell temperature of 80 °C. Currents normalised by the electrochemically active Pt area at the anode calculated from the principal CO stripping peak of a cyclic voltammogram recorded beforehand and the magnitude of these currents plotted logarithmically.**

The ordering in performance essentially remains unchanged when looking at the specific activity plot. Differences between the two can be used to highlight economic advantages of certain catalysts, in terms of lowering the Pt content, while maintaining performance. For instance, a sample that has been heated to a higher temperature may possess a larger particle size reducing the available surface area. Therefore, the performance would be noticeably worse in the mass activity plot compared with the specific activity plot.

Single cell polarisation data was also observed for the same series of PtMo catalyst using (i) 100 ppm CO in H_2 and (ii) 1 % CO in H_2 gas mixtures to the anode. Table 22 shows how the mass activities obtained at 0.8 V differ for the anode catalysts with the three different gas mixtures.

Table 22 Mass activities for the series of PtMo catalysts obtained at 0.8 V vs. RHE with different fuel streams to the anode

Catalyst	(Route) Heat treatment	Mass activity / A mg^{-1}(Pt) at 0.8 V vs. RHE		
		H_2 to anode	100 ppm CO in H_2 to anode	1% CO in H_2 to anode
29.7 wt. % Pt / 11.4 wt. % Mo	(1) 900 °C	0.157	0.103	0.043
35.4 wt. % Pt / 5.3 wt. % Mo	(2) 620 °C	0.244	0.190	0.043
36.9 wt. % Pt / 5.7 wt. % Mo	(2) 900 °C	0.282	0.142	0.001
19.9 wt. % Pt / 1.8 wt. % Mo	(3) 1000 °C	0.439	0.107	0.010
20.3 wt. % Pt / 3.5 wt. % Mo	(3) 1000 °C	0.292	0.173	-
19.3 wt. % Pt / 3.6 wt. % Mo	(3) 650 °C	0.664	0.208	0.012
19.3 wt. % Pt / 3.6 wt. % Mo	(3) 1000 °C	0.330	0.131	0.042
18.0 wt. % Pt / 4.3 wt. % Mo	(3) 1000 °C	0.331	0.195	0.015
17.0 wt. % Pt / 7.6 wt. % Mo	(3) 1000 °C	0.060	0.036	0.018
CSR PtMo ½ monolayer.	(CSR) 200 °C	0.259	0.180	0.009

It can be seen that the presence of CO in the anode fuel stream causes a decrease in performance for all of the catalyst samples. The lowest performing sample with both pure H_2 and 100 ppm CO in H_2 is the 17.0 wt. % Pt / 7.6 wt. % sample, which also has the highest ratio of Mo to Pt. The 29.7 wt. % Pt / 11.4 wt. % Mo sample has the second highest ratio and is the second worse performing sample with pure H_2 and 100 ppm CO in H_2. This seems to suggest that increasing Mo at the surface will inhibit catalyst utilisation to some extent. The highest performing catalyst is the 19.3 wt. % Pt / 3.6 wt. % Mo sample prepared by route 3 and heated to only 650 °C. This is because, for the same amount of Pt present, this sample has the largest Pt surface area because of

the smallest particle size. The second highest performing catalyst with pure H_2 is the 19.9 wt. % Pt / 1.8 wt. % Mo. Even though this catalyst has the largest particle size out of the route 3 catalysts heated to 1000 °C, the small amount of Mo at the surface means that minimal inhibition of the catalyst utilisation is occurring. When the fuel stream is switched to 100 ppm CO in H_2, this catalyst shows a significant drop in mass activity leading to it having the lowest performance. It is clear, therefore, that a minimum level of Mo is required to enhance the performance, but that a close to 1: 1 Pt: Mo atomic ratio is too high. Out of the route 3 codeposited samples heated to 1000 °C, the 18.0 wt. % Pt / 4.3 wt. % Mo sample (with a 2: 1 atomic ratio) has the highest performance with 100 ppm CO in H_2 after the 650 °C catalyst. The CSR PtMo catalyst has one of the lowest performances in a pure H_2 fuel stream, but comes mid-range for the 100 ppm CO reformate gas, even though with half a monolayer of Mo present, the expected surface ratio of Pt: Mo should be close to 1: 1. As EXAFS results have shown for all of the catalysts supplied by Johnson Matthey, completely well-mixed samples have not been achieved, with the ratio of Mo to Pt at the surface being uniformly higher than in the bulk. Therefore, while the 17.0 wt. % Pt / 7.6 wt. % Mo sample has an expected Pt: Mo ratio of 1: 1 if well-mixed, the ratio at the surface is likely weighted even more in favour of the Mo, explaining the diminished performances. Finally, it can be observed that with a 1 % CO in H_2 gas mixture to the anode, the catalysts are all essentially poisoned; as seen by the drop in mass activities at 0.8 V vs. RHE to below 0.05 A mg^{-1}(Pt).

Figures 24 and 25 show the mass activity and specific activity plots respectively for the series of PtMo samples in an *in situ* single cell with a 100 ppm CO in H_2 gas mixture. The mass activity plot shows how the results for the majority of the catalyst are quite close in the linear region occurring between around 0.95 and 0.90 V (with the exception of the 17.0 wt. % Pt / 7.6 wt. % Mo route 3 catalyst and the two 900 °C route 1 and 2 catalysts). Below 0.90 V, the effects of mass transport limitations become more apparent. This is most noticeable for the CSR sample and the 19.9 wt. % Pt / 1.8 wt. % Mo sample; presumably as these two catalysts have the largest particle sizes.

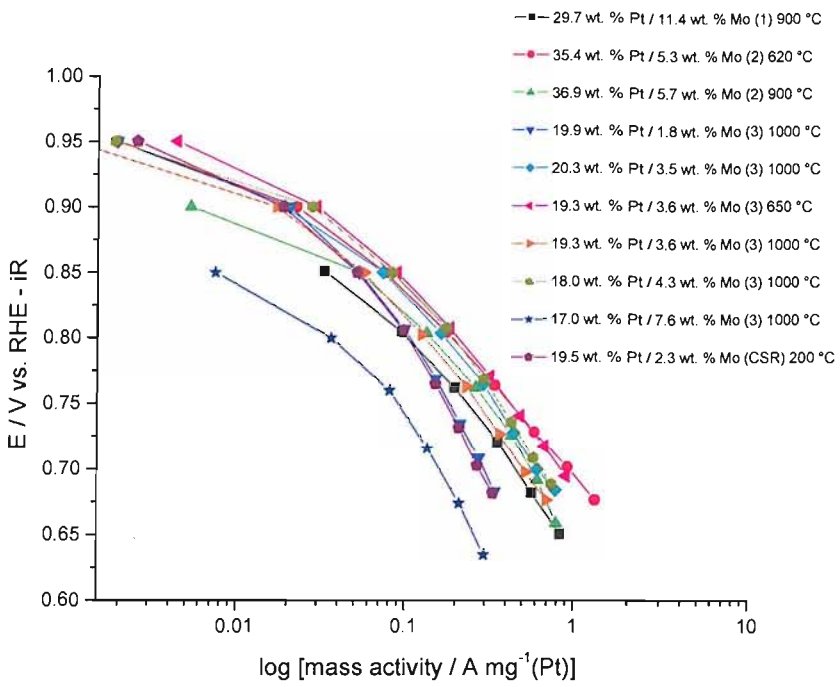

Figure 24 **Mass activity plots for single cell polarisation data in an *in-situ* mini PEM fuel cell for a series of PtMo anode catalysts as part of Flemion® bonded MEAs. Cathode catalyst is 60 wt. % Pt/Ketjen. Oxygen flowed to cathode (60 cm^3 min^{-1}) and a 100 ppm CO in hydrogen gas mixture flowed to anode (40 cm^3 min^{-1}). Cell temperature of 80 °C. Currents normalised by the Pt loading at the anode and the magnitude of these currents plotted logarithmically.**

The specific activity plot seen in figure 25 again shows no large differences in order of performance.

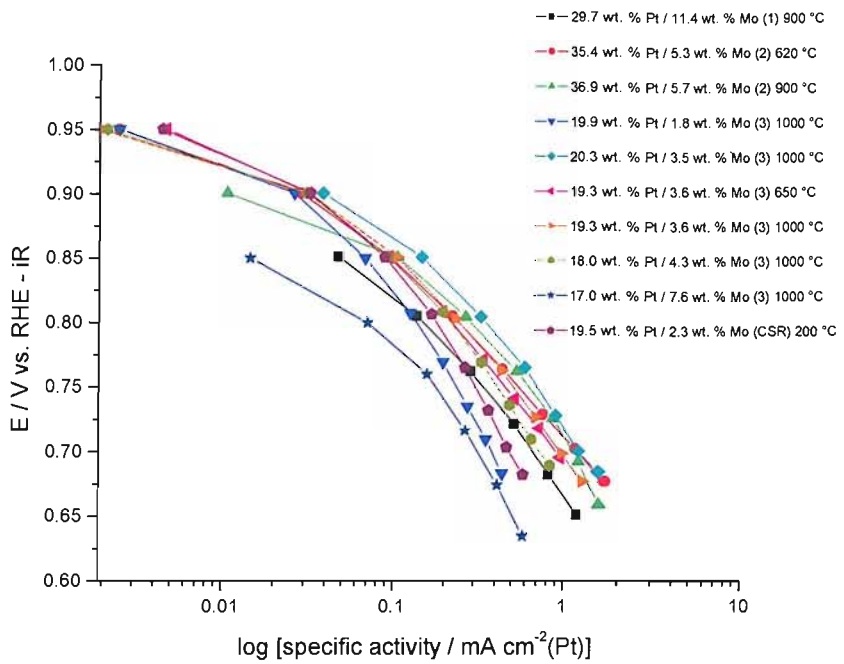

Figure 25 **Specific activity plots for single cell polarisation data in an *in-situ* mini PEM fuel cell for a series of PtMo anode catalysts as part of Flemion® bonded MEAs. Cathode catalyst is 60 wt. % Pt/Ketjen. Oxygen flowed to cathode (60 cm^3 min^{-1}) and a 100 ppm CO in hydrogen gas mixture flowed to anode (40 cm^3 min^{-1}). Cell temperature of 80 °C. Currents normalised by the electrochemically active Pt area at the anode calculated from the principal CO stripping peak of a cyclic voltammogram recorded beforehand and the magnitude of these currents plotted logarithmically.**

Figures 26 and 27 show the mass activity and specific activity plots respectively for the series of PtMo samples in an *in situ* single cell with a 1 % CO in H_2 gas mixture. The performance data shows that, at this level of CO concentration, all of the PtMo samples are poisoned and unable to achieve usable current densities.

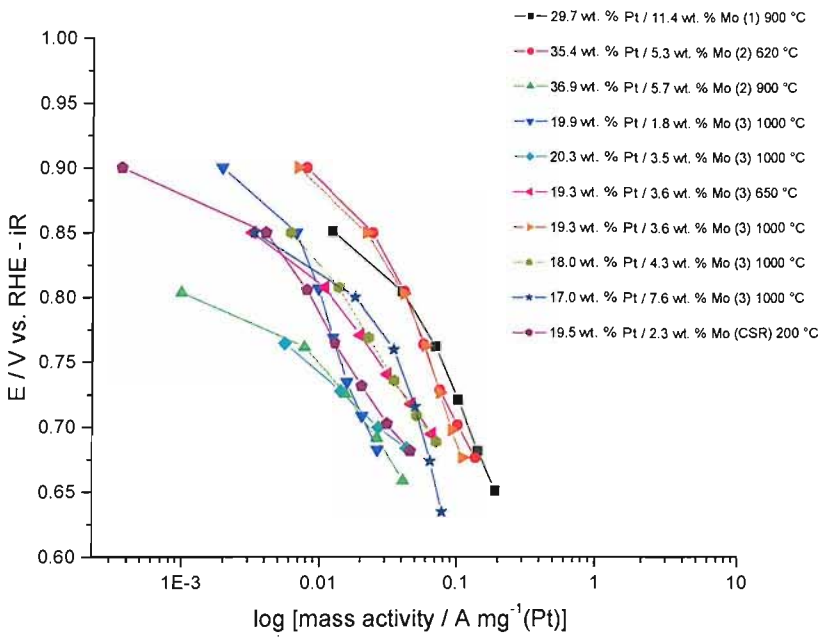

Figure 26 **Mass activity plots for single cell polarisation data in an *in-situ* mini PEM fuel cell for a series of PtMo anode catalysts as part of Flemion® bonded MEAs. Cathode catalyst is 60 wt. % Pt/Ketjen. Oxygen flowed to cathode (60 cm^3 min^{-1}) and a 1 % CO in hydrogen gas mixture flowed to anode (40 cm^3 min^{-1}). Cell temperature of 80 °C. Currents normalised by the Pt loading at the anode and the magnitude of these currents plotted logarithmically.**

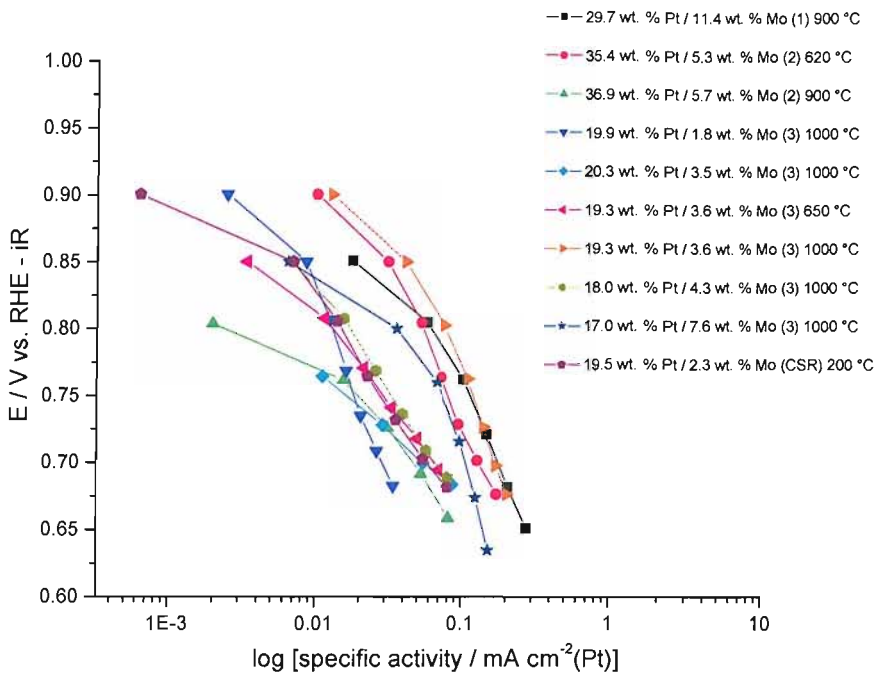

Figure 27 **Specific activity plots for single cell polarisation data in an *in-situ* mini PEM fuel cell for a series of PtMo anode catalysts as part of Flemion® bonded MEAs. Cathode catalyst is 60 wt. % Pt/Ketjen. Oxygen flowed to cathode (60 cm^3 min^{-1}) and a 1 % CO in hydrogen gas mixture flowed to anode (40 cm^3 min^{-1}). Cell temperature of 80 °C. Currents normalised by the electrochemically active Pt area at the anode calculated from the principal CO stripping peak of a cyclic voltammogram recorded beforehand and the magnitude of these currents plotted logarithmically.**

It can be seen that for PEMFCs using typical reformate gas streams containing close to 100 ppm CO in H_2 (after the levels have been reduced from closer to 1-2 % CO using a water gas shift reactor) performance levels can be increased by the presence of Mo, as seen by the improvements in performance of all the samples compared with the very low Mo content of the 19.9 wt. % Pt / 1.8 wt. % Mo catalysts.

For CO levels close to 100 ppm, it has been reported that PtMo catalysts can outperform conventional PtRu catalysts [1,9]. However, the CO_2 tolerance of PtMo catalysts falls short of that found for PtRu [1] for reformate containing close to 25 % CO_2. Reasons for this may include the fact that PtRu forms well-mixed alloys leading to an intrinsic change in the electronic structure such that the adsorption of CO_2 on Pt is weakened, whereas PtMo has more unmodified Pt sites. In addition, PtMo is found to

have an increased ability to promote the electroreduction of CO_2 to CO. Testing of CO_2 tolerance on these catalysts by Johnson Matthey found that the 20.3 wt. % Pt / 3.5 wt. % Mo and 18.0 wt. % Pt / 4.3 wt. % Mo catalysts prepared by route 3 show the lowest performance losses with 25 % CO_2, and that an optimum Pt: Mo ratio exists in the same way as for the CO tolerance. However the optimum ratio for CO_2 tolerance is closer to 3: 1, while for CO tolerance it is closer to 2: 1. For combined CO and CO_2 tolerance, the 3: 1 PtMo has the edge (corresponding to the 20.3 wt. % Pt / 3.5 wt. % Mo sample).

4 Conclusions

A combination of electrochemical and XAS techniques have been carried out in order to characterise a series of carbon supported PtMo catalysts. The samples tested comprised a number of varying Pt: Mo ratios and were prepared by a variety of different methods, including the reaction of a Pt/C catalyst with a Mo oxide precursor compound and a codeposition method involving the sequential deposition of Pt oxide and Mo oxide onto the carbon support. These catalyst preparation methods were followed by thermal reduction at a range of high temperatures. A third method involved the preparation of a surface modified PtMo/C catalyst with the aim of maximising the Pt-Mo interactions at the surface for enhancing the promotional effect giving improved CO tolerance compared with Pt/C.

Cyclic voltammetry measurements of CO stripping were undertaken and showed peak shapes and positions similar to those reported in the literature for other supported PtMo catalysts. In particular, the principal CO stripping peak was shifted to lower potentials than is found on conventional Pt/C catalysts, although not to the same extent as found with supported PtRu samples. The presence of a pre-wave stripping peak occurring at potentials similar to that of the Mo redox oxidation peak on the forward cycle provides evidence of the promotional effect whereby Pt-CO sites are oxidised by neighbouring surface Mo oxide species when in the +6 oxidation state. Mass normalised Pt areas for the samples were often similar to or even exceeding those found with similar Pt/C catalysts, and showed a strong correlation with content of Mo. Increasing Mo in the

sample has been shown to reduce particle agglomeration of the catalysts, even during high temperature heat treatments, leading to increased surface area. There appears to be an optimum value however, as the highest Mo-containing samples began to show a drop in Pt area, presumably due to decreased catalyst utilisation by the presence of surface Mo species.

The combination of electrochemical and XANES analyses was able to show that the samples were not well-mixed, as evidenced by the areas of the Mo redox peaks and average Mo oxidation states. The amount of surface oxides undergoing the redox transition with potential was found to be less than expected, indicating either a greater proportion of Mo in the bulk of the samples than at the surface, or islands of Mo on the surface of the nanoparticles where the Mo atoms within these clusters are unable to be fully oxidised. Neither technique was able to establish whether the surface Mo atoms undergo a IV/VI or a V/VI redox transition with any certainty; however, the average Mo oxidation states for the surface modified PtMo/C sample, where all the Mo is present on the surface, indicates that the IV/VI transition is more likely. Structural information obtained from corresponding EXAFS data was able to show that the samples were not well-mixed, and indicated that more Mo is likely to be found on the surface than within the bulk of the particles supporting the Mo surface cluster argument. The structural information obtained from these techniques was used to show considerable differences occurring as a result of the different catalyst preparation methods. The codeposited catalysts, regardless of heat treatment, were shown to possess a greater degree of mixing between the Pt and Mo in the sample, than for those prepared by the method involving addition of Mo oxide to a preformed Pt/C catalyst. Increased temperature of subsequent heat treatments was found to force more Mo into the bulk of the catalyst from the surface, albeit to varying degrees. It was shown that no true PtMo alloy was formed however, which would appear to limit supported PtMo catalysts to offering improved CO tolerance by the promotional effect only, and that no intrinsic effect is possible, unlike PtRu. The surface modified PtMo sample was shown to be present predominantly as a surface oxide; however this was seen to be reduced by lowering the potential, leading to increased association with the surface Pt atoms. The technique used to prepare this catalyst was found to offer better control of the Mo deposition than observed previously.

In situ XAS data were obtained for some of the samples in a modified single (or mini) cell utilising humidified gases and an operational temperature of 80 °C, representing the first time such data has been collected for supported PtMo catalysts. The results were compared with half cell studies using a 1 M H_2SO_4 electrolyte. It was found that the catalysts had a lower number of Mo-Pt neighbours when in the mini cell, which was evidence of increased Mo dissolution from the surface in the presence of the aqueous electrolyte found in the half cell. It was also observed that the catalysts prepared using the earlier route 1 and 2 methods could only be sufficiently oxidised in air, while the environments found in both the half cell and the mini cell, induced a permanent reduced state that could not be significantly altered with potential. The codeposited catalysts were found to be more easily oxidised, even in the mini cell, with the environment at 0.5 V found to be similar to that found for the samples in air. These catalysts should therefore possess enhanced promotional abilities, due to the improved mixing at the surface maximising the number of Pt-Mo neighbouring sites, and their increased ability to be oxidised more fully in single cell conditions. This is likely to be connected to the increased mobility of Mo in these codeposited samples, which appears to allow the surface Mo atoms to move into and out of the surface layer, occurring with changes in potential, as shown by the EXAFS data.

Methanol oxidation half cell testing of these catalysts showed some small enhancement when compared with Pt/C, with the biggest improvements found for the codeposited samples. Performance data obtained for the samples as anode catalysts within a single cell operating with pure (i) H_2/O_2, (ii), 100 ppm CO in H_2/O_2 and (iii) 1 % CO in H_2 fuel streams again showed some improvements, with an optimum ratio of 2:1 Pt: Mo giving the best results.

5 References

1. Ralph, T. R.; Hogarth, M. P. *Platinum metals Rev.* **2002**, *46*, 117.
2. Carrette, L.; Friedrich, K. A.; Stimming, U. *Chemphyschem* **2000**, *1*, 162.
3. Watanabe, M.; Motoo, S. *Journal of Electroanalytical Chemistry* **1975**, *60*, 275.
4. Crabb, E. M.; Ravikumar, M. K. *Electrochimica Acta* **2001**, *46*, 1033.
5. Hoogers, G.; Thompsett, D. *Cattech* **2000**, *3*, 106.
6. Niedrach, L. W.; Weinstock, I. B. *Electrochem. Technol.* **1965**, *3*, 270.
7. Grgur, B. N.; Markovic, N. M.; Ross, P. N. *Journal of Physical Chemistry B* **1998**, *102*, 2494.
8. Grgur, B. N.; Zhuang, G.; Markovic, N. M.; Ross, P. N. *Journal of Physical Chemistry B* **1997**, *101*, 3910.
9. Grgur, B. N.; Markovic, N. M.; Ross, P. N. *Journal of the Electrochemical Society* **1999**, *146*, 1613.
10. Mukerjee, S.; Lee, S. J.; Ticianelli, E. A.; McBreen, J.; Grgur, B. N.; Markovic, N. M.; Ross, P. N.; Giallombardo, J. R.; De Castro, E. S. *Electrochemical and Solid State Letters* **1999**, *2*, 12.
11. Mukerjee, S.; Urian, R. C.; Lee, S. J.; Ticianelli, E. A.; McBreen, J. *Journal of the Electrochemical Society* **2004**, *151*, A1094.
12. Ball, S.; Hodgkinson, A.; Hoogers, G.; Maniguet, S.; Thompsett, D.; Wong, B. *Electrochemical and Solid State Letters* **2002**, *5*, A31.
13. Mukerjee, S.; Urian, R. C. *Electrochimica Acta* **2002**, *47*, 3219.
14. Neto, A. O.; Giz, M. J.; Perez, J.; Ticianelli, E. A.; Gonzalez, E. R. *Journal of the Electrochemical Society* **2002**, *149*, A272.
15. Russell, A. E.; Maniguet, S.; Mathew, R. J.; Yao, J.; Roberts, M. A.; Thompsett, D. *Journal of Power Sources* **2001**, *96*, 226.
16. Crabb, E. M.; Ravikumar, M. K.; Qian, Y.; Russell, A. E.; Maniguet, S.; Yao, J.; Thompsett, D.; Hurford, M.; Ball, S. C. *Electrochemical and Solid State Letters* **2002**, *5*, A5.
17. Shropshire, J. A. *Journal of the Electrochemical Society* **1965**, *112*, 465.
18. Zhang, H. Q.; Wang, Y.; Fachini, E. R.; Cabrera, C. R. *Electrochemical and Solid State Letters* **1999**, *2*, 437.

19. Li, W. S.; Tian, L. P.; Huang, Q. M.; Li, H.; Chen, H. Y.; Lian, X. P. *Journal of Power Sources* **2002**, *104*, 281.
20. Gotz, M.; Wendt, H. *Electrochimica Acta* **1998**, *43*, 3637.
21. Lima, A.; Coutanceau, C.; Leger, J. M.; Lamy, C. *Journal of Applied Electrochemistry* **2001**, *31*, 379.
22. Samjeske, G.; Wang, H. S.; Loffler, T.; Baltruschat, H. *Electrochimica Acta* **2002**, *47*, 3681.
23. Keck, L.; Buchanan, J. S.; Hards, G. A. U.S. Patent 5,067,161, 1991.
24. Grambow, L.; Bruckenstein, S. *Electrochimica Acta* **1977**, *22*, 377.
25. Couto, A.; Perez, M. C.; Rincon, A.; Gutierrez, C. *Journal of Physical Chemistry* **1996**, *100*, 19538.
26. Mansour, A. N.; McBreen, J.; Melendres, C. A. *Journal of the Electrochemical Society* **1999**, *146*, 2799.
27. O'Grady, W. E.; Pandya, K. I.; Swider, K. E.; Corrigan, D. A. *Journal of the Electrochemical Society* **1996**, *143*, 1613.
28. Cramer, S. P.; Eccles, T. K.; Kutzler, F. W.; Hodgson, K. O.; Mortenson, L. E. *Journal of the American Chemical Society* **1976**, *98*, 1287.
29. Bett, J.; Kinoshita.K; Routsis, K.; Stonehart.P. *Journal of Catalysis* **1973**, *29*, 160.
30. Ressler, T.; Timpe, O.; Neisius, T.; Find, J.; Mestl, G.; Dieterle, M.; Schlogl, R. *Journal of Catalysis* **2000**, *191*, 75.
31. Macias, B.; Malet, P.; Paradinas, R.; Rives, V.; Villa, M. V. *Inorganica Chimica Acta* **1999**, *288*, 127.
32. Maniguet, S.; Mathew, R. J.; Russell, A. E. *Journal of Physical Chemistry B* **2000**, *104*, 1998.
33. McBreen, J.; Mukerjee, S. *Journal of the Electrochemical Society* **1995**, *142*, 3399.
34. Benfield, R. E. *Journal of the Chemical Society-Faraday Transactions* **1992**, *88*, 1107.
35. Mukerjee, S.; McBreen, J. *Journal of Electroanalytical Chemistry* **1998**, *448*, 163.
36. Lebedeva, N. P.; Janssen, G. J. M. *Electrochimica Acta* **2005**, *51*, 29.
37. Christoffersen, E.; Liu, P.; Ruban, A.; Skriver, H. L.; Norskov, J. K. *Journal of Catalysis* **2001**, *199*, 123.

Chapter Four: Platinum-Tungsten Anode Catalyst

1 Introduction

Current research in the field of anode catalysts for PEMFCs is concentrating on developing materials that minimise the amount of precious metals used, while at the same time attempting to increase their CO tolerance. Poisoning of the catalytic surface by CO blocks these sites from adsorption and oxidation of hydrogen (or methanol) fuel. There is a high overpotential associated with the oxidation of CO to CO_2, which greatly lowers the overall cell efficiency. While CO-free hydrogen fuel sources are the preferred option, this remains impractical due to the nature of storing and transporting pure hydrogen gas. This necessitates the use of other fuel sources such as methanol (either directly or used to produce reformate) which leads to the production of CO as a by-product. Extra components must then be added to the fuel cell that can be used to lower the amount of CO in the fuel stream, (such as water gas shift reactors, air bleeds and selective catalytic oxidation methods), however these are also undesired because of the increased cost, size and complexity to the overall system.

The use of PtMo catalysts as anodes in PEMFCs for enhanced activity of hydrogen oxidation with reformate fuel streams was discussed in chapter 3. This is one of a class of catalysts that are believed to operate via a promoted mechanism, whereby oxides on the secondary metal surface can oxidise adsorbed CO on neighbouring platinum sites at low potentials. This chapter will discuss results obtained for a set of $PtWO_x/C$ anode catalysts that also operate via a promoted mechanism.

The promotional effect of W oxides on the H_2 oxidation activity of Pt with CO/H_2 mixtures was observed as early as 1965 by Niedrach and Weinstock [1], using a series of tungsten oxides that had been admixed with platinum black. The weak adsorption of CO on the oxides allowed for the presence of water molecules that, at the Pt-oxide interface, could be used for anodic oxidation of CO on neighbouring Pt sites. Hobbs

and Tseung later postulated that active hydrogen adsorbed on the Pt could "spillover" onto the tungsten oxide leading to the rapid formation of "hydrogen tungsten bronzes", H_xWO_3 ($0.3<x<0.5$), which could act as intermediates in the oxidation of hydrogen, providing an alternative reaction path [2]. The basic mechanism is as follows:

$$WO_3 + x\text{Pt-H} \rightarrow H_xWO_3 + x\text{Pt} \qquad \textbf{Eq. 1}$$

(formation of hydrogen tungsten bronze)

$$H_xWO_3 \rightarrow xH^+ + xe^- + WO_3 \qquad \textbf{Eq. 2}$$

(oxidation of hydrogen tungsten bronze)

This would allow lower Pt loadings and extend the reaction zone into the catalyst support. The reduction of WO_3 by hydrogen in the presence of Pt to form the blue hydrogen tungsten bronze was reported in the literature [3,4] and was found to occur even at room temperature, as long as an adsorbed layer of water was present.

WO_3 electrodes have been investigated for their electrochromic properties of changing colour with applied potential because of the mixed-valent tungsten oxides that can form. Such electrodes were prepared by a variety of methods including vacuum evaporated films and anodic oxidation of W, along with polycrystalline and single crystal electrodes [3,5,6]. Films produced by vacuum evaporation were found to hydrate less fully, creating problems with proton transfer and poor kinetics for charge transport. Anodically produced films of tungsten hydrated more fully, however, metallic tungsten was required on the substrate and it was hard to control the growth of the oxide. In addition, the amorphous WO_3 films were found to dissolve in aqueous acid solutions.

Later work by Kulesza and Faulkner looked at using electrodes modified with tungsten for the purposes of creating microstructures on electrodes with specific functionalities [7,8]. These materials were designed to possess good electronic conductivity and exhibit catalytic activity. Non-stoichiometric tungsten (VI, V) oxide films were grown by electrodeposition from sulphuric acid solutions onto carbon substrates. In particular, the presence of tungsten oxide bronzes was desired due to their chemical inertness and stability in strong acids. Based upon the earlier work by Niedrach *et al*

[1], the usefulness of these materials as possible supports for Pt microparticles to aid in electro-oxidation of hydrogen and carbon monoxide mixtures was investigated. Kulesza and Faulkner were able to create three-dimensional tungsten (VI, V)-oxide matrices containing spherical Pt microparticles of varying sizes via a simultaneous reductive electrodeposition process onto carbon electrodes from WO_3/chloroplatinate colloidal suspensions in H_2SO_4 [8]. The close interaction that exists between Pt metal and W-oxide substrates was shown to be greater than previously thought when it was found that even traces of Pt were responsible for accelerating the reduction of WO_3 sites to highly reactive hydrogen tungsten (oxide) bronzes.

The increasing interest in developing fuel cell technology in recent years has also seen intensified study into the use of Pt-W catalytic systems in a number of fuel cell applications. Shim *et al* have investigated Pt-WO_x/C catalysts as anode catalysts in a PEMFC system using pure hydrogen as a fuel [9]. The catalysts were prepared by depositing tungsten oxide particles onto a 10 wt% Pt/C catalyst from a reaction between a tungsten precursor (sodium tungstate) and hydrochloric acid. XRD of the powder samples showed only the presence of crystalline WO_3. They found an increase in catalyst performance up to 5% tungsten oxide content, but that the performance then decreased with a greater amount of tungsten oxide present. Shifts in peak positions observed between cyclic voltammograms of Pt/C and Pt-WO_3/C indicated that the increasing content of tungsten oxides weakens the adsorption strength of hydrogen on the platinum surface. The electrochemically active surface area of these catalysts, determined by measuring the coulombic charge for hydrogen desorption, was found to be significantly greater than pure platinum; no doubt mostly due to the formation of hydrogen tungsten bronzes.

PtRu-WO_x electrodes have also been investigated as possible anode catalysts for the oxidation of H_2 from a reformate source containing high levels of CO [10-12]. Tseung *et al* used catalysts prepared by electroplating onto a gold substrate from an $HClO_4$ solution containing chloroplatinic acid, ruthenium chloride and dissolved tungsten in order to experiment with CO oxidation. Using cyclic voltammetry, they found that the CO oxidation peaks were considerably broader than for pure Pt with a significantly lower onset potential (150 mV less overpotential) than for unmodified PtRu catalysts. The charges measured from the CO oxidation peaks indicate that there is more than a

monolayer of CO is present. In addition, galvanostatic oxidation measurements of adsorbed CO show two regions of CO oxidation; one occurring at lower potentials than the other. It has been suggested that the excess CO may in fact be physically adsorbed on top of a chemisorbed monolayer. A series of PtRu-WO_3/C catalysts were also prepared using a chemical codeposition method by adding activated carbon support to a mixture of chloroplatinic acid and dissolved tungsten solution. These were then freeze-dried to ensure uniform dispersion of the Pt crystallites on the carbon surface, allowing the fabrication of Teflon-bonded electrodes. These were either thermally reduced at 360 °C under vacuum [10,11] or by hydrogen reduction [10]. Gas streams of 100 ppm CO in H_2 were used for the testing. The performance of the thermally reduced PtRu-WO_3 catalysts was found to be greater than that of Pt/C, PtRu/C and PtWO_3/C catalysts prepared in a similar fashion. The Pt/C catalyst dropped to a current density of 30 A/cm^2 after 300 min and continued to decrease. The PtRu/C and PtWO_3/C catalysts dropped to less than 100 mA/cm^2 after 290 min, while the PtRu-WO_3/C catalyst initially dropped to 220 mA/cm^2 after 15 mins, however no further drop was observed after 360 min. The performance of the ternary catalyst appears to benefit from a combination of the hydrogen spillover effect coupled with the bifunctional mechanism, with Ru contributing significantly to the latter with the oxidation of adsorbed CO taking place at the interface between PtRu and WO_3. The catalysts that were hydrogen reduced showed even better performance as a result of the smaller particle sizes that arise from not heat treating the sample. This allows for an increased number of interface sites between PtRu and WO_3.

Johnson Matthey have also investigated hydrogen oxidation on a WO_3 doped Pt catalyst using 100 ppm CO in H_2 and with pure CO (in a half cell environment using 1 M $H_2SO_{4\,(aq)}$ at 80 °C). It was observed that the performance of the Pt-WO_3 catalyst was similar to that of a PtRu alloy with 100 ppm CO, although with pure CO, the onset potential of CO oxidation was close to 0 V; a substantial increase compared to the PtRu [13].

A number of groups have examined the methanol electrooxidation capabilities of such catalysts for possible use in DMFCs. Shen and Tseung prepared co-deposited Pt-WO_3 electrodes via an electrodeposition method. WO_3 itself has been shown to have no activity for the oxidation of methanol in acid solutions [14], however they found

increased activity with their Pt-WO_3 electrodes compared to conventional Pt and PtRu alloy catalysts [15]. This is believed to be due to the continuous "spillover" of hydrogen from Pt sites to the WO_3 surface where formation and oxidation of hydrogen tungsten bronzes can occur. Shukla *et al* prepared chemically co-deposited carbon supported Pt-WO_{3-x} electrodes by liquid-phase reduction of a homogeneous solution of chloroplatinic acid and ammonium metatungstate precursor with sodium borohydride [16]. They also found increased activity towards methanol oxidation and suggested that the WO_x in the sample is present in the sample as an oxyhydroxide based on XPS and XRD data. This could lend itself to promotion of CO species on Pt sites by oxygen transfer; the presence of CO being due to its formation as an intermediate by-product of the methanol oxidation reaction. The tungsten is believed to be active as a redox catalyst, and a rapid change between the proposed W(VI/IV) [16], or W(V/IV) [17], should render the tungsten sites active for the dissociative adsorption of water or the oxidation of adsorbed hydrogen by dehydrogenation of methanol. Other groups have also reported work on PtW alloy nanoparticles [18] and on ternary catalysts such as PtRu-W [19]; all of which continue to show enhanced activity towards methanol oxidation compared to Pt and current PtRu alloy catalysts.

There have also been some recent investigations into using Pt-WO_3 based electrocatalysts in other types of fuel cell systems. Chen *et al* have looked at using Pt-WO_3 systems as anode catalysts in room temperature direct ethyl formate fuel cells [20]. This research was prompted by the fact that ethyl formate is more reactive than methanol and harmless to the skin. Using Pt-WO_3 catalysts prepared by electrochemical codeposition [15], they found that there was good activity for ethyl formate oxidation, however cross-over of the fuel through the 1 M propanoic acid / 0.1 M sulphuric acid electrolyte led to cathode poisoning, which greatly lowered the cell performance. Attempts to reduce this effect by using a solid Nafion membrane led to very poor results due to the high resistance of the Nafion at room temperature. The boiling point of ethyl formate is 54°C, which prevents the temperature of the system being increased sufficiently to increase the Nafion proton conductivity.

Chen and Tseung [21] have also investigated the stability of Pt/WO_3 electrodes for possible fuel cell applications, following on from earlier work by Randin [22]. It had been observed that using WO_3 electrochromic films in sulphuric acid led to a small

degree of WO_3 dissolution at room temperature. Chen and Tseung showed that by coating their electrodes with a thin layer of Nafion, the solubility of the tungsten oxide was greatly reduced, while the electrode performance was stable, and the electrode activity for processes such as methanol oxidation was not affected.

2 Experimental Details

2.1 Catalysts

Two $PtWO_x$ catalysts supported on XC72R were supplied by Johnson Matthey. These were prepared by depositing tungsten onto a pre-formed 20 wt. % Pt/C catalyst and annealing first to 800 °C under H_2/N_2, then under argon at 1000 °C. The catalyst compositions and corresponding atomic ratios are shown in Table 1:

Table 1 Composition of $PtWO_x$/C catalysts by weight and atomic ratio

Pt wt. %	W wt.%	Atomic Ratio Pt:W
18.3	8.11	2.1: 1 (68.0: 32.0)
18.8	4.85	3.7: 1 (78.5: 21.5)

2.2 Electrode preparation

The catalysts were fabricated into electrodes by first making inks using Nafion® as described in chapter 2, section 1.3. For half-cell work involving cyclic voltammetry and steady state polarisation measurements, the inks were painted onto carbon paper electrodes to give loadings of between 0.2 and 1.0 mg Pt cm^{-2}. Circular electrodes with an area of 1.32 cm^2 were cut from the resulting sheet. For half cell XAS measurements, the inks were thickened to give a paste and spread manually onto carbon paper in a 3 x 3 cm template to give a loading of 1.5 to 3.0 mg Pt cm^{-2} and larger electrodes with an area of 2.54 cm^2 were punched out and used. The electrodes were then placed in boiling water for 20 minutes to ensure that they were fully hydrated. Note that the use of Nafion to bind the catalyst electrodes should ensure minimal dissolution of tungsten oxides in the acid solution used.

2.3 MEA preparation

MEAs of the catalyst samples were prepared as described in chapter 2, section 1.3. For XAS measurements in the modified mini cell, the anodes were produced by painting catalyst inks onto carbon paper electrodes to give loadings of 1 mg Pt cm^{-2}. 20 wt. % Pd/C was used for the cathodes. MEAs for single cell electrochemical work involving cyclic voltammetry and steady state polarisation measurements used anodes with catalyst inks painted on to give loadings of 0.22 mg Pt cm^{-2}. The cathodes consisted of carbon paper with a screen printed catalyst layer of 60 wt. % Pt/Shawinigan with a loading of 0.38 mg Pt cm^{-2}. Electrodes with an area of 12.56 cm^2 for use in the modified XAS mini cell, or 3.14 cm^2 for use in the unmodified mini cell, were then cut out in preparation for hot pressing. A Flemion® membrane, 30 μm, was used to make the MEAs.

2.4 Electrochemistry

2.4.1 Cyclic Voltammetry

CVs were carried out on the catalysts as working electrodes in a three-electrode half cell. A platinum gauze was used as the counter electrode and all potentials were measured with respect to a MMS reference electrode. All potentials have been converted to the RHE scale, as determined by calibrating with respect to a dynamic hydrogen/Pt electrode. 2.5 M $H_2SO_{4(aq)}$ purged with nitrogen was the electrolyte. CO stripping experiments were performed by holding at 0.05 V vs. RHE while first CO, then N_2, were purged through the electrolyte for 30 minutes each. The electrode was then cycled between 0 and 1 V vs. RHE. The practical procedure is described in more detail in chapter 2, section 2.2.

2.4.2 Methanol Oxidation

A similar three-electrode cell as above was used. After determining the metal area using CO stripping in 1 M H_2SO_4, the electrode was transferred to a cell with 2 M methanol in 1 M $H_2SO_{4\,(aq)}$. The electrode was conditioned by cycling between 0.05

and 0.8 V vs. RHE with a scan rate of 10 mV s^{-1}. The electrode was then polarised using the same potential range and a step potential of 0.05 V. The current was recorded after a stabilisation time of 30 seconds. Current interrupt measurements were taken at 0.65, 0.7 and 0.75 V vs. RHE to correct the data for cell resistance. The temperature was controlled by placing the cell in a water bath and the procedure was carried out at 30 °C and 80 °C.

2.4.3 Mini Cell electrochemical measurements

The MEA under investigation was assembled in the mini cell and compressed to 70 % thickness. A water bath was used to pump water through the gas humidifiers and the water channel of the cell; keeping it at a temperature of 80 °C. Gas flow rates of 60 and 40 ml min^{-1} were used for the cathode and anode respectively, and the cell pressure regulators adjusted to keep both sides of the mini cell pressurised to 14 psi-gauge. The system was first flushed with nitrogen gas. Setting the cathode as the working electrode, and the anode as the counter/reference electrode, the anode gas was switched to hydrogen, with nitrogen as the cathode gas. Once a stable open circuit potential had been reached, the cell was polarised to 0.5 V vs. RHE and the current measured. This current quantifies the hydrogen crossover from the anode to the cathode, and was usually found to be below 20 mA. CO stripping measurements were collected at the cathode using cyclic voltammetry. The potential was held at 0.125 V vs. RHE with CO flowed over the cathode for two mins, followed by 43 mins with the cathode gas switched back to nitrogen. CVs were then measured by cycling from a lower limit of 0.075 V to an upper limit of 1.0 V vs. RHE, with a scan rate of 10 mV s^{-1}. Successive scans were recorded until no CO was present; typically three scans were recorded.

Steady state polarisation measurements were recorded when operating the cell under fuel cell conditions. Oxygen gas was flowed to the cathode, while polarisation curves were measured with hydrogen to the anode. Ten fast polarisation curves were recorded first in order to condition the cell. The potential was first held at 0.65 V vs. RHE for 3 min before measuring between 0.95 and 0.65 V vs. RHE, using a step potential of 0.05 V and a maximum time interval of 5 s. Two normal polarisation curves were then recorded in the same manner, with the maximum time interval increased to 60 s.

Current interrupt measurements were taken at 0.05 V intervals from 0.9 to 0.6 V vs. RHE and back again, to correct the data for cell resistance. Further polarisation curves were then obtained in the same way with the anode gas switched first to 100 ppm CO in H_2; followed by 1 % CO in H_2.

CO stripping measurements were then collected at the anode using cyclic voltammetry, after switching the connections so that the anode was now the working electrode. With the cathode gas now switched to hydrogen, CO stripping CVs were obtained for the anode using the same procedure described above for the cathode.

2.5 XAS measurements

All measurements were taken using station 16.5 at the Synchrotron Radiation Source (SRS) at the Daresbury Laboratory, UK. The station operates with a multipole wiggler source and double crystal Si (220) monochromator and is optimized for ultra-dilute EXAFS between 9 and 40 keV. Table 2 shows the corresponding energies for the K, L_I, L_{II} and L_{III} edges for both Pt and W.

Table 2 X-ray absorption edge energies for Pt and W / keV

Edge	W	Pt
K	69.5250	78.3948
L_I	12.0998	13.8799
L_{II}	11.5440	13.2726
L_{III}	10.2068	11.5637

It can be seen from these values that only the L_I, L_{II} and L_{III} edges are suitable for study on this particular beam line. Usually, in the case of Pt, it is preferred to collect data at the L_{III} edge as there will be no overlap with any other Pt edges at this energy. However, it is obvious that for a sample containing both Pt and W, an overlap will occur between the W L_{II} and the Pt L_{III} edges. This is shown in figure 1 below:

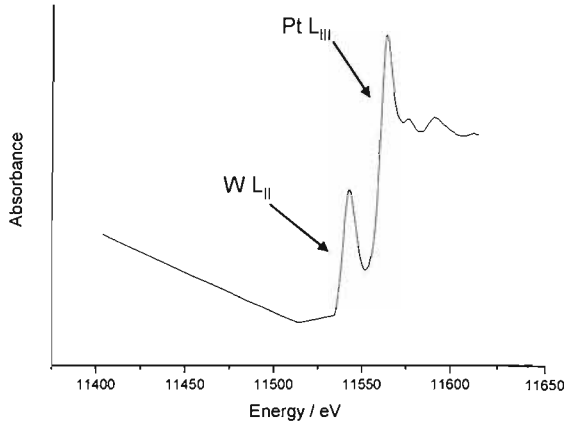

Figure 1 Overlap of W L_{II} and Pt L_{III} XAS edges

This necessitates the collection of data at the W L_{III} and the Pt L_{II} edges. In the case of the Pt L_{II} edge, it should be noted that the Pt L_I edge overlaps slightly in the high energy region of the EXAFS, requiring the data to be cut before this point during the analysis.

2.5.1 MEA in air

EXAFS data were collected for the 18.3 wt. % Pt/ 8.11 wt. % W sample as an as-prepared MEA in air for the W L_{III} edge and the Pt L_{II} edge in fluorescence mode. XANES data were collected for the MEA in air at the Pt L_{III} edge. No *in-situ* measurements in the mini cell were collected.

2.5.2 Electrochemical Half Cell

Data was collected for the 18.3 wt. % Pt/ 8.11 wt. % W sample at the W L_{III} edge and the Pt L_{II} edge in the fluorescence XAS cell described previously in chapter 2, section 3.2.6. XANES data were collected at the Pt L_{III} edge also. The electrode was placed against a gold wire current collector and an electrolyte of 1.0 M H_2SO_4 was flowed through the cell. A platinum gauze was used for the counter electrode and all potentials were measured with respect to a Hg/Hg_2SO_4 (MMS) reference electrode. All potentials shown have been corrected to the RHE scale. The cell was positioned at 45° with respect to the incident beam and a 30-element solid state detector used to measure the X-ray fluorescence, I_f.

XAS data were collected at two potentials: 0.05 and 0.85 V vs. RHE. The electrode was polarised to these potentials and the experiment started once the current had decayed to a constant value.

3 Results and Discussion

The performance of the $PtWO_x$ anode catalysts has been investigated using a range of electrochemical techniques, including half cell cyclic voltammetry of CO oxidation, and methanol oxidation polarisation curves, as well as *in-situ* performance data in the mini cell operating with varying amounts of CO present. The results will be discussed in relation to catalyst composition data obtained using XAS techniques.

3.1 Electrochemistry

3.1.1 Cyclic Voltammetry

Cyclic voltammetry measurements were obtained for the two $PtWO_x/C$ catalysts in addition to a 20 wt. % Pt/C catalyst for comparison. Electrodes for the $PtWO_x$ samples were prepared several months after catalyst manufacture, and again approximately one year later. CVs of the 18.3 wt. % Pt: 8.11 wt. % W sample obtained by cycling in 2.5 M H_2SO_4 are shown in figure 2. Differences in the CVs between the electrodes prepared from the as-received sample and fresh electrodes prepared one year later indicate ageing effects of the catalyst. The CV of the aged catalyst shows a decrease in the charge associated with oxide formation and stripping areas, although the most interesting feature is in the hydrogen region where there is a sharp increase in current on the reverse sweep, occurring near the point of hydrogen evolution. Despite appearances, this is not due to the process of hydrogen evolution because there is no corresponding reoxidation peak of hydrogen trapped in the lattice at similar potential on the following forward scan.

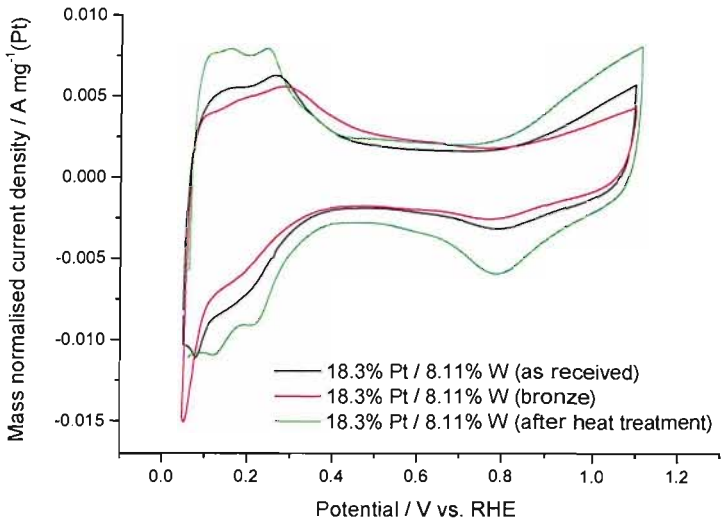

Figure 2 **Cyclic voltammograms of 18.3 wt. % Pt; 8.11 wt. % W / XC72R using the as-received sample (black line), the same sample one year later (red line), and the sample after heat treatment (green line). Carried out in 2.5 M $H_2SO_{4\,(aq)}$ with a scan rate of 10 mV s^{-1}. Currents normalised to the Pt loading.**

Hydrogen evolution can be observed in figure 3 for the 18.8 wt. % Pt / 4.85 wt. % W catalyst when the lower potential limit is made 0.05 V more negative; a reoxidation peak is clearly visible.

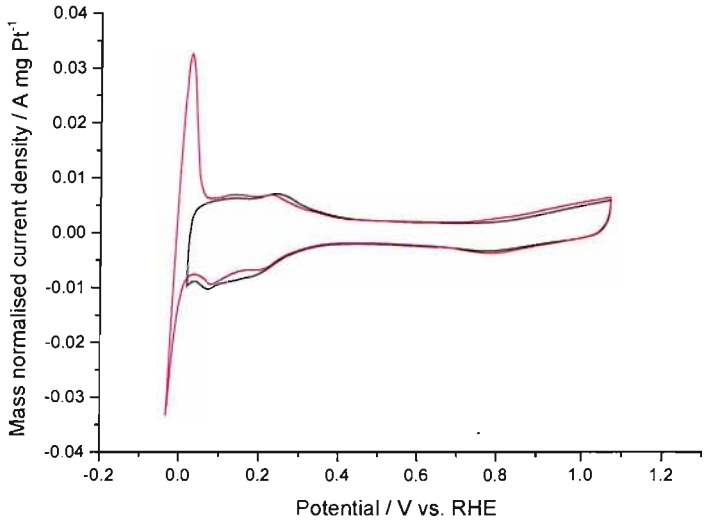

Figure 3 **Cyclic voltammogram of 18.8 wt. % Pt / 4.85 wt. % W catalyst between 0.02 and 1.10 V vs. RHE (black) and between -0.03 and 1.10 V vs. RHE (red) showing evidence of hydrogen evolution. Carried out in 2.5 M $H_2SO_{4\,(aq)}$ with a scan rate of 10 mV s^{-1}. Currents normalised to the Pt loading.**

The peak at 0.05 V on the reverse sweep in the CV in figure 2 is visually similar to that seen for CVs on amorphous WO_3 and W(VI, V) films due to electrochromic processes [3,7]. However, Kulesza *et al* have also shown a cathodic peak at similar potential occurring with cyclic voltammetry of 5mM chloroplatinate in 2M H_2SO_4 solution at a glassy carbon electrode modified with W(VI, V)-oxide, which they have attributed to a Pt(IV) to Pt(0) one step, 4-electron mechanism [8]. They surmise that the presence of hydrogen tungsten bronze sites can promote this rapid reduction process. It is well known in the literature that electro-reduction of WO_3 leads to the formation of hydrogen tungsten bronzes in the presence of aqueous acid electrolytes [3,8,14,23]. It has also been reported that WO_3 can be reduced to a hydrogen tungsten bronze in air, as long as there is platinum present and there is water preadsorbed on the mixture [4]. The Pt dissociates the molecular hydrogen while the water increases the rate of transport of the dissociated hydrogen atoms to the tungsten trioxide surface; one theory suggests this takes place via an adsorbed layer of water, possibly as H_3O^+ with exchange migration of hydrogen ions between adjacent water molecules [4]. The catalyst samples that had been allowed to age were likely to have a greater amount of adsorbed water present, aiding in more rapid bronze formation. The electrodes prepared from the as-received sample were stored in water and tested again one year later and no difference was found. This suggests that the appearance of the increased peak current at 0.05 V depends on the condition of the catalyst at the point of preparing the catalyst inks before eventual spreading. Once the catalyst is impregnated with Nafion, further intake and adsorption of water into the actual catalyst is prevented. The stabilising effect of Nafion has already be shown by Chen *et al* who found that Nafion increases the stability of Pt/WO_3 electrodes by preventing dissolution of tungsten oxide in acidic media [21].

To confirm the hypothesis, the samples were heated in an attempt to remove the water and possibly aid in thermal decomposition of any bronzes present [24]. This process involved placing a sample of the catalyst in a round-bottomed flask and flowing nitrogen over it for 30 min, followed by heating to 200 °C and holding at that temperature for 1 hr under nitrogen, followed by an hour under hydrogen, then cooling back down to room temperature and switching back to nitrogen for 30 min. Half cell electrodes were prepared of the heat treated sample and cyclic voltammograms

obtained as before. The CV for the 18.3 wt. % Pt: 8.11 wt. % W catalyst is shown in figure 2 overlaid with the CV for the as-received sample and that of the aged sample.

The CV for the heat treated sample in figure 2 shows that the reduction peak previously seen at 0.05 V on the reverse sweep is no longer present, and that there is increased definition in the hydrogen adsorption/desorption regions. In fact, the area under the hydrogen peaks is larger, indicating that any catalytic area lost as the catalyst aged has been recovered. Whilst the feature in the reverse sweep for the aged catalyst has not been definitively explained, it seems very likely that it arises due to the presence of a tungsten bronze. A sharp current increase in the same potential region has also been observed for MoO_3 electrodes and attributed to the formation of hydrogen molybdenum bronze [25,26], and is sometimes seen for Mo modified Pt/C catalysts when the Mo is present predominantly as an oxide and having very little association with the Pt. The ageing affect was not seen for the PtMo catalysts in chapter 3 as there was no increased evidence of bronzing with catalysts tested several years after catalyst preparation. In any event, the aged PtW catalysts are labelled as bronzes from this point on. Measurements of charge passed under the hydrogen desorption region are very close to those obtained in the hydrogen absorption region, including the sharp peak at 0.05 V vs RHE. The hydrogen desorption region also appears to continue to a more positive potential than with the as-received and heat treated samples, suggesting that more than just normal hydrogen desorption processes from Pt sites are taking place. Oxidation of hydrogen tungsten bronzes must be occurring in this region [7].

Figure 4 shows the CO stripping cyclic voltammograms obtained for the two PtW catalysts in both the "bronze" form, and after being heat treated. CVs of a 20 wt. % Pt/C catalyst have been included for comparison. Table 3 summarises the electrochemical parameters obtained from the CVs shown in figure 4.

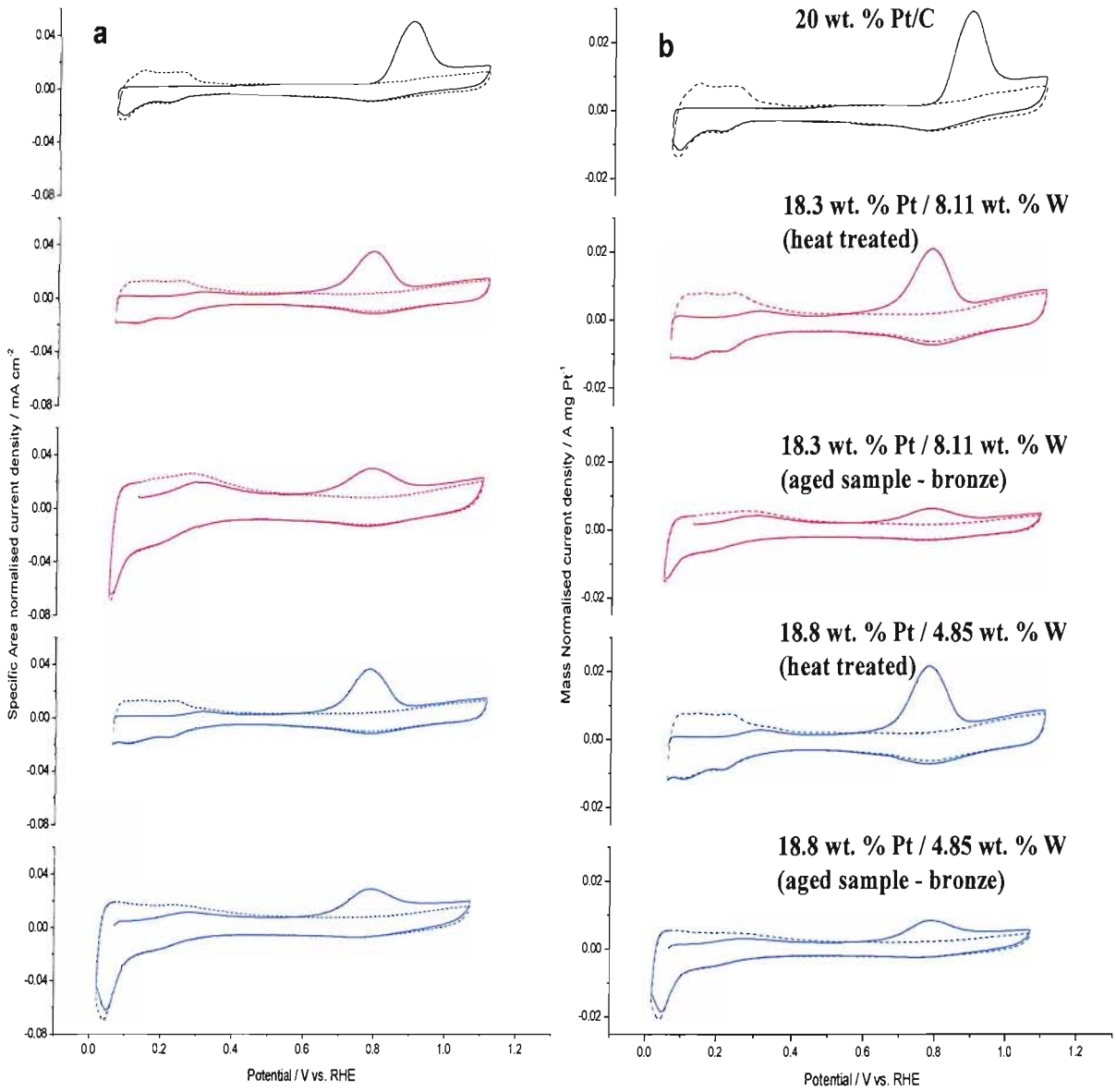

Figure 4 **Cyclic voltammograms for two $PtWO_x$/C catalysts along with a 20 wt. % Pt/C catalyst for comparison. Carried out in 2.5 M $H_2SO_{4\,(aq)}$ with a scan rate of 10 mV s^{-1}. Currents normalised to (a) the platinum surface area determined by the largest of the CO stripping peaks only and (b) the platinum loading.**

Table 3 Table of electrochemical parameters for the PtW samples and a Pt/C catalyst for comparison

Catalyst	Pt loading / mg cm^{-2}	Hydrogen adsorption charge / C	CO stripping peak position / V vs. RHE	CO stripping peak charge / C	Pt surface area / cm^2	Mass normalised Pt surface area ($Ptarea_m$) / m^2 Pt g^{-1} Pt
20 wt. % Pt/C	0.27	3.48×10^{-2}	0.895	8.82×10^{-2}	210	58.9
18.3 wt. % Pt / 8.11 wt. % W (heat treated)	0.23	4.11×10^{-2}	0.783	7.78×10^{-2}	186	61.2
18.3 wt. % Pt / 8.11 wt. % W (bronze)	0.86	1.30×10^{-1}	0.778	1.04×10^{-1}	248	21.9
18.8 wt. % Pt / 4.85 wt. % W (heat treated)	0.23	4.21×10^{-2}	0.781	7.64×10^{-2}	182	60.5
18.8 wt. % Pt / 4.85 wt. % W (bronze)	0.52	8.56×10^{-2}	0.781	8.49×10^{-2}	202	29.6

In all circumstances, it can be seen that during the forward sweep after bubbling CO through the electrolyte and holding the potential at 0.05 V, the region corresponding to hydrogen desorption has been suppressed due to the presence of a nearly complete surface layer of adsorbed CO. After one complete sweep, the hydrogen desorption peaks are in evidence indicating complete removal of the adsorbed CO. For all the PtW samples, a shift in peak position for the principal CO stripping peak to lower potentials is observed compared with the Pt/C catalyst. In addition, these catalysts also give rise to a smaller oxidation peak occurring close to 0.3 V vs. RHE. These regions of oxidation current are also observed with PtMo catalysts (see chapter 3) and are believed to be the oxidation of small amounts of CO occurring at much lower potentials than the majority of the adsorbed CO, indicating a highly heterogenous catalyst surface [27-30]. At these low potentials, it has been proposed that CO adsorbed on Pt sites is being oxidised by a promotion effect from neighbouring oxygenated Mo atoms, but that the majority of adsorbed CO can only be removed at higher overpotentials by the reaction on Pt sites between the CO and Pt-OH [27]. This corresponds well with the work carried out by Shen *et al.* They found that CO oxidation could begin at much lower potentials on co-deposited Pt-Ru/WO_3 and Pt-WO_3 because of the presence of WO_3 even at 0 V vs. SHE. OH_{ads} species present on the surface of the WO_3 can oxidise adsorbed CO on neighbouring Pt sites [11,12,31,32]. However, adsorbed CO on Pt sites not at the Pt-WO_3 interface can only be oxidised at higher overpotentials.

The peak positions for the principal CO stripping peaks are unchanged within experimental error for both catalysts in bronze and non-bronze forms. The charge passed under this peak was used to calculate the mass normalised Pt surface area. Whereas the heat treated samples possess the same area as the unmodified Pt/C catalyst, the values for the bronze catalysts are 36 and 49 % of the area for the 18.3 wt. % Pt: 8.11 wt. % W and the 18.8 wt. % Pt: 4.85 wt. % W catalysts respectively. There is a corresponding small increase in the charge passed under the early oxidation peaks found for the bronze catalysts, suggesting an increase in the amount of CO adsorbed on Pt at interface sites that can be oxidised at lower potentials by promotion effects. This small increase is still much lower than the loss in charge passed under the principal CO peak, so that even if the areas were included from the early oxidation peaks, the mass normalised Pt areas for the bronze catalysts are still significantly smaller than those

found with the heat treated samples. This suggests that the CO coverage for the bronze catalysts is lower implying that the formation of a bronze has effectively blocked a portion of the available Pt sites from adsorption by CO or that the ageing process results in an increase in particle size (leading to a decrease in particle dispersion). Heating of the samples resulted in recovery of catalytic surface area supporting the former interpretation, i.e. the blocking of Pt sites by the tungsten bronze. The apparent formation and oxidation processes of the hydrogen tungsten bronze are only observed in the cyclic voltammograms of the aged catalysts. The formation of the bronze appears then to be linked to the ageing of the samples, and not a purely electrochemically driven process in this instance. As reported earlier, the rapid formation of hydrogen tungsten bronzes has been observed by the electroreduction of WO_3-containing electrodes in aqueous acid solutions [3,8,14,23] indicating that electrochemically driven formation of tungsten bronzes is possible for non-aged samples; however these electrodes were not bound with Nafion. The presence of Nafion appears to increase the stability of the catalyst sample preventing ageing (the adsorption of water leading to slow formation of bronze at room temperature in air) and preventing the electrochemically driven bronze formation and oxidation processes. The aged catalysts, while still bound with Nafion, have already formed a small amount of hydrogen tungsten bronzes prior to the addition of Nafion, which can then be observed in cyclic voltammograms by the electrochemical formation and oxidation processes.

Further cyclic voltammograms were obtained to attempt to characterise the early oxidation peak. Figure 5 shows a CV of the 18.8 wt. % Pt: 4.85 wt. % W catalyst (heat treated) with no CO present, followed by adsorbing CO onto the surface and holding at 0.05 V vs. RHE and then cycling only in the potential region of the early stripping peak. The oxidation peak is present in the first scan, but not the second after CO adsorption. This shows that even though a portion of the Pt sites have been freed of CO, they cannot be used for further oxidation of the remaining CO. The adsorbed CO will not move onto these free sites to be oxidised by promotion effects in the timescale of the measurement; only by increasing the overpotential and allowing OH species to form on these free Pt sites will allow the remaining CO to be oxidised. The second scan shows reduced double layer charging compared to the CV when no CO was present, indicating that there is still a large coverage of adsorbed CO present. It has

been suggested that part of the early oxidation peak with PtW catalysts may be the result of some other slow-forming species, as positive current has been observed in this region, when holding at 0.05 V for a period of time without any CO present in solution [11,12,33,34]. This effect was not observed for the catalysts tested here.

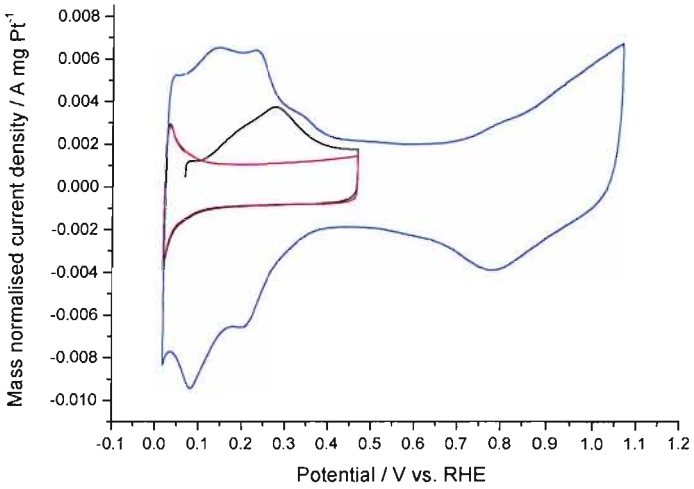

Figure 5 **Cyclic voltammogram of 18.8 wt. % Pt / 4.85 wt. % W catalyst between 0.0 and 1.1 V vs. RHE with no CO present (blue), overlaid with first (black) and second (red) scans after holding at 0.05 V vs. RHE with a CO purge for 30 mins, followed by a N_2 purge for 30 mins, cycled between 0.0 V and 0.5 V vs. RHE. Carried out in 2.5 M $H_2SO_{4\,(aq)}$ with a scan rate of 10 mV s^{-1}. Currents normalised to the Pt loading.**

3.2 XAS measurements

3.2.1 XANES

The XANES region of XAS spectra can be used to calculate the fractional d-band vacancies of the Pt atoms in the catalyst, by analysing the white lines at the Pt L_{II} and L_{III} edges. The white lines in the Pt L_{II} and L_{III} edges arise due to transitions from $2p_{1/2}$ to $5d_{3/2}$ states and from $2p_{3/2}$ to $5d_{5/2}$ states respectively; these d states being empty states in the vicinity of the Fermi level. These transitions are restricted by the dipole selection rules, $\Delta L = \pm 1$ and $\Delta J = 0, \pm 1$ (where L is the orbital angular momentum number and J is the total angular momentum number), such that excitations to the d-orbitals are the most favoured [35]. Transitions to s states are also possible; however the s-symmetric portion of the density of states is small and spread out in energy, while

the d-symmetric portion is large and narrow. The occurrence of white lines is mainly due to a high density of final states, thus they are attributed to the p → d transitions. For a Pt atom, the only unoccupied d level has a J value of 5/2. The Pt L_{II} white line only arises due to transitions to states where $J = 3/2$. The final states with $J = 5/2$ contribute 14 times more than those with $J = 3/2$, with the result that the white line for the L_{III} edge is much more intense than that of the L_{II} edge [36].

The d-band vacancies relative to a reference material can be quantified from the difference in areas under the Pt L_{III} and Pt L_{II} absorption edges, between the sample and a pure Pt reference foil [35]. The fractional change, f_d, in the number of d-band vacancies relative to the reference material can be expressed using the following equation:

$$f_d = \frac{\Delta A_3 + 1.11\Delta A_2}{A_{3,r} + 1.11A_{2,r}} \qquad \textbf{Eq. 3}$$

The terms A_2 and A_3 represent the area under the white line at the L_{II} and L_{III} absorption edges respectively. These values are usually determined by integration of the normalised spectra from 10 eV below the absorption edge to 13 eV above the absorption edge. $\Delta A_3 = (A_{3s} - A_{3r})$ and $\Delta A_2 = (A_{2s} - A_{2r})$, where s refers to the sample being studied, and r refers to the reference material. The quantity $A_{3r} + 1.11A_{2r}$ is the combined area per unoccupied d electron. This is a constant for the element being studied and has been determined according to the procedure of Brown *et al* [36]. The f_d value (equation 3) can be used to calculate the total number of unoccupied d-states per Pt atom in the samples as follows:

$$(h_J)_{t,s} = (1.0 + f_d)(h_J)_{t,r} \qquad \textbf{Eq. 4}$$

where h_J = the number of unoccupied d-states that are characterised by the angular momentum quantum number, J. The subscript, t, denotes total. $(h_J)_{t,r}$ for Pt has been shown to be 0.3 [36]. A large value of $(h_J)_{t,s}$ indicates a smaller d-electron density and an increased d band vacancy as compared to those for bulk Pt.

A comparison of the L_2 and L_3 edges of the PtW catalyst under various conditions, a Pt foil and a 20 wt. % Pt/C catalyst in air, are shown in figure 6. The 18.3 wt. % Pt / 8.11 wt. % W catalyst tested was in a semi-bronze state at the time of electrode preparation.

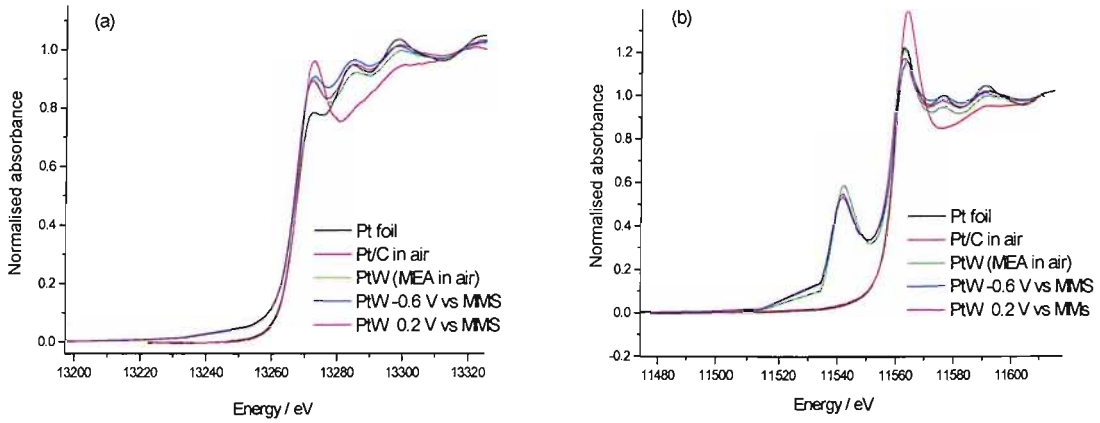

Figure 6 **Comparison of Pt L_{II} edge (a) and L_{III} (b) spectra of Pt foil, and an 18.3 wt. % Pt / 8.11 wt. % W catalyst as an MEA in air, and in an *in-situ* half cell at 0.05 V vs. RHE and 0.85 V vs. RHE with a 1 M H_2SO_4 electrolyte**

The XANES spectra for the Pt L_{III} edges with the PtW catalyst in figure 6 show an overlap with the W L_{II} absorption edge. For this reason, the integrated areas used are between 2 eV below the absorption edge to 13 eV past the absorption edge. In addition, the EXAFS region for the W L_{II} edge will interfere to some extent with the Pt L_{III} white line. The values of $(h_J)_{t,s}$ obtained should not, therefore, be thought of as strictly quantitative due to the possible errors involved, and instead be used only to establish relative trends.

At the L_{II} edge, the white line intensity is lowest for the Pt foil while, at the Pt L_{III} edge, the Pt foil and the MEA in air both show a very slight increase in white line intensity compared to the *in-situ* electrodes. The Pt/C catalyst has the greatest white line intensity. This is evident in both edges, although more so in the Pt L_{III} edge due to its heightened sensitivity to transitions between states. The PtW sample in all environments has the least white line intensity at the L_{III} edge. This is likely to be due to the fact that the catalyst sample was heated up to 1000 °C after preparation resulting in larger particle sizes. This results in a lower dispersion of Pt at the surface. The absorption coefficient for surface atoms are not the same as those for bulk atoms,

which will influence the white line intensity [37]. The calculated $(h_J)_{t,s}$ values are given in Table 4. The errors shown are related to the accuracy with which the integration can be accomplished.

Table 4 Pt d-band vacancies for Pt and a PtW catalyst in different environments

Electrocatalyst		$(h_J)_{t,s}$
20 wt. % Pt/C in air		0.328 ± 0.001
18.3 % Pt: 8.11 % W	MEA in air	0.316 ± 0.003
18.3 % Pt: 8.11 % W	0.05 V vs. RHE	0.325 ± 0.005
18.3 % Pt: 8.11 % W	0.85 V vs. RHE	0.320 ± 0.002

The d-band vacancy found for the Pt/C catalyst is similar to that found by Mukerjee *et al* [38]. Their value was obtained at 0.54 V vs. RHE, and a significant increase in $(h_J)_{t,s}$ was found upon increasing the potential to 0.84 V vs. RHE. This effect was not seen for a series of different Pt alloys, and indeed was not observed here for the PtW catalyst at two different potentials. The fact that the values for the PtW catalyst are not larger than that of the Pt/C catalyst indicates that the catalyst is not well-alloyed; suggesting that most of the tungsten must be present as a surface oxide.

Figure 7 shows the XANES spectra for the PtW catalyst at the W L_{III} edge, as well as a tungsten foil for comparison. The spectra for the PtW catalyst overlay very well for the MEA in air as well as in the half cell at 0.05 and 0.85 V vs. RHE. The edge position remains the same in all circumstances, indicating that the tungsten is very stable and cannot be reduced, even under potential control in an acidic environment.

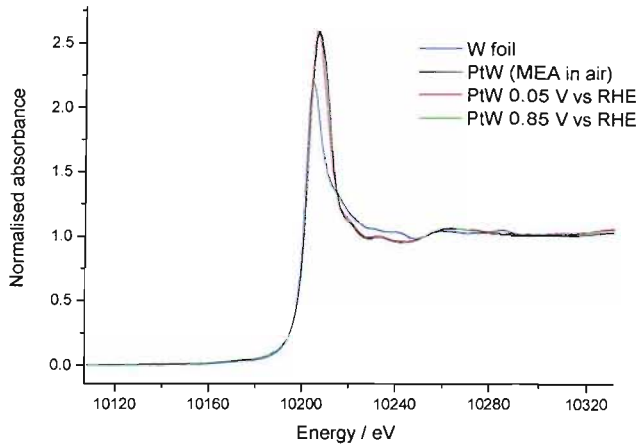

Figure 7 **Comparison of W L_{III} edge spectra of W foil, and an 18.3 wt. % Pt / 8.11 wt. % W catalyst as an MEA in air, and in an *in-situ* half cell at 0.05 V vs. RHE and 0.85 V vs. RHE with a 1 M H_2SO_4 electrolyte.**

The white line intensity is less for the tungsten foil. This is presumably because, while surface tungsten atoms may have oxides, the vast majority of the atoms are in a metallic state in the bulk. The tungsten atoms in the PtW catalyst are present not only within the bulk of small nanoparticles but a significant fraction of these atoms will be present at the surface as well and form oxides. The average number of W-O neighbours should therefore be greater in the PtW catalyst. The edge position for the tungsten foil is also approximately 1 eV less. Although this is only a small difference, it is a further indication that the PtW catalyst is more oxidised.

3.2.2 EXAFS - MEA in air

EXAFS data were collected for the 18.3 wt. % Pt: 8.11 wt. % W catalyst sample as a painted electrocatalyst layer on the anode of a prepared MEA. This data was collected in air at the Pt L_{II} and the W L_{III} edges. The k^2 weighted data are shown in figure 8. The solid lines represent the raw data and the dotted/red lines represent the fit.

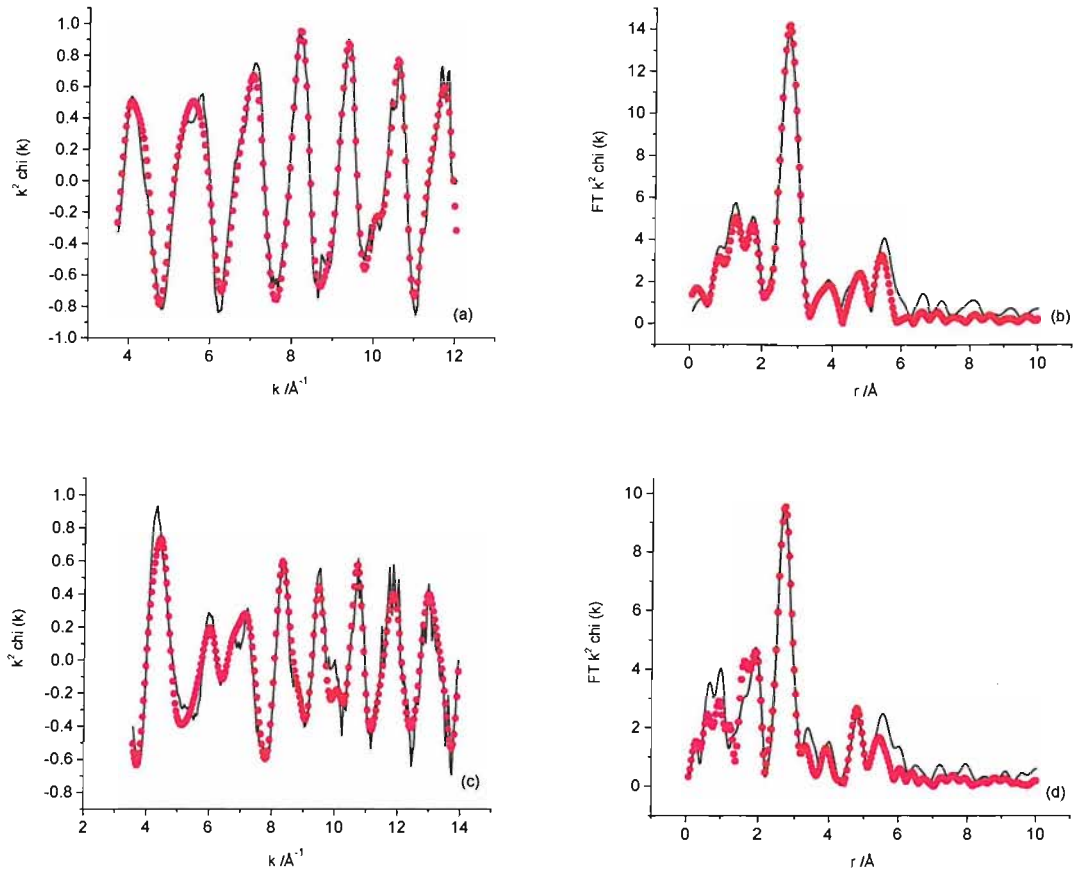

Figure 8 **k^2-weighted EXAFS for the 18.3 wt. % Pt/ 8.11 wt. % W catalyst MEA in air at (a and b) the Pt L_{II} edge, (c and d) the W L_{III} edge. (a and c) experimental data (solid line) and fit (dots). (b and d) the corresponding Fourier transforms, phase corrected for backscattering from Pt.**

Figures 8(a) and 8(b) show the k^2 weighted chi data and corresponding Fourier Transform plots for the data obtained at the Pt L_{II} edge. The fit shown was obtained by only fitting platinum and oxygen neighbours. This provides a very close match between the theoretical and experimental data. It was found that some of the Pt-Pt coordination shells could be substituted with Pt-W neighbours with the overall goodness of fit remaining the same. For example, it was possible to fit a shell of 4.9 Pt-Pt neighbours at 4.81 Å, or a shell of 5.3 Pt-W neighbours at 4.81 Å equally well. The exception to this is the first shell, where total replacement of platinum neighbours with tungsten neighbours resulted in a significant drop in goodness of fit. A mixed coordination shell of both platinum and tungsten neighbours was still possible. Previous data analysis of EXAFS results from PtW catalysts by Alexeev *et al* [39,40]

have determined that because of the closeness of the Pt L_{II} and Pt L_I edges, it is only really practical to fully analyse the first coordination shell. The first shell parameters obtained for two alternative fittings of the PtW catalyst in air are shown in Table 5:

Table 5 **Structural parameters for the 18.3 % Pt / 8.11 % W catalyst in air at the Pt L_{II} edge**

Fitting	Shell	N	R / Å	$2\sigma^2$ / Å^2	E_f / eV	R_{exafs}
Pt and O neighbours	Pt-Pt	7.7 ± 0.4	2.76 ± 0.01	0.011 ± 0.001	-12.7 ± 1.1	33.76
	Pt-O	0.6 ± 0.2	2.04 ± 0.04	0.012 ± 0.009		
Pt, W and O neighbours	Pt-Pt	4.6 ± 1.3	2.74 ± 0.03	0.010 ± 0.004	-11.2 ± 1.7	32.34
	Pt-W	3.2 ± 1.3	2.79 ± 0.03	0.013 ± 0.007		
	Pt-O	0.6 ± 0.2	2.03 ± 0.04	0.012 ± 0.010		

The fact that Pt-Pt and Pt-W neighbours appear to be so interchangeable is likely due to the fact that they have very similar atomic weights (Pt = 195.08 g mol^{-1}; W = 183.84 g mol^{-1}) making it difficult to distinguish between the two with the software at hand because the backscattering amplitudes will be almost identical.

The k^2 weighted chi data and corresponding Fourier Transform plots for the data obtained at the W L_{III} edge are shown in figure 8(c) and 8(d) respectively. Around k ~ 6 Å^{-1}, a region of low amplitude oscillations can be seen in the chi data. This is an area of destructive interference between the backscattered photoelectron wave and the atomic neighbours when the backscattering is 180° out of phase. The greatest amplitude can also be seen at very low k-space (4 Å^{-1}) meaning that this sample has a high amount of back scattering from low z neighbours. This suggests that a large proportion of the tungsten is present as an oxide.

Structural parameters obtained at the corresponding W L_{III} edge are shown in Table 6. It was again possible to fit either platinum or tungsten neighbours equally well in all coordination shells. Unlike at the Pt L_{II} edge, it is not possible to fit both platinum and tungsten together in the first coordination shell as this creates significant errors in the fitting of the W-W neighbours.

Table 6 **Structural parameters for the 18.3 % Pt / 8.11 % W catalyst in air at the W L_{III} edge**

Shell	N	R / Å	$2\sigma^2$ / Å^2	E_f / eV	R_{exafs}
W-Pt *(or W-W)*	3.6 ± 0.2	2.75 ± 0.04	0.011 ± 0.001	-12.1 ± 0.8	42.85
W-O	1.6 ± 0.1	1.84 ± 0.01	0.019 ± 0.003		

While it is not possible to determine whether the metal neighbours are platinum or tungsten, it can be seen that the average tungsten atom in the sample has 3.6 1st shell metal neighbours compared with approximately 7.7 1st shell metal neighbours at the platinum edge. This, coupled with the large number of W-O neighbours (1.6), indicates that a large proportion of the tungsten atoms are present on the surface of the nanoparticles as an oxide and that, even with heat treatment to 1000 degrees, the catalyst has not formed a well-mixed alloy.

In order to validate the fits obtained, the relationship between the Pt-W ($N_{Pt\text{-}W}$) and W-Pt ($N_{W\text{-}Pt}$) contributions and the total number of platinum (n_{Pt}) and tungsten (n_W) atoms in the sample should satisfy the following equation:

$$\frac{N_{Pt-W}}{N_{W-Pt}} = \frac{n_W}{n_{Pt}} \qquad \textbf{Eq. 5}$$

Using 3.2 Pt-W neighbours from the Pt L_{II} edge and 3.6 W-Pt neighbours from the W L_{III} only gives a ratio of 1.13 Pt: 1 W atoms, whereas the atomic ratio in the sample is actually 2.1 Pt: 1 W. This result implies that the alternative fittings are more likely (i.e. only Pt-Pt and W-W neighbours are present). The number of Pt-W and W-Pt neighbours may be very small and the tungsten only present as surface clusters. However, due to the difficulty of distinguishing between platinum and tungsten, the detailed structure cannot be determined with precision.

3.2.3 EXAFS - Half Cell

EXAFS data were collected for the 18.3 wt. % Pt: 8.11 wt. % W catalyst sample as a painted electrode in a half cell in 1 M $H_2SO_{4\,(aq)}$ held at potentials of 0.05 V and 0.85 V vs. RHE. This data was collected at both the Pt L_{II} and the W L_{III} edges.

The k^2 weighted chi data at both edges are shown in figure 9 with data for the two potentials overlaid.

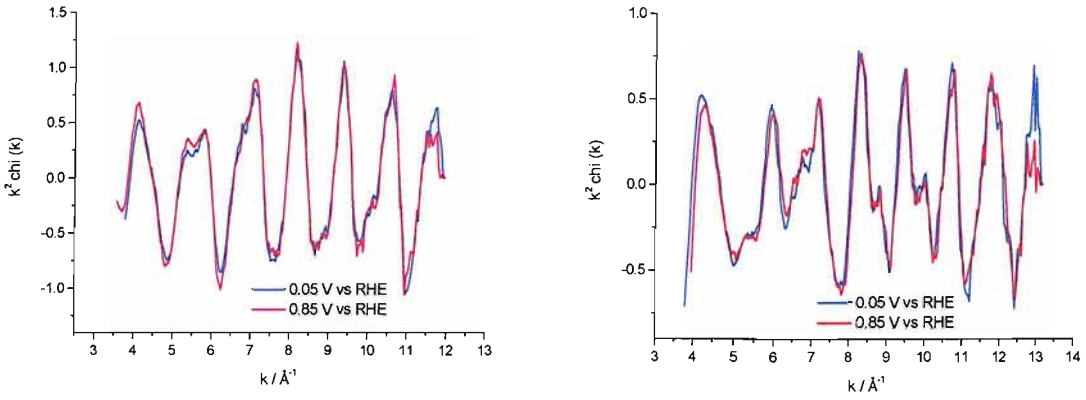

Figure 9 **Comparison of 18.3 wt. % Pt: 8.11 wt. % W catalyst as electrode in half cell with 1 M $H_2SO_{4\ (aq)}$ electrolyte at 0.05 V vs. RHE (blue line) and 0.85 V vs. RHE (red line) at the Pt L_{II} edge (left) and W L_{III} edge (right).**

Visual inspection of the chi plots in figure 9 show that there appears to be no significant differences between the average platinum and tungsten environments when held at 0.05 and at 0.85 V vs. RHE. The corresponding Fourier Transforms and theoretical fits to the data are found in figure 10 for the data obtained at 0.05 V vs. RHE. The first coordination shell structural parameters obtained from the fits can be found in Table 7.

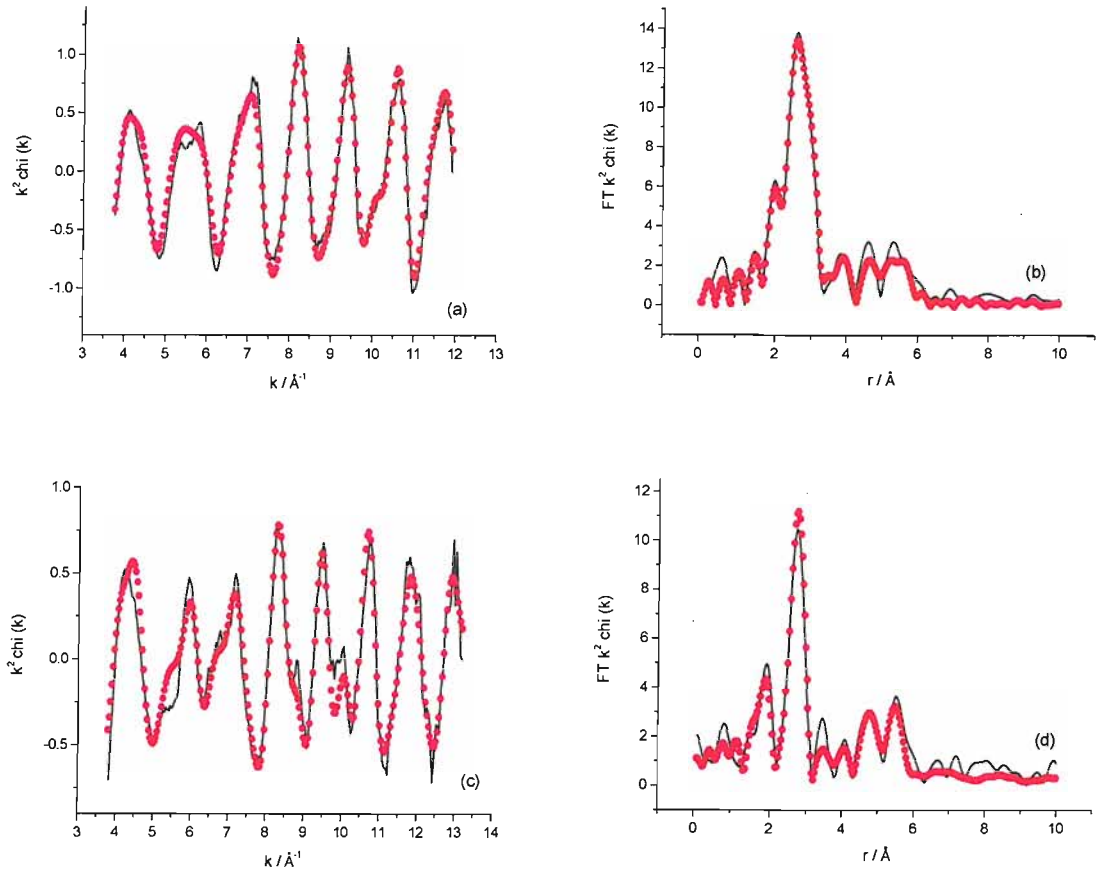

Figure 10 **k^2-weighted EXAFS for the 18.3 wt. % Pt/ 8.11 wt. % W catalyst MEA in electrochemical half cell at 0.05 V vs. RHE at (a and b) the Pt L_{II} edge, (c and d) the W L_{III} edge. (a and c) experimental data (solid line) and fit (dots). (b and d) the corresponding Fourier transforms, phase corrected for backscattering from Pt.**

Table 7 **Structural parameters for the 18.3 % Pt / 8.11 % W catalyst in the electrochemical half cell at 0.05 and 0.85 V vs. RHE at the Pt L_{II} and the W L_{III} edges**

Edge	Potential/ V vs. RHE	Shell	N	R / Å	$2\sigma^2$ / Å^2	E_f / eV	R_{exafs}
Pt L_{II}	0.05 V	Pt-Pt	8.4 ± 0.4	2.76 ± 0.01	0.011 ± 0.001	-10.7 ± 1.1	33.51
	0.85 V	Pt-Pt	8.7 ± 0.5	2.76 ± 0.01	0.012 ± 0.001	-12.1 ± 1.2	36.41
W L_{III}	0.05 V	W-Pt	4.9 ± 0.4	2.75 ± 0.01	0.010 ± 0.001		
		W-O	0.8 ± 0.2	1.86 ± 0.02	0.012 ± 0.006	-14.4 ± 1.4	41.20
		W-W	1.7 ± 0.8	3.90 ± 0.02	0.013 ± 0.005		
	0.85 V	W-Pt	4.5 ± 0.4	2.75 ± 0.01	0.010 ± 0.001		
		W-O	0.7 ± 0.2	1.85 ± 0.03	0.011 ± 0.007	-12.7 ± 1.6	48.66
		W-W	1.7 ± 0.8	3.88 ± 0.03	0.011 ± 0.005		

While platinum and tungsten neighbours are often interchangeable, the parameters shown are for which the R_{exafs} value is lowest, even though this is usually only by a value of 1 or 2. In the first coordination shells, when attempting to fit both platinum and tungsten together, the errors become greatest for the tungsten, further supporting the view that platinum atoms make up the majority of the first coordination shell at both edges. Using equation 5 to calculate the amount of expected neighbours based on the known ratio of platinum and tungsten atoms in the sample, it would be expected that at 0.85 V with 4.5 W-Pt neighbours, there would be approximately 2 Pt-W neighbours in the first coordination shell at the Pt L_{II} edge. The fact that this is not seen is likely to be due to the fact that with the backscattering amplitudes being almost identical for the two atoms, the software used will have trouble trying to fit both platinum and tungsten at similar distances, so tends to give a better fit when only fitting platinum neighbours as these form the majority of neighbours. At the W L_{III} edge, the number of W-W neighbours is likely to be lower than the number of W-Pt neighbours, which is again why the best fit obtainable is by classifying all of the first shell metal neighbours as Pt and fitting them as one shell.

At the Pt L_{II} edge, the reduction of Pt atoms is complete as the number of oxygen neighbours decreases from 0.6 in air to 0 in the half cell. This is accompanied by a small increase in the total number of metal neighbours in the first shell from 7.7 to 8.4. In contrast, the tungsten component of the particles does not appear to become fully reduced in flooded half cell conditions. The number of oxygen neighbours at the W L_{III} edge is 1.6 in air, compared with 0.8 in the flooded half cell at 0.05 V vs. RHE. The XANES data was not sensitive enough to detect this change as seen in section 3.2.1. The number of first shell metal neighbours is also seen to increase from 3.6 in air to between 4 and 5 in the half cell. The reduction of the tungsten in the sample appears to be independent of potential as the values for first shell metal and oxygen neighbours remains the same at 0.05 and 0.85 V vs. RHE within error. The fact that tungsten remains relatively well oxidised under these conditions, whereas other elements such as Ru and Mo in bimetallic Pt particles are seen to become completely reduced at 0.05 V vs. RHE in a flooded half cell [41] (and chapter 3, this thesis) means that, even at operating potential in a real fuel cell system, the tungsten should still have a significant surface oxide presence, aiding in the oxidation of CO to CO_2 on neighbouring Pt sites.

3.3 Electrochemical performance testing

3.3.1 Methanol Oxidation

3.3.1.1 Low temperature methanol oxidation

Figures 11 and 12 present the anode half cell polarisation data for methanol oxidation of the PtW catalysts and that of a Pt/C catalyst included for comparison, reported as mass activity and specific activity. These measurements were recorded at 30 °C. Two successive polarisation curves were recorded in each instance. The data presented is the average of the two curves, as the data was found to overlay in all cases.

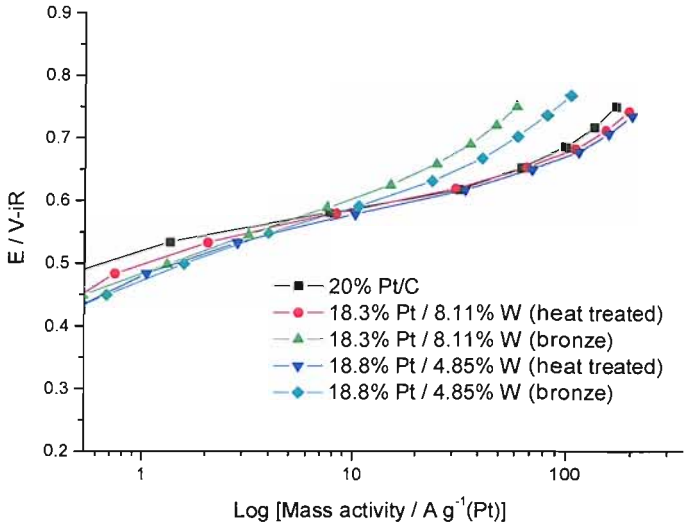

Figure 11 **Comparison of the mass activity of the $PtWO_x$ catalysts and a 20 wt. % Pt/C catalyst for comparison in 2 M MeOH / 1 M H_2SO_4 at 30 °C.**

Figure 11 shows a Tafel plot of the mass activities for the PtW catalysts at 30 °C. In this plot, the data has been normalised with respect to the total mass of platinum in each catalyst. This allows the catalyst performances to be compared as a function of the platinum content. It can be seen that the 18.8 wt. % Pt: 4.85 wt. % W catalyst after heat treatment shows the best performance, although there is very little difference between this and the other heat treated sample and the Pt/C catalyst. Indeed, at the beginning of the linear region, the bronze catalysts display similar performances; although these two samples appear to become limited by mass transport affects earlier. This could imply that there is some hindrance to methanol entering the structure and CO_2 being able to escape by the presence of the bronze. The differences in the curves could also indicate a change in mechanism for the oxidation of methanol. Multi-path mechanisms have been proposed with full decomposition reactions leading to the formation of stable adsorbed CO species, or incomplete dehydrogenation processes leading to intermediates such as $HCOO_{ad}$ and formaldehyde occurring depending on the Pt sites available and the potential [42]. It is also possible that the increased thickness of the electrocatalyst layers due to the higher loadings used for the bronze catalysts has lowered the overall utilisation. However, this effect should be negligible as the electrodes are used in a flooded cell environment, so the electrolyte should, theoretically, be able to penetrate the entire electrode structure and utilise all of the

electrocatalyst. This should only become a problem when testing catalyst performances using MEAs.

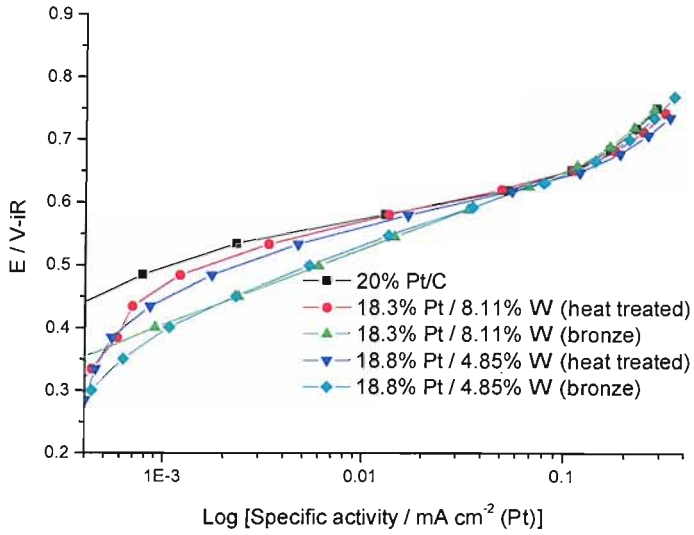

Figure 12 **Comparison of the specific activity of the $PtWO_x$ catalysts and a 20 wt. % Pt/C catalyst for comparison in 2 M MeOH / 1 M H_2SO_4 at 30 °C.**

Figure 12 shows the same data plotted as potential versus specific activity. This allows the intrinsic activity of the catalysts to be compared, independent of the surface area of the catalysts. It should be noted, however, that the active catalyst area measurements used to normalise the data are derived using the principal CO stripping peak only. This is because the presence of the pre-peak has not been definitively explained. The total available catalytic area of the platinum was found to drop significantly for the bronze catalysts when tested using cyclic voltammetry. This now shows the bronze catalysts to be performing better than the heat treated samples (by about 40 mV at 0.01 mA cm^{-2} (Pt)), although at higher current densities the performances of all the catalysts were all similar, owing to increased mass transport limitations. The fact that the bronze catalysts perform slightly better may be due to the ability of the bronze to act as a spillover site for hydrogen, which can result in continuous formation and oxidation of hydrogen tungsten bronzes and freeing up Pt sites in the process as posited by Shen *et al* [15].

3.3.1.2 High temperature methanol oxidation

Figures 13 and 14 present the anode half cell polarisation data for methanol oxidation of the PtW catalysts and that of a Pt/C catalyst for comparison. Results are presented as mass activity and specific activity. These measurements were recorded at 80 °C. Two successive polarisation curves were recorded in each instance. The data presented is the average of the two curves, as the data was found to overlay in all cases. Measurements were recorded at 80 °C because satisfactory performances can only be achieved at such temperatures due to the low activity for methanol oxidation on typical platinum-based electrocatalysts. At such temperatures, WO_3 tends to dissolve; however the presence of Nafion should negate this effect.

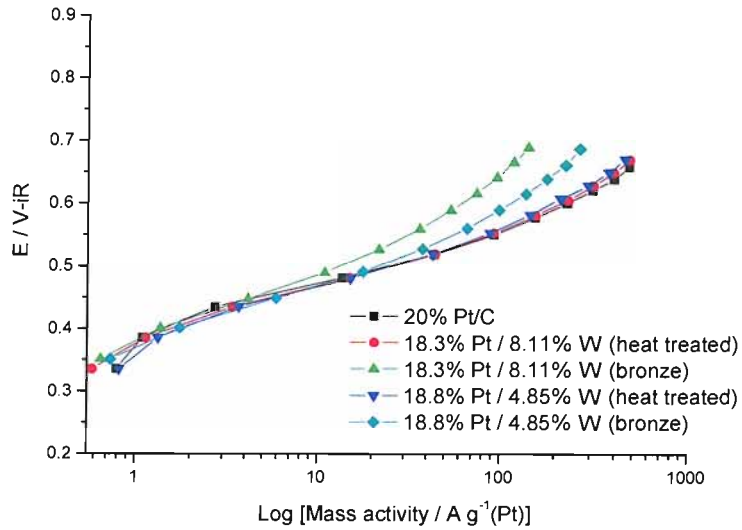

Figure 13 **Comparison of the mass activity of the $PtWO_x$ catalysts and a 20 wt. % Pt/C catalyst for comparison in 2 M MeOH / 1 M H_2SO_4 at 80 °C.**

Figure 13 shows a Tafel plot of the mass activities for the PtW catalysts at 80 °C. A large increase in performance was observed for all catalyst samples compared to the data collected at 30 °C. For low mass activity values, the performance is about the same for all the catalysts, however, at higher activity values, the performance of the bronze catalysts worsens, possibly due to increasing mass transport limitations.

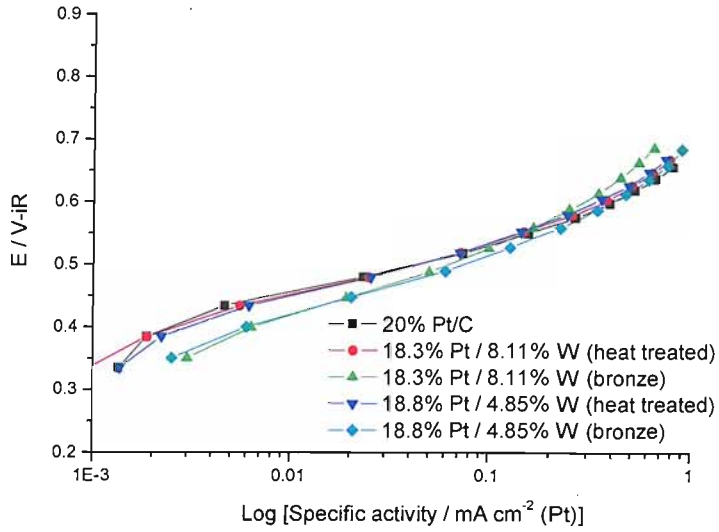

Figure 14 **Comparison of the specific activity of the $PtWO_x$ catalysts and a 20 wt. % Pt/C catalyst for comparison in 2 M MeOH / 1 M H_2SO_4 at 80 °C.**

Figure 14 shows the same data plotted as potential versus specific activity. This again shows much increased performances compared to the measurements recorded at 30 °C. For instance, for the 18.8 wt. % Pt: 4.85 wt. % W heat treated catalyst, at 0.55 V vs RHE, the specific activity has increased from 0.007 mA cm^{-2} to 0.145 mA cm^{-2}. There is no significant enhancement in activity for the PtW catalysts compared with the Pt/C sample, regardless of the state of the tungsten. As before, the bronze catalysts show only a small improvement in performance over the heat treated PtW and the Pt/C catalysts, although this benefit becomes lost at higher activites (above about 0.1 mA cm^{-2}). The fact that all of the catalysts show some evidence of current drop-off at high potentials, may indicate mass transport effects as previously mentioned. Another possibility is formation of a passive oxide film which results in the deactivation of the electrode.

3.3.2 Electrochemical Mini Cell testing

Figure 15 displays the polarisation data for the series of PtW catalysts obtained in an *in situ* single cell. The data was collected using the cathode connected as the working electrode and the anode as a combined counter/reference electrode. The measured potential is actually the overall cell potential, however, as it includes any potential losses associated with the hydrogen oxidation reaction occurring at the anode. The cathode catalyst and oxygen fuel stream were the same in all instances, so any change in performance is the direct result of changing the anode catalyst and/or fuel stream. It can be seen that there is a large drop in performance when the anode fuel stream is switched from pure hydrogen to a 100 ppm CO in hydrogen gas mixture, and that a 1% CO in hydrogen gas mixture appears to completely poison the catalyst with the current dropping nearly to zero.

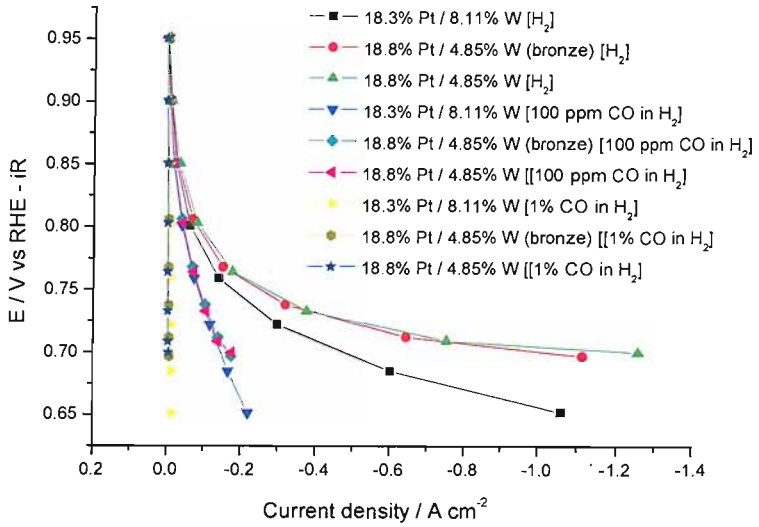

Figure 15 **Single cell polarisation data collected in an *in-situ* mini PEM fuel cell. Anode catalysts are 18.3 wt. % Pt / 8.11 wt. % W non-bronze, and 18.8 wt. % Pt / 4.85 wt. % W bronze and non-bronze as part of Flemion® bonded MEAs. Anode loading 0.22 mg Pt cm^{-2}. Cathode catalyst is 60 wt. % Pt/Ketjen; loading 0.38 mg Pt cm^{-2}. Oxygen flowed to cathode (60 cm^3 min^{-1}) and (i) hydrogen, (ii) 100ppm CO in H_2, or (iii) 1% CO in H_2 flowed to anode (40 cm^3 min^{-1}). Cell temperature of 80 °.**

Figure 16 shows the same data as above only plotted as the logarithm of the magnitude of the mass activity.

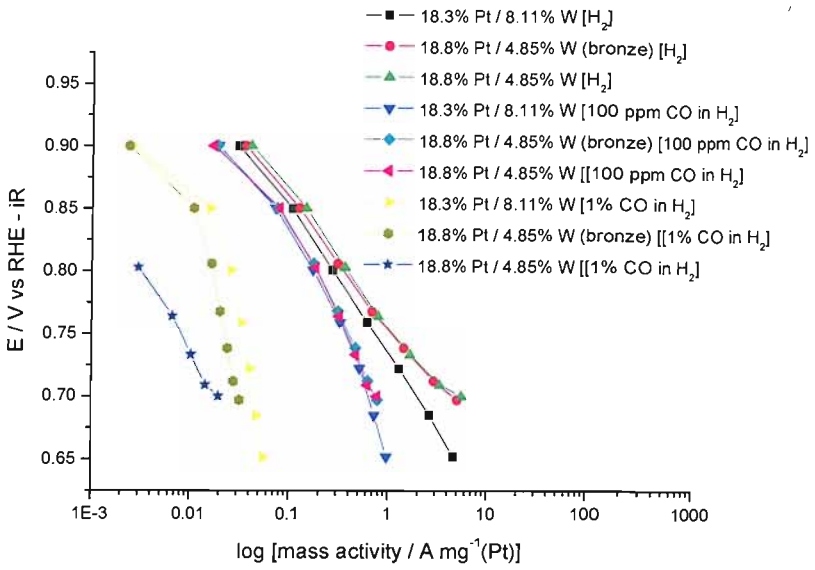

Figure 16 **Mass activity plots for single cell polarisation data in an *in-situ* mini PEM fuel cell. Series of $PtWO_x$ anode catalysts as part of Flemion® bonded MEAs. Cathode catalyst is 60 wt. % Pt/Ketjen. Oxygen flowed to cathode (60 cm^3 min^{-1}) and (i) hydrogen, (ii) 100ppm CO in H_2, or (iii) 1% CO in H_2 flowed to anode (40 cm^3 min^{-1}). Cell temperature of 80 °. Currents normalised by the Pt loading at the anode and the magnitude of these currents plotted logarithmically.**

The mass activities obtained are listed below in Table 8. For the (i) H_2 and (ii) 100 ppm CO in H_2 fuel streams, the 18.8 wt. % Pt: 4.85 wt. % W has the best performance, followed by the bronze form of the same catalyst. The 18.3 wt. % Pt: 8.11 wt. % W catalyst has the lowest performance, although the difference is not significant. At the highest CO concentration (1% in H_2), this order is reversed, however, at such low current values, the errors are likely to become more significant. In any event, the currents passed are so close to zero as to make these catalysts useless at such high levels of CO.

Figure 17 shows the same data plotted as a function of specific activity. The currents were normalised by the electrochemically active Pt area at the anode calculated from the principal CO stripping peak of a cyclic voltammogram recorded beforehand and the magnitude of these currents plotted logarithmically.

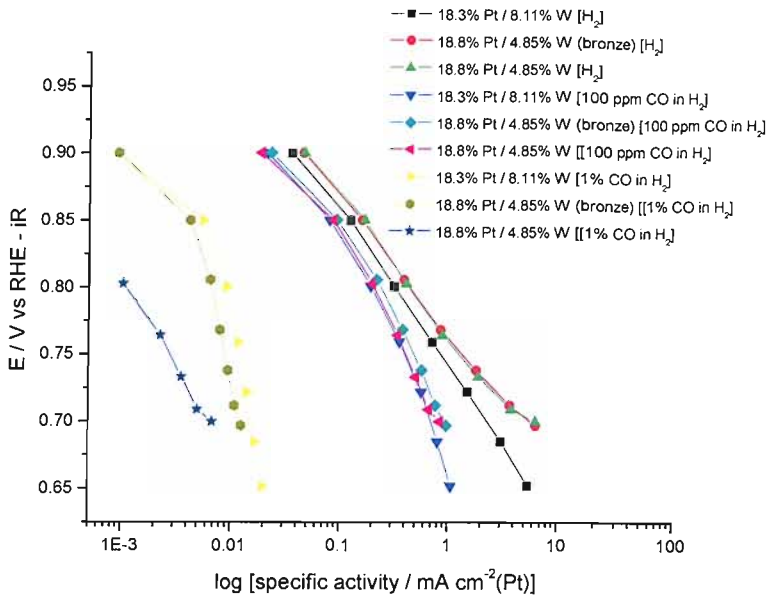

Figure 17 **Specific activity plots for single cell polarisation data in an *in-situ* mini PEM fuel cell. Series of $PtWO_x$ anode catalysts as part of Flemion® bonded MEAs. Cathode catalyst is 60 wt. % Pt/Ketjen. Oxygen flowed to cathode (60 cm^3 min^{-1}) and (i) hydrogen, (ii) 100ppm CO in H_2, or (iii) 1% CO in H_2 flowed to anode (40 cm^3 min^{-1}). Cell temperature of 80 °. Currents normalised by the electrochemically active Pt area at the anode calculated from the principal CO stripping peak of a cyclic voltammogram recorded beforehand and the magnitude of these currents plotted logarithmically.**

The ordering in performance essentially remains unchanged when looking at the specific activity plot. Differences between the two can be used to highlight economic advantages of certain catalysts, in terms of lowering the Pt content, while maintaining performance. For instance, a sample that has been heated to a higher temperature may possess a larger particle size reducing the available surface area. Therefore, the performance would be noticeably worse in the mass activity plot compared with the specific activity plot.

Table 8 **Mass activities for the series of PtW catalysts obtained at 0.8 V vs. RHE with different fuel streams to the anode**

Anode gas	Catalyst	Mass activity / A mg^{-1}(Pt) at 0.8 V vs. RHE
H_2	18.3% Pt / 8.11% W	0.270
	18.8% Pt / 4.85% W (bronze)	0.305
	18.8% Pt / 4.85% W	0.355
100 ppm CO in H_2	18.3% Pt / 8.11% W	0.171
	18.8% Pt / 4.85% W (bronze)	0.174
	18.8% Pt / 4.85% W	0.180
1% CO in H_2	18.3% Pt / 8.11% W	0.026
	18.8% Pt / 4.85% W (bronze)	0.016
	18.8% Pt / 4.85% W	0.003

The polarisation data for the 18.8 wt. % Pt: 4.85 wt. % W catalysts (bronze and non-bronze forms) show almost identical behaviour when operating with a pure H_2 fuel stream. When the current density is low, the 18.3 wt. % Pt: 8.11 wt. % W sample exhibits similar behaviour, however, mass transport effects become more significant with this catalyst as the current density increases. This can also be seen in the Tafel plots of mass activity and specific activity shown in figures 16 and 17 respectively. This drop-off in performance correlates with an increase in tungsten in the sample, and formation of oxide on the surface tungsten sites may be inhibiting catalyst utilisation at the higher current densities.

The polarisation data obtained for the PtW catalysts with a 100 ppm CO in H_2 stream is also shown in figure 15. As previously noted, there is a significant drop in current densities obtained, compared with the pure hydrogen gas stream, due to the catalyst poisoning by the presence of CO. From the accompanying Tafel plots of mass activity and specific activity (figures 16 and 17) it can be seen that there is very little difference between the catalyst samples, with the 18.3 wt. % Pt: 8.11 wt. % W catalyst just

starting to show a drop in performance above about 0.5 A mg^{-1} (Pt). This is likely due to the fact that, at such low current densities, mass transport limitations have no effect.

In the presence of a 1% CO in hydrogen fuel stream the performance is drastically reduced, as evidenced by the 10 mA cm^{-2} or less current density being obtained; even with potentials of 0.7 V. The catalyst surface is effectively completely poisoned. It would appear that the bronze catalyst of the 18.8 wt. % Pt: 4.85 wt. % W sample is showing some increased performance relative to the non-bronze catalyst, however the low currents passed and errors involved make such comparisons less meaningful.

There are no significant differences in performance of these catalysts due to increased CO tolerance with respect to each other. This is evidenced by the earlier cyclic voltammetry experiments where the principal CO stripping peak occurs at virtually the same potential for all of the PtW samples.

4 Conclusions

A combination of electrochemical and XAS techniques have been carried out in order to characterise a set of co-deposited bimetallic platinum-tungsten catalysts supported on carbon. Cyclic voltammetry has shown improved CO tolerance of these catalysts with respect to a similar Pt/C catalyst as evidenced by a lower overpotential for the oxidation of CO to CO_2, although this effect is not as great as that observed for the best PtRu catalysts currently available. However, the presence of a pre-wave oxidation peak indicates that at certain sites, the tungsten can in fact promote the oxidation of CO at very low overpotentials. This is likely to be occurring at interface sites between surface tungsten oxides and neighbouring Pt-CO_{ads} species. The bulk of the CO is still oxidised at higher overpotentials and is attributed to the reaction between CO and Pt-OH species. The small improvement over pure Pt for this process may be due to some association of the tungsten with the platinum drawing electron density away, thereby weakening the Pt-CO bond (although the XAS results indicate that this effect is marginal), or by the earlier oxidation of CO at interface sites freeing up some platinum to form Pt-OH species.

The formation of hydrogen tungsten bronzes was observed by cyclic voltammetry and directly linked to the process of catalyst aging occurring by exposure to atmospheric water vapour. The aging of the samples leading to bronze formation was found to occur within 18 months after the initial catalyst preparation. The electrochemical formation and oxidation processes of the bronze were observed in cyclic voltammetry experiments and characterised by a sharp reduction peak occurring around 0.05 V vs. RHE on the reverse sweep, followed by the hydrogen adsorption region continuing to a more positive potential than was observed for the non-bronze forms of the catalyst samples. The presence of the bronze caused a decrease in the available Pt surface area as determined by CO stripping voltammetry. Heating of the aged catalyst samples to 200 °C before electrode preparation was found to return them to a non-aged state, as evidenced by the absence of bronze formation and oxidation processes in the corresponding CVs. The Pt surface area was also recovered, indicating that the loss of area in the presence of the bronze is the result of available sites becoming blocked, rather than an effect of increased particle size. The binding of the samples with Nafion during electrode preparation was found to halt further aging of the catalysts as evidenced by the unchanging appearance of CVs of the as-received samples when the same electrodes were tested one year apart. However, the presence of the Nafion did not prevent the electrochemical bronze formation and oxidation processes occurring in samples that had been aged before being fabricated into electrodes.

Preliminary XAS data were collected for the 18.3 wt. % Pt/ 8.11 wt. % W sample as an MEA in air, and within an electrochemical half cell using an aqueous acid electrolyte. At the time of electrode fabrication, this sample was in a semi-bronze state. XANES analysis using data collected at the Pt L_{II} and L_{III} edges, as well as the W L_{III} edge, would appear to confirm that the sample was not well-mixed, with the majority of the tungsten being present as a surface oxide. The collection of EXAFS data proved problematic due to the overlap in energy between the Pt L_{III} edge with the W L_{II} edge, necessitating collection of data at the Pt L_{II} and W L_{III} edges. Overlap of the high energy region of the Pt L_{II} edge with the Pt L_{I} edge required the data to be cut before this point, essentially limiting the fitting process to the first coordination shell only at this edge. Due to the similar atomic weights of Pt and W causing the backscattering amplitudes to be virtually identical for the two elements, it was found that, in the majority of instances, Pt and W neighbours were interchangeable. Comparison of the

total number of first shell metal neighbours for Pt and W provided further evidence for the ratio of tungsten to platinum atoms at the surface of the particles being greater than in the bulk. It was also found that, in the half cell environment, complete reduction of the platinum component was achieved as expected. However, the tungsten component was found to remain in an oxidised form independent of applied potential, which is in contrast to results obtained for Mo and Ru in similar bimetallic Pt-based catalysts. Further work on these catalysts could include collecting XAS data for additional samples with differing Pt/W ratios and prepared by alternative routes (such as Controlled Surface Modification methods), as well as single cell testing to determine changes in catalyst structure under more realistic fuel cell conditions.

Electrochemical performance testing showed no real enhancement for high temperature methanol oxidation by the PtW samples by either bronze or non-bronze forms, when compared to a standard Pt/C sample. The bronze forms performed marginally better at low current densities but showed an increased amount of current drop-off as the potential was increased due to mass transport limitations; presumably as a result of blocking of some of the available catalytic Pt sites by the hydrogen tungsten bronze present. Performance data obtained for the samples as anode catalysts within a single cell operating with pure (i) H_2/O_2, (ii), 100 ppm CO in H_2/O_2 and (iii) 1 % CO in H_2 fuel streams again showed no increased tolerance to CO by the presence of the bronze. At high current densities, there is a small drop-off in performance with increasing tungsten content, presumably due to the presence of surface oxides inhibiting catalyst utilisation.

5 References

1. Niedrach, L. W.; Weinstock, I. B. *Electrochem. Technol.* **1965**, *3*, 270.
2. Hobbs, B. S.; Tseung, A. C. C. *Nature* **1969**, *222*, 556.
3. Reichman, B.; Bard, A. J. *Journal of the Electrochemical Society* **1979**, *126*, 583.
4. Benson, J. E.; Kohn, H. W.; M., B. *Journal of Catalysis* **1966**, 307.
5. Reichman, B.; Bard, A. J. *Journal of the Electrochemical Society* **1979**, *126*, 2133.
6. Reichman, B.; Bard, A. J.; Laser, D. *Journal of the Electrochemical Society* **1980**, *127*, 647.
7. Kulesza, P. J.; Faulkner, L. R. *Journal of Electroanalytical Chemistry* **1988**, *248*, 305.
8. Kulesza, P. J.; Faulkner, L. R. *Journal of the Electrochemical Society* **1989**, *136*, 707.
9. Shim, J.; Lee, C. R.; Lee, H. K.; Lee, J. S.; Cairns, E. J. *Journal of Power Sources* **2001**, *102*, 172.
10. Chen, K. Y.; Sun, Z.; Tseung, A. C. C. *Electrochemical and Solid State Letters* **2000**, *3*, 10.
11. Chen, K. Y.; Shen, P. K.; Tseung, A. C. C. *Journal of the Electrochemical Society* **1995**, *142*, L185.
12. Shen, P. K.; Chen, K. Y.; Tseung, A. C. C. *Journal of the Electrochemical Society* **1995**, *142*, L85.
13. Hoogers, G.; Thompsett, D. *Cattech* **2000**, *3*, 106.
14. Shen, P. K.; Tseung, A. C. C. *Journal of Materials Chemistry* **1992**, *2*, 1141.
15. Shen, P. K.; Tseung, A. C. C. *Journal of the Electrochemical Society* **1994**, *141*, 3082.
16. Shukla, A. K.; Ravikumar, M. K.; Arico, A. S.; Candiano, G.; Antonucci, V.; Giordano, N.; Hamnett, A. *Journal of Applied Electrochemistry* **1995**, *25*, 528.
17. Machida, K.; Enyo, M.; Adachi, G.; Shiokawa, J. *Journal of the Electrochemical Society* **1988**, *135*, 1955.

18. Lee, S. A.; Park, K. W.; Choi, J. H.; Kwon, B. K.; Sung, Y. E. *Journal of the Electrochemical Society* **2002**, *149*, A1299.
19. Gotz, M.; Wendt, H. *Electrochimica Acta* **1998**, *43*, 3637.
20. Chen, K. Y.; Tseung, A. C. C. *Journal of Electroanalytical Chemistry* **1998**, *451*, 1.
21. Chen, K. Y.; Tseung, A. C. C. *Journal of the Electrochemical Society* **1996**, *143*, 2703.
22. Randin, J. P. *Journal of Electronic Materials* **1978**, *7*, 47.
23. Hamelmann, F.; Gesheva, K.; Ivanova, T.; Szekeres, A.; Abrashev, M.; Heinzmann, U. *Journal of Optoelectronics and Advanced Materials* **2005**, *7*, 393.
24. Eda, K. *Journal of Materials Chemistry* **1992**, *2*, 533.
25. Endres, F.; Schwitzgebel, G. *Journal of Electroanalytical Chemistry* **1996**, *415*, 23.
26. Zhang, H. Q.; Wang, Y.; Fachini, E. R.; Cabrera, C. R. *Electrochemical and Solid State Letters* **1999**, *2*, 437.
27. Mukerjee, S.; Lee, S. J.; Ticianelli, E. A.; McBreen, J.; Grgur, B. N.; Markovic, N. M.; Ross, P. N.; Giallombardo, J. R.; De Castro, E. S. *Electrochemical and Solid State Letters* **1999**, *2*, 12.
28. Crabb, E. M.; Ravikumar, M. K.; Qian, Y.; Russell, A. E.; Maniguet, S.; Yao, J.; Thompsett, D.; Hurford, M.; Ball, S. C. *Electrochemical and Solid State Letters* **2002**, *5*, A5.
29. Russell, A. E.; Maniguet, S.; Mathew, R. J.; Yao, J.; Roberts, M. A.; Thompsett, D. *Journal of Power Sources* **2001**, *96*, 226.
30. Ball, S.; Hodgkinson, A.; Hoogers, G.; Maniguet, S.; Thompsett, D.; Wong, B. *Electrochemical and Solid State Letters* **2002**, *5*, A31.
31. Shen, P. K.; Chen, K. Y.; Tseung, A. C. C. *Journal of the Chemical Society-Faraday Transactions* **1994**, *90*, 3089.
32. Tseung, A. C. C.; Shen, P. K.; Chen, K. Y. *Journal of Power Sources* **1996**, *61*, 223.
33. Couto, A.; Perez, M. C.; Rincon, A.; Gutierrez, C. *Journal of Physical Chemistry* **1996**, *100*, 19538.
34. Grgur, B. N.; Markovic, N. M.; Ross, P. N. *Journal of Physical Chemistry B* **1998**, *102*, 2494.

35. Mansour, A. N.; Cook, J. W.; Sayers, D. E. *Journal of Physical Chemistry* **1984**, *88*, 2330.

36. Brown, M.; Peierls, R. E.; Stern, A. *Physical Review B* **1977**, *15*, 738.

37. Rose, A. Structural Effects in Fuel Cell Electrocatalysts. PhD Thesis, University of Southampton, 2004.

38. Mukerjee, S.; Srinivasan, S.; Soriaga, M. P.; McBreen, J. *Journal of the Electrochemical Society* **1995**, *142*, 1409.

39. Alexeev, O.; Shelef, M.; Gates, B. C. *Journal of Catalysis* **1996**, *164*, 1.

40. Alexeev, O. S.; Graham, G. W.; Shelef, M.; Gates, B. C. *Journal of Catalysis* **2000**, *190*, 157.

41. Maniguet, S. EXAFS Studies of Carbon Supported Fuel Cells Electrocatalysts. PhD. Thesis, University of Southampton, 2002.

42. Cao, D.; Lu, G.-Q.; Wieckowski, A.; Wasileski, S. A.; Neurock, M. *Journal of Physical Chemistry B* **2005**, *109*, 11622.

Chapter Five: Probing Fuel Cell Catalysts using Inelastic Neutron Scattering

1 Introduction

Electrochemical energy production in PEM fuel cells is achieved by the oxidation of hydrogen on high surface area supported Pt and Pt alloy anode catalysts (with a corresponding oxygen reduction reaction occurring at the cathode). The initial catalytic step involves the dissociative adsorption of dihydrogen, which can eventually give rise to a strongly bound monolayer of H atoms, with an H: Pt surface ratio reaching unity. The subsequent oxidation can then occur at the electrochemical interface providing a suitable potential is applied.

Due to problems with storage and distribution, the hydrogen fuel used in PEM fuel cells is usually obtained from the reformation of liquid fuels, such as methanol. This process can create a reformate gas stream containing as much as 2 % carbon monoxide, which can easily poison the Pt surface, binding with a sticking probability close to 1. This has led to the development in recent years of modified Pt catalysts that are shown to be more tolerant to the presence of CO [1]. Examples of which include bimetallic alloys such as PtRu/C, which promotes the oxidation of CO via the "bifunctional" mechanism, and surface modified catalysts such as PtMo/C, where Mo oxyhydroxide species donate oxygen to adsorbed CO. It would be desirable to be able to probe the surface interactions of adsorbed CO, H and H_2 on Pt, and how these interactions are affected by modified catalysts.

The Pt-CO bond is readily observable *in situ* using IR spectroscopy, however interactions between Pt and hydrogen are much harder to probe. Surface-enhanced techniques have been used to probe the Pt-H bond [2-5], however these techniques are all unsuitable for the study of the interaction of H_2 with the surface. Inelastic Neutron Scattering (INS) has been shown to be an ideal technique for studying these systems as it is particularly sensitive to the presence of hydrogen due to its high neutron scattering

cross section (approximately 80 barn, where 1 barn = 10^{-28} m^2), and can also be used for bulk materials with no long range order. In INS, a fraction of the neutrons collide with the sample and lose energy by exciting vibrational modes in the sample. All vibrations are active because there are no dipole or polarisability selection rules unlike other vibrational spectroscopies such as IR and Raman. The scattering intensity is related to the concentration of the scatterer and is proportional to the scattering cross-section. The underlying theory and experimental processes involved in INS have been described earlier in chapter 2, section 4.

INS has been used previously to investigate interactions between carbon monoxide and hydrogen on catalytic systems. Kelley *et al* investigated the coadsorption of H_2 and CO on Raney-Nickel [6,7]. They found evidence for the coexistence of H and CO surface species at 80 K with very little interaction. Energy loss spectra obtained before and after exposure to CO were virtually identical, showing dissociated H predominantly in a three-fold site. The physisorption and chemisorption of dihydrogen has also been studied on Pt/SiO_2 and Raney Pt [8] and on carbon supported metal particles used as fuel cell electrocatalysts; most notably on Pt/C [9-12], Ru/C [13] and PtRu/C [11]. The vibrational modes present and their intensities are used to measure how much hydrogen is on the surface and in which sites. In particular, Parker *et al* have found no evidence for the on-top adsorption site for H on either the Pt/C or PtRu/C catalysts [11]. Recent work by this group has been used to discriminate between the vibrational modes of hydrogen atoms on different Pt sites, Pt-OH groups, Pt_xRu_y-OH groups and traces of adsorbed water, and has shown increased occupation of (111) terraces with increasing particle size [10]. Ramirez-Cuesta *et al* have used INS to investigate hydrogen spillover from platinum sites onto the carbon support for a Pt/C catalyst [12]. Hydrogen spillover is implicated in many catalytic reactions as it is believed to provide a reservoir of reactive H atoms. This is seen by enhanced scattering at higher energies. The interaction of H_2 molecules with the surface of the Ru/C was found to be much weaker, consisting of the adsorbed H_2 molecules at low temperatures (23 K), which dissociated when the temperature was increased to 120 K. However, no evidence of H atoms adsorbed on the surface was found and spillover onto the carbon support was proposed to account for the missing dissociated H [13].

The work presented in this chapter reports the first attempts to study the coadsorption of hydrogen and carbon monoxide on Pt/C, codeposited PtMo/C and surface modified PtMo/C catalyst surfaces; in particular, the interaction of dihydrogen with surfaces covered in adsorbed layers of H atoms and CO molecules. Unlike XAS techniques, *in-situ* electrochemical measurements are not possible when investigating these samples. This is due to the presence of water, which would completely swamp the spectra, and because INS measurements have to be collected at temperatures below 20 K in order to dampen the thermal vibrations in the sample.

2 INS investigation of adsorbed hydrogen and CO species on a Pt/C catalyst

2.1 Experimental

The sample was 19.85 g of a 20 wt. % Pt on XC-72R carbon catalyst supplied by Johnson Matthey [14]. Previously, the catalyst powder was characterised using TEM, XRD, and CO chemisorption measurements and found to consist of fcc Pt crystallites with an average diameter of 2.69 nm and a Pt surface area of 20.88 m^2 per gram of catalyst. The sample was sealed in a thin-walled aluminium (99.99%) cell and exposed to hydrogen (99.999% Messer-Griesheim) at room temperature. The cell was evacuated to 10^{-6} mbar using a turbomolecular pump (Leybold) to remove any oxides present on the surface by conversion to water. Hydrogen uptake was measured by the pressure change in the constant volume system. This pre-treatment was repeated three times. The system then was left pumping for six weeks. (It should be noted that this six-week delay is not thought to be necessary, but occurred following disruption to the ISIS beam.) Further specific experimental details regarding the actual measurements can be found in the following results and discussion section.

The INS spectra were measured on the TOSCA spectrometer at the ISIS pulsed neutron facility at Rutherford Appleton Laboratory, Chilton, UK. The energy transfer range is between 16 and 4000 cm^{-1} and the resolution is $\Delta E/E<2\%$. During the experiments, the sample was cooled down to 12 K using a closed-cycle helium cryostat to eliminate

thermal broadening of the spectra. The spectra are presented as the Scattering Law $S(\boldsymbol{Q},\omega)$ (or function) (S intensity; $\boldsymbol{Q}$ momentum transfer and ω energy transfer) plotted versus energy transfer. The vertical axis is the neutron scattering intensity expressed as the scattering law. (This is a dimensionless quantity, and the horizontal axis represents zero-value intensity unless otherwise stated). All the spectra presented are difference spectra; the corresponding background spectra of the container and sample when no hydrogen present having been subtracted.

2.2 Results and Discussion

The pretreated catalyst was dosed with dihydrogen to equilibrium at 110 K, with an uptake of 320 cm^3. This low temperature was used in order to allow dosing with the sample within the cryostat of the spectrometer ready for data collection. The system requires a significant time to cool down to the required 12 K for data collection, making it impractical to dose the sample at room temperature and reload into the spectrometer every time. At 110 K, hydrogen is known to dissociatively adsorb on Pt [15]. During the dosing, the temperature of the catalyst was seen to increase by 0.5 K, which is evidence that some dissociation has taken place. Excess, unadsorbed hydrogen was removed by repeatedly opening the cell to a calibrated evacuated volume until there was no further release of dihydrogen. The volume retained by the catalyst was 80 cm^3. The temperature was reduced to 12 K and an INS spectrum of the hydrogen-dosed catalyst was collected (see figure 1).

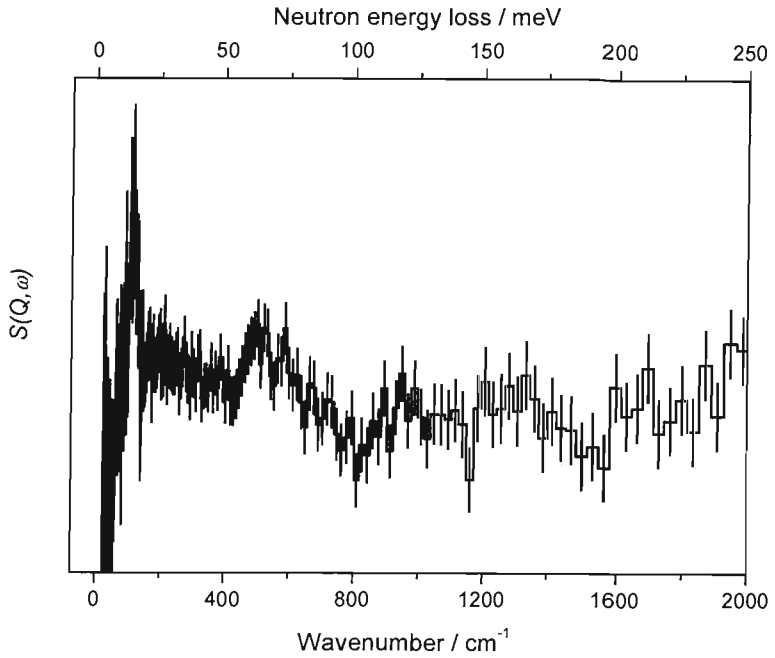

Figure 1 **INS spectrum at 12 K of 80 cm^3 H_2 retained on the 20 wt. % Pt/C catalyst after equilibrium dosing with H_2 at 110 K.**

The dihydrogen rotational (or rotor) peak is present at 120 cm^{-1} [16], indicating the presence of undissociated molecular hydrogen, and arises due to rotational transitions of this diatomic molecule. The broader peaks at higher wavenumbers correspond to vibrational modes of dissociated H adsorbed on the Pt surface [8-11]. INS spectra obtained by Albers *et al* [10] for H adsorbed on a similar 40 wt. % Pt/C catalyst show peaks at about 470 cm^{-1} and 550 cm^{-1}, which they assigned to the *E* modes of the fourfold and threefold sites, respectively. In addition, a peak at 650 cm^{-1} was assigned to the bending mode of linearly adsorbed H and the *A1* mode of the fourfold site. These assignments were based on earlier reported work [8,9], and are in good agreement with the spectrum shown in figure 1. One notable exception is the absence of peaks between 200 and 400 cm^{-1}, which are present in the spectrum by Albers *et al*, and were attributed to Pt-OH translational modes. This suggests that the pre-treatment process for the study reported here was more successful in removing residual adsorbed OH species.

The temperature was subsequently increased to 140 K and the sample was evacuated to a base pressure of 10^{-7} mbar for 30 min. The sample was then cooled to 12 K and the INS spectrum shown in figure 2 was obtained.

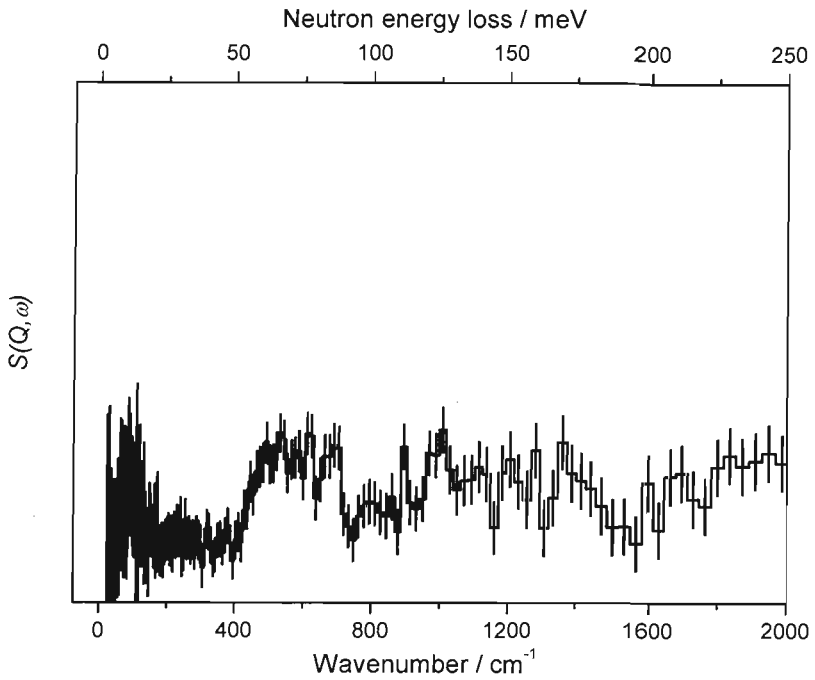

Figure 2 **INS spectrum at 12 K of H_2 exposed 20 wt. % Pt/C catalyst as in figure 1 after evacuation at 140 K.**

Figure 2 shows that evacuating the sample was successful in removing the undissociated molecular hydrogen, as evidenced by the absence of the H_2 rotor peak at 120 cm^{-1}. All other features of the spectrum remain essentially unchanged, indicating that the chemisorbed atomic hydrogen surface layer is still present.

In order to consider the locations of the dissociated H atoms adsorbed on the Pt/C catalyst more carefully, theoretical INS spectra of adsorbed H atoms on a variety of Pt surfaces was produced by computer modeling methods (details of which can be found in chapter 2, section 4.4). Using the Density Functional Theory (DFT) code DMol3 [17], vibrational eigenvalues and eigenvectors were calculated for hydrogen atoms placed in high symmetry sites on Pt(100), Pt(110) and Pt(111) surfaces. It was found that model structures with H atoms situated on atop sites were unstable and the calculations would not converge. The vibrational frequencies computed by DMol3 were used to generate theoretical INS spectra using the aClimax program [18]. Figure 3 shows these spectra overlaid with the experimental spectrum from figure 2. From these plots, it can be seen that the closest visual match comes from hydrogen located predominantly in hollow (three-fold) sites on Pt(111), with some contribution from hydrogen on multi-fold adsorption sites on a Pt(110) plane. This is in agreement with

INS studies reported previously [10,12]. The results also agree well with work published by Attard *et al* [19] who used cyclic voltammetry of various single crystal Pt electrodes in order to identify the combination of Pt sites that are present on a typical model cubo-octahedral Pt nanoparticle used in carbon-supported fuel cell catalysts. They found evidence of adsorbates binding preferentially to Pt(111) terrace sites on the nanoparticle.

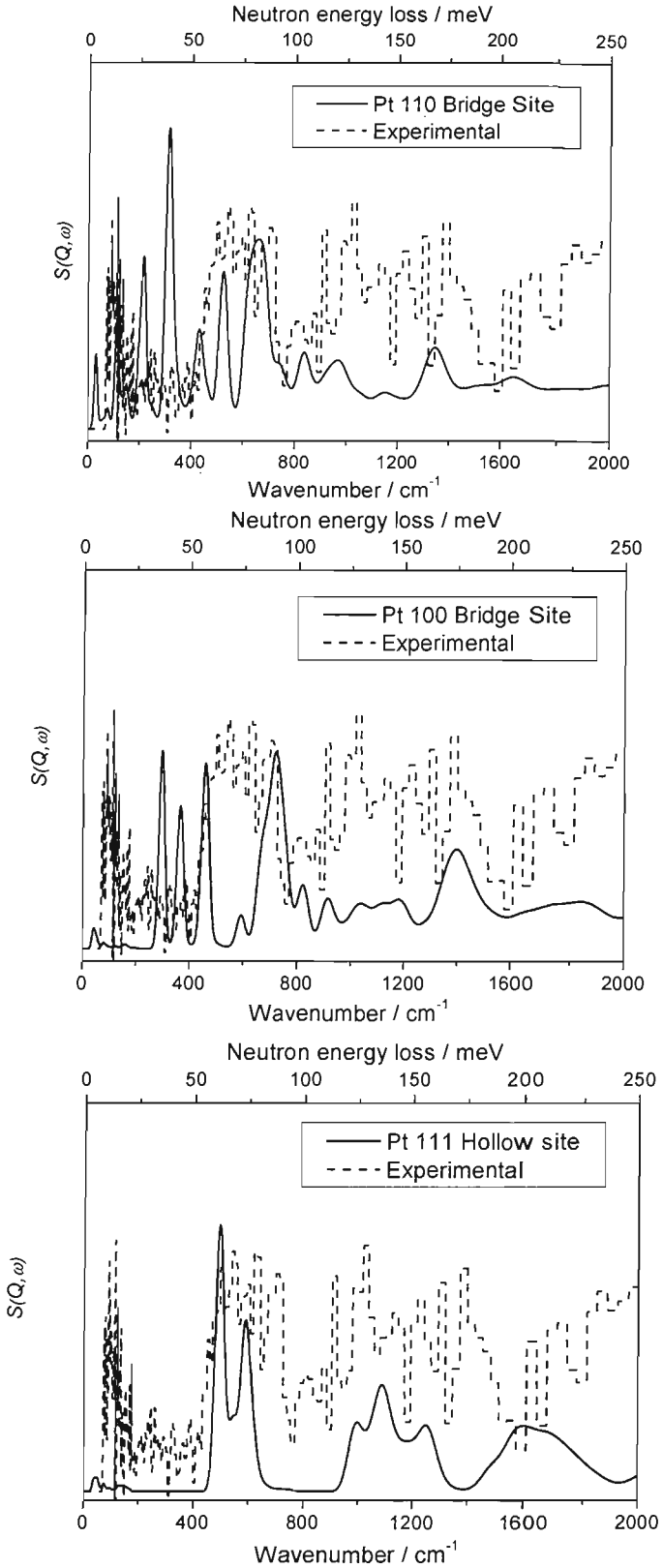

Figure 3 **Fitting of experimental INS data obtained at 12 K of H_2 exposed 20 wt. % Pt/C catalyst as in figure 1 after evacuation at 140 K to theoretical INS spectra of H adsorbed on a Pt(110) [top], Pt(100) [middle], and Pt(111) [bottom] surfaces.**

The atomic hydrogen covered Pt catalyst was subsequently dosed with CO (BOC, Research Grade N3.7) at 120 K to equilibrium. The system was not evacuated at this point in order to keep all hydrogen still present inside the sample can. The temperature was lowered to 12 K and the INS spectrum obtained subsequently can be seen in figure 4:

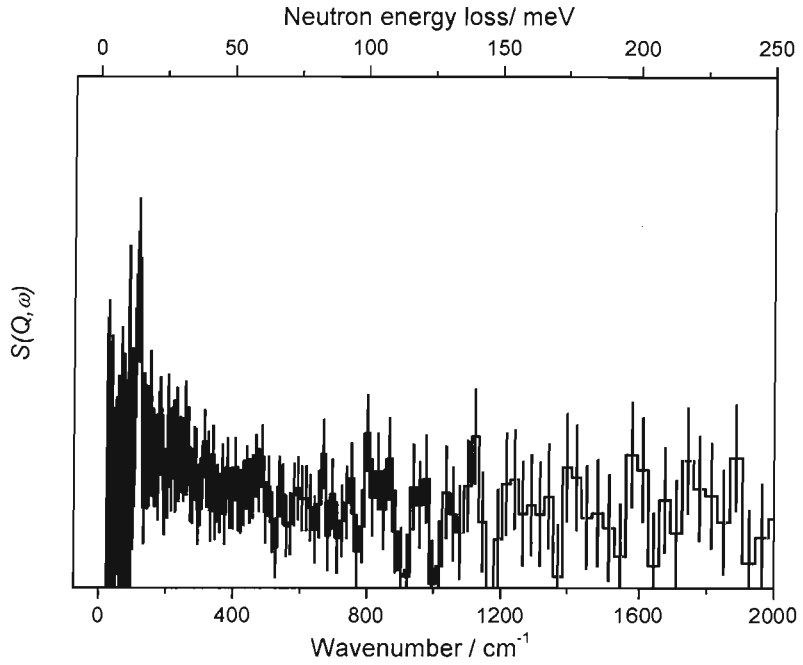

Figure 4 **INS spectrum at 12 K of H_2 exposed 20 wt. % Pt/C catalyst as in figure 2 after dosing to equilibrium with CO at 120 K.**

This spectrum shows the reappearance of the hydrogen rotor peak at 120 cm^{-1}, coupled with loss of features in the vibrational region. CO is known to adsorb strongly onto Pt sites, with a sticking coefficient close to 1. *Ab initio* calculations [20] and *in situ* electrochemical EXAFS studies of CO adsorbed on Pt/C fuel cell catalysts [21] indicate that CO is predominantly linearly adsorbed at the on-top sites. The lack of features, especially within the 400 to 800 cm^{-1} region, show that all of the dissociated H atoms adsorbed on the Pt surface have been fully displaced by CO, regardless of their adsorption sites. The displaced hydrogen appears to have reformed molecular hydrogen, as evidenced by the reappearance of the H_2 rotor peak.

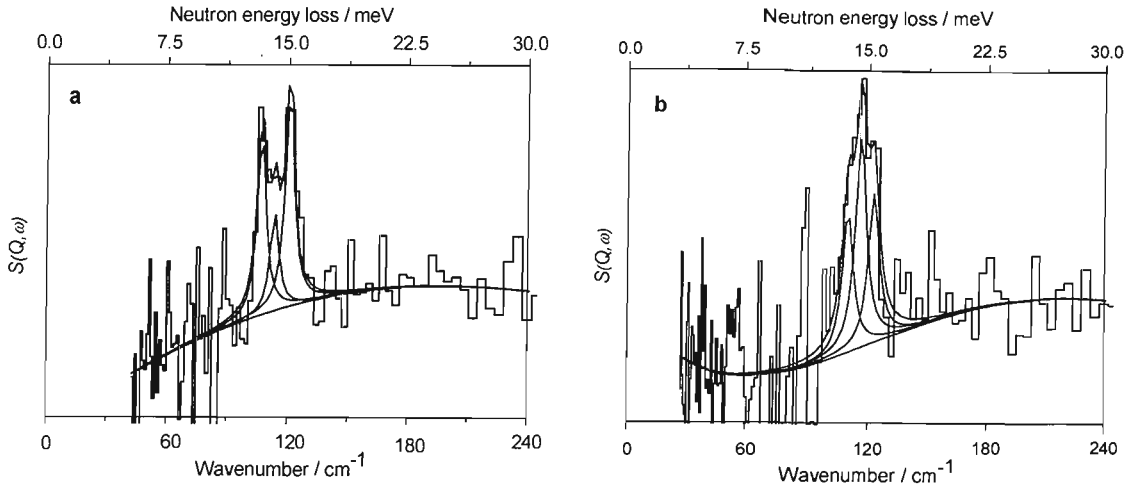

Figure 5 **Zoomed-in view of (a) H_2 rotor peak corresponding to the INS spectra shown in figure 1 after dihydrogen dosing, and (b) H_2 rotor peak corresponding to the INS spectra shown in figure 4 after CO dosing.**

The dihydrogen rotor peaks corresponding to figures 1 and 4, the catalyst sample exposed to 80 cm^3 H_2 and after the equilibrium dose of CO, respectively, are shown in more detail in figure 5. These intense peaks arise due to the $J(1\leftarrow0)$ transition of parahydrogen (p-H_2) [13,16], where J is the principal rotational quantum number. Parahydrogen is the ground state of hydrogen with allowed rotational states of those with even values of J, including 0. The second form is orthohydrogen (o-H_2), which has only odd values of J permitted, including the first rotational state, $J = 1$. Transitions between the states are rare as this requires a spin-flip mechansim; usually dihydrogen is composed of a stable mixture of 75 % ortho- and 25 % para- forms of hydrogen. However, cooled to below its boiling point (20.4 K), liquid dihydrogen will slowly convert from o-H_2 to p-H_2 over several days; a process greatly accelerated by the presence of paramagnetic centres found in the catalyst sample.

INS allows observation of the pure rotational transitions for hydrogen, whereas, in IR spectroscopy, these are forbidden because of the dipole selection rule for symmetrical diatomic molecules. For p-H_2 transitions from the $J = 0$ ground state and within its manifold, the coherent cross section of hydrogen is 1.8 barns. Transitions to J = odd states, however, are controlled by the incoherent cross section of 79.7 barns as a result of spin exchange with the neutron, which explains the significant intensity of the $J(1\leftarrow0)$ transition in the INS spectra.

The rotor peaks were fitted to three Lorentzians of equal width, FWHM (Full Width at the Half Maximum) and the results are shown as the smooth curves in figures 5a and 5b and the corresponding peak fitting parameters are summarised in Table 1. It can be seen that the central peak has much greater intensity for the H_2 interacting with the CO/Pt surface, implying significantly different interactions between the molecular hydrogen and the two adsorbate-covered surfaces. The position of the central peak (14.5 meV), which is the same as the intensity weighted average of the low and high energy peaks, is the same as that of H_2 on single walled carbon nanotubes [22] and similar to that for H_2 interstitially adsorbed in the octahedral site of C_{60} [23]. It seems likely, therefore, that the H_2 displaced by CO is only associated with the carbon support. It is believed that any dihydrogen associated with the carbon support does not give rise to any significant shift or splitting of the rotational peak from the gas values.

Table 1 Fitting parameters for rotor peaks corresponding to figures 5a and 5b

Sample condition / fixed peak width	Peak position / meV	Peak height	Integrated area
H/Pt (fig 5a) 0.665 meV	13.35	0.122	36.7
	14.17	0.063	19.0
	15.09	0.147	44.2
CO/Pt (fig 5b) 0.843 meV	13.67	0.092	28.0
	14.50	0.139	42.4
	15.33	0.097	29.6

The rotational energy of the $J(1\leftarrow0)$ transition is

$$E_{J(1\leftarrow0)} = 2B \qquad \textbf{Eq. 1}$$

where B is the rotational constant, and is given by

$$B = \frac{\hbar^2}{mR^2} \qquad \textbf{Eq. 2}$$

where m is the mass of a hydrogen atom, $\hbar$ is the reduced Planck constant, and R is the hydrogen molecule bond length. The rotational transition for a free hydrogen molecule in the solid state occurs at 118 cm^{-1} [14.7 meV] corresponding to the rotational constant, B = 59.3 cm^{-1} [16]. The shifts to lower energies of the central Lorentzian peaks in the peak fittings for figures 5a and 5b indicate elongations of the H-H bond

distance according to equation 2 above. The shift to 14.5 meV for the H_2 interacting with the CO covered surface corresponds to a bond elongation of 0.7 %, while that for H_2 interacting with the H covered surface corresponds to an elongation of 1.9 %. This indicates an increased interaction for the H_2 molecule when associated with the H modified Pt surface suggesting that a degree of charge transfer is taking place.

The splitting of the peaks is believed to be due to perturbation of the H_2 molecule; i.e. it is no longer free to rotate in all three dimensions. In essence, the hydrogen molecule is experiencing an anisotropic potential whereby the energy levels of the $J = 1$, $M = 0$, and $J = 1$, $M = \pm 1$, excited states are no longer degenerate, where M is the magnetic quantum number and reflects the z component of the angular rotation momentum vector, with z being defined as the molecular axis of dihydrogen.

The rotational energy levels with respect to the ground rotational state $J = 0$ are approximately given as

$$E_J = BJ(J + 1) \qquad \textbf{Eq. 3}$$

The degree of perturbation of the diatomic H_2 molecule can be deduced by calculating the height of the rotational barrier [24,25]. This is achieved by identifying the magnitude of the peak splitting and by subsequent referral to the rotational energy level diagram, as shown in figure 6.

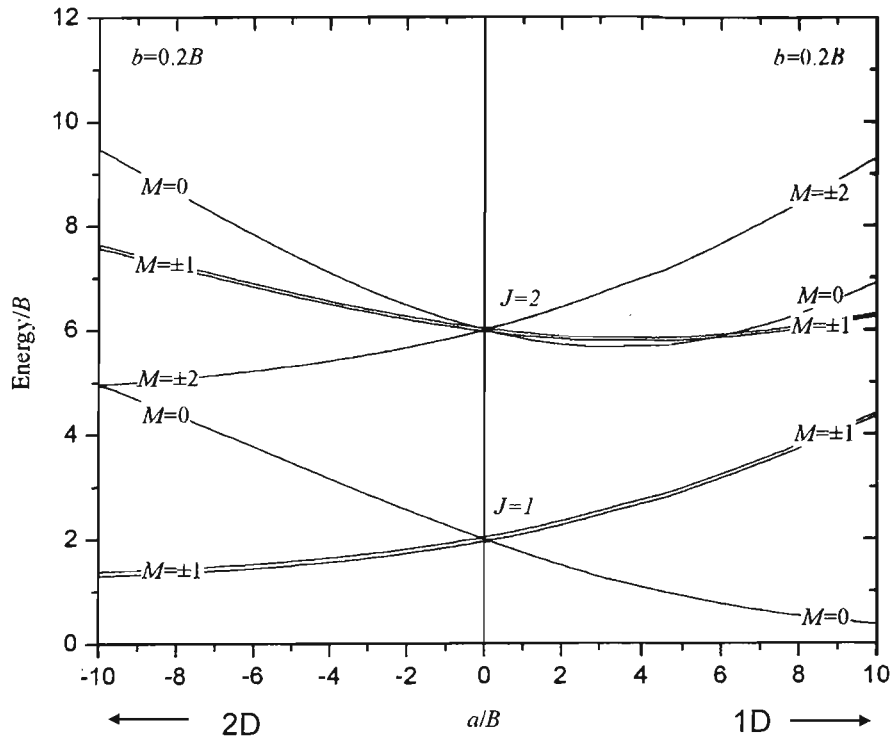

Figure 6 **Rotational states of constrained H_2 relative to the $J = 0$ ground state; energy in units of the rotational constant, B, vs. the perturbation parameter, a. [26]**

The total splitting for the H_2 interacting with the H/Pt surface is 1.74 meV. This splitting corresponds to the difference between the $M = 0$ and $M = \pm 1$ lines for the $J = 1$ rotational level. The value of a, the perturbation parameter corresponding to the rotational field strength, can be identified by reading off the x-axis at the point where the energy difference between the lines equals 1.74 meV. This gives a rotational barrier of $a = 4.36$ meV. The difference in energy between the outer peaks fitted for the rotor of H_2 interacting with the CO-covered surface is 1.66 meV, which gives rise to a similar rotational barrier height of 4.16 meV.

The relative integrated intensities of the lower and higher energy peaks can be used to determine the orientation of the H_2 molecules [22,25,27]. For molecules oriented perpendicular to the surface, a 1D rotor corresponding to positive values of a in figure 6, the $J = 1$, $M = 0$ state is lower in energy than the corresponding $M = \pm 1$ states. The higher energy peak should be the strongest transition and an intensity ratio of 1:2 is predicted. For cases of the molecule oriented parallel to the surface, a 2D rotor

corresponding to negative values of a in figure 6, the $M = \pm 1$ states are lower in energy, therefore it is now the lower energy peak which should have the greatest intensity, with an intensity ratio to the higher energy peak of 2: 1. The ratios calculated from the values shown in Table 1 are 0.83: 1 and 0.94: 1 for the H_2/Pt and CO/Pt respectively, which indicates that there may be a small preference for the perpendicular orientation of the H_2 molecules with respect to the surface of the catalyst particles, however the quality of the data makes such a conclusion tenuous at best.

3 INS investigation of adsorbed hydrogen and CO species on a co-deposited PtMo/C catalyst

3.1 Experimental

The sample was 18.14 g of a co-deposited 19.2 wt. % Pt / 4.3 wt. % Mo catalyst supported on XC-72R supplied by Johnson Matthey [14]. The catalyst had been heat treated to 1000 °C in argon after preparation. Previously, the catalyst powder was characterised using XRD and CO chemisorption measurements and found to consist of Pt crystallites with an average diameter of 3.0 nm and a Pt surface area of 2.33 m^2 per gram of catalyst. The sample was sealed in a thin-walled aluminium (99.99%) cell and the temperature set to 80 °C. The cell was evacuated to 10^{-7} mbar using a turbomolecular pump (Leybold) for 3 days. The sample was then exposed to hydrogen (99.999% Messer-Griesheim) at room temperature and the cell evacuated to 10^{-6} mbar to remove any oxides present on the surface by conversion to water. Hydrogen uptake was measured by the pressure change in the constant volume system. The system then was left pumping for a further three days. At this point, the cell was placed within the cryostat. The temperature was lowered to 12 K and an INS spectrum recorded for use as a background. Further specific experimental details regarding the actual measurements can be found in the following results and discussion section.

3.2 Results and Discussion

The pretreated catalyst was dosed with dihydrogen to equilibrium at 110 K, with an uptake of 74 cm^3. Excess, unadsorbed hydrogen was removed by opening the cell to a calibrated evacuated volume. The volume retained by the catalyst was 53 cm^3. The temperature was reduced to 12 K and an INS spectrum of the hydrogen-dosed catalyst was collected. The spectrum obtained had evidence of a dihydrogen rotor peak; however the spectrum was very noisy; most likely due to the very low signal corresponding to a significantly smaller amount of hydrogen in the cell compared with the previous experiment. An attempt was then made to add more hydrogen into the cell. The temperature of the cell was raised to 110 K, while that of the cryostat was increased to 80 K to remove any solid nitrogen that may have been present. The sample was dosed with dihydrogen twice in succession with a total uptake of 122 cm^3. An evacuated gas bottle was used to recover 71 cm^3 of dihydrogen. The total volume retained by the catalyst was now 104 cm^3. The temperature was reduced to 12 K and an INS spectrum of the hydrogen-dosed catalyst was collected (as shown in figure 7).

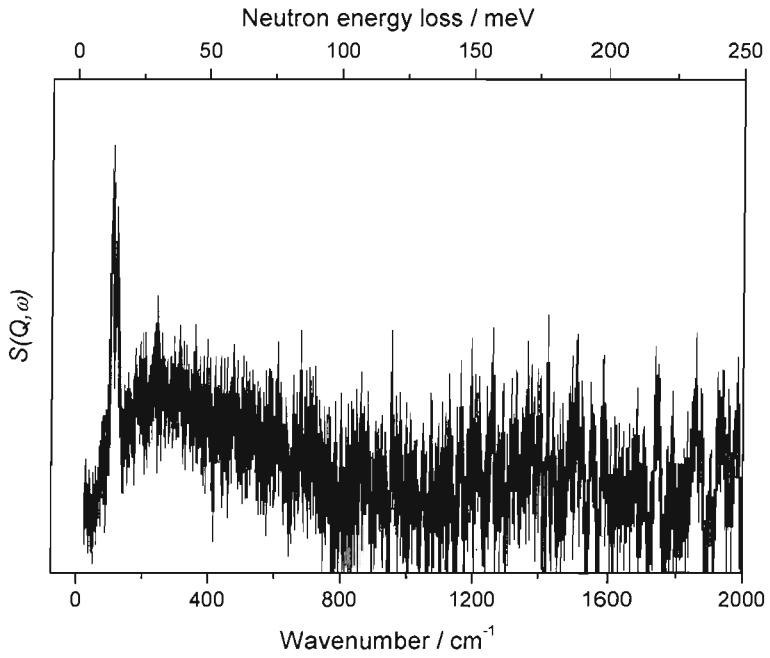

Figure 7 **INS spectrum at 12 K of 104 cm^3 H_2 retained on the 19.2 wt. % Pt / 4.3 wt. % Mo catalyst after equilibrium dosing with H_2 at 110 K.**

The dihydrogen rotational (or rotor) peak is present at 120 cm^{-1} [16], indicating the presence of undissociated molecular hydrogen. There is positive intensity in the vibrational energy range indicating the presence of dissociated H atoms bound to the surface of the catalyst. This region is less well defined than was seen previously for the 20 wt. % Pt/C catalyst, which may indicate that rather than having specific planes available on the Pt nanoparticle, the presence of Mo has created a much more inhomogenous surface. There appears to be regions of intensity between 200 and 600 cm^{-1}, and between 1200 and 1600 cm^{-1}. More features may be present, however, the large amount of noise and significant associated error make this difficult to determine. The vibrational intensity between 200 and 600 cm^{-1} appears to be a broad recoil tail, although this is more pronounced than for the Pt/C catalyst. This feature arises from the molecular recoil experienced by a molecule after the impact of a neutron. This causes a large portion of the intensity relating to the rotational transition to be contained in broad features above the rotational transition value. This effect is largest for light and weakly bound molecules. Inelastic scattering data on Mo samples has been obtained previously by Mitchell *et al* [28]. The samples under investigation were molybdenum trioxide supported on alumina. They found that, as the catalysts aged, there was an uptake of bound water giving rise to a broad peak in the INS spectra with a maximum near 450 cm^{-1}. This is attributed to a torsional or "twist" mode of a water molecule bound to the Mo through the oxygen atom. The co-deposited PtMo catalyst investigated here has been shown to have a significant portion of the Mo atoms within the surface layer of the nanoparticles in the form of either an oxide or an oxyhydroxide [see chapter 3]. The intensity in figure 7 could be due to water bound to these surface Mo atoms that was not removed by the initial pre-treatment and pumping process due to the strength of the interaction, or due to dissociated hydrogen forming surface oxyhydroxides with the Mo, or even going into the bulk and forming an hydrogen molybdenum bronze. Alternatively, Albers *et al* have reported peaks in the 200 – 400 cm^{-1} energy region corresponding to Pt-OH translational modes [10], which could occur if the pre-treatment process was not successful in completely reducing the Pt surface. This latter explanation is a possibility as this sample was only dosed with hydrogen once and evacuated for a shorter period of time during the catalyst pre-treatment, unlike the 20 wt. % Pt/C sample, which was dosed three times and left pumping for six weeks.

An attempt was made to improve the signal to noise ratio in the vibrational region by increasing the amount of hydrogen dissociation taking place and removing any remaining molecular hydrogen. This involved increasing the temperature of the cell to 170 K with the cell opened to an evacuated volume. Once this temperature was reached, the cell was isolated, the temperature lowered to 12 K and an INS spectrum obtained (see figure 8).

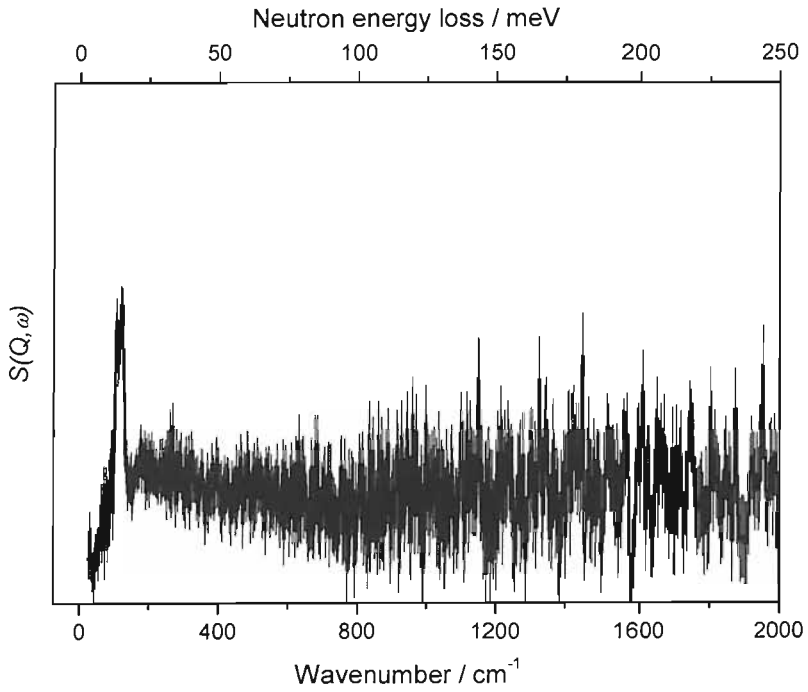

Figure 8 **INS spectrum at 12 K of H_2 dosed 19.2 wt. % Pt / 4.3 wt. % Mo catalyst as in figure 7 after increasing temperature to 170 K and opening cell to evacuated volume.**

The rotor peak is still present in the spectrum shown in figure 8, although the intensity has dropped compared to that in figure 7 suggesting that some of the weakly bound dihydrogen has been evacuated and/or the amount of dissociation has taken place. There does not appear to be an overall rise in the intensity of the vibrational region and the vibrational band between 200 and 600 cm^{-1} has also diminished. It is unlikely that any further dissociation has taken place to any significant degree and that the available surface area already has a complete monolayer of H atoms.

The temperature was subsequently increased incrementally and the sample opened to an evacuated volume while monitoring the pressure. The pressure increased steadily, eventually beginning to drop after the cell was held at 230 K for one hour. The sample was then cooled to 12 K and the INS spectrum shown in figure 9 was obtained. The cell was left open to pumping during the cooling process.

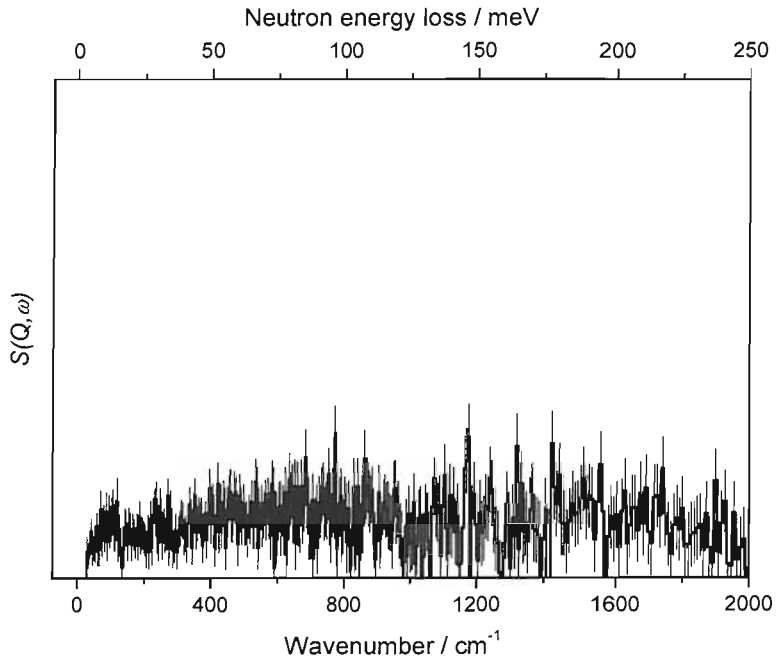

Figure 9 **INS spectrum at 12 K of H_2 dosed 19.2 wt. % Pt / 4.3 wt. % Mo catalyst as in figure 7 after temperature increased to 230 K and cell pumped out.**

The absence of the hydrogen rotor peak confirms that the evacuation of the molecular hydrogen has been successful. There is still positive intensity corresponding to vibrations of dissociated H atoms, although this overall intensity is lower than that observed in figures 7 and 8. Unlike the equivalent spectrum obtained for the 20 wt. % Pt/C catalyst (figure 2), there are no discernable features present for the vibrational spectrum in figure 9.

The atomic hydrogen covered Pt catalyst was subsequently dosed with CO (BOC, Research Grade N3.7) at 120 K to equilibrium. The system was not evacuated at this point in order to keep all hydrogen still present inside the sample can. The temperature

was lowered to 12 K and the INS spectrum obtained subsequently can be seen in figure 10:

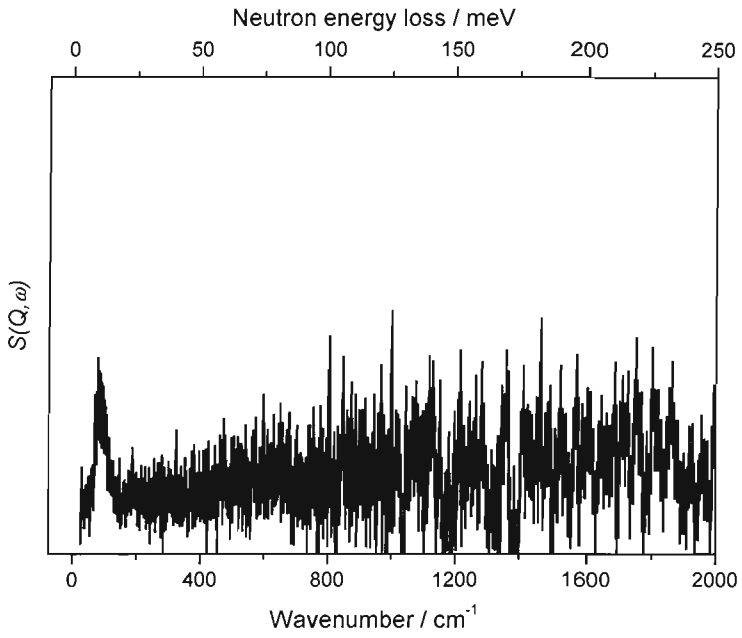

Figure 10 **INS spectrum at 12 K of H_2 exposed 19.2 wt. % Pt / 4.3 wt. % Mo catalyst as in figure 9 after dosing to equilibrium with CO at 120 K.**

The reappearance of the hydrogen rotor peak at 120 cm^{-1} is clearly observed in the spectrum, as was found for the Pt/C catalyst; however the intensity and integrated area under this peak are much lower than for Pt/C. The presence of this peak is the result of reforming of H_2 molecules from adsorbed H atoms following displacement by competitively adsorbed CO. The low signal level of the H_2 rotor is attributed to the much smaller coverage of adsorbed H on the PtMo/C catalyst compared to Pt/C.

The dihydrogen rotor peak corresponding to figure 7, the catalyst sample exposed to 104 cm^3 H_2, is shown in more detail in figure 11. (The rotor peak shown in figure 10 after CO dosing could not be fitted due to the poor signal: noise ratio.) A broad peak occurring around 8 meV is also visible, which was not present on the Pt/C catalyst and is attributed to a stronger interaction of some of the H_2 molecules with surface Mo species.

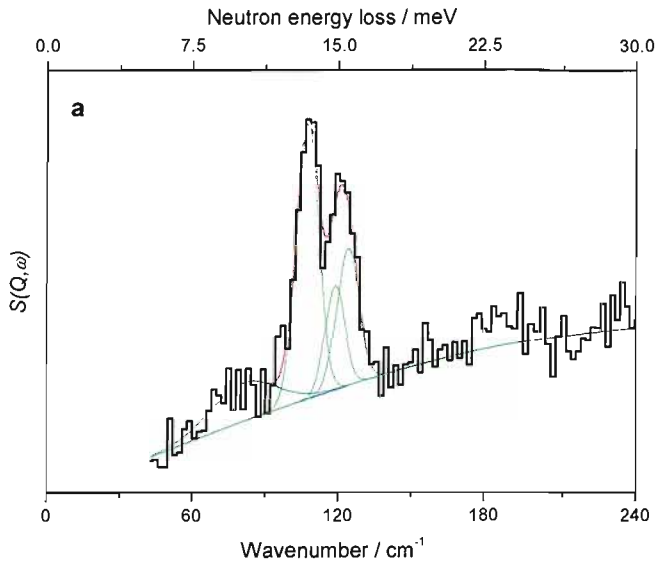

Figure 11 **H_2 rotor peak corresponding to the INS spectra shown in figure 7 after dihydrogen dosing.**

The rotor peak shown in figure 11 was fitted with three Gaussians of equal width, FWHM (Full Width at the Half Maximum) and the results are shown as the smooth curves in figure 11a. The results are summarised in Table 2.

Table 2 **Fitting parameters for rotor peak corresponding to figure 11**

Sample condition / fixed peak width	Peak position / meV	Peak height	Integrated area
H/Pt (fig 11)	13.30	0.260	44.8
1.312 meV (outer peaks)	14.70	0.099	15.3
1.159 meV(central peak)	15.34	0.130	22.4

For the H_2 interacting with the H/PtMo surface, the rotor peak is again seen to be split as was previously the case for the 20 wt. % Pt/C catalyst sample. The area of the lowest energy peak is twice that of the highest energy peak. This indicates that the majority of the molecular hydrogen is preferentially oriented parallel to the surface. This is in contrast to the Pt/C catalyst where there were almost equal amounts of molecules oriented parallel and perpendicular with only a slight preference toward perpendicular. The height of the rotational barrier was calculated and found to be -4.95 meV, which is slightly higher in magnitude than was found with the Pt/C catalyst, possibly due to interactions with surface Mo oxides. The H-H bond was found to be

elongated by 2.0 %, which is approximately the same as that for H_2 interacting with a H/Pt surface in section 2.

4 INS investigation of adsorbed hydrogen and CO species on a surface modified PtMo/C catalyst

Two separate experiments were conducted using the surface modified PtMo/C catalyst. The first experiment was an attempt to use INS to determine whether any hydrogen molybdenum bronzes (H_xMoO_3) were present in the sample. There are four distinct phases of the bronzes depending on the degree of hydrogen insertion, with values of $0 < x < 2$. Glemser *et al* showed that compounds of this type could be prepared by the reduction of MoO_3 in aqueous acidic media using zinc [29,30]. It has also been found that electroreduction of the least reduced bronze (where $0.23 < x < 0.40$) in sulphuric acid can give rise to the more reduced phases. Zhang *et al* performed cyclic voltammetry experiments on MoO_3 electrodes and observed a sharp current increase at -0.25 V, which has been associated with the formation of hydrogen bronzes [31,32], even without first converting to the least reduced bronze form using zinc in aqueous acid media.

The hydrogen molybdenum bronzes are analogous to the series of tungsten bronzes. WO_3 has been shown to form a bronze when heated to above 673 K in hydrogen, or even at room temperature in the presence of both Pt and adsorbed water [33]. Ressler *et al* have also shown the formation of hydrogen molybdenum bronzes during a temperature programmed reduction of MoO_3 in the presence of hydrogen between 300 and 773 K [34].

By analogy to the tungsten bronzes, it seems possible that a hydrogen molybdenum bronze may form during the preparation of the CSR PtMo/C catalyst, which involves a final reduction step of heating to 473 K in hydrogen. This would of course be dependent on the surface molybdenum atoms being sufficiently oxidised upon exposure to air during the filtration and drying step before the final reduction. It would also be dependent on the temperature being high enough or, if it is not, on the presence

of Pt aiding in the formation as seen with the tungsten bronzes. What is clear, however, is that there would not be a significant amount of adsorbed water present at this stage. However, this generally occurs with aging (exposure to atmospheric water vapour) over a few months.

In order to see if there was any bronze present, an INS spectrum of the prepared CSR PtMo/C catalyst was obtained. The sample was then heated so that any bronzes present would be removed by a process of thermal dehydrogenation as described in the literature [35,36]. A subsequent INS spectrum subtracted from the first should show positive intensity if any bronzes were initially present.

The second experiment on a separate sample of the same catalyst sample involved dosing with hydrogen and carbon monoxide in the same manner as the earlier experiments on Pt/C and co-deposited PtMo samples.

4.1 Experimental

4.1.1 Sample tested for presence of hydrogen molybdenum bronzes

A 40 wt. % Pt/XC72R catalyst prepared by proprietary methods [14] was supplied by Johnson Matthey. The catalyst was not heat treated. The catalyst dispersion was 0.261 and the metal area was determined by CO chemisorption measurements and found to be 64.5 $m^2 g^{-1}$ Pt (corresponding to 25.8 $m^2 g^{-1}$ of catalyst). The average crystallite size by XRD was approximately 4.4 nm. The controlled surface reaction (CSR) method described in chapter 2, section 1.2.2 was used to deposit a ½ monolayer of Mo on the surface of the Pt nanoparticles. Elemental analysis by ICP-ES determined the final composition to be 40.5 wt. % Pt and 2.44 wt. % Mo. The new metal area was determined by CO chemisorption measurements and found to be 13.29 $m^2 g^{-1}$ Pt (corresponding to 5.38 $m^2 g^{-1}$ of catalyst) and the crystallite size by XRD was approximately 10.3 nm.

13.71 g of the Mo modified sample was sealed in a steel experimental cell. This cell was used because, unlike the aluminium can, it did not require a strip of indium metal

as a seal, thereby allowing the sample to be heated up to 673 K; indium would melt at this temperature. The cell was mounted onto the base of a centre-stick and the temperature set to 353 K. The cell was evacuated to 10^{-7} mbar using a turbomolecular pump (Leybold) for 3 days. The sample was exposed to hydrogen (99.999% Messer-Griesheim) at room temperature and the cell evacuated to 10^{-6} mbar to remove any oxides present on the Pt surface by conversion to water. The Mo oxyhydroxides will remain. Hydrogen uptake was measured by the pressure change in the constant volume system. The system then was left pumping for a further three days. At this point, the cell was placed within the cryostat. The temperature was lowered to 12 K and an INS spectrum recorded for use as a background. Further specific experimental details regarding the actual measurements can be found in the following results and discussion section.

4.1.2 Sample dosed with hydrogen and carbon monoxide

The sample was 18.07 g of surface modified PtMo/XC72R as described in section 4.1.1. The sample was sealed in a thin-walled aluminium (99.99%) cell and the temperature set to 353 K. The cell was evacuated to 10^{-7} mbar using a turbomolecular pump (Leybold) for 3 days. The sample was exposed to hydrogen (99.999% Messer-Griesheim) at room temperature and the cell evacuated to 10^{-6} mbar to remove any oxides present on the surface by conversion to water. Hydrogen uptake was measured by the pressure change in the constant volume system. The system then was left pumping for a further three days. At this point, the cell was placed within the cryostat. The temperature was lowered to 12 K and an INS spectrum recorded for use as a background. Further specific experimental details regarding the actual measurements can be found in the following results and discussion section.

4.2 Results and discussion

4.2.1 Sample tested for presence of hydrogen molybdenum bronzes

The background INS spectrum of the sample was collected as described in section 4.1.1. The cell was then removed from the cryostat and heated within a portable heating furnace to 573 K. This temperature was chosen as it is just above the first dehydrogenation temperature of 563 K reported by Eda *et al*; with the second occurring at 651 K. (It should be noted that the dehydrogenations described in the literature occurred in a nitrogen environment). The sample can was pumped out during heating, and a corresponding increase in base pressure was observed, indicating that something was desorbing. This may be removal of water from the bronze by thermal dehydrogenation, or residual organics from the preparation of the sample, although the latter is unlikely. The cell was isolated and placed back in the cryostat. After being cooled to below 20 K, an INS spectrum was obtained. Figure 12 shows the initial INS spectrum after subtraction of the spectrum after heating to 573 K.

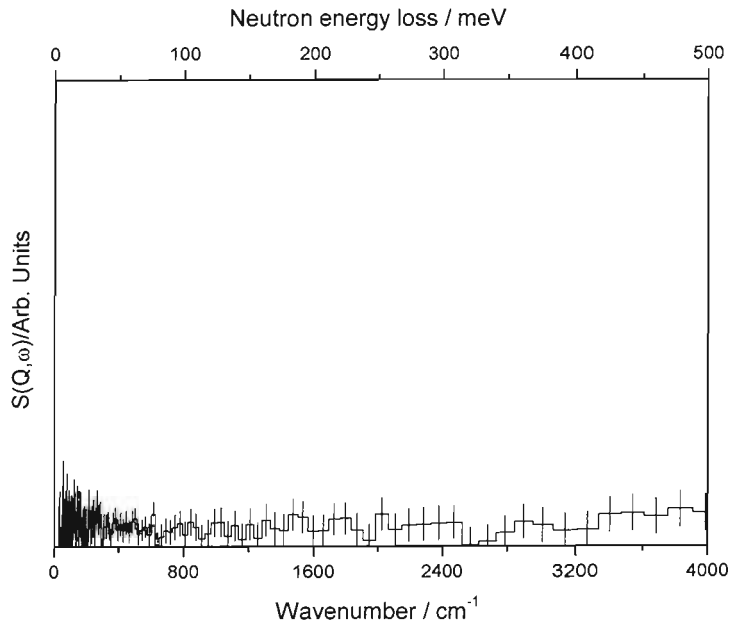

Figure 12 **INS spectrum below 20 K of CSR PtMo/C catalyst after heating to 573 K with pumping.**

Figure 12, with the x-axis corresponding to y = 0, shows positive intensity for the difference spectrum, indicating that there was more hydrogen present in the sample before heating.

The sample can was removed from the cryostat and again placed within a portable heating furnace. The temperature was increased to 673 K and the base pressure measured as the exhaust was pumped out. The initial pressure was 1.1 x 10^{-6} mbar, which increased to 2.2 x 10^{-4} mbar once the sample reached 673 K. The heater was turned off, and the sample left to cool overnight. The sample can was then placed back in the cryostat and an INS spectrum obtained whilst cooling.

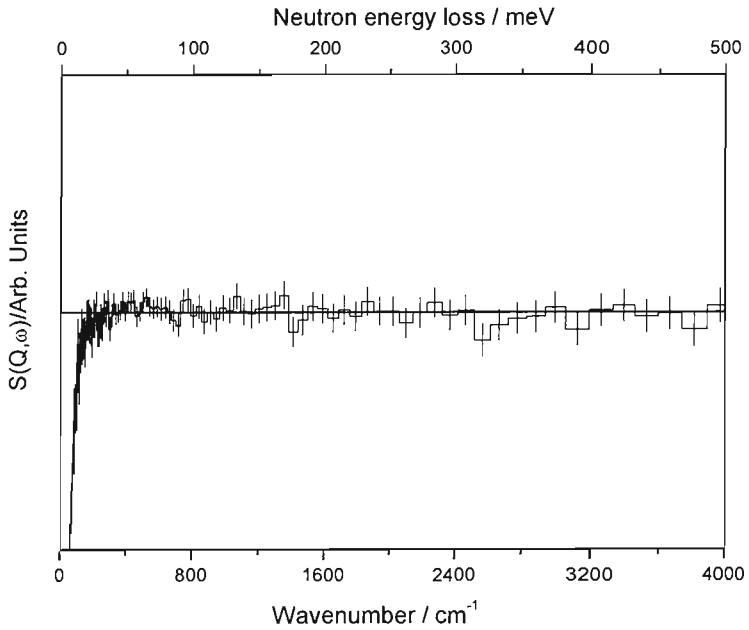

Figure 13 **INS spectrum of CSR PtMo/C catalyst after heating to 673 K with pumping (horizontal line corresponds to y = 0).**

The measured intensity is very small and is, on average, negative. This result contradicts that for the sample heated to 573 K. There were, however, problems with temperature control at this point, leading to the spectrum being recorded above 20 K with only one scan taken. The difference spectrum is essentially unusable.

Inelastic neutron studies of the four hydrogen molybdenum bronze phases carried out by Dickens *et al* found that, for $H_{0.34}MoO_3$, the H was present as –OH with an intense band at 1267 cm^{-1}, while the more reduced forms only had peaks associated with $–OH_2$

groups present around 1600 cm^{-1} [37]. Unfortunately, the signal intensities measured during this experiment are so small, that it is impossible to determine if any such peaks are present in this instance. In summary, while there is evidence that heating the sample led to some chemical species being detected in the exhaust as seen by an increase in base pressure, and that a small, but positive, intensity was seen in the difference spectrum after heating to 573 K; there is no way to determine if this is in fact evidence of any hydrogen molybdenum bronze phase being present initially.

4.2.2 Sample dosed with hydrogen and carbon monoxide

The pretreated second sample of CSR PtMo/C was dosed with dihydrogen from a gas bottle filled to atmospheric pressure to equilibrium at 110 K. This process was then repeated a further two times. The combined uptake of hydrogen was 295 cm^3. Excess, unadsorbed hydrogen was removed by opening the cell to a calibrated evacuated volume. The volume retained by the catalyst was 73 cm^3 of hydrogen. A further dosing and two subsequent evacuations yielded no significant addition of hydrogen. The temperature was reduced to below 20 K and an INS spectrum of the hydrogen-dosed catalyst was collected.

Figure 14 shows the difference spectrum obtained after subtraction of the background recorded after catalyst pre-treatment. The signal intensity is quite small with no discernable features present in the vibrational region.

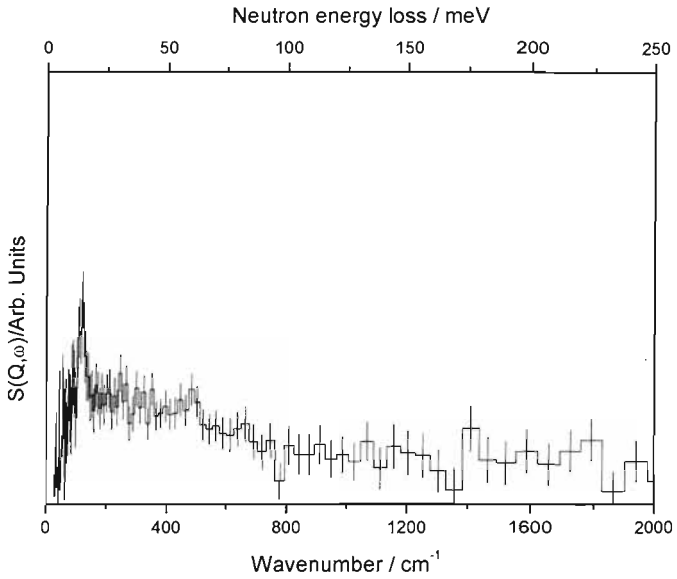

Figure 14 **INS spectrum recorded below 20 K of 73 cm^3 H_2 retained on the CSR PtMo/C after equilibrium dosing with H_2 at 110 K.**

There is a small rotor peak present around 120 cm^{-1}, which can be seen in more detail in figure 15, although it is apparent that a sensible peak fitting can not be attempted due to the low intensity resulting in a decreased signal to noise ratio.

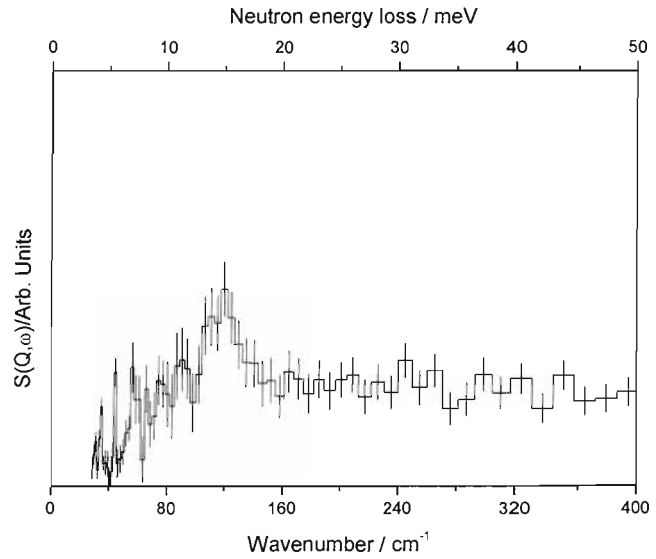

Figure 15 **INS spectrum recorded below 20 K of 73 cm^3 H_2 retained on the CSR PtMo/C after equilibrium dosing with H_2 at 110 K, close-up on rotor peak.**

It is impossible to determine whether the rotor peak is split in this instance, which would indicate weakly adsorbed dihydrogen (interacting with strongly bound dissociated H atoms adsorbed on the Pt surface), where the rotational motion is hindered in at least one plane. The weakness of the signal intensity is likely due to the small amount of hydrogen actually present within the sample can. The Pt/C catalyst in section 2 was seen to take up 320 cm^2 of dihydrogen, compared with just 73 cm^3 (or less) for this catalyst. This is due to the greatly reduced Pt catalytic area present on this catalyst. This area is similar to that found with the co-deposited PtMo/C catalyst described in section 3, which had been heated to 1273 K in Argon in an attempt to increase the alloying of the two metals. This greatly increases the catalyst particle size due to sintering. The CSR catalyst, however, was heated to only 473 K so the effect of sintering should be significantly less. The 40 wt. % Pt/C catalyst used in the CSR preparation initially had a Pt catalytic area of 25.8 $m^2 g^{-1}$ catalyst, compared with 5.4 $m^2 g^{-1}$ catalyst once the ½ monolayer of Mo (as confirmed by the assay results) was present on the surface. The fact that only a fifth of available surface area remains available may be partly due to a small amount of catalyst sintering occurring, although it is also likely that the Mo rapidly forms oxides upon exposure to air, which can not be removed by the catalyst pre-treatment, and may block more of the Pt sites.

The sample was again dosed to equilibrium at 110 K, with an uptake of 244 cm^3 of dihydrogen. In order to observe the maximum possible hydrogen signal, no recovery was attempted. The cell was isolated and an INS spectrum obtained once the temperature had dropped to below 20 K. Figure 16 shows the difference spectrum obtained after subtraction of the background. The signal intensity obtained is much greater than was seen for the sample as shown in figure 14.

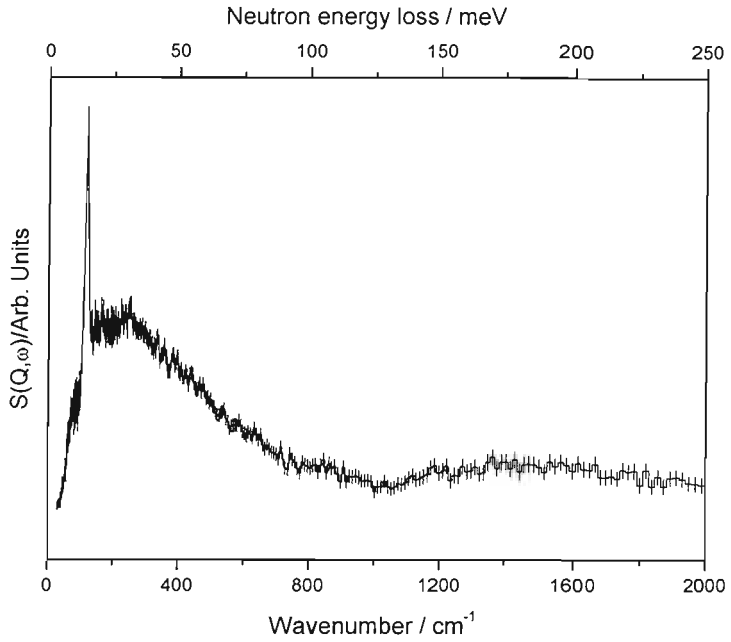

Figure 16 **INS spectrum recorded below 20 K of additional 244 cm^3 H_2 added to the sample cell containing the CSR PtMo/C after equilibrium dosing at 110 K with no recovery.**

The vast majority of hydrogen is present within the sample can as molecular hydrogen as seen by the intense molecular rotor peak and following recoil feature, which obscures any vibrational features that would be present from dissociated H atoms adsorbed on the Pt surface. The lack of vibrational features seen in the spectrum shown in figure 14 indicates that the available Pt area is so small that these features are likely to be indiscernible, regardless of the presence of the recoil feature in the spectrum.

A peak fitting of the rotor peak is shown in figure 17.

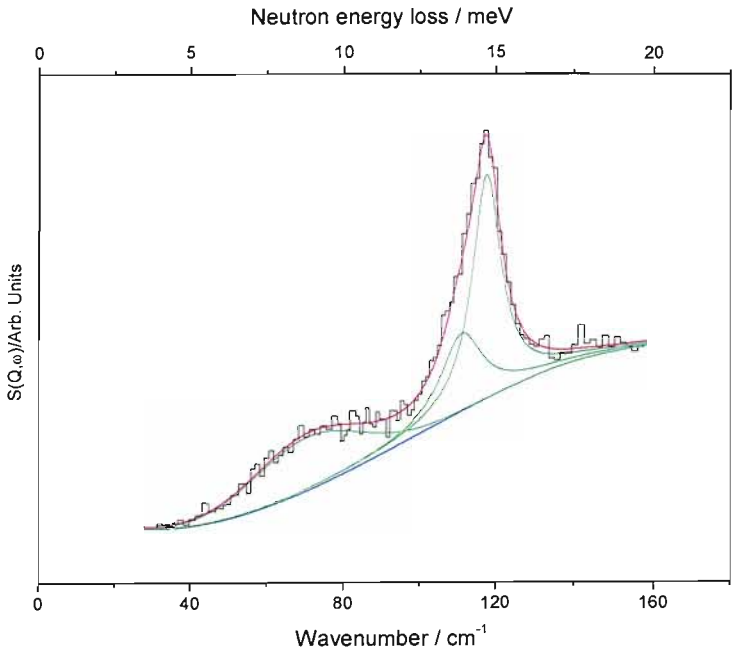

Figure 17 **H_2 rotor peak corresponding to the INS spectra shown in figure 16 after dihydrogen dosing.**

Table 3 **Fitting parameters for rotor peak corresponding to figure 17**

Sample condition / fixed peak width	Peak position / meV	Fixed peak width / meV	Peak height	Integrated area
H/Pt (fig 17)	8.81	4.14	0.285	27.6
	13.87	1.65	0.419	23.3
	14.68	1.14	1.207	49.2

The peak fitting was achieved using the Origin software package. Different fixed peak widths were used in order to achieve the best visual fit. From the peak fitting, it can be seen that the rotor peak can be fitted with one large peak occurring at 14.68 meV – the expected position for a rotational transition of a free hydrogen molecule in the solid state. A small shoulder can also be fitted at 13.87 meV, indicating that the rotation of some of the dihydrogen present may be hindered in at least one dimension, causing a small amount of peak splitting. This effect has been attributed to dihydrogen interacting with the H/Pt surface, as seen with the Pt/C and codeposited PtMo/C catalysts investigated previously. However, the majority of the hydrogen appears to be

present as free dihydrogen as a result of dosing the sample, but not attempting a recovery to remove any hydrogen that is not adsorbed (either strongly or weakly). The other feature of note is the broad shoulder occurring centered at 8 meV. This feature was also present on the co-deposited PtMo/C catalyst investigated in section 3, but was not found for the Pt/C catalyst investigated in section 2. This feature only exists in the presence of Mo, and is likely the result of a strong interaction between the dihydrogen and the oxygen lone pairs of the surface Mo oxides.

An attempt was then made to try to reduce the sample further, to try to minimise the amount of surface oxides present so that the available Pt area may be increased. This involved heating the cell to 363 K and pumping out for four hours. Four successive dosing/recovery procedures with dihydrogen took place. Slow recovery times were recorded initially indicating the removal of water. An INS spectrum of the re-reduced sample was recorded once the temperature of the cell was cooled to below 20 K.

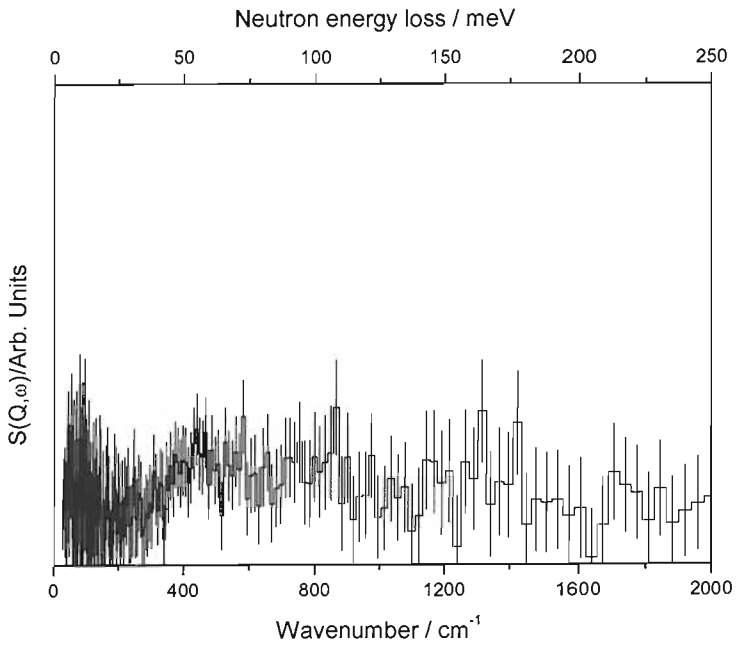

Figure 18 **INS spectrum recorded below 20 K of re-reduced CSR PtMo/C after dosing with dihydrogen at 363 K and pumping out over four hours**

The difference spectrum shown in figure 18 has a positive signal, which indicates the presence of hydrogen. The absence of a rotor peak means that only strongly adsorbed, dissociated hydrogen is present. The removal of all molecular hydrogen has also

allowed some features to be visible in the vibrational region of the spectrum; notably between 400 and 450 cm^{-1}, around 800 cm^{-1}, and between 1100 and 1300 cm^{-1}. The features around 400 and 1200 cm^{-1} were seen previously for hydrogen adsorbed on a Pt(111) hollow site when using the DFT code DMol3 in section 2.2.

The sample was heated to 110 K and dosed with dihydrogen to see if the coverage could be increased further. After recovery, an additional 31 cm^3 of H_2 had gone into the cell. The cell was not pumped out directly meaning that dihydrogen having an interaction with the H/Pt, or the Mo oxides, is likely to be present.

The catalyst was subsequently dosed with CO (BOC, Research Grade N3.7) at 110 K to equilibrium. The system was not evacuated at this point in order to keep all hydrogen still present inside the sample can. The temperature was lowered to below 20 K and the INS spectrum obtained subsequently can be seen in figure 19:

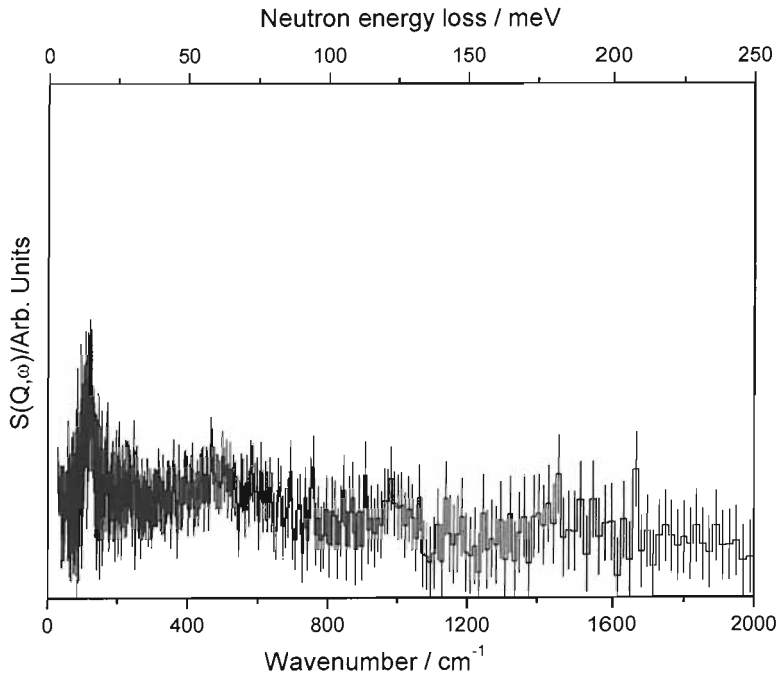

Figure 19 **INS spectrum at 12 K of H_2 exposed CSR PtMo/C catalyst after dosing to equilibrium with CO at 110 K**

Figure 19 shows the presence of a small rotor peak. There are also visible regions of intensity in the vibrational region, notably between 400 and 600 cm^{-1}, 1000 cm^{-1}, and between 1400 and 1500 cm^{-1}. This is in contrast to results obtained for the Pt/C and

codeposited PtMo/C catalysts, where the introduction of CO caused a complete loss of features in the vibrational region of the spectrum due to the displacement of the dissociated H atoms from the Pt sites. The fact that some are still visible indicates either that not all of the H atoms have been displaced from the Pt sites, or the features are due to dissociated H atoms that have spilled over onto the carbon support, and/or H atoms that have formed OH species with the Mo surface oxides.

Figure 20 shows the peak fitting obtained for the rotor peak for the spectrum shown in figure 19.

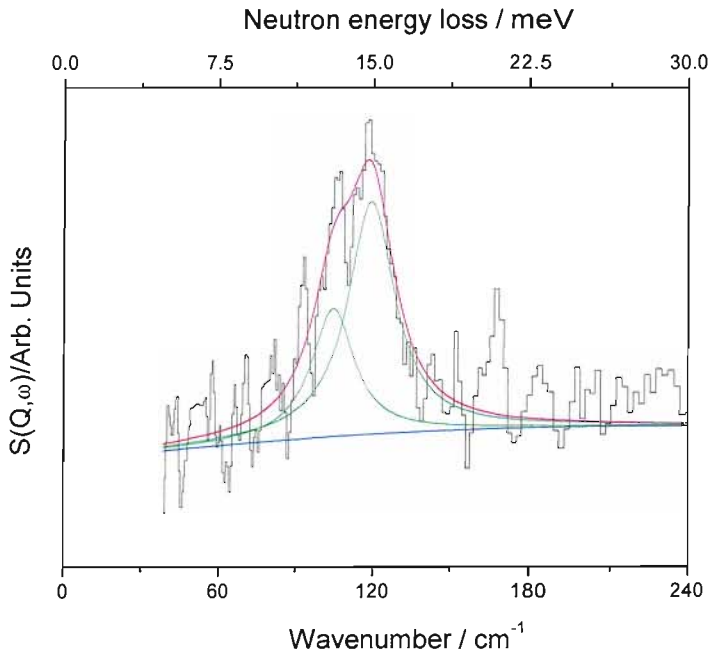

Figure 20 **H_2 rotor peak corresponding to the INS spectra shown in figure 19 after carbon monoxide dosing**

It is evident that the signal intensity is very low resulting in a large degree of noise. Comparison of the areas under the spectra indicate that there is approximately 60 cm^3 of hydrogen present in the sample cell; half of which was present as dissociated hydrogen after the repeated sample reductions, and the other half being added subsequently. It appears that the peak is split to some degree, which is again in direct contrast to previous experiments to the Pt/C experiment.

Table 4 Fitting parameters for rotor peak corresponding to figure 20

Sample condition / fixed peak width	Peak position / meV	Fixed peak width / meV	Peak height	Integrated area
CO dosed (fig 20)	13.06	2.49	0.020	33.5
	14.91	2.75	0.036	66.5

The area of the higher energy peak is twice that for the lower energy peak. The increased size of the higher energy peak is a strong indication that the H_2 is interacting with the sample in such a way that it is perpendicular to the surface; i.e. a 1-D type system. Calculation of the rotational barrier is therefore achieved using the energy levels on the right-hand side of figure 6. Using this diagram, the apparent value of $2B$ for the hydrogen interacting with a CO dosed catalyst is found to be 14.277 meV. This shift from the transition value of 14.7 meV for a free hydrogen molecule corresponds to a bond elongation of 1.4 % when calculated using equation 2. This value is approximately mid-way between the value of 0.7 % obtained for H_2 interacting with a H/Pt surface, and 1.9 % obtained for H_2 interacting with a CO/Pt surface when testing the Pt/C catalyst in section 2. The increased bond elongation found here, when compared with Pt/C, means that the some of the dihydrogen present is interacting with something other than a CO covered Pt surface. This could either be H/Pt sites not displaced by CO due to steric hindrance by Mo oxides, or it could be interacting with the Mo oxides themselves. The latter is likely to be a stronger interaction due to the lone pairs on the oxygen atoms, and is therefore more likely the cause of the broad peak seen in figure 17 at around 8 meV. This feature is not seen in figure 20; however, the signal is weak and noisy, hindering a more complete investigation. The height of the rotational barrier was calculated to be 4.61 meV, which is fairly consistent with the results obtained on the previous catalysts, although the higher energy peak has double the intensity meaning that the majority of H_2 molecules are oriented perpendicular to the catalyst surface.

5 Conclusions

Inelastic Neutron Scattering studies have been carried out on Pt and PtMo-based electrocatalysts for hydrogen oxidation in PEMFCs. These experiments are the first examples of studying the interactions of the H_2 molecule with hydrogen and carbon monoxide-modified Pt nanoparticle surfaces, as well as marking the first time that PtMo-based catalysts have been investigated using INS.

INS techniques were used because of their particular sensitivity to the presence of hydrogen due to its large cross-section value. The energy range over which the data can be collected allows information on the interactions of dihydrogen molecules with the sample to be investigated by studying the sharp rotational peak at lower energy; plus the features in the vibrational range of the spectrum can be fitted theoretically providing information on the specific surface sites on which dissociated H atoms are situated.

There are some limitations to the technique, however. The spectra can only be collected at temperatures below 20 K, to remove the effect of thermal broadening. In addition, there can be no water present, as the resulting features would swamp the spectra. This determines that the catalyst can only be studied *ex situ*, which puts the technique at a disadvantage when compared with EXAFS measurements, where the sample can be studied as an electrode in an operational fuel cell. In addition, the neutron scattering is quite a weak effect and the intensity is directly proportional to the concentration of the sample; or more precisely the amount of hydrogen present in the sample. For the purposes of the experiments reported here, this involved using up to 20 g of catalyst sample in order to maximise the signal obtained.

The Pt/C catalyst was found to have the highest quality data out of the three systems studied, as a result of the larger available Pt surface area. This is made possible by the fact that this catalyst is not required to be heat treated, so particle agglomeration is very small. The larger available area allows for a greater amount of adsorbed hydrogen atoms to be present, which results in more signal intensity and less noise. This makes it possible to determine specific regions of intensity in the vibrational spectrum, which can be compared with theoretical data produced by computing eigenvalues for H atoms

sitting on specific Pt crystal planes using the DFT-based software DMol3, which are then translated into an INS spectrum using the aClimax program. This was used to show that the hydrogen atoms are located predominantly in hollow (three-fold) sites on Pt(111), with some contribution from hydrogen on multi-fold adsorption sites on a Pt(110) plane.

The splitting and shifting of the H_2 rotor peak was used to identify the strength of the interactions with the hydrogen and carbon monoxide modified Pt surfaces. The hydrogen molecule interacting with the H/Pt surface was found to be strongly perturbed. The calculated H-H bond elongation of 1.9 % indicates that a degree of charge transfer is taking place between the molecule and the surface atoms, while the rotational barrier value and nature of the splitting indicate that the molecule is hindered and is no longer free to rotate in all directions. Indeed the intensity of the split peaks infers a perpendicular orientation of the molecule with respect to the metal surface. In contrast, the minimal elongation of the H-H bond and the intensity of the central peak indicate that the dihydrogen formed by the displacement of hydrogen atoms by CO is only weakly associated with the catalyst surface. The shifting of the central peak to 14.5 meV also suggests that this reformed molecular hydrogen is situated on the carbon support.

The data for the codeposited PtMo/C catalyst showed a notable decrease in quality compared to that for Pt/C. This is a direct result of the drastic reduction in the Pt surface area, so that the amount of hydrogen retained by the catalyst was greatly decreased. The catalyst used was representative of one of the higher performing PtMo samples produced by Johnson Matthey, containing approximately 20 wt. % Pt. Whilst a higher wt. % of Pt in the sample (e.g. 40 wt. %) may have increased the Pt area and improved the signal somewhat, these higher loadings are not desirable in real fuel cell systems due to the high cost of the precious metal. In addition, higher wt. % Pt –based catalysts tend to have larger nanoparticle sizes, resulting in lower dispersion values. This means that the gain in surface area is not as large as is often expected. The most important factor to consider here is the preparation method used. One of the aims with the codeposited PtMo/C catalysts is attempting to increase the amount of alloying between the two metals, in the same way as is achieved with PtRu systems, so that the

chemisorption properties of the catalysts will be altered making them more tolerant to the presence of CO. This is achieved by heating the samples up to 1000 °C. Particle sintering is an unfortunate side affect of this process, greatly reducing the catalyst dispersion, causing a drop in Pt area to a tenth of that seen with the unmodified Pt/C catalyst. As seen with the data obtained, this is on the limit of what can be measured to any sensible degree with the current INS spectrometer. The increased noise makes it impossible to determine if there are any real features present in the vibrational region of the spectra. Intensities can be measured, which can give an indication of the presence and amount of dissociated hydrogen, although no information regarding the adsorption sites could be obtained. Of course, the presence of Mo in the catalyst may mean that the surface of the catalyst is actually very inhomogenous. This is impossible to tell from the INS data; although cyclic voltammetry results clearly suggest this.

Peak fitting of the rotor peak was possible for the dihydrogen-dosed catalyst and is again found to be split, suggesting some of the H_2 molecules are interacting with the H/Pt surface. Three peaks were fitted, with the lowest energy peak having the greatest intensity, which indicates that the majority of H_2 molecules present are arranged parallel to the surface (a 2-D rotor). Peak fitting after introduction of CO was not possible due to the weak signal intensity.

The CSR PtMo catalyst showed an improvement in data quality as a result of improvements made to the equipment used. Splitting of the rotor peak when a large amount of free dihydrogen was left in the cell shows increased intensity of the peak shifted to slightly higher energy (14.9 meV) than that of the free molecule (14.7 meV), compared to the lower energy peak (13.1 meV). However, overlap of the higher energy peak with that corresponding to residual free H_2, as indicated by the width of the peak, means that it is not possible to correctly deduce the orientation of the weakly adsorbed H_2 molecules on the H/Pt surface based on relative peak intensities in this instance.

Both PtMo samples gave rise to a broad peak around 8 meV (approximately 70 cm^{-1}) in the INS spectra of the hydrogen-dosed catalysts. This is believed to be the result of H_2 interacting with the Mo oxides present on the surface.

An attempt to characterise the presence of bronze by obtaining spectra on the CSR catalyst before and after heating proved inconclusive.

In summary, information can be obtained for hydrogen adsorbed on a range of fuel cell catalysts, with the most information being found for the catalyst with the highest Pt surface area. While it is possible to collect spectra on modified catalysts with smaller areas, the amount of information is correspondingly less.

6 References

1. Ralph, T. R.; Hogarth, M. P. *Platinum metals Rev.* **2002**, *46*, 117.
2. Kunimatsu, K.; Uchida, H.; Osawa, M.; Watanabe, M. *Journal of Electroanalytical Chemistry* **2006**, *587*, 299.
3. Kunimatsu, K.; Senzaki, T.; Tsushima, M.; Osawa, M. *Chemical Physics Letters* **2005**, *401*, 451.
4. Tadjeddine, A.; Peremans, A. *Surface Science* **1996**, *368*, 377.
5. Tadjeddine, A.; Peremans, A. *Journal of Electroanalytical Chemistry* **1996**, *409*, 115.
6. Kelley, R. D.; Rush, J. J.; Madey, T. E. *Chemical Physics Letters* **1979**, *66*, 159.
7. Kelley, R. D.; Cavanagh, R. R.; Rush, J. J. *Journal of Catalysis* **1983**, *83*, 464.
8. Renouprez, A. J.; Jobic, H. *Journal of Catalysis* **1988**, *113*, 509.
9. Albers, P.; Auer, E.; Ruth, K.; Parker, S. F. *Journal of Catalysis* **2000**, *196*, 174.
10. Albers, P. W.; Lopez, M.; Sextl, G.; Jeske, G.; Parker, S. E. *Journal of Catalysis* **2004**, *223*, 44.
11. Parker, S. F.; Taylor, J. W.; Albers, P.; Lopez, M.; Sextl, G.; Lennon, D.; McInroy, A. R.; Sutherland, I. W. *Vibrational Spectroscopy* **2004**, *35*, 179.
12. Ramirez-Cuesta, A. J.; Mitchell, P. C. H.; Parker, S. F.; Tomkinson, J.; Thompsett, D. *Studies in Surface Science and Catalysis* **2001**, *138*, 55.
13. Mitchell, P. C. H.; Parker, S. F.; Tomkinson, J.; Thompsett, D. *Journal of the Chemical Society-Faraday Transactions* **1998**, *94*, 1489.
14. Keck, L.; Buchanan, J. S.; Hards, G. A. U.S. Patent 5,067,161, 1991.
15. Gee, A. T.; Hayden, B. E.; Mormiche, C.; Nunney, T. S. *Surface Science* **2002**, *512*, 165.
16. Silvera, I. F. *Reviews of Modern Physics* **1980**, *52*, 393.
17. Delley, B. *Journal of Chemical Physics* **2000**, *113*, 7756.
18. Ramirez-Cuesta, A. J. *Computer Physics Communications* **2004**, *157*, 226.
19. Attard, G. A.; Ahmadi, A.; Jenkins, D. J.; Hazzazi, O. A.; Wells, P. B.; Griffin, K. G.; Johnston, P.; Gillies, J. E. *Chemphyschem* **2003**, *4*, 123.

20. Curulla, D.; Clotet, A.; Ricart, J. M.; Illas, F. *Journal of Physical Chemistry B* **1999**, *103*, 5246.
21. Maniguet, S.; Mathew, R. J.; Russell, A. E. *Journal of Physical Chemistry B* **2000**, *104*, 1998.
22. Georgiev, P. A.; Ross, D. K.; De Monte, A.; Montaretto-Marullo, U.; Edwards, R. A. H.; Ramirez-Cuesta, A. J.; Colognesi, D. *Journal of Physics-Condensed Matter* **2004**, *16*, L73.
23. FitzGerald, S. A.; Yildirim, T.; Santodonato, L. J.; Neumann, D. A.; Copley, J. R. D.; Rush, J. J.; Trouw, F. *Physical Review B* **1999**, *60*, 6439.
24. Ramirez-Cuesta, A. J.; Mitchell, P. C. H.; Parker, S. F.; Barrett, P. A. *Chemical Communications* **2000**, 1257.
25. Ramirez-Cuesta, A. J.; Mitchell, P. C. H.; Parker, S. F. *Journal of Molecular Catalysis a-Chemical* **2001**, *167*, 217.
26. Mitchell, P. C. H.; Parker, S. F.; Ramirez-Cuesta, A. J.; Tomkinson, J. *Vibrational Spectroscopy with Neutrons*; World Scientific, 2005.
27. Novaco, A. D.; Wroblewski, J. P. *Physical Review B* **1989**, *39*, 11364.
28. Mitchell, P. C. H.; Tomkinson, J.; Grimblot, J. G.; Payen, E. *Journal of the Chemical Society-Faraday Transactions* **1993**, *89*, 1805.
29. Glemser, O.; Lutz, G.; Meyer, G. *Zeitschrift für anorganische und allgemeine Chemie* **1956**, *285*, 173.
30. Glemser, O.; Lutz, G. *Zeitschrift für anorganische und allgemeine Chemie* **1951**, *264*, 17.
31. Endres, F.; Schwitzgebel, G. *Journal of Electroanalytical Chemistry* **1996**, *415*, 23.
32. Zhang, H. Q.; Wang, Y.; Fachini, E. R.; Cabrera, C. R. *Electrochemical and Solid State Letters* **1999**, *2*, 437.
33. Benson, J. E.; Kohn, H. W.; M., B. *Journal of Catalysis* **1966**, 307.
34. Ressler, T.; Wienold, J.; Jentoft, R. E. *Solid State Ionics* **2001**, *141*, 243.
35. Birtill, J. J.; Dickens, P. G. *Journal of Solid State Chemistry* **1979**, *29*, 367.
36. Eda, K. *Journal of Materials Chemistry* **1992**, *2*, 533.
37. Dickens, P. G.; Birtill, J. J.; Wright, C. J. *Journal of Solid State Chemistry* **1979**, *28*, 185.

Chapter Six: Conclusions and Further Work

The aim of this thesis has been to evaluate a series of carbon-supported Pt-based catalysts that have been modified by the addition of a secondary metal for the purpose of achieving improved performance as anode catalysts in Polymer Electrolyte Membrane Fuel Cells (PEMFCs) when operating with reformate fuel streams containing impurities such as CO and CO_2 when compared with Pt alone.

A study of a series of PtMo catalysts prepared by varying routes and with a range of compositions was carried out in chapter 3. Catalysts of this type are able to promote the oxidation of CO adsorbed on Pt to CO_2 at lower potentials than with Pt alone by the donation of oxygen from neighbouring Mo oxyhydroxide species. Catalysts were characterized using cyclic voltammetry and XAS techniques in order to yield compositional information. Catalysts prepared via the codeposition route were shown to have the greatest degree of mixing between the Pt and Mo in the sample, however in all cases the ratio of Mo: Pt at the surface was greater than in the bulk of the nanoparticles. Increasing the temperature of the subsequent heat treatments was found to drive more Mo into the bulk, although no true PtMo alloys could be formed under these conditions. The surface modified PtMo sample was shown to be present predominantly as a surface oxide; however this was seen to be reduced by lowering the potential, leading to increased association with the surface Pt atoms. The technique used to prepare this catalyst was found to offer better control of the Mo deposition than observed previously.

Comparative XAS studies of a number of different PtMo samples were carried out in a half cell environment, and with the more realistic conditions found in an *in situ* XAS mini cell. Using the mini cell was found to limit the amount of Mo dissolution taking place by virtue of the presence of a solid electrolyte. The catalyst environment found in the mini cell was seen to induce a permanent reduced state for PtMo catalysts prepared via the Mo oxide precursor reaction with Pt/C route, while those prepared via the codeposition route were able to be oxidised with potential, as required for increased CO tolerance via the promotional mechanism. The codeposited catalysts have an

increased proportion of Mo-Pt interfaces and improved Mo mobility making this the preferred preparation route, with the PtMo catalyst with a 2: 1 ratio having the highest activity for hydrogen oxidation when operating with reformate fuel streams.

A study of a set of co-deposited bimetallic platinum-tungsten catalysts was carried out in chapter 4. Catalysts were characterized using cyclic voltammetry and XAS techniques in order to yield compositional information. The overlap of absorption edges and similar backscattering amplitudes of Pt and W led to some difficulties in obtaining EXAFS data; however, it was still possible to show that the sample tested was not well-mixed, with the majority of the tungsten present on the surface of the catalyst particles as an oxide. When in a half cell environment, the surface tungsten became slightly reduced as characterized by a 50 % drop in oxygen neighbours and a corresponding small increase in first shell metal neighbours. Unlike results observed with similar PtMo catalysts, the tungsten was not completely reduced by decreasing the applied potential, instead remaining in a significantly oxidized state. While it was shown that the catalyst tested was not present as a well-mixed sample or alloy, the presence of the surface oxides was found to be instrumental in the oxidation at low overpotentials of some of the adsorbed CO to CO_2 at Pt-W interface sites, as observed by a pre-wave peak in the cyclic voltammograms.

The formation of hydrogen tungsten bronzes was observed by cyclic voltammetry and directly linked to the process of catalyst aging occurring by exposure to atmospheric water vapour. This process was found to be reversed by heating the samples to 200 °C. Hydrogen tungsten bronzes have been mentioned in the literature as being desirable due their extended reaction zone for the oxidation of hydrogen. However, no significant performance was observed for the bronze form of the catalysts compared to the non-bronze forms. No real enhancement for methanol oxidation was observed compared to a standard Pt/C catalyst. Single cell testing of hydrogen oxidation using reformate fuel streams showed that, while there was enhanced tolerance to CO by virtue of the promotional effect of the surface W oxides, there was no further increase in performance observed when the bronze was present. Further work could involve testing a larger set of carbon-supported platinum-tungsten catalysts prepared with differing atomic ratios and by varying methods, including the Controlled Surface Modification (CSR) process. In addition, EXAFS data should be collected for these

catalysts within the XAS mini cell to determine the catalyst structure under more realistic conditions.

Inelastic Neutron Scattering studies were carried out on Pt and PtMo-based electrocatalysts for hydrogen oxidation in PEMFCs, and the results reported in chapter 5. These experiments are the first examples of studying the interactions of the H_2 molecule with hydrogen and carbon monoxide-modified Pt nanoparticle surfaces, as well as marking the first time that PtMo-based catalysts have been investigated using INS. The Pt/C catalyst was found to have the highest quality data out of the three systems studied, as a result of the larger available Pt surface area. Features in the vibrational region of the hydrogen-modified catalyst spectrum were fitted by comparison with theoretical data derived using DFT methods and used to show that the hydrogen atoms are located predominantly in hollow (three-fold) sites on Pt(111), with some contribution from hydrogen on multi-fold adsorption sites on a Pt(110) plane. Due to experimental limitations resulting from the equipment used, the signal from the PtMo-based catalysts was too low to enable equivalent fitting of the vibration region of the spectra.

The splitting and shifting of the H_2 rotor peak was used to identify the strength of the interactions with the hydrogen and carbon monoxide modified Pt surfaces. The hydrogen molecule interacting with the H/Pt surface of the Pt/C sample was found to be strongly perturbed, with the hydrogen molecule appearing to be orientated perpendicular to the metal surface. In contrast to this, dihydrogen interacting with the carbon monoxide-modified sample was found to be only weakly associated with the catalyst surface. Peak fitting of the H_2 rotor peak for the codeposited PtMo/C sample was used to determine that there is again a strong interaction between molecular hydrogen and the H/Pt surface, however, the hydrogen molecules appeared to be preferentially arranged parallel to the metal surface. In addition, the hydrogen-modified spectra for both this and the CSR PtMo/C catalyst show evidence of H_2 interacting with Mo oxides on the surface of the catalyst particles. An attempt to characterise the presence of a hydrogen molybdenum bronze by obtaining spectra on the CSR catalyst before and after heating proved inconclusive. Further work could include investigating ways of maximising the signal-to-noise ratio obtainable by improvements in the experimental set-up used to collect the INS data, in order to more

fully characterise the vibrational region of the spectra for the PtMo samples, as well as extending the work to include other catalyst materials, such as PtRu and PtW, to characterise both hydrogen- and carbon monoxide-modified surfaces.